



HAL
open science

Solvation and adsorptions at the solid / water interface : developments and applications

Paul Clabaut

► **To cite this version:**

Paul Clabaut. Solvation and adsorptions at the solid / water interface : developments and applications. Theoretical and/or physical chemistry. Université de Lyon, 2021. English. NNT : 2021LYSEN015 . tel-03284332

HAL Id: tel-03284332

<https://theses.hal.science/tel-03284332>

Submitted on 12 Jul 2021

HAL is a multi-disciplinary open access archive for the deposit and dissemination of scientific research documents, whether they are published or not. The documents may come from teaching and research institutions in France or abroad, or from public or private research centers.

L'archive ouverte pluridisciplinaire **HAL**, est destinée au dépôt et à la diffusion de documents scientifiques de niveau recherche, publiés ou non, émanant des établissements d'enseignement et de recherche français ou étrangers, des laboratoires publics ou privés.



Numéro National de Thèse : 2021LYSEN015

THÈSE DE DOCTORAT DE L'UNIVERSITÉ DE LYON

opérée par

l'École Normale Supérieure de Lyon

École Doctorale N° 206

École Doctorale de Chimie (Chimie, Procédés, Environnement)

Spécialité : Chimie Théorique

Discipline : Chimie

Soutenue publiquement le 11/06/2021, par :

Paul CLABAUT

Solvation and adsorptions at the solid/water interface : Developments and applications

Solvation et adsorptions à l'interface solide/eau : Développements et applications

Devant le jury composé de :

| | | | |
|-------------------|---------------------------|-------------------------------|-----------------------|
| Marialore SULPIZI | Professeure | Johannes Gutenberg University | Rapporteuse |
| Romuald POTEAU | Professeur | Université Paul Sabatier | Rapporteur |
| Carine CLAVAGUERA | Directrice de Recherche | Université Paris-Saclay | Examinatrice |
| Mathieu SALANNE | Professeur | Sorbonne Université | Examineur |
| Carine MICHEL | Chargée de recherche CNRS | ENS de Lyon | Directrice de thèse |
| Stephan STEINMANN | Chargé de recherche CNRS | ENS de Lyon | Co-encadrant de thèse |

J'ai marqué « vivre » sur la liste des choses à faire avant de mourir
Ouais je vais me bouger et ranger ce bazar, car le hasard fait bien les choses
Mais on ne fait jamais de choses bien par hasard

Aujourd'hui ce qui fera déborder le vase sera un bouquet de fleur

BigFlo et Oli



Acknowledgements

La liste des personnes à remercier pour cette thèse est longue, puisque presque chaque personne que j'ai croisé pendant ces 3(+) années a contribué, de près ou de loin, à mon état et donc à ma capacité à mener cette thèse.

Je tiens à remercier plus particulièrement Carine et Stephan, mes deux directeurs de thèse - quoi qu'en disent les papiers administratifs - qui m'ont épaulé dans ma thèse mais aussi dans toute ma vie pendant ces quelques années. Merci pour tout. Pour toutes les connaissances sur la science mais également sur le fonctionnement du monde académique. Pour l'aide technique, mais aussi pour tout les coups de pouces liés à l'organisation, l'administration, et la construction de mon parcours. Pour les heures de discussions sur tout et n'importe quoi, au bureau, en salle café ou ailleurs. Pour la bonne humeur et le soutien indéfectible, et tout le temps accordé. Pour tous ces projets variés, ces collaborations et ces voyages. Merci.

Un immense merci aussi à celle qui est devenue ma femme au cours de ce voyage : Emma. Merci d'avoir toujours été là, même si nos impératifs nous ont souvent maintenus à distance. Merci d'avoir supporté mes répétitions orales, mes moments d'inquiétude, de mélancolie, de fatigue... Merci pour ces semaines confinées pendant lesquels nous avons enfin pu passer plus de temps ensemble. Merci d'avoir été le liant de tout ceci mais aussi d'avoir pu me sortir de mon univers de temps en temps.

Tout particulièrement aussi, merci à Vicky, mon coloc' et ami si proche. Nous avons en quelque sorte fait notre thèse en un duo fort équilibré. On a ri ensemble, décompressé ensemble, stressé ensemble des fois aussi. Je n'ose compter le nombre d'heures de films et séries partagés. Je souhaite à tout le monde de s'entendre aussi bien sur tout avec un colocataire. Un grand merci pour tout et pour cette amitié qui n'est pas prête de se terminer et bonne chance pour tes expériences futures. Et rendez-vous au nouvel an!

Merci à tous mes amis, du labo, de l'ENS, d'enfance ou d'ailleurs. Merci à Vincent, Matthieu, Félix, et Nono, mon inséparable bande d'amis lyonnais, compagnons de tant d'après-midi de jeux, de films, de séances de ciné, de restaurant, de vacances et de bon moments tout

Acknowledgements

simplement. Merci aussi à ceux, plus lointains mais toujours présents avec nous : Estelle, Théo, Louis... Merci à Emilien, Côme, Dodo et Laurie aussi, pour tout ce que vous avez fait pour moi avant la thèse, mais aussi pour m'avoir offert des bouffés d'air frais en dehors du monde de la recherche de temps à autre. Merci à Florence, Benjamin, Martin, Thibault, Pauline, Sarah, Ruben, Tao et Jérôme qui ont fait du labo un lieu d'échange en plus du travail, et de belles discussions à bâtons rompus. Merci aux collègues de la salle café, Christian, JC, Delphine, Sandrine, Laure, Olivier, Yann... pour toutes ces discussions et râleries partagées.

Merci aussi à ma famille, toujours là quand c'était nécessaire, merci pour les repas de famille « comme avant », pour les vacances, pour avoir (même si c'est toujours très difficile de l'extérieur) suivi ce que je faisais et mes échéances.

Merci, en général, à tout ceux que j'ai croisé et qui m'ont offert de bon moments, ma belle-famille, les Dauphins de Montplaisir, les lurons de Jackam', les gens de l'ultimate, les cinéphiles de tout poils, et tant d'autres... Merci.



Abstract

This Ph.D. thesis investigates the impact of solvation on adsorption at the solid/water interface and presents method developments to unravel and realistically capture these effects in theoretical studies.

The SolvHybrid package was built to compute the solvation free energy difference between a molecule solvated in bulk water and adsorbed at the Pt(111)/ water interface. SolvHybrid is based on a hybrid QM/MM description and thermodynamic integration. The scheme was validated on experimentally available adsorption free energies of benzene and phenol. To increase the quality of its MM description and widen the applicability of SolvHybrid beyond the Pt(111)/water interface, forcefield developments have been pursued.

The pairwise additive GAL19 forcefield was proposed to model water/noble-metal interactions. It demonstrated a great accuracy to reproduce the adsorption energy of a water molecule on ten metallic (100) or (111) surface made of Cu, Ag, Au, Pd, Pt. This force field was later extended to more corrugated surfaces and nano-particles. To understand the limitations of our pairwise additive force field for water layer structures, we also decomposed the total interaction energy of water layers on metallic surfaces as computed by DFT. Apart from additive water/metal contributions, polarisation and charge-transfer were determined and quantified as major many-body effects, suggesting routes to second generation forcefields.

Metallic oxides were then investigated as a subsequent step in surface complexity, because of their tendency to react and even restructure in contact with water. Metadynamics was chosen to investigate the surface reconstruction of alumina in water. Our work demonstrated the crucial role of the surface water structure in this process and its modification in the presence of adsorbates. A panoply of methods (SolvHybrid, a GAL19-inspired forcefield, metadynamics, and thermodynamic integration) were then applied and compared on the complex chemistry of the adsorption of ethanol on alumina in water, combining all previous challenges.

Keywords: Solvation, water/solid interface, adsorption, methods, alumina



Résumé

Cette thèse étudie l'impact de la solvatation sur l'adsorption à l'interface solide/eau et présente des développements méthodologiques afin d'expliquer et de reproduire de manière réaliste ces effets au sein d'études théoriques.

Elle présente le développement du programme SolvHybrid, conçu pour évaluer la différence d'énergie libre de solvatation associée à l'adsorption d'une molécule à l'interface eau/Pt(111). SolvHybrid s'appuie sur une description hybride QM/MM et la méthode de l'intégration thermodynamique. Ses prédictions sont validées par des données expérimentales. L'extension de son domaine d'application à d'autres métaux et de sa précision nécessite des développements supplémentaires.

Le champ de force GAL19 est proposé pour simuler les interactions eau/métal noble. Il reproduit avec une grande précision les énergies d'adsorption de molécules d'eau sur 10 surfaces métalliques (100) ou (111) de Cu, Ag, Au, Pd ou Pt ainsi que sur des surfaces imparfaites et des nanoparticules. On propose également une décomposition de l'énergie totale DFT d'adsorption de différents modèles de couches d'eau sur des surfaces métalliques qui démontre l'importance de la polarisation et du transfert de charges dans l'adsorption, une piste pour de futurs développements de champs de force.

On étudie ensuite les surfaces d'oxydes métalliques pour leur tendance à modifier leur surface dans l'eau. On démontre par une étude de métadynamique le rôle de la modification de structure de l'eau en présence d'adsorbats dans le processus d'hydrolyse de l'alumine. On propose ensuite un parangonnage de méthodes pour étudier le complexe problème de l'adsorption de l'éthanol sur l'alumine dans l'eau.

Mots-clés : Solvatation, interface solide/eau, adsorption, méthodologie, alumine



Contents

| | |
|--|------------|
| Acknowledgements | v |
| Abstract | vii |
| Résumé | ix |
| Table of Contents | xi |
| Introduction | 1 |
| References | 3 |
| 1 Bibliographic study | 5 |
| 1.1 Static approaches of adsorption at liquid water/solid interface | 6 |
| 1.2 Dynamic approaches of the adsorption: the rare event problem | 10 |
| 1.2.1 Adsorption on metallic surfaces : the possibility to decorrelate surface reactivity and solvation | 11 |
| 1.2.2 Adsorption on oxides surfaces: accelerating the sampling with the rare events methods | 14 |
| 1.3 Lower levels of description for water/solid interactions | 19 |
| 1.4 Conclusion | 21 |
| References | 21 |
| I Computing adsorption free energies at the liquid water/metal interface | 31 |
| 2 Solvation Free Energies and Adsorption Energies at the Metal/Water Interface from Hybrid Quantum-Mechanical/Molecular Mechanics Simulations | 35 |
| 2.1 Introduction | 37 |
| 2.2 Theory | 39 |
| 2.2.1 SolvHybrid: Principles and Workflow | 39 |
| 2.2.2 Electrostatic interactions between the solvent and the metallic surface . | 41 |
| 2.3 Computational Details | 42 |
| 2.3.1 Molecular mechanics simulations | 42 |
| 2.3.2 DFT computations | 43 |
| 2.3.3 MM setup via SolvHybrid | 44 |
| 2.3.4 Settings for thermodynamic integrations | 44 |

Contents

| | | |
|--|--|------------|
| 2.4 | Results and discussion | 45 |
| 2.4.1 | H ₂ O@Pt(111) solvation energies to monitor inconsistencies | 46 |
| 2.4.2 | Solvation free energy of the Pt(111) surface | 49 |
| 2.4.3 | Adsorption of benzene and phenol at the Pt(111)/water interface | 50 |
| 2.5 | Conclusion | 54 |
| | References | 54 |
| II Investigating water/metal interactions | | 63 |
| 3 Ten Facets, One Force Field: The GAL19 Force Field for Water - Noble Metal Inter- faces | | 67 |
| 3.1 | Introduction | 69 |
| 3.2 | Theory | 71 |
| 3.2.1 | Object definitions and functional form | 71 |
| 3.2.2 | Fitting method and data set | 75 |
| 3.3 | Computational details | 76 |
| 3.3.1 | DFT | 76 |
| 3.3.2 | Molecular Mechanics | 76 |
| 3.4 | Results and discussion | 77 |
| 3.4.1 | Low-coverage water adsorption | 77 |
| 3.4.2 | Ice layers on the (111) facets | 81 |
| 3.4.3 | The mono-metallic/water interface | 82 |
| 3.4.4 | Water structure at the alloy/water interface | 86 |
| 3.5 | Conclusion | 90 |
| | References | 90 |
| 4 Beyond the extended metallic surface/water interface with the GAL21 force field | | 99 |
| 4.1 | Introduction | 100 |
| 4.2 | Theory | 101 |
| 4.2.1 | Computation of GCN | 101 |
| 4.2.2 | GAL21 functional form | 102 |
| 4.2.3 | Fitting method and data set | 105 |
| 4.3 | Computational details | 106 |
| 4.4 | Results | 107 |
| 4.5 | Discussion and Conclusion | 110 |
| | References | 111 |
| 5 Water adlayers on noble metal surfaces: Insights from energy decomposition analy- sis | | 115 |
| 5.1 | Introduction | 116 |
| 5.2 | Methods | 117 |
| 5.3 | Computational Details | 120 |
| 5.4 | Results and Discussion | 121 |
| 5.4.1 | Relative Stability of Ice-like Layers | 121 |

| | |
|---|------------|
| 5.4.2 Electronic Analysis | 122 |
| 5.4.3 Energy Decomposition Analysis | 124 |
| 5.5 Conclusion | 135 |
| References | 135 |
| III Unravelling the link between hydration and adsorption on reactive oxide surfaces | |
| | 143 |
| 6 Reactivity of shape-controlled crystals and metadynamics simulations | |
| | 147 |
| 6.1 Introduction | 148 |
| 6.2 Methods | 149 |
| 6.2.1 Atomistic model. | 149 |
| 6.2.2 Molecular simulations. | 149 |
| 6.2.3 Theoretical aspects of Metadynamics | 150 |
| 6.3 Results and Discussion | 152 |
| 6.3.1 Identification of the facet whence the decomposition initiates. | 152 |
| 6.3.2 Identification of the atomic sites on the (110) facet whence the decomposition initiates. | 154 |
| 6.3.3 Xylitol/water interface | 155 |
| 6.3.4 Reactivity with chemisorbed xylitol. | 158 |
| 6.4 Conclusions | 161 |
| References | 161 |
| 7 Adsorption study of ethanol at the γ-alumina/water interface | |
| | 167 |
| 7.1 Introduction | 168 |
| 7.2 Computational details | 169 |
| 7.2.1 Initial structures | 169 |
| 7.2.2 General parameters for DFT dynamics | 170 |
| 7.2.3 Free energy differences | 171 |
| 7.2.4 Specific parametrization for the metadynamics study (section 7.3.1) | 171 |
| 7.2.5 General parameters for static DFT computations with VASP | 172 |
| 7.2.6 Molecular mechanics computations with AMBER | 173 |
| 7.2.7 Specific parametrization for the Thermodynamic integration study (section 7.3.3) | 173 |
| 7.3 Results | 174 |
| 7.3.1 Metadynamics | 174 |
| 7.3.2 Thermodynamic differences | 178 |
| 7.3.3 Thermodynamic Integration | 180 |
| 7.4 Conclusion and discussion | 182 |
| References | 183 |
| Conclusions and Outlook | |
| | 187 |

| | |
|---|------------|
| Appendix | 189 |
| A Solvation Free Energies and Adsorption Energies at the Metal/Water Interface: Appendix | 191 |
| A.1 Thermodynamic integration: The principle | 192 |
| A.2 Logarithmic spacing for TI windows | 192 |
| A.3 Comparison with Particle Mesh Ewald Electrostatics | 194 |
| A.4 Error Estimates for Adsorption Free Energies | 194 |
| A.5 Details for Surface Energy Computation | 195 |
| A.6 Most Stable Adsorption Configuration for Phenol on Pt(111) | 195 |
| A.7 Study of the of Local Coverages | 197 |
| A.8 Decomposition Analysis | 198 |
| References | 198 |
| B The GAL19 Force Field for Water - Noble Metal Interfaces: Appendix | 201 |
| B.1 Configuration set | 202 |
| B.1.1 Complete set | 202 |
| B.1.2 Fitting set | 203 |
| B.2 Force-field parameters | 203 |
| B.3 Additional Tables and Figures | 205 |
| References | 205 |
| C The GAL21 force field: Appendix | 219 |
| C.1 Configuration set | 220 |
| C.1.1 Complete set | 220 |
| C.1.2 Fitting set | 221 |
| C.2 Force-field parameters | 221 |
| C.3 Additional Tables and Figures | 223 |
| D Water adlayers on noble metal surfaces: Appendix | 225 |
| D.1 Additional Analysis | 226 |
| D.1.1 Water–Water interaction | 226 |
| D.2 Additional Tables and Figures | 226 |
| References | 226 |
| E Reactivity of shape-controlled crystals and metadynamics simulations: Appendix | 235 |
| E.1 Experimental methods | 236 |
| E.2 γ -Al ₂ O ₃ nanoparticles with different shapes | 237 |
| E.3 Adsorption of Sorbitol and Xylitol and Inhibition of Decomposition | 239 |
| E.3.1 Adsorption isotherms | 239 |
| E.3.2 Inhibition of decomposition and inhibiting coverage | 241 |
| E.3.3 Relation between inhibiting coverages and the morphology of the nanoparticles. | 242 |
| E.3.4 Can kinks and edges be involved in the decomposition mechanism of alumina? | 243 |

References 244



Introduction

Water/solid interfaces are ubiquitous as water covers 71% of the earth and are responsible for myriads of natural chemical transformations (corrosion,¹ fouling,² ...). But also, as many chemical species can easily be solvated at standard operation conditions, many industrial processes are conducted at these water/solid interfaces, for example in the fields of tribology,³ heterogeneous catalysis⁴ and electrochemistry.^{5;6} However, little is actually known about these complex systems. Indeed, experimental knowledge about water/solid interfaces is hindered by the difficulty to recover information and signal from the very small volume of the interface compared to the massive one of the bulk solid and liquid that it separates.

Available information about water structuration at these interfaces are therefore limited to very thin water layers in vacuum chamber (obtained *via* spectroscopy^{7;8} or microscopy⁹) or under applied electric potentials (deduced from electrochemical measurement).¹⁰ Moreover, water being quite reactive and having a high chemical affinity for many different solids like metal and oxides, its structuration is believed to vary extensively depending on the nature or morphology of the surface it covers. Also, to understand chemical processes at the liquid water/solid interface, investigating surface solvation energies is not sufficient, and attention must be paid to its modification in presence of other molecules adsorbed at the interface, and reciprocally, to the solvation change undergone by these adsorbed molecules compared to the bulk liquid phase. The interactions of water with both the molecule and the surface can drastically modify the adsorption properties of the molecule. Not forgetting that the surface structure can also restructure itself when immersed in water, thus affecting any other adsorption. It is really a subtle triangular interaction that is at stake between the liquid water, the solid, and adsorbed molecules at the water/solid interface. Each one of them is affected by the other two and each interaction between two of them is affected by the third one as schematically illustrated in Fig. 1. This complex triangle is the main concern of the present work. The major problem in studying this triangle lies in the absence of efficient and accurate pre-established tools to simulate water/solid interfaces. Indeed the coexistence of a solid presenting a band electronic structure, thus requiring accurate electronic description, with a liquid, featuring a high-dimension phase space, remains a challenge for theoretical models. Our goal is therefore to develop tools and methodology to carry these simulations

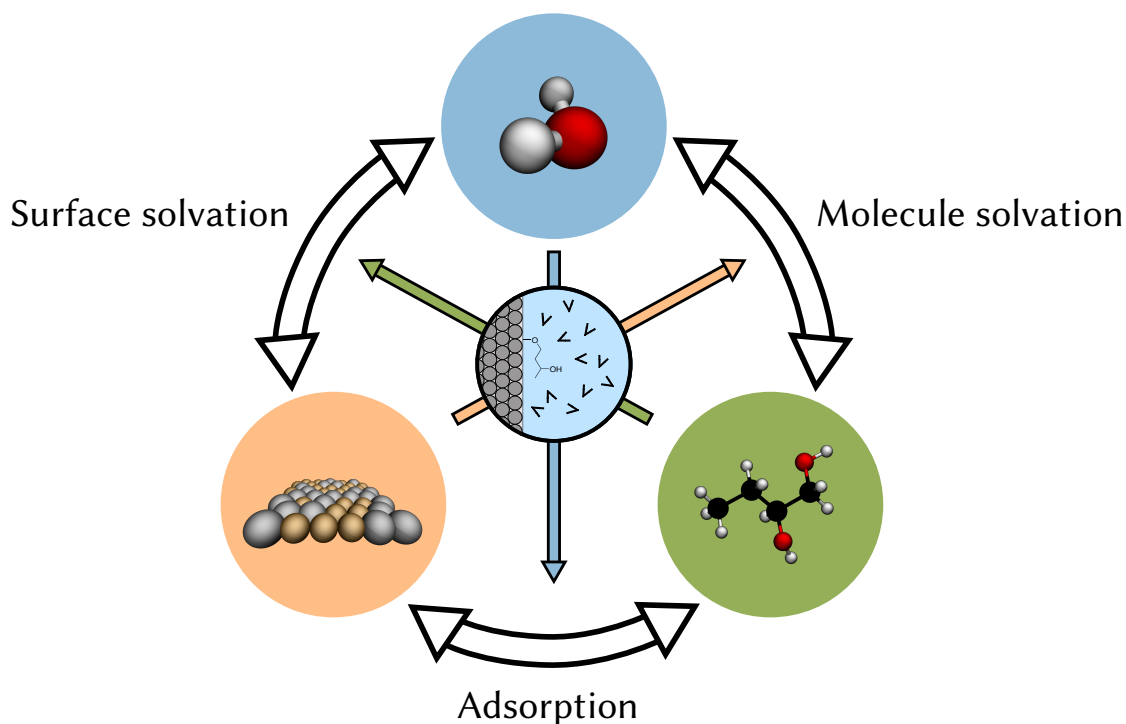


Figure 1 – Schematic representation of the three kinds of chemical systems interacting in the process of adsorption at the water/solid interface.

and understand the entanglements between the solvation and the adsorption of compounds at the liquid water/solid interface. To cover these topics, the present manuscript is organised as follows:

At first, in chapter 1, we propose a review of the state-of-the-art methodology relevant to the computation of adsorption energy at the liquid water/solid interfaces. We present the limitation of static computations but also the necessity to go beyond pure molecular dynamics, toward thermodynamic cycles and rare events methods, articulated about the example of molecule adsorption at the water/metal and water/oxides interfaces.

Having identified the hybrid quantum/classical simulations as a promising candidate to compute adsorption free energy differences at the water/solid interface, we present in part I an extension of the MM-FEP computation scheme¹¹ as a fully operational computational package (named SolvHybrid) designed to compute adsorption free energies of compounds at the liquid water/solid interface and validated on experimental data for the adsorption of benzene and phenol on Pt (111) surfaces.

In order to extend the applicability of the SolvHybrid underlying method to other surfaces and metals, we investigate the possibilities of the description of water/metal interactions in part II. Indeed, few available force-fields were entirely satisfying in terms of both accuracy and

wide application to diverse metallic surfaces and we decided to build novel formulations and proposed leads to future enhancement of our force-fields.

Stepping up in complexity, we decided to investigate oxide surfaces in part III, bringing up the problem of water reactivity at the surface. We studied the role of water in the hydrolysis of alumina and the interactions between water molecules and adsorbed alcohols that can prevent this hydrolysis.

The present manuscript presents the main developments that we proposed to enlarge the possibilities of theoretical investigations of the adsorption at the water/solid interfaces. These developments range from novel force field functional forms to reproduce water/metal interactions to a complete computational package predicting solvation energies at the interfaces, through adaptation of existing methods to the water/solid interface challenges. Using these tools, we also acquired knowledge about the interfacial structuration of water in contact with metallic or oxide surfaces, about the impact of solvation on the adsorption of organic molecules, but also about the evolution of surface states in contact with water. These tools and knowledge are important steps toward the understanding of the subtle triangular interactions between adsorbed molecules, surfaces, and water, even if we also demonstrate that numerous questions remain unanswered.

Bibliography

- [1] Schweitzer, P. A. *Fundamentals of Corrosion : Mechanisms, Causes, and Preventative Methods*; CRC Press, 2009.
- [2] Institution, W. H. O. *Marine fouling and its prevention ; prepared for Bureau of Ships, Navy Dept.*; United States Naval Institute, 1952; Accepted: 2005-11-23T20:52:48Z.
- [3] Shenghua, L.; He, Y.; Yuansheng, J. Lubrication Chemistry Viewed from DFT-Based Concepts and Electronic Structural Principles. *Int. J. Mol. Sci.* **2003**, 5, 13.
- [4] Ravenelle, R. M.; Copeland, J. R.; Van Pelt, A. H.; Crittenden, J. C.; Sievers, C. Stability of Pt/ γ -Al₂O₃ Catalysts in Model Biomass Solutions. *Top Catal* **2012**, 55, 162–174.
- [5] Akpa, B. S.; D'Agostino, C.; Gladden, L. F.; Hindle, K.; Manyar, H.; McGregor, J.; Li, R.; Neurock, M.; Sinha, N.; Stitt, E. H.; Weber, D.; Zeitler, J. A.; Rooney, D. W. Solvent effects in the hydrogenation of 2-butanone. *J. Catal.* **2012**, 289, 30.
- [6] Seh, Z. W.; Kibsgaard, J.; Dickens, C. F.; Chorkendorff, I.; Nørskov, J. K.; Jaramillo, T. F. Combining theory and experiment in electrocatalysis: Insights into materials design. *Science* **2017**, 355, eaad4998.

Contents

- [7] Schiros, T.; Andersson, K. J.; Pettersson, L. G. M.; Nilsson, A.; Ogasawara, H. Chemical bonding of water to metal surfaces studied with core-level spectroscopies. *Journal of Electron Spectroscopy and Related Phenomena* **2010**, *177*, 85–98.
- [8] Velasco-Velez, J.-J.; Wu, C. H.; Pascal, T. A.; Wan, L. F.; Guo, J.; Prendergast, D.; Salmeron, M. The structure of interfacial water on gold electrodes studied by x-ray absorption spectroscopy. *Science* **2014**, *346*, 831–834.
- [9] Björneholm, O.; Hansen, M. H.; Hodgson, A.; Liu, L.-M.; Limmer, D. T.; Michaelides, A.; Pedevilla, P.; Rossmeisl, J.; Shen, H.; Tocci, G.; Tyrode, E.; Walz, M.-M.; Werner, J.; Bluhm, H. Water at Interfaces. *Chem. Rev.* **2016**, *116*, 7698–7726.
- [10] Toney, M. F.; Howard, J. N.; Richer, J.; Borges, G. L.; Gordon, J. G.; Melroy, O. R.; Wiesler, D. G.; Yee, D.; Sorensen, L. B. Voltage-dependent ordering of water molecules at an electrode–electrolyte interface. *Nature* **1994**, *368*, 444–446.
- [11] Steinmann, S. N.; Sautet, P. Assessing a First-Principles Model of an Electrochemical Interface by Comparison with Experiment. *J. Phys. Chem. C* **2016**, *120*, 5619–5623, Publisher: American Chemical Society.



1 Bibliographic study

In the following chapter, we provide an overview of the methods that have been employed to investigate the adsorption of molecules at the liquid water/solid interface. We classify them roughly by computational cost, thus going from heaviest approximations and low cost to more advanced but expensive ones. We start with static methods. We present the different approximations invoked to reproduce the effect of the solvent on the adsorption of molecules without actually sampling the interface's phase space. We then address the dynamic methods and the problem of unreasonably long sampling required to establish the thermodynamics and kinetics of adsorption at the solid/liquid interface. From this point, we distinguish two kinds of liquid water/solid interfaces: those featuring a metallic surface (with limited surface reactivity in water) and those featuring an oxide surface (undergoing surface reconstruction or surface state change at usual operating conditions). For metallic surfaces, because their surface state can be considered as unreactive towards water, we may consider methods dividing adsorption into two decorrelated steps: the interaction between the molecule and the metallic surface on one hand, and the water restructuring on the other hand. The free energy difference corresponding to the two steps can then be obtained at different levels of theory: quantum mechanics for molecule/surface interaction and classical mechanics for water restructuring. Hence, we present also a quick overview of the force-fields available for the liquid water/metal interfaces, required for the classical simulation. For oxide surfaces, the surface reactivity implies that the most stable surface state may depend on the presence of adsorbed molecules, which prevents the elaboration of a simple two-steps decomposition. Therefore, we present the biased molecular dynamics approach that accelerates rare events. Rare event methods can deal with the large phase space of such systems by biasing the exploration of some well-chosen degrees of freedom during a dynamic sampling. Unless specified otherwise, the method to evaluate the energy of a system relies on Density Functional Theory (DFT). Indeed, the accuracy and capability to describe chemical reactions of DFT are required to describe the chemisorption at the interface as well as the band-structure of surfaces.

1.1 Static approaches of adsorption at liquid water/solid interface

To begin with, let us consider the static methods, relying on energy differences between optimised geometries for the solvated molecule (M), solid surface (S), and molecule adsorbed on the surface (M@S). This means that we limit ourselves to static computations that only result in a structure of the chemical system at 0 K. Therefore, these static computations cannot account for all the possible other structures that can be reached by thermal fluctuations at 300 K and feature different bond lengths or interactions between molecules. This means that some interactions between molecules will be overestimated or underestimated. A first very crude approximation to compute these energy differences is to completely neglect the solvent, thus conducting gas-phase computations. Adsorption free energy ($\Delta_{ads}G$) can be approximated by adding analytical entropic terms to the adsorption energy computed by DFT

1.1. Static approaches of adsorption at liquid water/solid interface

($\Delta_{ads}E = E(M@S) - E(M) - E(S)$). These analytical terms account for the biggest contributions of non-sampled translational and rotational degrees of freedom, while the less important vibrational degrees of freedom are usually neglected. The analytical forms are based on the model of an ideal gas with molecules acting as non-interacting rigid rotators:

$$S_{trans} = k_b \left[\ln \left(\left(\frac{2\pi m k_b T}{h^2} \right)^{\frac{3}{2}} \frac{k_b T}{P^\circ} \right) + \frac{5}{2} \right] \quad (1.1)$$

$$S_{rot} = k_b \left[\ln \left(\left(\frac{8\pi^2 k_b T}{h^2} \right)^{\frac{3}{2}} \frac{\sqrt{\pi I_A I_B I_C}}{\sigma} \right) + \frac{3}{2} \right] \quad (1.2)$$

with k_b and h being Boltzmann's and Planck's constants, m the mass of the molecule, I_X its principal moments of inertia and σ the number of rotations upon which the molecule is invariant, T the temperature of the system, and P° the standard pressure (1 atm).

When studying adsorption free energy differences, it is usually considered that the rotational and translational degrees of freedom of a molecule become additional vibrational motions upon adsorption and are, thus, neglected for M@S.¹

$$\Delta_{ads}G \approx \Delta_{ads}E - T\Delta_{ads}S = \Delta_{ads}E + TS_{trans,gas} + TS_{rot,gas} \quad (1.3)$$

A possibility to account also for the presence of the solvent is here to modify these two entropic terms by semi-empirical relations mimicking the reduced translational and rotational freedom in water:²

$$S_{aq} = 0.54 \cdot S_{gas} + 2.86 \cdot 10^{-4} \text{ (eV} \cdot \text{K}^{-1}) \quad (1.4)$$

But, of course, reducing the translational and vibrational freedom of M in bulk solution is not the only effect of the water solvent. Historically, to account for more direct solvation effects, water molecules were directly included in simulations and the structure of water was relaxed along with the conformations of M, S, and M@S. Two techniques are here to be distinguished, the expensive optimisation of complete water phases (built as ice-like layers or extracted from short dynamic runs), around M or deposited on S or M@S,^{3;4} and the optimisation of the

conformation of a very small number of water molecules, strategically placed around the adsorbate.⁵⁻⁸ The latter, which is named microsolvation, drastically reduces computation cost compared to the full optimisation by assuming that most of the solvent effect is local and due to short-range interactions like H-bonds with co-adsorbed water molecules (for M@S) or molecules from the first solvation sphere (for M). The biggest difficulties of microsolvation are the choice of the number and position of the water molecules for each system (S, M, and M@S) which can be estimated from chemical insight but with no certainty, and must respect the chemical reaction balance.⁹

Another approximation has been used to include solvent effects at long-range without actual sampling and that do not suffer from this difficult single geometry question: implicit solvents. Implicit solvents are equivalent to averaging the position of all water molecules as a mean-field that screen long-range electronic interactions and are therefore usually referred to as Polarizable Continuum Model (PCM). Implicit solvation can be simply included by modifying the dielectric constant of the system, eventually complemented by semi-empirical cavitation contributions to account for the free energy cost of opening holes in the solvent to accommodate a solute. Here, solute would refer to the whole chemical system except the water molecules *i.e.* to M, S, or M@S. Implicit solvation models are long-known and used in homogeneous simulations.¹⁰ It is, however, only quite recently that they were applied to periodic plane-wave computations¹¹ and later even in VASP, widely used for metallic system simulations¹². This explains why they were historically employed for solid/liquid computations later than explicit solvation schemes while computationally cheaper. In the specific VASPsol implementation, two terms are added to the Kohn-Sham potential used in DFT to mimic the modification of electrostatic interactions and reproduce the cavitation respectively:

$$V_{VASPsol} = \frac{d\epsilon(n_{solute})}{dn_{solute}} \frac{|\nabla\phi|^2}{8\pi} + \tau \frac{d|\nabla S|}{dn_{solute}} \quad (1.5)$$

where ϵ is the local relative permittivity of the solvent, n_{solute} the electronic density of the solute, ϕ the electrostatic potential (due to both electrons and nuclei of the solute), τ is the effective surface tension parameter of the solvent, and S is the cavity shape used to evaluate the cavitation term, whose shape is defined as the volume delimited by a minimal electronic density of the solute (as detailed in the following paragraph and illustrated in Fig 1.1). ϕ is obtained by solving the generalised Poisson-Boltzmann equation:

$$\nabla[\epsilon(n_{solute})\nabla\phi] = -4\pi[N_{solute} - n_{solute}] \quad (1.6)$$

1.1. Static approaches of adsorption at liquid water/solid interface

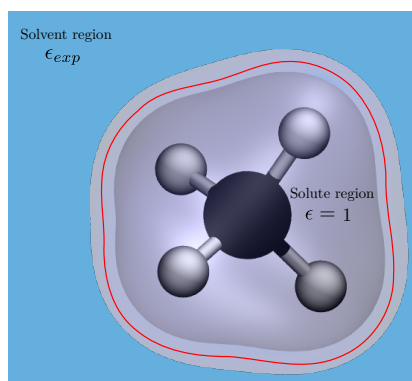


Figure 1.1 – Schematic representation of the definition of the local relative permittivity of the solvent ϵ and the cavity shape S in the VASsol implementation. The blue area represents the solvent region where the local relative permittivity equals the experimental relative permittivity (ϵ_{exp}) of the solvent. The glassy region represents the solute region where the solvent relative permittivity equals 1. The grey region represents the transition region where the relative permittivity of the solvent is switched from ϵ_{exp} to 1. Crosses represent the position of the nuclei of the solute. Black lines represent the beginning and end of the transition area while the red one is the isodensity surface for which the electronic density n_{solute} equals the cut-off density n_c , used as the definition of the cavity S

with N_{solute} the charge density due to the nuclei of the solute. ϵ is chosen as equal to the experimental value for the solvent region (ϵ_{bulk}) and switched off smoothly around a critical electronic density for the solute n_c *i.e.* when entering the region occupied by the solute, as depicted in Fig. 1.1.

$$\epsilon(n_{solute}) = 1 + \frac{1}{2}(\epsilon_{bulk} - 1) \operatorname{erfc} \left(\frac{\log(n_{solute}/n_c)}{\sigma\sqrt{2}} \right) \quad (1.7)$$

with σ determining the smoothness of the switch. Overall, three empirical factors are used in this approach, the density cut-off (n_c), the so-called cavity width σ , and the surface tension parameter τ . These were fitted to reproduce experimental solvation free energies of small molecules in diverse solvents. However, several major flaws restraint such methods. The lack of experimental data, especially at the interface hinders a proper verification and fitting of the three aforementioned empirical parameters for interfaces. Also, they were chosen to reproduce solvation free energies at a certain temperature and the parameter extrapolation to other ranges of temperature can be questioned. Moreover, implicit solvents miss to a major extent the direct interactions between the solvent molecules and the adsorbed molecules (*e.g.* H-bonds) or with the surface (*e.g.* co-adsorption or competitive adsorption). They should therefore be employed with cautiousness, especially to model the highly reactive water solvent.

Quite naturally, because microsolvation can reproduce direct and close-range solvation effects, while the implicit solvent is tailored to indirect long-range effects, the two approaches have also been frequently combined. They were used to compute solvation free energies of

molecules in homogeneous liquid phase^{13;14} or to assess the impact of water over catalytic processes at the liquid water/metal interface.¹⁵⁻¹⁷ However, they have not been used to evaluate adsorption free energies because of the same limitations as pure microsolvation, *i.e.* the difficulty to respect both the balance of water molecule during the adsorption process and to ensure a sufficient solvation of the chemical species.

Overall, the straightforward usage and the close-to-negligible computational cost of implicit solvent make them excellent candidates when the direct effect of solvent upon the adsorption is limited, which is rarely the case for water. In contrast, microsolvation schemes (alone or combined with implicit solvent) are effective to evaluate direct solvation effect on reactions at the interface but are not adapted for the study of adsorption. Explicit complete water phases are efficient too, even if these methods simplify the water structure to a single geometry, but their computational cost remains high. Now, with these limitations of static computations in mind, we turn to the more costly dynamic methods.

1.2 Dynamic approaches of the adsorption: the rare event problem

Molecular dynamics (MD) allow a better description of the entropic effects of water, as well as its dynamic structure. MD is the name given to the simulated evolution of a system under the action of its internal atomic forces and in a given thermodynamic ensemble. MD are used to explore the accessible phase space of a system in given Temperature and Pressure conditions. Indeed, according to the ergodicity hypothesis, a long enough dynamic evolution of a system allows a complete sampling of its accessible phase space. A temporal average of the visited configurations can therefore be used to establish the partition function of the system and compute ensemble averages of any of its properties. Therefore, the most straightforward method to obtain meaningful information about a high-entropy system like an interface between liquid water and a solid would be a fully equilibrated MD. The drawback of such an approach is the amount and cost of all the energy evaluations at DFT level that it requires. Especially, when the surface is made of metallic atoms, the computational cost can be very high (*e.g.* 1'000-10'000 CPUh per ps of simulation for a liquid water/Pt interface)¹⁸. Nevertheless, these *Ab Initio* MD (AIMD) are commonly employed to understand the pure structuration of liquid water/solid interface. Relatively short sampling duration (<<500 ps) and/or a limited number of water molecules are considered to be sufficient (or at least to be a reasonable compromise within our computational capabilities) to obtain a realistically averaged picture of these interfaces. Moreover, simulation lengths have increased from only 1 to 100 ps with time and computer capabilities over the last twenty years, improving our sampling capabilities and thus, knowledge of these interfaces. The explanation of diverse experimental observations motivated these studies, for example Low-Energy Electron Diffraction (LEED) measurements, electronic-microscope observation of regular hexagonal moieties for ultra-thin water layers deposited on metallic surfaces and under vacuum, or the differences of wetting between

1.2. Dynamic approaches of the adsorption: the rare event problem

metals (Cu and Pt)^{19–26}. Interfaces with oxides surfaces were also investigated, but more in view to understand the surface state of oxides in water.^{27–31}

However, studying reactions at the solid/liquid interface is even more challenging than characterising the structural properties of this interface. Indeed, reactions are rare events that necessitate an enhanced sampling. While a reaction can be an extremely fast event (a bond can break in a few fs), its occurrence can be extremely rare (above the ms). This temporal gap means that at least 10^{12} or 10^{15} simulation steps (at 1 fs/step) would be required to sample actual spontaneous adsorption with an unbiased MD, which is computationally prohibitive. From here, we shall distinguish two different kinds of surfaces: the metallic surfaces, and the oxide surfaces. The reason for this is that their reactivity with water is quite different. On one hand, noble metal surfaces can be considered as non-reactive in water at room temperature because the nature of their exposed surface state will be mainly determined by the preparation methods and will not change during typical adsorption time scales. Plus, water molecules are not likely dissociated on top of these surfaces (with the notable exception of Ru and Co surfaces), meaning that the surface state will not be changing. On the other hand, oxide surfaces may vary their surface state heavily depending on the nature of adsorbed species and adsorption conditions but also in typically short duration, with proton exchange, surface reconstruction, or water dissociation being most notable.

1.2.1 Adsorption on metallic surfaces : the possibility to decorrelate surface reactivity and solvation

To compute adsorption free energies at the water/metal interface, several techniques have been developed over the last ten years that aim at sampling the solvation difference between $M+S$ and $M@S$. This decomposition is presented in the thermodynamic cycle of Fig. 1.2. The free energy being a state function, this cycle holds true for any adsorption process, and adsorption free energies in water can be computed as:

$$\Delta_{ads}G_{aq} = \Delta_{ads}G_{gas} + \Delta_h G(M@S) - \Delta_h G(S) - \Delta_h G(M) \quad (1.8)$$

However, the major consequence of the non-reactivity of metallic surfaces is the possibility to entirely decorrelate the adsorption of the molecule on the surface from the modification of the liquid water structure. Indeed, because the surface state of the metal and the adsorption mode of M do not depend on the water structure, it is a good approximation to compute $\Delta_h G$ (the free energy of hydration of M, S or $M@S$) by sampling only the phase space accessible to the water molecules and not the conformational phase space of M, S or $M@S$. Hence, only the computationally inexpensive evaluation of $\Delta_{ads}G_{gas}$, which is usually being approximated by

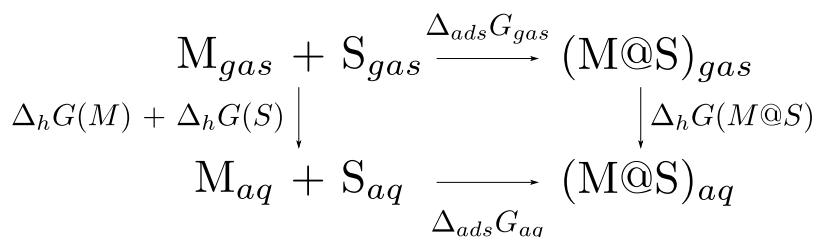


Figure 1.2 – Example of thermodynamic cycle used to compute the adsorption free energy of a molecule M on a surface S in water ($\Delta_{ads}G_{aq}$). Subscript *ads* stands for adsorption, *h* for hydration, *gas* for gas phase and *aq* for aqueous phase.

$\Delta_{ads}E_{gas}$, has to be performed at the DFT level. The main advantage of this is the possibility to sample the solvent at a lower (computationally less costly) level of theory than DFT since they require to compute interactions of water molecules with S, M, or other water molecules but not the more complex interactions between S and M.

Several schemes have been developed around this idea as the pioneer eSMS scheme (Explicit Solvation for Metal Surface) from Heyden and co-workers, that was used to study the reactivity of molecules adsorbed at liquid/metal interfaces.^{32;33} The method proposes to first generate configurations for the active site (*i.e.* the adsorbate and the metallic atoms closest to it) and then to run short MDs of the water solvent while the active site is kept frozen. These MD can therefore be carried at the Molecular Mechanics (MM) computation level to reduce their cost. Potential of Mean Force (PMF) (*i.e.* the average force exerted by the water on the active site) are then extracted from each MD and integrated over a path connecting the different active site configurations to evaluate the difference of hydration energies ($\Delta_h G$) between them in a perturbative manner. The main difficulty of this method is to correctly describe the interactions between the solvent molecules and the active site. In the work of Heyden and co-workers, interactions between the two systems are obtained considering Van der Waals and Coulombic interactions between the solvent molecules and the active site but no mutual polarisation of the charge distributions between the two systems. The partial charges of the water molecules are therefore fixed and determined by the classical TIP3P water model)³⁴ while the active site atoms charges are deduced from gas-phase DFT computations.

It must be noted that other solutions exist to describe the coupling between the active site and the solvent region, as the DFT-CES (Classical Explicit Solvent) methods developed by Lim and co-workers.³⁵ In the DFT-CES scheme, the active site is treated as immersed in a mean electrostatic field produced by the solvent and deduced from a Poisson equation, while the solvent molecules are themselves submitted to the electrostatic potential due to the charge density of the active site. The solvent field and the charge density are then adjusted iteratively until convergence is reached. This method was developed for solvation free energy evaluation in homogeneous liquid phase but later successfully applied to investigate water/metal interface structure and question the popular model of the ice-like bilayer structure

1.2. Dynamic approaches of the adsorption: the rare event problem

that was commonly observed in AIMD water/metal simulations.³⁶ Also worth mentioning is the recently proposed scheme by Giovannini *et al.*³⁷, which couples the active site (here a solvated molecule in bulk solution) and solvent by extracting fluctuating charges and dipoles of the solute atoms from DFT computations and then include them as parameters for classical interactions with the solvent. It was designed to specifically address polarisability and has not yet been employed for interfacial simulations but could be efficient to account for the pronounced polarisability of the metallic surface.

Overall, the scheme developed by Heyden and co-workers is very useful to correct the free energy differences corresponding to reactions at the water/metal interface and it could be improved by the inclusion of more advanced coupling schemes between its MM and DFT systems. However, this method is based on a path of intermediate configurations that connects the two end states of a studied reaction. In the case of adsorption, the requirement of such a path would imply simulating S and M in the same computation but separated enough to consider them as non-interacting. The presence of an adsorbate or a surface can have an effect on the structure of water on up to 15 Å. To be able to consider that the structuring of water implied by S has no impact on the solvation of M and *vice versa*, at least 30 Å of water should therefore separate the molecule from the surface. The size and number of water molecules required for such a system would therefore make these simulations computationally expensive. To prevent that and to be able to compute adsorption free energies at the liquid water/metal interfaces Steinmann and co-workers³⁸ expressed the total adsorption free energy as a sum of gas-phase adsorption energy and a variation of the solvation free energy during the adsorption. To compute the latter, they exploited another kind of path which is an alchemical transformation. The principle behind it is to run several simulations where the interaction potential (V) of the active site with the solvent is scaled down depending on a parameter (λ). The values of λ span the range from 0 (total interaction between the two systems) to 1 (no interaction between the two systems), as depicted in Fig. 1.3:

$$V(\lambda) = V_{interacting}(1 - \lambda) + V_{non-interacting}(\lambda) \quad (1.9)$$

Physically, it is equivalent to a progressive disappearance of the active site in the simulation, hence the name: alchemical transformation. This disappearance allows the water molecules to progressively enter the space previously occupied by the active site. This way, the solvation change between M@S and S can be computed smoothly and the chemical balance is completed by a similar computation of the appearance of M in liquid bulk. This method is further developed in the current thesis as chapter 2 where its refining and implementation as a computation package are described. A very similar idea was used by Getman and co-workers to compute the adsorption free energy of compounds involved in catalytic reactions on a Pt

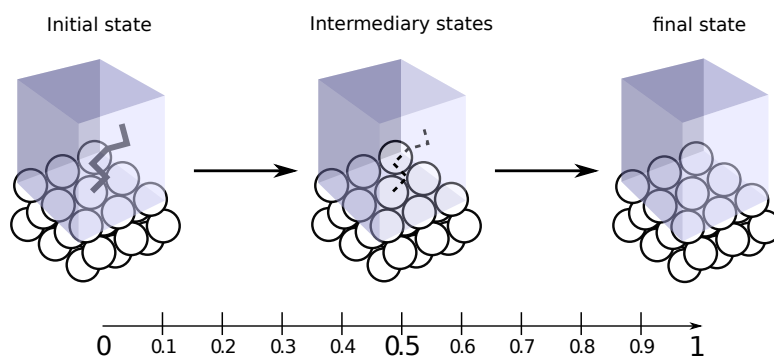


Figure 1.3 – Schematic representation of the division of a transformation path (here, the disappearance of an adsorbate at the metal/water interface) into several discrete windows characterised by an advancement parameter from initial state (0) to final state(1). Each window represents a MD simulation at a given λ .

surface immersed in a mixed water/methanol solution.³⁹

Last but not least, a limitation of all aforementioned schemes must be outlined: the lack of kinetic information. Indeed, as these models are based on thermodynamic differences, they do not convey any information about eventual kinetic bottlenecks that could prevent adsorption. Even in methods featuring a solvation difference that explicitly sample the modification of the liquid structure, the alchemical transformation means that the adsorbate is “shrunk” at the surface, and not much can be said about the kinetics of adsorption. Indeed an adsorbate could be stabilised on the surface but would never actually reach it due to a high barrier for adsorption. This might eventually be overcome by identifying the transition state of such adsorption and computing free energy difference between this transition state and the adsorbed or solvated state. In practice, these transition states are difficult to identify and depend significantly on the solvation model.

1.2.2 Adsorption on oxides surfaces: accelerating the sampling with the rare events methods

Let us now consider our second category of adsorptions at water/solid interfaces: the adsorption at the liquid water/oxide interface. Metallic oxide surfaces often result from complex oxidation processes of non-noble metallic surfaces like aluminum, iron, titanium, etc... Oxides being usually very oxophilic, their surface is covered, even simply exposed to air, by several water molecules, chemisorbed, or even dissociated. The surface can then undergo partial reconstruction under the action of these adsorbed molecules. Therefore, the surface state and acidity of oxide surfaces are highly sensitive to operating conditions, and consequently, poorly known. In practice, this means that a unique surface model cannot be defined to study a liquid water/oxide interface. Therefore, if we were to apply the same methods as previously mentioned for adsorption at the liquid water/metal interface, the most stable adsorption geometry would be much more difficult to define as we should consider and evaluate every

1.2. Dynamic approaches of the adsorption: the rare event problem

possible surface state. Instead, to study reactions (like adsorption) at these interfaces, we mainly use methods that are reactive toward the surface. These methods can sample an eventual change of surface state as they accurately describe interactions within the surface and not only between the surface and the liquid or adsorbed molecules. Also, oppositely to pure thermodynamic methods, they offer information about the kinetics of the transition between two geometries which is especially important for oxides surfaces, as high kinetic barriers are to be expected between different surface states. Free energy differences are therefore not sufficient to investigate adsorption at the water/oxide interface, which drives us back to fully explicit sampling *via* MD. But once again, simple dynamics cannot be considered as they would be too computationally costly.

However, another broad category of methods was designed to prevent such problems: rare events methods. These techniques rely on biased dynamics to accelerate the sampling of the phase space along specific degrees of freedom of the system. Unlike simple free energy differences, these techniques sample the phase space during the transition between two stable states. By re-analysing *a posteriori* the bias required to accelerate the exploration along the studied degree of freedom, the unbiased free energy landscape of the system can be recovered. However, the choice of a limited number of degrees of freedom in these methods implies that all other transverse degrees of freedom will not be biased and might be more difficult to sample. In some cases, if important transverse degrees of freedom are ignored, the rare events methods can provide an incomplete picture of the kinetics of the system. Therefore, these methods must rely on the assumption that any other barrier of the system is small and easily overcome at the studied temperature, both to be computationally efficient and chemically relevant.

Among the rare events methods, we find the Thermodynamic Integration (TI).⁴⁰⁻⁴³ The main idea behind TI is to sample the phase space of a system minus one specific degree of freedom. This degree of freedom should be characteristic of the studied chemical transformation (*e.g.* a single bond breaking or a distance to the surface in the case of adsorption), and is usually referred to as a collective variable (CV). Different starting geometries of the systems are built, each featuring a different value for this CV. Independent dynamics are then run from these starting geometries, keeping the value of the CV frozen by the means of constraints. These dynamics are named “windows”. By measuring the biasing forces of the constraints, a difference of free energy between each window is obtained. These differences can then be used to rebuild the complete free energy profile along the frozen coordinate (at a resolution depending on the spacing of the coordinate value between the windows).⁴⁴⁻⁴⁸ A visual sum-up of the method and comparison with standard MD can be found in Fig. 1.4. TI is a useful method to cross high free energy barriers that can be described by a single (reaction path) variable as adsorption for example.^{49;50} However while TI reduces the dimensionality of the phase space of the system by freezing one of its degrees of freedom, the remaining space can still be quite lengthy to sample. Especially, as mentioned earlier, free energy barriers

can remain along transverse degrees of freedom, as the ones responsible for the surface state modification in the case of oxides. These ignored degrees of freedom can be both computationally costly to sample and flaw the representation of the system. It would be theoretically possible, though, to build multidimensional TI (2D, 3D, ...) and to fix a set of 2 or more coordinates. But to do so, a multidimensional array of windows should be built, each necessitating full equilibration which would considerably raise the computational cost of the method (from n windows to n^d windows, d being the number of dimensions). TI was employed, in the water/solid interface context, to investigate the acidity and surface state of clays in water⁵¹, or the acidity modification of molecules upon adsorption on such surfaces.⁵²

A second popular rare event method is umbrella sampling^{53;54}. It relies on an added biasing force that will lead the evolution of the system along a prior-established path. Post-simulation analysis of the applied bias along the path allows retrieving the corresponding free energy profile. Different from TI, the evolution of the system is continuous and therefore cannot miss a hidden barrier between two chosen values of the CV. Also, just like TI, it requires a path to be used, that must be found prior to any study and can be difficult to establish. Many methods based on statistic computations have aimed at reducing the uncertainty on the free energy obtained through umbrella sampling like WHAM (Weighted Histogram Analysis Method)^{55;56} for example, or to build a more efficient bias potential to accelerate the convergence of the free energy profile like Variational approach for Enhanced sampling (VES),⁵⁷

The latest among the popular rare event sampling methods is metadynamics^{58;59} that was sparsely but successfully applied to water/solid interface investigations as, for example, to study the solid NaCl decomposition in water.⁶⁰ This method allows a fast exploration of a limited number of degrees of freedom of the system, described by collective variables. Practically, this method also proceeds by sampling the phase space with a biased MD. During the MD and at a given pace, the position of the chemical system is projected on one or several CVs, and a small repulsive Gaussian potential is added to the Free Energy Surface (FES), centered on the projected coordinate of the system. The total bias is therefore built during the simulation and depends on the history of exploration. It repels the system from conformations that would have the same coordinates along the CV as previously adopted conformations. Therefore, the bias drives the system away from known portions of the FES and accelerates the exploration of new ones. This exploration is carried until the entire original (unbiased) FES is filled with repulsive potentials, meaning that the system free energy does not depend anymore on its configuration. The system is then said to be diffusive (as its trajectory becomes completely stochastic) and the unbiased FES can be retrieved as the opposite of the total added bias (see Fig. 1.4). As for TI or Umbrella sampling, the typical difficulty of metadynamics is to correctly identify the collective variables that correspond to the studied chemical transformation. Just as for TI or Umbrella sampling, no hindered motion of the system should be forgotten by these variables in order to avoid the issues previously mentioned. However, in metadynamics, large parts of the phase space of the

1.2. Dynamic approaches of the adsorption: the rare event problem

system are projected on the same set of coordinates along the CV (for example, degrees of freedom of distant water molecules will not reflect on a CV corresponding to the distance between an adsorbate and a surface). Therefore, metadynamics will be quickly driven outside of it and save considerable sampling time. This is the reason why metadynamics can be, and is, routinely employed to explore several CV. Nevertheless, two new drawbacks emerge from this method. First, even if the sampling of the collective variables is biased and thus, accelerated, it can still be longer compared to the one of TI because it does not impose a hard value of this coordinate. The exploration still needs to overcome free energy barriers instead of starting directly at specific coordinates that might be chosen on top of the barrier as in TI. Note that the exploration speed can be tuned by adjusting the height of the deposited gaussian potentials but it cannot be raised too much to avoid hill surfing phenomenons (when the system is trapped in a metastable state on top of a gaussian). Second, because no discrete set of values of the coordinate is imposed, the system can potentially evolve indefinitely along the collective variables and the FES is not converged as long as the sampling of this variable is not completed. That is typically the case when a CV is relevant to the chemical transformation in a certain range but not outside. An example can be given of the distance between a molecule and a surface that is relevant to describe adsorption at small values but not anymore at long distance (when the molecule is, anyhow, in bulk liquid). These issues can be partially addressed with well-tempered metadynamics.⁶¹ In this method, the height of the deposited gaussians is progressively reduced at a rate depending on a user-defined “temperature”. It was mathematically demonstrated that this method ensures a better convergence of the FES and a smaller uncertainty on the level of free energy. The reduction of the gaussians also prevents exploring too far away from the starting point of the dynamic which is quite useful in the aforementioned problem of non-bounded variables.⁶²

Several other flavors of metadynamics are available that push the concept further and try to speed up the exploration of the phase space. For example, the multiple walkers version parallelises the exploration by using different simultaneous dynamics, starting from various initial geometries.⁶³ and was used by Marx and co-workers to investigate alcohol oxidation at the surface of Titania-supported Gold nanoparticles in water.⁶⁴ The parallel tempering method goes even further and use multiple dynamics featuring different temperatures that can exchange configurations between each other to simultaneously explore quickly new free energy wells (at high temperature), and sample them carefully (at low temperature).⁶⁵ Schneider and co-workers also proposed a scheme resembling parallel tempering to compute adsorption energies of peptides over oxidised Si or Ti surfaces.⁶⁶ But instead of using parallel dynamics at different homogeneous temperatures, they borrowed the idea of REST (Replica exchange with solute tempering)⁶⁷ to only warm up an active centre of the simulation (defined by the user) and not the solvent away from it, thus improving selectively the sampling of the configuration around the active site.

We stand now at a point where several tools are at our disposal for rare events sampling, each

Chapter 1. Bibliographic study

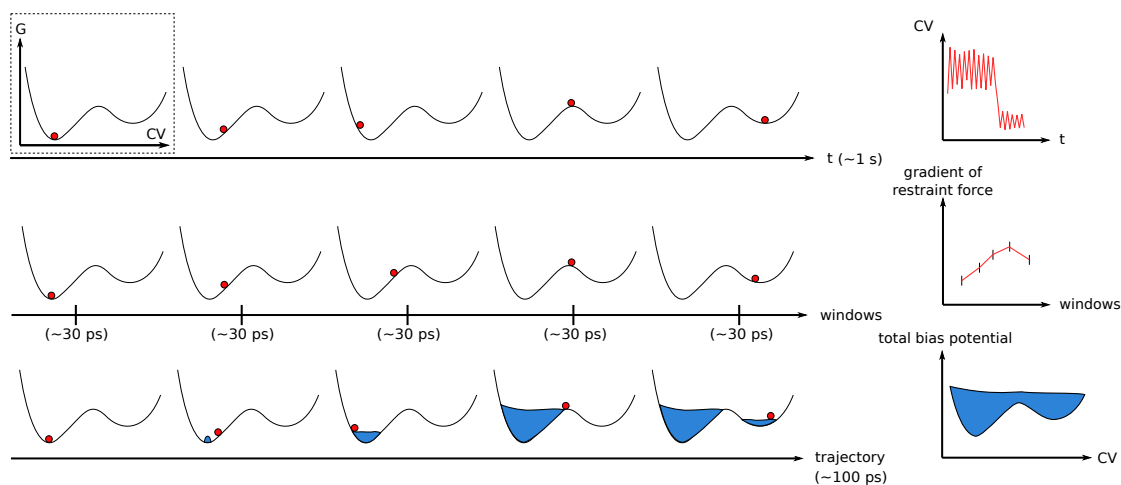


Figure 1.4 – Schematic representation of the simulations required to obtain a free energy profile along a given collective variable (CV) for three different methods: Conventional MD, TI, and metadynamics (from top to bottom). On the left is represented the evolution of the system (red circle) on the free energy surface (black curved line) depending on the simulation time, simulation windows, or evolution of the trajectory for MD, TI, and metadynamics respectively. The blue portion on the bottom-most evolution represents the added bias repulsive potential for the metadynamics. On the right, we show the data gathered from the left-side evolution which will be used to extract free energy information. In the topmost plot, we represent the value of the CV in function of the time, from which frequency of apparition of each value of the CV is extracted to rebuild the partition function of the system. In the middle, we show the value of the gradient of the constraint force for each window, which, integrated, gives the free energy difference between any two points of the free energy profile. In the bottom-most plot, we represent the sum of all deposited gaussians, *i.e.* the total bias potential to add to the free energy surface to obtain a diffusive system. The opposite of this added potential, therefore, gives the exact shape of the free energy surface.)

1.3. Lower levels of description for water/solid interactions

with its own strengths and weaknesses. A graphical summary of each of these families of methods can be found in Figure 1.4. Few applications of these methods at the water/solid interface exist yet. The few ones found in the literature mainly focus solely on the study of oxides surface state exposed to water,^{28;29;51} or rarely on molecular adsorption on such surfaces but ignoring surface reactivity^{52;64;66}. Indeed, computational capabilities have only recently reached a point allowing the simulation of several hundreds of ps of dynamics at liquid water/oxide interfaces, which are required even for these rare events methods. With the help of these methods, we have performed a study of the interaction between alcohol adsorption at the water/alumina interface and the hydrolysis of the alumina surface that is developed in Part III. We expect many more applications of the enhanced sampling methods in the upcoming years now that they are computationally accessible. However, the major difference of typical time scales and phase space dimensions in general between the solid and liquid phases will continue to be a huge challenge in these future studies. It must be noticed too, that if simulating several hundreds of ps for water/oxides interfaces, it remains hardly possible for water/metals interface. Pure thermodynamic approaches remain thus the standard methodology employed for the study of such interfaces.

1.3 Lower levels of description for water/solid interactions

Up to now, we mainly considered DFT computations, because, as quickly mentioned in the introduction, DFT allows a complete description of inter-atomic interactions while molecular mechanics (MM) ignore quantum mechanics-related effects. But in section 1.2.1, we also mentioned a lower level of theory used to describe interactions within the solvent. Indeed, classical force-fields were developed for a long time now to describe, for example, water-water interactions. Water models range from the simple and rigid TIP3P water³⁴ to more advanced ones, including up to 6 interacting sites to model a single water molecule⁶⁸, or to the quite recent MB-pol model, splitting interactions into short and long range contributions for better performances.⁶⁹ However, describing interactions between water molecules and S or M are also required to investigate adsorptions at the water/solid interface. But if a consensus was more or less reached for molecule/molecule force-fields (as between water and M), this is not the case for solid/molecule force-fields. Indeed, the complex interaction between the delocalized electronic structure of a metal or semiconductor and a molecule is quite difficult to model. The near-chemisorption is rather strong, directional but also not as strong as usual chemical bonds. This implies that no definitive connectivity can be established between molecules and surface atoms, which is the trick usually employed to simplify the force field treatment of chemical bonds (*e.g.* harmonic potentials generate unbreakable bonds). Here, we focus on the specific problem of water/solid force-field, which is core to interfacial MM simulations.

Several generations of water/noble-metal forcefields have been developed, starting with the

pioneering work of Spohr *et al.* who proposed at first a potential for water-Pt interactions as a simple sum of Lennard-Jones and Coulombic interaction. The parameters of the forcefield were directly deduced from previous Pt-Pt and water-water force-fields.⁷⁰ In subsequent work they changed the philosophy of their description and introduced a pure analytic potential to reproduce at best the experimental observations of water dipole pointing away from the surface and partially fitted over extended Hückel computations.^{71;72} Later, Siepmann *et al.* proposed a many-body interaction between pairs of metallic atoms and water's oxygen atom to explicitly include an energetic dependence to the angle formed by these three atoms⁷³. This force-field was still used in a recent investigation of platinum surface wetting by Chandler and co-workers⁷⁴. Less accurate but more general, the more recent approach of Heinz *et al.* (METAL force-field) is only based on physisorption⁷⁵ but parametrised over a large range of metals and thus, widely applicable. Virtual sites interacting with water molecule *via* Lennard-Jones interactions were also experimented by Iori *et al.*⁷⁶ to correct the wrong adsorption site predicted by the METAL force-field (hollow instead of top site as predicted by DFT or experimental observations for a single water molecule). Even more recently, Steinmann *et al.*, included again explicit angular dependence of the adsorption energy combined with attractive potential on top sites to reproduce both the preferential adsorption orientation and position of water molecules on Pt (111) surfaces¹⁸. Unfortunately, the latter approach relies on a description of the interaction of a water molecule with the whole metallic surface. Such an approach excludes any description of the interactions between water molecules and an alloy surface as a specific parametrisation would be required for any composition and spatial arrangement of alloy. To overcome this problem, we proposed a forcefield named GAL19, based on the same ideas as the one from Steinmann *et al.* but adapted and reformulated for an atom pair-wised formulation as described in more details in chapter 3.

Another wide category of forcefield is formed by the so-called reactive force-fields. Not explicitly designed for metal/surfaces interaction, these complex functional forms should in principle be adaptable to any kind of interactions and may be parametrised to describe the water/metal interactions. Among them are the AI(REBO)⁷⁷⁻⁷⁹ force fields for hydrocarbons and carbon-based structures, ReaXFF,^{80;81} initially built for hydrocarbons but later extended to various systems, and RexPON, an advanced model for water including numerous quantum-inspired interactions.⁸² Also the COMB3 forcefield by Cheng *et al.*⁸³ was parametrised for Pt or Cu /water interactions.⁸⁴ The major problem of such approaches is that they usually rely on a long and cumbersome task of parametrisation which can be very system-specific. However, machine-learning techniques (ML), and Neural-network approaches specifically, also rely on a heavy parametrisation and a huge amount of preliminary data generation but perform generally better. Indeed they rely on a very flexible functional form, build with less physically sound terms but a much higher amount of them compared to reactive forcefields, which allow them to accurately reproduce any physical interaction without prior intuition. Therefore, ML techniques, despite sharing the weaknesses of reactive forcefields, have been in the centre of

an increasing interest, fuelled by the generalisation of data-driven approaches.⁸⁵⁻⁹¹

Another difficult aspect of force-fields is polarisability. Indeed, metallic atoms are much more polarizable than other hetero-atoms, according to experimental data. Therefore, if several technical solutions have been developed, once again, for molecule/molecule interactions, like Drude particles^{92;93} (that dissociate the partial charges from the centers of the atoms and materialise them as elastically-bound particles with no other interactions than Coulombic ones) or dipole/charge and dipole/dipole interactions,⁹⁴⁻⁹⁷ these technical solutions usually fail to describe metal polarisation. Indeed, converging the amplitude of the instantaneous dipole of each individual metallic atom of a slab can be difficult, because of the strong mutual polarisation that they undergo. Dipoles can even diverge, a phenomenon known as polarisation catastrophe. None entirely satisfying and general solution has therefore been found yet, even if attempts were made in the case of charged interfaces.⁹⁸ The importance of polarisation in water/metal interaction description is further developed in chapter. 5, in a view to understanding better the amplitude of this missing interaction in water/metal forcefields.

1.4 Conclusion

In this chapter, we presented the state-of-the-art methods used to investigate adsorption at the water/solid interface. As highlighted by the diversity of existing methods, no unique solution has been adopted by the scientific community. Some heavily approximated but computationally cheap methods are commonly used to include the solvent effect for adsorption studies. However, their shortcomings are well-acknowledged when it comes to solvent effects that have a more “dynamic” origin, *i.e.*, related to the reorganisation of the water phase. Explicitly sampling the phase-space of water seems to be the only way to include these effects but approximations are still required to reduce the associated computational cost. The specificity of the studied solid surface then determines which approximations are reasonable. While adsorption studies at the metal/water interface can rely on de-coupled sampling of the adsorption and solvation because of their limited reactivity with water, studying oxides surfaces requires more advanced sampling techniques as rare events methods. However, the methods developed in both of these cases are still very recent (10 to 20 years) and no consensus has yet emerged on the most appropriate method to be applied. Therefore, yet, most of these methods have been only sparsely used and their performances are not often widely benchmarked against each other. The goal of this thesis is therefore to both develop new tools to study the adsorption at these water/solid interfaces, but also to apply existing methods that have not been used in the context of interfaces yet to better understand the relationship between solvation and adsorption at the interface.

Bibliography

- [1] Réocreux, R.; Michel, C.; Fleurat-Lessard, P.; Sautet, P.; Steinmann, S. N. Evaluating Thermal Corrections for Adsorption Processes at the Metal/Gas Interface. *J. Phys. Chem. C* **2019**, *123*, 28828–28835.
- [2] Wertz, D. H. Relationship between the gas-phase entropies of molecules and their entropies of solvation in water and 1-octanol. *J. Am. Chem. Soc.* **1980**, *102*, 5316–5322.
- [3] Akpa, B. S.; D’Agostino, C.; Gladden, L. F.; Hindle, K.; Manyar, H.; McGregor, J.; Li, R.; Neurock, M.; Sinha, N.; Stitt, E. H.; Weber, D.; Zeitler, J. A.; Rooney, D. W. Solvent effects in the hydrogenation of 2-butanone. *J. Catal.* **2012**, *289*, 30.
- [4] Zope, B. N.; Hibbitts, D. D.; Neurock, M.; Davis, R. J. Reactivity of the Gold/Water Interface During Selective Oxidation Catalysis. *Science* **2010**, *330*, 74–78.
- [5] Michel, C.; Zaffran, J.; Ruppert, A. M.; Matras-Michalska, J.; Jedrzejczyk, M.; Grams, J.; Sautet, P. Role of water in metal catalyst performance for ketone hydrogenation: a joint experimental and theoretical study on levulinic acid conversion into gamma-valerolactone. *Chem. Commun.* **2014**, *50*, 12450–12453.
- [6] Gao, W.; Keith, J. A.; Anton, J.; Jacob, T. Theoretical Elucidation of the Competitive Electro-oxidation Mechanisms of Formic Acid on Pt(111). *J. Am. Chem. Soc.* **2010**, *132*, 18377–18385.
- [7] Michel, C.; Auneau, E.; Delbecq, F.; Sautet, P. C–H versus O–H Bond Dissociation for Alcohols on a Rh(111) Surface: A Strong Assistance from Hydrogen Bonded Neighbors. *ACS Catal.* **2011**, *1*, 1430–1440.
- [8] Hibbitts, D. D.; Neurock, M. Influence of oxygen and pH on the selective oxidation of ethanol on Pd catalysts. *J. Catal.* **2013**, *299*, 261–271.
- [9] Rendón-Calle, A.; Builes, S.; Calle-Vallejo, F. Substantial improvement of electrocatalytic predictions by systematic assessment of solvent effects on adsorption energies. *Appl. Catal., B* **2020**, *276*, 119147.
- [10] Tomasi, J.; Persico, M. Molecular Interactions in Solution: An Overview of Methods Based on Continuous Distributions of the Solvent. *Chem. Rev.* **1994**, *94*, 2027–2094.
- [11] Fattebert, J.-L.; Gygi, F. First-principles molecular dynamics simulations in a continuum solvent. *Int. J. Quantum Chem.* **2003**, *93*, 139.
- [12] Mathew, K.; Sundararaman, R.; Letchworth-Weaver, K.; Arias, T. A.; Hennig, R. G. Implicit solvation model for density-functional study of nanocrystal surfaces and reaction pathways. *J. Chem. Phys.* **2014**, *140*, 084106.

- [13] Pliego, J. R.; Riveros, J. M. The Cluster-Continuum Model for the Calculation of the Solvation Free Energy of Ionic Species. *J. Phys. Chem. A* **2001**, *105*, 7241–7247.
- [14] Wu, W.; Kieffer, J. New Hybrid Method for the Calculation of the Solvation Free Energy of Small Molecules in Aqueous Solutions. *J. Chem. Theory Comput.* **2019**, *15*, 371–381.
- [15] Wang, H.-F.; Liu, Z.-P. Formic Acid Oxidation at Pt/H₂O Interface from Periodic DFT Calculations Integrated with a Continuum Solvation Model. *J. Phys. Chem. C* **2009**, *113*, 17502–17508.
- [16] Gu, Q.; Sautet, P.; Michel, C. Unraveling the Role of Base and Catalyst Polarization in Alcohol Oxidation on Au and Pt in Water. *ACS Catal.* **2018**, *8*, 11716–11721, Times Cited: 7.
- [17] Schweitzer, B.; Steinmann, S. N.; Michel, C. Can microsolvation effects be estimated from vacuum computations? A case-study of alcohol decomposition at the H₂O/Pt(111) interface. *Phys. Chem. Chem. Phys.* **2019**, *21*, 5368–5377.
- [18] Steinmann, S. N.; Ferreira De Morais, R.; Götz, A. W.; Fleurat-Lessard, P.; Iannuzzi, M.; Sautet, P.; Michel, C. Force Field for Water over Pt(111): Development, Assessment, and Comparison. *J. Chem. Theory Comput.* **2018**, *14*, 3238–3251.
- [19] Izvekov, S.; Voth, G. A. *Ab initio* molecular dynamics simulation of the Ag(111)-water interface. *J. Chem. Phys.* **2001**, *115*, 7196–7206.
- [20] Schnur, S.; Groß, A. Properties of metal–water interfaces studied from first principles. *New J. Phys.* **2009**, *11*, 125003.
- [21] Carrasco, J.; Hodgson, A.; Michaelides, A. A molecular perspective of water at metal interfaces. *Nat. Mater.* **2012**, *11*, 667–674.
- [22] Yoon, Y.; Rousseau, R.; Weber, R. S.; Mei, D.; Lercher, J. A. First-Principles Study of Phenol Hydrogenation on Pt and Ni Catalysts in Aqueous Phase. *J. Am. Chem. Soc.* **2014**, *136*, 10287–10298.
- [23] Sakong, S.; Forster-Tonigold, K.; Groß, A. The structure of water at a Pt(111) electrode and the potential of zero charge studied from first principles. *J. Chem. Phys.* **2016**, *144*, 194701.
- [24] Björneholm, O.; Hansen, M. H.; Hodgson, A.; Liu, L.-M.; Limmer, D. T.; Michaelides, A.; Pedevilla, P.; Rossmeisl, J.; Shen, H.; Tocci, G.; Tyrode, E.; Walz, M.-M.; Werner, J.; Bluhm, H. Water at Interfaces. *Chem. Rev.* **2016**, *116*, 7698–7726.
- [25] Bellarosa, L.; García-Muelas, R.; Revilla-López, G.; López, N. Diversity at the Water–Metal Interface: Metal, Water Thickness, and Confinement Effects. *ACS Cent. Sci.* **2016**, *2*, 109–116.

Chapter 1. Bibliographic study

- [26] Heenen, H. H.; Gauthier, J. A.; Kristoffersen, H. H.; Ludwig, T.; Chan, K. Solvation at metal/water interfaces: An ab initio molecular dynamics benchmark of common computational approaches. *J. Chem. Phys.* **2020**, *152*, 144703, Publisher: American Institute of Physics.
- [27] Skelton, A. A.; Fenter, P.; Kubicki, J. D.; Wesolowski, D. J.; Cummings, P. T. Simulations of the Quartz(101 $\bar{1}$)/Water Interface: A Comparison of Classical Force Fields, Ab Initio Molecular Dynamics, and X-ray Reflectivity Experiments. *J. Phys. Chem. C* **2011**, *115*, 2076–2088.
- [28] Sulpizi, M.; Gaignot, M.-P.; Sprik, M. The Silica-Water Interface: How the Silanols Determine the Surface Acidity and Modulate the Water Properties. *J. Chem. Theory Comput.* **2012**, *11*.
- [29] Khatib, R.; Backus, E. H. G.; Bonn, M.; Perez-Haro, M.-J.; Gaignot, M.-P.; Sulpizi, M. Water orientation and hydrogen-bond structure at the fluorite/water interface. *Sci. Rep.* **2016**, *6*, 24287, Number: 1 Publisher: Nature Publishing Group.
- [30] Ren, Z.; Liu, N.; Chen, B.; Li, J.; Mei, D. Theoretical Investigation of the Structural Stabilities of Ceria Surfaces and Supported Metal Nanocluster in Vapor and Aqueous Phases. *J. Phys. Chem. C* **2018**, *13*.
- [31] Réocreux, R.; Jiang, T.; Iannuzzi, M.; Michel, C.; Sautet, P. Structuration and Dynamics of Interfacial Liquid Water at Hydrated γ -Alumina Determined by ab Initio Molecular Simulations: Implications for Nanoparticle Stability. *ACS Appl. Nano Mater.* **2018**, *1*, 191–199.
- [32] Faheem, M.; Heyden, A. Hybrid Quantum Mechanics/Molecular Mechanics Solvation Scheme for Computing Free Energies of Reactions at Metal–Water Interfaces. *J. Chem. Theory Comput.* **2014**, *10*, 3354–3368, Publisher: American Chemical Society.
- [33] Saleheen, M.; Heyden, A. Liquid-Phase Modeling in Heterogeneous Catalysis. *ACS Catal.* **2018**, *8*, 2188–2194.
- [34] William L. Jorgensen.; Chandrasekhar, J.; Madura, J. D.; Impey, R. W.; Klein, M. L. Comparison of simple potential functions for simulating liquid water. *J. Chem. Phys.* **1983**, *79*, 926–935.
- [35] Lim, H.-K.; Lee, H.; Kim, H. A Seamless Grid-Based Interface for Mean-Field QM/MM Coupled with Efficient Solvation Free Energy Calculations. *J. Chem. Theory Comput.* **2016**, *12*, 5088–5099, Publisher: American Chemical Society.
- [36] Gim, S.; Cho, K. J.; Lim, H.-K.; Kim, H. Structure, Dynamics, and Wettability of Water at Metal Interfaces. *Sci. Rep.* **2019**, *9*, 1–7.

- [37] Giovannini, T.; Puglisi, A.; Ambrosetti, M.; Cappelli, C. Polarizable QM/MM Approach with Fluctuating Charges and Fluctuating Dipoles: The QM/FQF μ Model. *J. Chem. Theory Comput.* **2019**, *15*, 2233–2245.
- [38] Steinmann, S. N.; Sautet, P. Assessing a First-Principles Model of an Electrochemical Interface by Comparison with Experiment. *J. Phys. Chem. C* **2016**, *120*, 5619–5623, Publisher: American Chemical Society.
- [39] Zhang, X.; DeFever, R. S.; Sarupria, S.; Getman, R. B. Free Energies of Catalytic Species Adsorbed to Pt(111) Surfaces under Liquid Solvent Calculated Using Classical and Quantum Approaches. *J. Chem. Inf. Model.* **2019**, *59*, 2190–2198.
- [40] Kirkwood, J. G. Statistical Mechanics of Fluid Mixtures. *J. Chem. Phys.* **1935**, *3*, 300–313.
- [41] Martins, S. A.; Sousa, S. E.; Ramos, M. J.; Fernandes, P. A. Prediction of Solvation Free Energies with Thermodynamic Integration Using the General Amber Force Field. *J. Chem. Theory Comput.* **2014**, *10*, 3570–3577.
- [42] Steinbrecher, T.; Mobley, D. L.; Case, D. A. Nonlinear scaling schemes for Lennard-Jones interactions in free energy calculations. *J. Chem. Phys.* **2007**, *127*, 214108.
- [43] Gao, Y.; Zhu, T.; Chen, J. Exploring drug-resistant mechanisms of I84V mutation in HIV-1 protease toward different inhibitors by thermodynamics integration and solvated interaction energy method. *Chem. Phys. Lett.* **2018**, *706*, 400–408.
- [44] Carter, E. A.; Ciccotti, G.; Hynes, J. T.; Kapral, R. Constrained reaction coordinate dynamics for the simulation of rare events. *Chem. Phys. Lett.* **1989**, *156*, 472–477.
- [45] Mülders, T.; Krüger, P.; Swegat, W.; Schlitter, J. Free energy as the potential of mean constraint force. *J. Chem. Phys.* **1996**, *104*, 4869–4870, Publisher: American Institute of Physics.
- [46] RUIZ-MONTERO, M. J.; FRENKEL, D.; BREY, J. J. Efficient schemes to compute diffusive barrier crossing rates. *Mol. Phys.* **1997**, *90*, 925–942, Publisher: Taylor & Francis _eprint: <https://doi.org/10.1080/002689797171922>.
- [47] Sprik, M.; Ciccotti, G. Free energy from constrained molecular dynamics. *J. Chem. Phys.* **1998**, *109*, 7737, Publisher: American Institute of PhysicsAIP.
- [48] Frenkel, D.; Smit, B. *Understanding Molecular Simulation*; Elsevier, 2002.
- [49] De Vivo, M.; Masetti, M.; Bottegoni, G.; Cavalli, A. Role of Molecular Dynamics and Related Methods in Drug Discovery. *J. Med. Chem.* **2016**, *59*, 4035–4061.
- [50] Ekimoto, T.; Yamane, T.; Ikeguchi, M. Elimination of Finite-Size Effects on Binding Free Energies via the Warp-Drive Method. *J. Chem. Theory Comput.* **2018**, *14*, 6544–6559.

Chapter 1. Bibliographic study

- [51] Tazi, S.; Rotenberg, B.; Salanne, M.; Sprik, M.; Sulpizi, M. Absolute acidity of clay edge sites from ab-initio simulations. *Geochim. Cosmochim. Acta* **2012**, *94*, 1–11.
- [52] Parashar, S.; Lesnicki, D.; Sulpizi, M. Increased Acid Dissociation at the Quartz/Water Interface. *J. Phys. Chem. Lett.* **2018**, *9*, 2186–2189.
- [53] Torrie, G. M.; Valleau, J. P. Monte Carlo study of a phase-separating liquid mixture by umbrella sampling. *J. Chem. Phys.* **1977**, *66*, 1402–1408, Publisher: American Institute of Physics.
- [54] Torrie, G. M.; Valleau, J. P. Nonphysical sampling distributions in Monte Carlo free-energy estimation: Umbrella sampling. *J. Comput. Phys.* **1977**, *23*, 187–199, Publisher: Academic Press.
- [55] Kumar, S.; Rosenberg, J. M.; Bouzida, D.; Swendsen, R. H.; Kollman, P. A. THE weighted histogram analysis method for free-energy calculations on biomolecules. I. The method. *J. Comput. Chem.* **1992**, *13*, 1011–1021, _eprint: <https://onlinelibrary.wiley.com/doi/pdf/10.1002/jcc.540130812>.
- [56] Souaille, M.; Roux, B. Extension to the weighted histogram analysis method: combining umbrella sampling with free energy calculations. *Comput. Phys. Commun.* **2001**, *135*, 40–57.
- [57] Valsson, O.; Parrinello, M. Variational approach to enhanced sampling and free energy calculations. *Phys. Rev. Lett.* **2014**, *113*, 090601.
- [58] Laio, A.; Parrinello, M. Escaping free-energy minima. *PNAS* **2002**, *99*, 12562–12566, Publisher: National Academy of Sciences Section: Physical Sciences.
- [59] Laio, A.; Gervasio, F. L. Metadynamics: a method to simulate rare events and reconstruct the free energy in biophysics, chemistry and material science. *Rep. Prog. Phys.* **2008**, *23*.
- [60] Liu, L.-M.; Laio, A.; Michaelides, A. Initial stages of salt crystal dissolution determined with ab initio molecular dynamics. *Phys. Chem. Chem. Phys.* **2011**, *13*, 13162.
- [61] Barducci, A.; Bussi, G.; Parrinello, M. Well-Tempered Metadynamics: A Smoothly Converging and Tunable Free-Energy Method. *Phys. Rev. Lett.* **2008**, *100*.
- [62] Bussi, G.; Laio, A. Using metadynamics to explore complex free-energy landscapes. *Nature Reviews Physics* **2020**, *2*, 200–212, Number: 4 Publisher: Nature Publishing Group.
- [63] Raiteri, P.; Laio, A.; Gervasio, F. L.; Micheletti, C.; Parrinello, M. Efficient Reconstruction of Complex Free Energy Landscapes by Multiple Walkers Metadynamics[†]. *J. Phys. Chem. B* **2006**, *110*, 3533–3539.

- [64] Munoz-Santiburcio, D.; Camellone, M. F.; Marx, D. Solvation-Induced Changes in the Mechanism of Alcohol Oxidation at Gold/Titania Nanocatalysts in the Aqueous Phase versus Gas Phase. *Angew. Chem. Int. Ed.* **2018**, *57*, 3327–3331, WOS:000427235600006.
- [65] Bussi, G.; Gervasio, F. L.; Laio, A.; Parrinello, M. Free-Energy Landscape for β Hairpin Folding from Combined Parallel Tempering and Metadynamics. *J. Am. Chem. Soc.* **2006**, *128*, 13435–13441.
- [66] Schneider, J.; Colombi Ciacchi, L. Specific Material Recognition by Small Peptides Mediated by the Interfacial Solvent Structure. *J. Am. Chem. Soc.* **2012**, *134*, 2407–2413.
- [67] Liu, P.; Kim, B.; Friesner, R. A.; Berne, B. J. Replica exchange with solute tempering: A method for sampling biological systems in explicit water. *PNAS* **2005**, *102*, 13749–13754.
- [68] Nada, H.; van der Eerden, J. P. J. M. An intermolecular potential model for the simulation of ice and water near the melting point: A six-site model of H₂O. *J. Chem. Phys.* **2003**, *118*, 7401–7413, Publisher: American Institute of Physics.
- [69] Babin, V.; Medders, G. R.; Paesani, F. Development of a “First Principles” Water Potential with Flexible Monomers. II: Trimer Potential Energy Surface, Third Virial Coefficient, and Small Clusters. *J. Chem. Theory Comput.* **2014**, *10*, 1599–1607, Publisher: American Chemical Society.
- [70] Spohr, E.; Heinzinger, K. Molecular dynamics simulation of a water/metal interface. *Chem. Phys. Lett.* **1986**, *123*, 218–221.
- [71] Spohr, E.; Heinzinger, K. A Molecular Dynamics Study on the Water/Metal Interfacial Potential. *Berichte der Bunsengesellschaft für physikalische Chemie* **1988**, *92*, 1358–1363.
- [72] Spohr, E. Computer simulation of the water/platinum interface. *J. Phys. Chem.* **1989**, *93*, 6171–6180.
- [73] Siepmann, J. I.; Sprik, M. Influence of surface topology and electrostatic potential on water/electrode systems. *J. Chem. Phys.* **1995**, *102*, 511–524, Publisher: American Institute of Physics.
- [74] Limmer, D. T.; Willard, A. P.; Madden, P.; Chandler, D. Hydration of metal surfaces can be dynamically heterogeneous and hydrophobic. *Proc. Natl. Acad. Sci. U. S. A.* **2013**, *110*, 4200–4205.
- [75] Heinz, H.; Vaia, R. A.; Farmer, B. L.; Naik, R. R. Accurate Simulation of Surfaces and Interfaces of Face-Centered Cubic Metals Using 12-6 and 9-6 Lennard-Jones Potentials. *J. Phys. Chem. C* **2008**, *112*, 17281–17290.

Chapter 1. Bibliographic study

- [76] Iori, F.; Di Felice, R.; Molinari, E.; Corni, S. GoLP: An atomistic force-field to describe the interaction of proteins with Au(111) surfaces in water. *J. Comput. Chem.* **2009**, *30*, 1465–1476, Publisher: Wiley Subscription Services, Inc., A Wiley Company.
- [77] Brenner, D. W. Empirical potential for hydrocarbons for use in simulating the chemical vapor deposition of diamond films. *Phys. Rev. B* **1990**, *42*, 9458–9471.
- [78] Stuart, S. J.; Tutein, A. B.; Harrison, J. A. A reactive potential for hydrocarbons with intermolecular interactions. *J. Chem. Phys.* **2000**, *112*, 6472–6486.
- [79] Brenner, D. W.; Shenderova, O. A.; Harrison, J. A.; Stuart, S. J.; Ni, B.; Sinnott, S. B. A second-generation reactive empirical bond order (REBO) potential energy expression for hydrocarbons. *J. Phys.: Condens. Matter* **2002**, *14*, 783–802.
- [80] van Duin, A. C. T.; Dasgupta, S.; Lorant, F.; Goddard, W. A. ReaxFF: A Reactive Force Field for Hydrocarbons. *J. Phys. Chem. A* **2001**, *105*, 9396–9409.
- [81] van Duin, A. C. T.; Strachan, A.; Stewman, S.; Zhang, Q.; Xu, X.; Goddard, W. A. ReaxFF_{SiO} Reactive Force Field for Silicon and Silicon Oxide Systems. *J. Phys. Chem. A* **2003**, *107*, 3803–3811.
- [82] Naserifar, S.; Goddard, W. A. The quantum mechanics-based polarizable force field for water simulations. *J. Chem. Phys.* **2018**, *149*, 174502.
- [83] Cheng, Y.-T.; Liang, T.; Martinez, J. A.; Phillpot, S. R.; Sinnott, S. B. A charge optimized many-body potential for titanium nitride (TiN). *J. Phys.: Condens. Matter* **2014**, *26*, 265004.
- [84] Antony, A. C.; Liang, T.; Sinnott, S. B. Nanoscale Structure and Dynamics of Water on Pt and Cu Surfaces from MD Simulations. *Langmuir* **2018**, *34*, 11905–11911.
- [85] Artrith, N.; Behler, J. High-dimensional neural network potentials for metal surfaces: A prototype study for copper. *Phys. Rev. B* **2012**, *85*.
- [86] Artrith, N.; Kolpak, A. M. Understanding the Composition and Activity of Electrocatalytic Nanoalloys in Aqueous Solvents: A Combination of DFT and Accurate Neural Network Potentials. *Nano Lett.* **2014**, *14*, 2670–2676.
- [87] Behler, J. Constructing high-dimensional neural network potentials: A tutorial review. *Int. J. Quantum Chem.* **2015**, *115*, 1032–1050.
- [88] Natarajan, S. K.; Behler, J. Neural network molecular dynamics simulations of solid–liquid interfaces: water at low-index copper surfaces. *Phys. Chem. Chem. Phys.* **2016**, *18*, 28704–28725.

- [89] Schlexer Lamoureux, P.; Winther, K. T.; Garrido Torres, J. A.; Streibel, V.; Zhao, M.; Bajdich, M.; Abild-Pedersen, E.; Bligaard, T. Machine Learning for Computational Heterogeneous Catalysis. *ChemCatChem* **2019**, *0*.
- [90] Singraber, A.; Behler, J.; Dellago, C. Library-Based LAMMPS Implementation of High-Dimensional Neural Network Potentials. *J. Chem. Theory Comput.* **2019**,
- [91] Loeffler, T. D.; Chan, H.; Sasikumar, K.; Narayanan, B.; Cherukara, M. J.; Gray, S.; Sankaranarayanan, S. K. R. S. Teaching an Old Dog New Tricks: Machine Learning an Improved TIP3P Potential Model for Liquid–Vapor Phase Phenomena. *J. Phys. Chem. C* **2019**, *123*, 22643–22655.
- [92] Geada, I. L.; Ramezani-Dakhel, H.; Jamil, T.; Sulpizi, M.; Heinz, H. Insight into induced charges at metal surfaces and biointerfaces using a polarizable Lennard–Jones potential. *Nat. Commun.* **2018**, *9*, 716.
- [93] Goloviznina, K.; Canongia Lopes, J. N.; Costa Gomes, M.; Pádua, A. A. H. Transferable, Polarizable Force Field for Ionic Liquids. *J. Chem. Theory Comput.* **2019**, *15*, 5858–5871, Publisher: American Chemical Society.
- [94] Ponder, J. W.; Wu, C.; Ren, P.; Pande, V. S.; Chodera, J. D.; Schnieders, M. J.; Haque, I.; Mobley, D. L.; Lambrecht, D. S.; DiStasio, R. A.; Head-Gordon, M.; Clark, G. N. I.; Johnson, M. E.; Head-Gordon, T. Current Status of the AMOEBA Polarizable Force Field. **2009**, 16.
- [95] Yesylevskyy, S. O.; Schäfer, L. V.; Sengupta, D.; Marrink, S. J. Polarizable Water Model for the Coarse-Grained MARTINI Force Field. *PLoS Comput. Biol.* **2010**, *6*, e1000810.
- [96] Lamoureux, G.; MacKerell, A. D.; Roux, B. A simple polarizable model of water based on classical Drude oscillators. *J. Chem. Phys.* **2003**, *119*, 5185–5197, Publisher: American Institute of Physics.
- [97] Ren, P.; Ponder, J. W. Polarizable Atomic Multipole Water Model for Molecular Mechanics Simulation. **2002**, 15.
- [98] Scalfi, L.; Salanne, M.; Rotenberg, B. Molecular Simulation of Electrode-Solution Interfaces. *arXiv:2008.11967 [cond-mat, physics:physics]* **2020**, arXiv: 2008.11967.

Computing adsorption free energies at the liquid water/metal interface

Part I

The following part presents a method allowing the computation of adsorption free energies: the MMSolv level of theory. The goal of this study was to propose an easy-to-use tool to include the effect of water solvation on adsorption energies. It aims to compete with the implicit solvation approaches by being simple to handle (even if not as simple as implicit solvent) but much more accurate and still keeping a low computational cost. The challenge of such explicit solvation computation lies in the conciliation of long sampling with accurately reproduced interactions between metallic surfaces and water. To reduce the cost of such sampling, hybrid molecular mechanics/quantum mechanics computations were used and implemented into a fully functional computation package: SolvHybrid. The theory, challenges, and applications of the MMSolv method and the SolvHybrid package are exposed in this part.

2 Solvation Free Energies and Adsorption Energies at the Metal/Water Interface from Hybrid Quantum-Mechanical/Molecular Mechanics Simulations

This Chapter is based on the following article: Solvation Free Energies and Adsorption Energies at the Metal/Water Interface from Hybrid Quantum-Mechanical/Molecular Mechanics Simulations, *Clabaut, P. and Schweitzer, B. and Götz, A. and Michel, C. and Steinmann, S.N.*, *Journal of Computational and Theoretical Chemistry*, 2020, [10.1021/acs.jctc.0c00632](https://doi.org/10.1021/acs.jctc.0c00632)

abstract: Modeling adsorption at the metal/water interfaces is a corner-stone towards an improved understanding in a variety of fields from heterogeneous catalysis to corrosion. We propose and validate a hybrid scheme that combines the adsorption free energies obtained in gas phase at the DFT level with the variation in solvation from the bulk phase to the interface evaluated using a molecular mechanics based alchemical transformation, denoted MMsolv. Using the GAL17 force field for the platinum/water interaction, we retrieve a qualitatively correct interaction energy of the water solvent at the interface. This interaction is of near chemisorption character and thus challenging, both for the alchemical transformation, but also for the fixed point-charge electrostatics. Our scheme passes through a state characterized by a well-behaved physisorption potential for the Pt(111)/H₂O interaction to converge the free energy difference. The workflow is implemented in the freely available SolvHybrid package. We first assess the adsorption of a water molecule at the Pt/water interface, which turns out to be a stringent test. The intrinsic error of our QM-MM hybrid scheme is limited to 6 kcal·mol⁻¹ through the introduction of a correction term to attenuate the electrostatic interaction between near-chemisorbed water molecules and the underlying Pt atoms. Next, we show that the MMsolv solvation free energy of Pt (-0.46 J·m⁻²) is in good agreement with the experimental estimate (-0.32 J·m⁻²). Furthermore, we show that the entropy contribution

Chapter 2. Solvation Free Energies and Adsorption Energies at the Metal/Water Interface from Hybrid Quantum-Mechanical/Molecular Mechanics Simulations

at room temperature is roughly of equal magnitude as the free energy, but with opposite sign. Finally, we compute the adsorption energy of benzene and phenol at the Pt(111)/water interface, one of the rare systems for which experimental data are available. In qualitative agreement with experiment, but in stark contrast with a standard implicit solvent model, the adsorption of these aromatic molecules is strongly reduced (*i.e.*, less exothermic by ~ 30 and $40 \text{ kcal}\cdot\text{mol}^{-1}$ for our QM/MM hybrid scheme and experiment, respectively, but ~ 0 with the implicit solvent) at the solid/liquid compared to the solid/gas interface. This reduction is mainly due to the competition between the organic adsorbate and the solvent for adsorption on the metallic surface. The semi-quantitative agreement with experimental estimates for the adsorption energy of aromatic molecules thus validates the soundness of our hybrid QM-MM scheme.

2.1 Introduction

Assessing the impact of water at the metal/liquid interface is a challenging task but mandatory to understand and predict numerous interfacial processes from heterogeneous catalysis to water treatment, metal plating and corrosion. The lack of extensive experimental data is clearly detrimental to validate proposed methods. As it serves as both, a theoretical and experimental model system for the understanding of metal/water interfaces, the platinum/water interface is the only exception in this respect. Pt is well characterized in surface science studies^{1;2} and highly relevant to heterogeneous catalysis and electrocatalysis.³⁻⁷ Furthermore, Pt(111)/water is one of the few solid/liquid interfaces for which a couple of experimental solvation energies are available.⁸⁻¹⁰ We herein will rely on this exceptionally well-characterized interface to validate our general approach by comparing our computed adsorption energies at the solid/liquid interface to the available experimental values.

Over the last twenty years, several approaches have been developed to computationally account for solvation effects at the metal/water interface. In the microsolvation scheme, a limited number of water molecules are co-adsorbed with the adsorbate of interest.¹¹⁻¹⁵ To achieve a balanced description of solvation along a reaction profile, these water molecules have to be carefully chosen and placed. In addition to being cumbersome, microsolvation only allows to retrieve the short range part of the solvation effects, also called direct solvation effects. The indirect solvation effects, *i.e.*, the modified electrostatic interactions as well as the entropy of solvation are completely neglected in this approach.¹⁶⁻²⁰ The implicit solvation models such as the polarizable continuum model, PCM,²¹ are precisely designed to retrieve the indirect solvation effects and are most successful to recover the average electrostatic interaction between solutes and the solvent which is described by its dielectric constant. However the lack of a database of reference solvation energies at the water/metal interface severely limits the parametrization and validation of implicit solvation models for the metal/liquid interface. The cluster-continuum model, where the direct (local) solvation effect is described by microsolvation and the indirect (bulk) solvation is approximated by the dielectric constant try to combine the best of both worlds.¹⁵ Alternatively the full water phase can be computed. However, phase-space sampling with an accurate energy description is the main issue with these approaches. In an early study along these lines a short molecular dynamics (MD) simulation was performed prior to the optimization of snapshots, yielding a metal/amorphous ice-like interface.²² Similar studies for various metal surface/adsorbate combinations have been performed with widely varying number of water molecules and sampling length.^{23;24} However, these studies have not assessed to which extent they actually mimic a metal/liquid water interface. Hybrid quantum-mechanical/molecular mechanics (QM/MM) approaches have also been suggested but have so far not been compared to the rare experimental data^{25;26}. Our two-step hybrid QM-MM level, that we had called MM-FEP,²⁷ consists in describing the surface-adsorbate interaction via a DFT optimization and accounting for the solvation

Chapter 2. Solvation Free Energies and Adsorption Energies at the Metal/Water Interface from Hybrid Quantum-Mechanical/Molecular Mechanics Simulations

effects of the frozen DFT geometry through free energy perturbation (FEP) exploiting efficient molecular mechanics. This allows to retrieve all the major solvation effect, including the competition between water and the adsorbate for adsorption on the surface. Independently and in parallel to our work, Getman and co-workers developed a similar approach to assess adsorption free energies of CO and sugars on Pt (111) and compared it with implicit solvation and ice-like structures optimisations.^{28;29} The accuracy of any kind of QM/MM heavily relies on the quality of the forcefield used to sample the phase-space of the solid/liquid interface. Even though several forcefields enjoy great popularity,³⁰⁻³³ it is only recently that we have introduced GAL17, the first qualitatively correct force field for the interaction between a water molecule and a Pt(111) surface.³⁴ This force field has subsequently been generalized to other metal surfaces.³⁵ Thus, we are now ready to tackle the solvation free energies at the Pt(111) surface with a reliable force field.

Alchemical transformations such as FEP or thermodynamic integration (TI) rely on comparably small changes in the Hamiltonian, most suitable for non-covalent interactions. However, the GAL17 force field correctly describes the interaction between water molecules and the metal surface by a “strong” interaction. Therefore, special attention needs to be paid during the alchemical transformation in order to avoid dependence of the results on the starting point (hysteresis), which is the first challenge addressed herein. The second challenge is how to make the chemisorption-like potential of GAL17 compatible with point-charge electrostatics. When developing GAL17, electrostatics between the surface and the water molecules have not been explicitly taken into account, *i.e.*, they are part of the interaction potential but not expressed in terms of point charges. This is comparable with biological force fields, where point-charges are not part of bond or angle terms. However, when adsorbates are present on the surface, the point charges are crucial for retrieving solvation energies at the metal/liquid interface. Nevertheless, double-counting needs to be avoided between GAL17 and the point-charges.

In this work, we perform computations in the spirit of MM-FEP, but adapting it according to the two identified challenges when using GAL17 in alchemical transformations. The thus obtained solvation energies are called “MMSolv” for molecular mechanics solvation energies. When combined with DFT interaction energies to give adsorption energies at the metal/liquid interface, we call the level of theory “hybrid”, to indicate the use of a QM and a MM constituent. We implement the approach in an easy-to-use package, SolvHybrid. By the comparison with experimental adsorption energies of benzene and phenol at the Pt(111)/water interface, we demonstrate a semi-quantitative accuracy of the devised hybrid level of theory. Given suitable force fields, SolvHybrid is applicable to the determination of solvation energies at any solid/liquid interface. Therefore, we expect SolvHybrid to become a valuable tool for mechanistic investigations in heterogeneous (electro-)catalysis and for other processes at the solid/liquid interface.

2.2 Theory

2.2.1 SolvHybrid: Principles and Workflow

The SolvHybrid package aims at computing the adsorption free energy of a molecule M on a surface S in a solvent using a hybrid scheme. This quantity, named here $\Delta_a G^{solv}$, can be decomposed in two terms:

$$\Delta_a G^{solv} = \Delta_a G^{vac} + \Delta_a \Delta_h G \quad (2.1)$$

where Δ_a designates the free energy difference of adsorption of M on S and the superscript *solv* and *vac* refer to the process in solvent (here water) and vacuum or gas-phase, respectively and Δ_h collects all solvent effects (h stands here for hydration). $\Delta_a \Delta_h G$ formally also includes the change of adsorbate–surface interaction due to the co-adsorption of solvent molecules and the polarization of the adsorbate due to the presence of the solvent.

The first contribution ($\Delta_a G^{vac}$) is the Gibbs Free Energy of adsorption of the molecule M on the surface S computed in the gas-phase. To a good approximation it does not require extensive phase-space sampling³⁶ and can, therefore, be evaluated by standard DFT optimizations, here performed using VASP.^{37;38} SolvHybrid computes the hybrid adsorption energy, combining the DFT energy $\Delta_a G^{vac}$ with the MMSolv energy correction term $\Delta_h \Delta_a G$. Hence, $\Delta_a G^{vac}$ and the corresponding optimized geometries, together with their Hirshfeld charges, of M , the surface S and the adsorbate-surface assembly ($M@S$) constitute the basis of SolvHybrid computations.

The MMSolv term ($\Delta_a \Delta_h G$) is the variation of the free energy of solvation ($\Delta_h G$), during the adsorption process, *i.e.*, from bulk solution to the interface. The solvation effects derive mostly from the reorganization of the solvent around the adsorbate (often referred to as the cavitation energy), the replacement of water molecules adsorbed on the surface by the adsorbate and from the change in interactions between the molecule in bulk solution and at the interface, *i.e.*, the change in polarization. Within the SolvHybrid package, the computation of $\Delta_a \Delta_h G$ is performed with molecular mechanics (MM) within the framework of thermodynamic integration (TI) as implemented in AMBER.^{39;40} The principles of the alchemical TI are summarized in section A.1 of the appendix chapter A. In principle, the MM requires the evaluation of three different types of interactions: (i) metal/adsorbate, (ii) water/adsorbate, (iii) water/metal. Since no accurate and general force field exists for the interaction between adsorbates and metal surfaces, we set this interaction to zero and keep the DFT determined geometry frozen during the MM computations. As a compensation, $\Delta_a G^{vac}$ is, of course, added in the end to obtain $\Delta_a G^{solv}$ (see Eq. 2.1). The most stable adsorption configuration at the solid/liquid interface can, nevertheless, be determined if the solvation energy is computed for different

Chapter 2. Solvation Free Energies and Adsorption Energies at the Metal/Water Interface from Hybrid Quantum-Mechanical/Molecular Mechanics Simulations

(gas-phase) configurations, *i.e.*, the configurational sampling is factored out of the TI and only performed in vacuum or implicit solvent. The water/metal interaction is conveniently described by the GAL17 force-field³⁴. Finally, the water/adsorbate interaction is approximated by established Lennard-Jones parameters⁴¹ and atomic charges computed with DFT.⁴² This approach approximates the polarization of the adsorbate by the presence of the solvent according to the scheme devised by Jorgensen and co-workers⁴³, but neglects the modification of adsorbate–surface interaction due to the co-adsorption of solvent molecules.

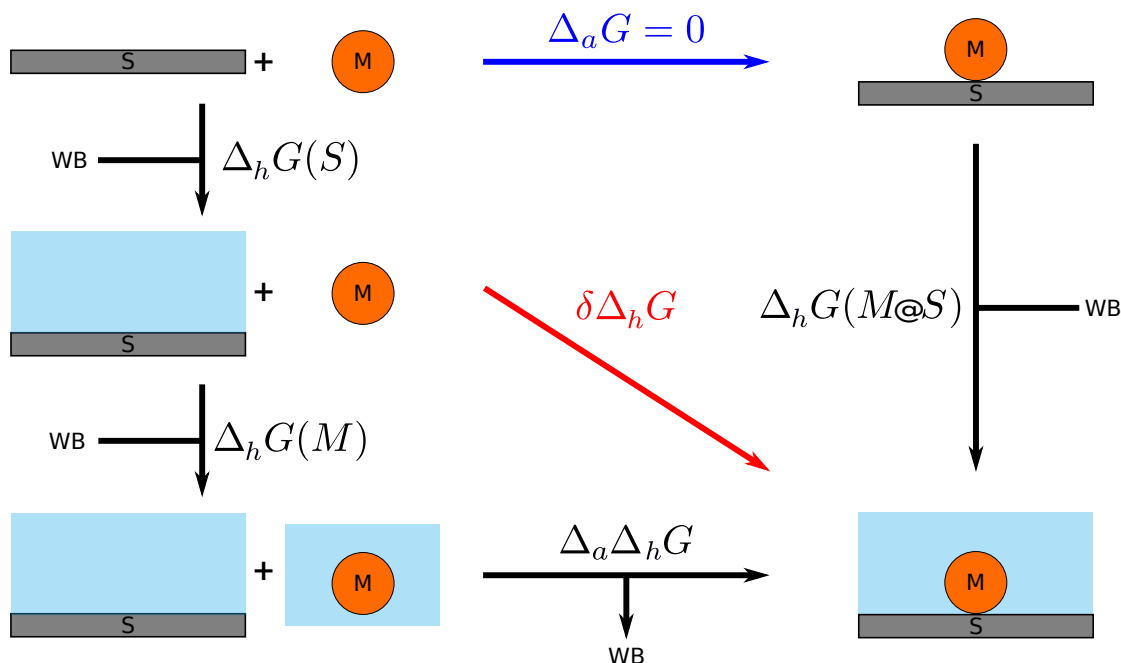


Figure 2.1 – Thermodynamic cycle used to determine $\Delta_a \Delta_h G$. M represents the studied molecule, S the metallic surface, $M@S$ the molecule adsorbed on the surface, and WB a water box of a sufficient size. $\Delta_h G$ expresses the solvation free energy of a compound, while $\Delta_a G$ is the adsorption free energy associated to $M + S \rightarrow M@S$. $\delta \Delta_h G$ is defined as the free energy change associated with the transformation depicted by the red arrow.

Following our previous work,²⁷ we thus exploit the thermodynamic cycle of Fig. 2.1 to evaluate $\Delta_a \Delta_h G$. In principle, $\Delta_a \Delta_h G$ can be computed in three ways: (i) by direct transformation (horizontal black line), (ii), following the rectangle of black arrows, exploiting the “standard” thermodynamic cycle, *i.e.*, $\Delta_a \Delta_h G = \Delta_a G + \Delta_h G(M@S) - \Delta_h G(S) - \Delta_h G(M)$, with $\Delta_a G$ being equal to zero in the chosen computation framework (MM with no interaction between the molecule and the surface), and (iii) invoking the triangle with the red, diagonal arrow, *i.e.*, $\Delta_a \Delta_h G = \delta \Delta_h G - \Delta_h G(M)$. The direct transformation (i) is difficult to achieve as it requires the simultaneous presence of two systems in the initial state, *i.e.*, a very large water box to mimic separated systems. The terms $\Delta_h G(S)$ and $\Delta_h G(M@S)$, required for process (ii), present an abrupt chemical change (the appearance of a full metallic surface in the bulk water), that is computationally costly to converge. As we have shown previously,²⁷ cycle (iii) avoids these issues and introduces a smoother transition, $\delta \Delta_h G$, between the empty surface S and $M@S$,

both immersed in water.

The two transformations corresponding to $\delta\Delta_h G$ and $\Delta_h G(M)$ are, therefore, driven by the SolvHybrid package, in order to determine $\Delta_a\Delta_h G$. Note, that the surface part of $M@S$ and S is slightly different. Indeed, the deformation, polarisation and electron transfer induced by the adsorption of the molecule M is computed at DFT level, taken in account within $\Delta_a G^{vac}$ and is responsible for the different geometries and charges of the S (sub-)system.

In summary, the complete adsorption energy of a compound at the solid/liquid interface is computed by SolvHybrid as:

$$\Delta_a G^{solv} = \Delta_a G^{vac} + \Delta_a \Delta_h G = \Delta_a E_{DFT}^{vac} + \delta\Delta_h G_{MM} - \Delta_h G_{MM}(M) \quad (2.2)$$

2.2.2 Electrostatic interactions between the solvent and the metallic surface

The standard implementation of Coulombic interactions in AMBER for periodic systems relies on the use of the Particle-Mesh-Ewald (PME) method. While PME is highly efficient, it is intrinsically more complex than the direct space evaluation of the Coulomb interactions. An alternative to PME is to use “shifted” Coulombic interactions (E_C^{shift}) in direct space, which make the electrostatic interaction compatible with a cut-off distance r_{cut} . The role of the shift-function is to render the evaluation of the Coulomb interactions in direct space compatible with periodic boundary conditions while avoiding discontinuities in the energy or forces. Here, we rely on the following “shifted” Coulombic interactions, initially introduced in the CHARMM community⁴⁴⁻⁴⁶:

$$E_C^{shift}(r_{ij}, q_i, q_j) = q_i q_j \cdot \frac{1}{r_{ij}} \cdot \left(1 - \frac{r_{ij}^2}{r_{cut}^2}\right)^2 \quad (2.3)$$

where the squared term in parenthesis corresponds to the shift function, r_{ij} is the internuclear distance between atoms i and j . q_i and q_j are the respective atomic charges in suitable units. Beyond the cutoff distance r_{cut} , the Coulomb interactions are no longer evaluated. We use this expression for all charges that do not involve metal atoms.

The reason why we herein prefer the simplicity of Eq. 2.3 compared to PME is the following: In contrast to standard non-bonded parameters, the GAL17 force field captures weak chemisorption of water molecules with the metal surface. Therefore, the internuclear distance between Pt and O is rather short (about 2.5 Å) in the minimum. Furthermore, since GAL17 is a non-polarizable force field (the polarization energy that is easily recoverable being only about 1 kcal·mol⁻¹ for a single water molecule⁴⁷), we had assumed a zero atomic charge on Pt during its development. However, when adsorbates are present on the surface, we necessarily also need to take atomic charges into account to describe the electrostatic interaction between the

Chapter 2. Solvation Free Energies and Adsorption Energies at the Metal/Water Interface from Hybrid Quantum-Mechanical/Molecular Mechanics Simulations

solvent and the adsorbate. Since we determine these charges from first principles for the $M@S$ system, they unavoidably lead to partial charges on the Pt atoms. To make GAL17 compatible with atomic charges on Pt, we tested and adopted a strategy inspired by standard force fields, where the Coulomb interaction is set to zero for 1-2, 1-3 and scaled down for 1-4 covalently bonded neighbors.⁴⁴ In standard (fixed topology) force fields, these short-ranged Coulomb interactions are excluded (or scaled down) since the corresponding interaction terms are already implicitly taken into account through the chemical bonds. Since quantum-mechanical effects are dominating at such short internuclear distances, the variation in the Coulomb energy of point charges would, anyway, not be physically relevant. However, GAL17 is a “semi-reactive” force field in the sense that the water/Pt topology is not fixed, even though the internal connectivity of the water molecules and the metal surface cannot change, preventing water dissociation and metal dissolution. Due to the flexible water/Pt topology, we cannot simply exclude the corresponding Pt–O and Pt–H pairs, but smoothly switch off the Coulombic interactions at short distances, which is nearly trivial in direct space. This is achieved by introducing a Fermi damping function for the Pt–H₂O Coulombic interactions, resulting in:

$$E_C^{shift}(r_{Pt,j}, q_{Pt}, q_j) = q_{Pt}q_j \cdot \frac{1}{r_{Pt,j}} \cdot \left(1 - \frac{r_{Pt,j}^2}{r_{cut}^2}\right)^2 \cdot \left(\frac{1}{1 + \exp(-\sigma(\frac{r_{Pt,j}}{r_0} - 1))}\right) \quad (2.4)$$

where σ and r_0 are the adjustable parameters of the Fermi-damping, corresponding respectively to the switching slope and the characteristic distance of the short-range correction. The two damping parameters were adjusted to minimize the highest $\Delta_a\Delta_h G$ of water molecule on the Pt (111) surface, determined as presented in section 2.4.1. The final parameters were 25 and 3.3 Å, for σ and r_0 , respectively. The resulting Coulomb interaction is shown in Fig. 2.2, where it is compared to the bare and shifted Coulomb operator.

2.3 Computational Details

2.3.1 Molecular mechanics simulations

The MUSIC module for AMBER³⁹, implementing the GAL17 forcefield, was used to describe water–Pt interactions along with the set of published parameters³⁴. A second version of the forcefield, dubbed “sGAL17” for soft GAL17, was also used. It consists in exactly the same functional form, but all parameters with energy as a unit are divided by four.

Water–water interactions were computed *via* the TIP3P water model.⁴⁸ All Lennard-Jones interactions other than TIP3P are taken from the UFF force field⁴¹. In all computations, the non-aqueous part of the system (S , $M@S$ and M), was frozen using the belly algorithm of

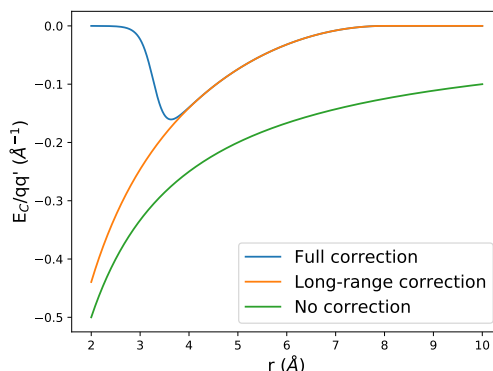


Figure 2.2 – Distance dependence of the electrostatic interactions, renormalized by the partial charges q_i, q_j . The green line corresponds to the bare Coulomb operator ($\frac{1}{r}$), while the orange curve is the shifted electrostatic interaction according to Eq. 2.3. The blue line results from the short-range damping of Eq. 2.4. r_{cut} , σ and r_0 were set to 8.0 Å; 25 and 3.3 Å, as used for all our computations.

AMBER. The shake algorithm was exploited to constrain the geometry of the water molecules, allowing to use a time step to 2 fs.^{49,50} The pressure was anisotropically scaled, *i.e.*, only the out-of-plane unit-cell vector was allowed to change by adapting the default Berendsen barostat of AMBER⁵¹ accordingly.

The thermodynamic integration was carried out using the default settings of AMBER17, including the softcore potential^{52;53} when performing the actual alchemical change.

2.3.2 DFT computations

All geometries for the molecule (S), the molecule adsorbed on the metallic surface ($M@S$) and the bare metallic surface (M) were optimized with VASP^{37,38}, using the conjugate-gradient algorithm. The PBE generalized gradient approximation^{54,55} was chosen as the exchange-correlation functional, complemented by the dDC dispersion correction⁵⁶, a setup that has previously been validated against experimental gas-phase adsorption energies⁵⁷. The plane-wave energy cutoff was set to 400 eV. The electron-ion interactions were described by the PAW formalism^{58;59}. A Γ -centered $3 \times 3 \times 1$ Monkhorst-Pack K-point⁶⁰ grid was used to sample the Brillouin zone. All slabs were built as initially ideal p(4x4) Pt(111) cells with 4 layers. Only the two topmost layers were allowed to relax during the optimizations. All geometries are available in the appendix chapter A. The VASPsol module^{21;61} was used to assess the effect of an implicit solvent for comparison. The default settings for cavitation energy are used, and the plane-wave energy cutoff was increased to 600 eV. When a Pt slab was present, a dipole correction was applied in the out-of-plane direction⁶², to avoid solvating a macroscopic dipole.¹⁸

2.3.3 MM setup via SolvHybrid

SolvHybrid allows to setup the MM computations automatically. In practice, it builds 3×3 supercells (other multipliers are supported) with respect to the DFT unit cells to extend the lateral size of the surface well beyond the MM cut-off distance and to improve statistics. Atomic charges for the surface and molecules are extracted from Hirshfeld charges of the VASP computations,⁴² re-scaled as CM5 charges⁶³ and multiplied by the recommended factor of 1.27⁴³. Single-point gas-phase MM energies (E_{MM}^{vac}) are computed for each system (S, M, and M@S). The M@S and M systems are then solvated by a ~ 30 Å thick TIP3P water box⁴⁸, via the algorithm of leap from the AmberTools. The resulting orthorhombic box completely surrounds the system. Water molecules not above the surface are then removed so that the final water box matches the original in-plane dimensions of the 3×3 supercells. The water boxes of M@S and M are then minimized for 2000 cycles to diminish highly repulsive forces. An exact copy of the water box of the M@S system is then extracted to be placed on top of S. This leads to two systems (S and M@S) that only differ by the coordinates of the atoms that are being transformed during the TI, as requested by AMBER.

2.3.4 Settings for thermodynamic integrations

As described in section 2.2.1, SolvHybrid performs two independent TIs. TI₁ connects M@S to S: $(M@S)^{solv} \rightarrow (S)^{solv}$ required to evaluate $\delta\Delta_h G$. TI₂ connects M to bulk liquid water: $(M)^{solv} \rightarrow (\emptyset)^{solv}$ and is the main constituent for $\Delta_h G(M)$, the MMsolv solvation energy of the entity M.

When performing the TIs, the self-energy of the fragments that are alchemically transformed are also annihilated/created. Hence, to comply with the thermodynamic cycle of Fig. 2.1, the corresponding energies in vacuum have to be subtracted, so that the effective MM adsorption energy in vacuum $\Delta_a E_{MM}^{vac}$ does not contribute to the final result:

$$\begin{aligned}\Delta_a \Delta_h G &= \delta\Delta_h G_{MM} - \Delta_h G_{MM}(M) \\ &= (-\Delta_{TI_1} G - E_{MM}^{vac}(M@S) + E_{MM}^{vac}(S)) - (-\Delta_{TI_2} G - E_{MM}^{vac}(M)) \\ &= \Delta_{TI_2} G - \Delta_{TI_1} G - \Delta_a E_{MM}^{vac}\end{aligned}\quad (2.5)$$

Finally, we can write the hybrid adsorption energy in solution as:

$$\Delta_a G^{solv} = \Delta_a E_{DFT}^{vac} - \Delta_a E_{MM}^{vac} + \Delta_{TI_2} G - \Delta_{TI_1} G \quad (2.6)$$

Following standard practice in AMBER, each TI is separated in several partial transformations,

which we call “step” herein. Each step is itself divided into 11 windows, corresponding to different values of the mixing parameter λ . For each window, individual minimization, heating and equilibration to 300 K and production at 1 bar are performed.

The minimization is carried out for 100 cycles at constant volume. Heating from 5 to 300 K is achieved over 200 ps, *i.e.*, at a heat rate of $1.475 \text{ K}\cdot\text{ps}^{-1}$, with a thermostat time constant of 1 ps while the pressure is kept constant at 1 bar. Equilibration is carried out for 100 ps in the NPT ensemble, keeping the the temperature at 300 K by a Langevin thermostat with a collision frequency of 2 ps^{-1} .⁶⁴ 200 ps of dynamics under the same conditions are used as the production phase.

The steps constituting the TIs are: (i) Discharge of the non aqueous part of $M@S$, *i.e.*, scaling the atomic charges of $M@S$ progressively to zero, (ii) For $M@S$ with no atomic charges, transforming the GAL17 forcefield to sGAL17, (iii) Alchemical change from $M@S$ to S with no atomic charges on S and $M@S$ and with sGAL17 for the water/Pt interaction, (iv) For S , transform the sGAL17 to the GAL17 forcefield, (v) Recharge of the non-aqueous part of S , *i.e.*, scaling atomic charges of S from zero to their physical values. We find that step (ii) and step (iv) are necessary to ensure reproducible results, avoiding hysteresis with windows being trapped in meta-stable states for several nanoseconds.

The discharge (i), recharge (v), and alchemical (iii) steps are conducted on 9 evenly spaced windows with λ ranging from 0.1 to 0.9, plus 2 windows at λ equal to 0.005 and 0.995. The softening of GAL17 (ii) and its reverse (iv) are performed in 11 logarithmic-spaced (spacing following $\ln(x)$) and decreasing logarithmic-spaced windows (spacing following $1 - \ln(x)$) ranging from 0.005 to 0.995, which reflects the exponential shape of $\langle \frac{\partial V(\lambda)}{\partial \lambda} \rangle_\lambda$ during these transformations (see Fig. A.1 and Fig. A.2 in the appendix chapter A).

Using an algorithm from Steinbrecher⁶⁵, free energy variations are gathered over the last 200 ps of each window, numerically integrated for each step and summed to the corresponding total free energy change.

2.4 Results and discussion

Having described the developed hybrid method in section 2.2.1, we now turn to the actual results obtained when combining DFT in vacuum with MMsolv solvation energies. By computing the solvation energy of $\text{H}_2\text{O}@Pt(111)$, we first investigate the intrinsic error, which is committed by the uneven description for adsorbates and the solvent. Then, we move to the solvation energy of the Pt(111) surface in order to obtain rough estimates of the energetic costs to displace water molecules from the surface. Finally, we validate our method by assessing the adsorption free energy of benzene and phenol at the Pt(111)/water interface, for which experimental estimates are available.

2.4.1 H₂O@Pt(111) solvation energies to monitor inconsistencies

To estimate the inconsistencies of the scheme due to the dual DFT/MM description, we here evaluate the adsorption free energy of water in the water solvent. The considered transformation is an exchange between two water molecules, one which is in the bulk solvent, and the other one is adsorbed on the surface. Hence, the energy balance of this exchange should be zero. Practically, in the MMSolv scheme, the adsorption of a water molecule is described by DFT, *i.e.*, via a DFT geometry optimization and $\Delta_a E_{DFT}^{vac}$, just like for any other adsorbate. Simultaneously, the desorption of MM-described water molecule(s) makes space for the DFT adsorbate. We consider this exchange as the worst-case scenario for the present scheme since it implies an exchange between two molecules that are supposedly identical, but are described by two different levels of theory. Furthermore, the adsorbate is small and interacts strongly with the solvent, so that there is barely room for error cancellation. The resulting adsorption free energy, compared to the expected zero energy balance, will, therefore, be particularly sensitive to discrepancies between the two levels of theory. This adsorption free energy was also assessed as a function of the distance of the water molecule from the surface. This evaluates the committed error, the smoothness and convergence behavior toward the expected zero energy result far away from the surface.

We will here use H₂O^{DFT} to distinguish it from the MM water molecules. In this case, $\Delta_a G^{solv}$ represents the free energy required to replace a MM water molecule on the surface by H₂O^{DFT}@Pt(111) and, simultaneously make H₂O^{DFT} disappear from the bulk water. H₂O^{DFT} is distinct from the MM water molecules in three ways: (i) its interaction with the surface is treated at the DFT level and consists in $\Delta_a E_{DFT}^{vac}$, (ii) it polarizes the platinum surface during its adsorption while the MM water molecules do not, (iii) it is frozen during the TI and therefore can neither be exchanged with other water molecules, nor move to optimize the organisation of the interfacial structure of water.

$\Delta_a G^{solv}(H_2O)$ is used to determine the effectiveness of the Coulomb correction described in section 2.2.2: Fig. 2.3 compares the results obtained with the standard (shifted) Coulomb interactions in orange (Eq. 2.3) with the short-range corrected interactions (in blue) of Eq. 2.4. Note, that the results for Particle Mesh Ewald are of equivalent quality to the orange lines of the standard shifted Coulomb scheme (see Fig. A.3).

According to Fig 2.3, $\Delta_a G^{solv}$ is positive at short distances and diminishes from 11 or 7 kcal·mol⁻¹ for the “standard” and “short-range corrected” Coulomb interactions, to about zero at long distance (> 8 Å) while consistently displaying a slight second peak of 2 kcal·mol⁻¹ at ~ 5 Å. The decay to zero after 8 Å means that from this distance on, there is no interaction between the molecule and the surface, and, furthermore, that even the water organization around the frozen molecule is the same as in the bulk. In contrast, at short distances the three differences mentioned above and discussed in the next paragraphs might contribute to make

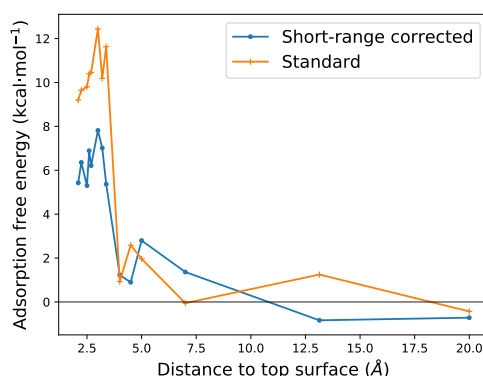


Figure 2.3 – Adsorption free energy $\Delta_a G^{solv}$ for immobilized DFT water molecule on a 4 layers slab of Pt(111) using a p(4x4) cell as a function of the distance of the oxygen to the surface. Its interactions with the slab are described at DFT level. Corrected refers to free energies computed with the coulombic correction proposed, in opposition to the uncorrected energies. Free energies are given an estimated ± 1.0 kcal·mol⁻¹ accuracy (See appendix chapter A, section A.4 for details).

$\Delta_a G^{solv}$ positive.

The obvious difference (i) is that the interaction of a MM molecule at the surface is replaced by $\Delta_a E_{DFT}^{vac}$ for $H_2O^{DFT}@Pt(111)$. However, this change is expected to be well described by the GAL17 forcefield,³⁴ and should, therefore, not lead to a considerable contribution.

The subtle difference (ii) is connected to the atomic charges: the charges of H_2O^{DFT} and the metallic atoms are modified by polarization and non-negligible charge transfer at the DFT level,⁶⁶ an effect that is only implicitly (at the single molecule level) taken into account in GAL17. Fig. 2.4 illustrates the DFT charge distribution at the DFT adsorption minimum. On average, the surface atoms are negatively charged, even though a strong positive charge is found for the Pt atom on which the oxygen is adsorbed. This positive charge is not very problematic in the MM computations since it is “shielded” by H_2O^{DFT} and only MM water molecules in the second layer will be affected by it. The negative charge, which accumulates in the vicinity of the hydrogen atoms, can, however, lead to substantial interactions with the oxygen atoms of co-adsorbed MM water molecules. Even a partial charge of only $-0.05 e^-$ at the adsorption minimum distance of of 2.5 Å yields an artificial repulsion of about 5 kcal·mol⁻¹ with the water oxygen atom. It is this repulsion that the Coulomb short-range correction of Eq. 2.4 is designed to attenuate. Indeed, switching the correction on reduces $\Delta_a G^{solv}$ at short distance from 11 kcal·mol⁻¹ to 7 kcal·mol⁻¹. We, therefore, assign this 4 kcal·mol⁻¹ difference as the cost of the unequal description of charge transfer. While the DFT polarization is, of course, physically meaningful, the issue here is that the MM water molecules do neither lead to such a polarization nor is the force field (GAL17) adapted to deal with the surface polarization, but built for a neutral surface, as discussed in section 2.2.2.

Chapter 2. Solvation Free Energies and Adsorption Energies at the Metal/Water Interface from Hybrid Quantum-Mechanical/Molecular Mechanics Simulations

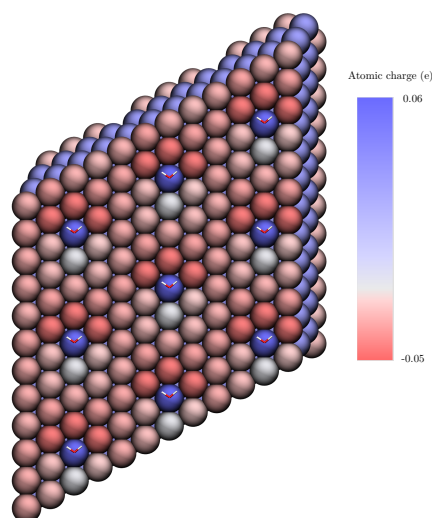


Figure 2.4 – Atomic charges computed for the slab interacting with “DFT water” molecules. The charges are CM5 charges scaled by 1.27 according to ref 43.

Finally, point (iii) questions if keeping a water molecule frozen at the interface significantly disturbs the interfacial organization. To quantify this effect, we perform TIs with frozen MM molecules instead of $\text{H}_2\text{O}^{\text{DFT}}$. These tests show that a MM frozen water molecule results in a $\Delta_a G^{\text{solv}}$ very close to 0, *i.e.*, that freezing in itself does not introduce a significant artifact.

Having addressed the three points above, we may ask ourselves where the remaining $7 \text{ kcal}\cdot\text{mol}^{-1}$ at short distance come from. In the spirit of our tests with frozen MM water molecules, we perform further tests to assess the impact of the internal polarization of the water molecule upon adsorption. We observe that the oxygen atom in $\text{H}_2\text{O}^{\text{DFT}}@Pt(111)$ is less negatively charged compared to the non-adsorbed water molecule (-0.7 vs. $-0.8 e^-$). Due to this weaker internal polarization, the interaction of $\text{H}_2\text{O}^{\text{DFT}}$ with the other water molecules at the interface is much weaker than it “should” be, resulting in the positive $\Delta_a G^{\text{solv}}$.

As a result of this analysis, we conclude that the Coulomb correction is an important component of solvation energies at metallic surfaces. However, direct solvent effects, *i.e.*, the modification of water–adsorbate interaction due to the surface are only approximately taken into account, as shown here by the remaining free energy difference, and already highlighted during the development of GAL17³⁴. Thus, if suspected to be important, the direct water effects should be treated via microsolvation.¹⁵ Our hypothesis is, however, that the water–water interaction at the interface is among the worst cases possible, which means that we expect errors below $7 \text{ kcal}\cdot\text{mol}^{-1}$ for general adsorbates.

2.4.2 Solvation free energy of the Pt(111) surface

In order to validate the scheme beyond the “intrinsic” worst-case scenario of section 2.4.1, we estimate the solvation free energy of the Pt(111) surface. This surface solvation free energy Γ_{surf} (see Eq. A.3 in the appendix chapter A) corresponds to the free energy change associated with the creation of a water interface with a platinum slab in the middle of bulk water. In other words, the Pt–vacuum surface free energy does not contribute. It is, therefore, negative if the stabilizing interactions between water and platinum are strong enough to overcome the cost of creating a “gap” in water that will be filled with platinum. Γ_{surf} can be computed similarly to the MMsolv term of Eq. 2.1 via SolvHybrid by adapting the latter to allow the creation of the full platinum slab instead of only the adsorbed molecule, with all the details exposed in the supplementary information (section A.5). Using the TIP3P water model Γ_{surf} is found to be $-0.46 \text{ J}\cdot\text{m}^{-2}$ ($-5.2 \text{ kcal}\cdot\text{mol}^{-1}\cdot\text{atom}^{-1}$). As a comparison, we also compute the corresponding value for the TIP4P water model and obtain $-0.51 \text{ J}\cdot\text{m}^{-2}$ ($-5.8 \text{ kcal}\cdot\text{mol}^{-1}\cdot\text{atom}^{-1}$). The corresponding value for the water/gas-phase interface has been determined to $0.052 \text{ J}\cdot\text{m}^{-2}$,⁶⁷ *i.e.*, about ten times less in absolute value and, of course, positive, as the creation of this interface costs energy. Compared to the value of $-0.32 \text{ J}\cdot\text{m}^{-2}$ reported by Campbell *et al.*,⁶⁸ the accuracy of the result is very encouraging and on the same order of magnitude as the estimate of $0.27 \text{ J}\cdot\text{m}^{-2}$ by Gim *et al.*⁶⁹ using a more sophisticated electrostatic embedding⁷⁰ but a less accurate water–metal force field compared to this present study. The sign of this value is consistent with the wettability of platinum. The magnitude is almost reduced by a factor of two with respect to the adsorption energy of a single water molecule on a platinum slab (roughly $-9 \text{ kcal}\cdot\text{mol}^{-1}$ according to DFT), which is coherent with the energetic and entropic cost to create the interface. The contribution due to the loss of water–water interactions due to the creation of the interface is, as stated above, only responsible for a reduction of about $0.5 \text{ kcal}\cdot\text{mol}^{-1}$ with respect to the vacuum adsorption energy, highlighting the significant difference between the solid/liquid and liquid/gas interface.

A remarkable feature of explicit solvent molecular dynamics is the possibility to evaluate the solvation free energy as a function of the temperature. This contrasts with continuum models such as PCM that are fitted for a given temperatures and cannot predict the temperature dependence.²¹ In practice, we evaluate Γ_{surf} for a range of temperatures and determine the enthalpy and entropy according to its derivative (see Fig. 2.5). The enthalpic component $\Delta_h H_{surf}$ of the surface solvation free energy is closely related to the stabilizing interaction between Pt and water, while its entropic counterpart $-T\Delta_h S_{surf}$ is linked to the interfacial reorganization. Since the molecules are partially immobilized at the interface, a fast reorganizing (hot) solvent is expected to loose more entropy than a cold solvent upon the formation of the interface. Despite the statistical noise, Γ_{surf} increases (becomes less negative) when increasing the temperature. The curve is fitted to a linear formula following $\Gamma_{surf} = \Delta_h H_{surf} - T\Delta_h S_{surf}$ with $\Delta_h H_{surf} = -0.86 \text{ J}\cdot\text{m}^{-2}$ and $\Delta_h S_{surf} = -1.34 \text{ mJ}\cdot\text{m}^{-2}\cdot\text{K}^{-1}$ ($R^2=0.81$). The negative entropy confirms the reduced mobility of water at the interface.

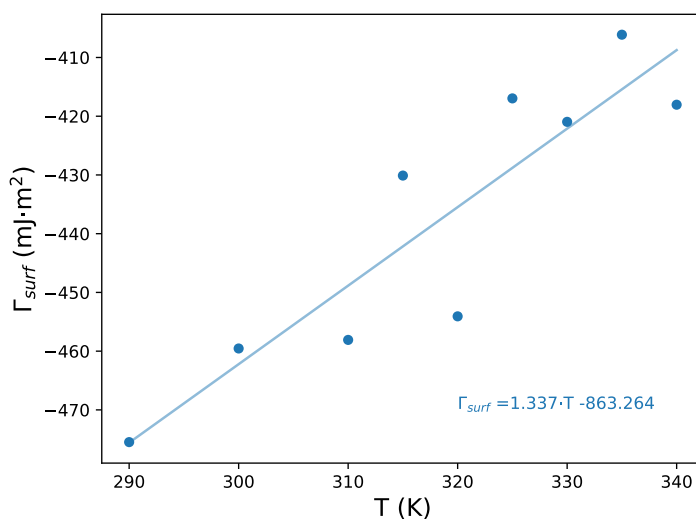


Figure 2.5 – Solvation free energy of the Pt(111) surface in function of the temperature

In conclusion, the solvation free energy of Pt(111) obtained with GAL17 and the adopted strategy to carefully converge the thermodynamic integrations results in good agreement with experimental estimates. Furthermore, we provide new insights on the decomposition of the entropy/enthalpy balance at the solid/liquid interface. This makes us confident to tackle the next step which is the solvation free energy of adsorbates at the Pt(111)/water interface.

2.4.3 Adsorption of benzene and phenol at the Pt(111)/water interface

The adsorption free energy of benzene and phenol are studied to quantitatively evaluate the accuracy level of our QM/MM hybrid scheme compared to the experimental estimates from Campbell *et. al.*⁶⁸ This provides us also the opportunity to compare MMSolv solvation energies to the one obtained with the widely used PCM, implemented in VASPsol.²¹

As a start, we compare the solvation energies of molecules in solution to their experimental counterparts, taken from the Minnesota database of solvation free energies.⁷¹ The experimental standard solvation free energies of water, phenol and benzene in water are reported to be -6.31, -6.62 and -0.87 kcal·mol⁻¹, respectively. The implicit solvent, which is fitted on this kind of reference data, is in qualitative agreement, yielding -7.5, -5.7 and -1.0 kcal·mol⁻¹. The MMsolv bulk solvation energies $\Delta_h G_{MM}(M)$ are -4.8, -4.9 and -2.3 kcal·mol⁻¹. While these solvation free energies are not highly accurate, although in agreement with previous reports,^{27;29} the error remains in the 1-2 kcal·mol⁻¹ range, which is acceptable in our context and comparable to PCM values. Such errors have also been proposed to originate from missing polarization and charge-transfer effects at the MM level.²⁹ These computations also

demonstrate that the computational setup is reasonable, *i.e.*, (a) a sound combination of atomic charges and Lennard-Jones parameters and (b) that the direct space computation of the Coulomb interaction does not introduce major inaccuracies or inconsistencies.

Since MM naturally includes the size of the solvent molecules, we can expect that the coverage-dependence of adsorption energies differs between PCM and MMSolv. The aromatic molecules have been suggested to adsorb flat on the so-called bridge position at the Pt(111)/water interface.^{68;72} To investigate the coverage dependence and the preferred adsorption mode, we consider four different coverages (from 1/7 to 1/36 monolayer (ML), where the ML is defined with respect to the number of surface Pt atoms) for the two most stable gas-phase adsorption modes, as proposed by Chaudhary *et.al.* (see Fig. A.4 in the appendix chapter A).⁷³ Since the relative stability of these two modes is conserved after the evaluation of solvation free energy, only the most stable mode are discussed below. We note that defining the coverage in terms of surface Pt atoms is most convenient as the saturation coverage is not unambiguously known. However, using this definition, care should be applied when comparing the coverage dependent adsorption energies of various molecules, as adding a small additional molecule (*e.g.* CO) has not the same effect as adding a large one (*e.g.* naphtalene). As described below, the size of the adsorbate also displaces a varying amount of water molecules from the first interfacial layer.

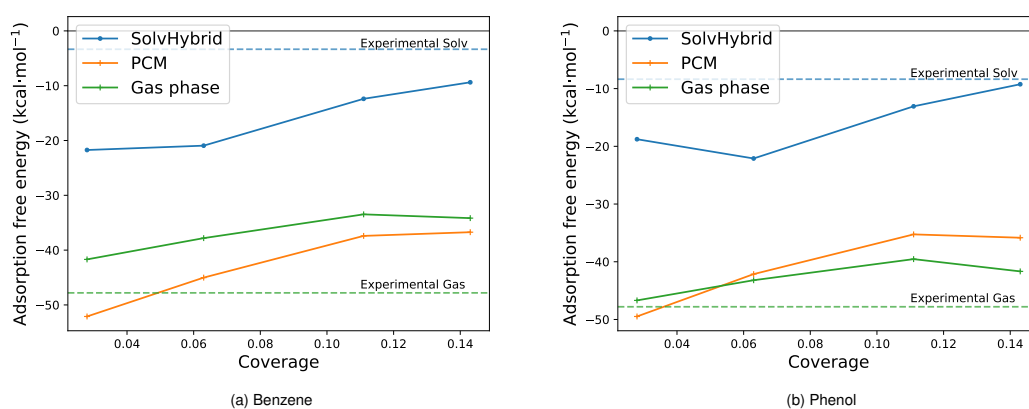


Figure 2.6 – Adsorption free energy $\Delta_a G^{solv}$, calculated with SolvHybrid or using the Polarizable Continuum Model (PCM) as an implicit solvent, for a benzene or phenol molecule at 4 different coverages on a (111) platinum slab. Gas phase result refers to DFT-based adsorption energy for the same systems. The molecule were all adsorbed on position Brg30° for Benzene and Brg30°C2 for Phenol (see Fig. A.4). The dashed lines correspond to the experimental values of ref⁷¹, whose precise coverage is unknown, with gas referring to gas phase adsorption energy and Solv to the free energy of adsorption in water.

The adsorption free energies of phenol and benzene as a function of the coverage are reported in Fig 2.6, where we compare gas-phase DFT to PCM and our QM/MM hybrid level. For all cases considered, a difference of less than 10 kcal·mol⁻¹ is observed between the adsorption free energy computed in the gas-phase and the implicit solvent. Qualitatively, PCM even

Chapter 2. Solvation Free Energies and Adsorption Energies at the Metal/Water Interface from Hybrid Quantum-Mechanical/Molecular Mechanics Simulations

stabilizes the adsorption of benzene at the Pt(111) interface, presumably due to the non-zero surface dipole moment obtained with the deformed benzene molecule (see Fig. 2.7) In contrast, the hybrid QM/MM adsorption free energy is reduced (in absolute value) by about 20 kcal·mol⁻¹ with respect to the gas-phase.

Campbell and co-workers have estimated the standard adsorption free energy (corresponding to ~ 0.05 ML) of benzene and phenol at the Pt(111)/water interface to be -3.4 kcal·mol⁻¹ and -8.4 kcal·mol⁻¹, respectively. This compares to their adsorption heat, measured both at about -47.8 kcal·mol⁻¹ at the Pt(111) gas-phase interface. Therefore, the trend between the gas-phase and aqueous-phase interface is qualitatively reproduced by our MMSolv results. In contrast, PCM predicts either no change (phenol) or a qualitatively wrong trend (benzene) and can, therefore, not be recommended to capture solvation effects at the Pt(111)/water interface, as also pointed out by Skylaris and co-workers.⁷⁴

In Fig. 2.6 we draw a dashed horizontal line for the experimentally estimated adsorption free energy. This does not indicate that the experimental value is assumed to be a constant as a function of the coverage. Indeed, for the gas-phase it is known that this is not the case.⁸ At the solid/liquid interface, however, the coverage dependence is not known and, furthermore, Campbell and co-workers have argued that the experimental values are most likely compatible with island formation, *i.e.*, locally much higher/lower coverages than on average. It is, therefore, difficult to judge the quantitative agreement between the experimental low-coverage, island-forming estimate and the homogeneous coverages investigated theoretically. As discussed in the section A.7 in the appendix chapter A, we have attempted to quantify the island-formation propensity according to a very simplified model. However, since applying the same framework to the gas-phase data leads to the prediction of island-formation, which goes against experiment evidence,⁷⁵ we conclude that the model is oversimplified. Hence, we conclude that the hybrid results of Fig 2.6 are just in qualitative agreement with experiment (especially at high coverage), but that a quantitative assessment of the coverage dependence is beyond the scope of this investigation.

The use of explicit solvent and extensive phase-space sampling also allows to quantify the coverage-dependent number of water molecules co-adsorbed with benzene or phenol. As an example Fig. 2.7 shows that most Pt top sites not directly covered by the adsorbate are occupied with water in the presence of 0.0625 ML benzene.

An analysis for 15 evenly spaced snapshots (corresponding to 300 ps of MD) of the first water layer (up to 4.5 Å above the topmost Pt atom) provides quantitative results as a function of the coverage. For benzene, a water coverage of 0.02, 0.32, 0.55, and 0.81 ML is observed for a benzene coverage of 0.14, 0.11, 0.06, and 0.03 ML, respectively which represent a nice linear decrease following approximately $\theta_{water} = 1 - 6.5 * \theta_{Benzene} = (n_{top} - 6.5 * n_{Benzene}) / n_{top}$ ($R^2 = 0.99$). From this we deduce that each adsorbed benzene molecule displaces 6.5 water

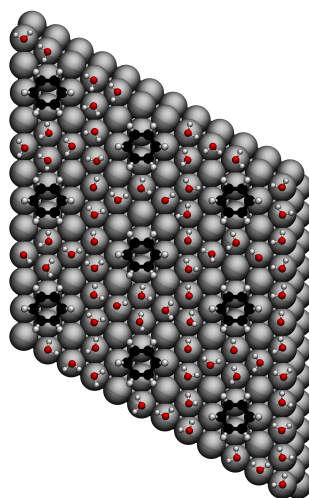


Figure 2.7 – Snapshot of the first solvation layer extracted from the production run of the computation of $\Delta_a G^{solv}$ of the benzene.

molecules at the interface. Similarly, water coverages of 0.01, 0.17, 0.53, and 0.80 ML were found for phenol, leading to a slope of -6.9 ($R^2 = 0.99$). In agreement with chemical intuition, this demonstrates that phenol takes somewhat more space on the surface than benzene. The fact that the difference is only small is likely to be attributed to the possibility of the hydroxyl group of phenol to be incorporated into the hydrogen-bond network of the first water layer. Furthermore, this quantification of the water displacement, together with a tentative^{76;77} decomposition of the solvation free energy change into an electrostatic and non-electrostatic component (see Table A.1 in the appendix chapter A) provides a strong evidence that the qualitative difference between the implicit solvation models and our explicit solvation scheme are related to the non-electrostatic energy terms associated with the displacement of water molecules upon adsorption.

On the one hand, these results illustrate the accuracy of our hybrid QM/MM scheme to predict experimental adsorption energies at the Pt(111)/water interface with a far better accuracy than the commonly used PCM. On the other hand, the explicit description and extensive phase-space sampling provides physical insight, such as the entropy/enthalpy balance at the interface and the competition between water and other adsorbates. In summary, our scheme is very promising and seems mostly limited by the accuracy of the MM energy expression, which can, however, be further improved without the need of adjustments in the adopted strategy. Hence we foresee a bright future for the SolvHybrid package for future investigations of solvation effects at the solid/liquid interface.

2.5 Conclusion

Alchemical transformations are powerful to determine solvation free energies at the molecular mechanics level of theory. As we have demonstrated herein, the near-chemisorption interaction of water with a prototypical Pt(111) surface necessitates adjustments of the “standard” thermodynamic cycle in order to reproducibly avoid hysteresis when computing the solvation free energies at the Pt/water interface. In our approach, this involves an intermediate state with weak interactions between the water solvent and the metal surface. Furthermore, the electrostatic interactions between the strongly adsorbed water molecules and the metal atoms is damped in order to avoid nonphysical contributions due to double counting. The resulting scheme, implemented in the freely available SolvHybrid software package that currently relies on the combination of VASP and AMBER, reliably determines solvation free energies at the Pt/water interface. It is validated by the assessment of the solvation free energy of the Pt(111) surface, which is, with $-0.46 \text{ J}\cdot\text{m}^{-2}$ for the TIP3P water model, in good agreement with the experimental estimate of $-0.32 \text{ J}\cdot\text{m}^{-2}$. More importantly, combined with DFT adsorption energies in gas-phase, adsorption energies from the bulk solution to the Pt/water interface are obtained at a hybrid DFT-MM level. As an example, a reduction of $\sim 30 \text{ kcal}\cdot\text{mol}^{-1}$ is obtained for the adsorption of benzene and phenol at the Pt(111)/water interface compared to the gas-phase. This compares well with the experimental estimates of $\sim 40 \text{ kcal}\cdot\text{mol}^{-1}$, while the implicit solvent estimate of ~ 0 is qualitatively incorrect. The major contribution at the hybrid level is traced back to the competition of the adsorbate with water molecules: the adsorption of a single aromatic molecule expels six to seven water molecules from the strongly bound first water layer. A further advantage of our approach compared to implicit solvents is that the explicit phase-space sampling with an atomistic water model naturally includes coverage and temperature effects, so that they can be conveniently quantified. In summary, our QM-MM hybrid scheme provides a routinely available semi-quantitative determination of adsorption energies at the metal/water interface, valuable in various contexts ranging from corrosion to liquid-phase heterogeneous catalysis.

Bibliography

- [1] Schiros, T.; Andersson, K.; Pettersson, L.; Nilsson, A.; Ogasawara, H. Chemical bonding of water to metal surfaces studied with core-level spectroscopies. *J. Electron Spectrosc. Relat. Phenom.* **2010**, *177*, 85–98.
- [2] Brown, W. A.; Kose, R.; King, D. A. Femtomole Adsorption Calorimetry on Single-Crystal Surfaces. *Chem. Rev.* **1998**, *98*, 797–832.
- [3] Besson, M.; Gallezot, P.; Pinel, C. Conversion of Biomass into Chemicals over Metal Catalysts. *Chem. Rev.* **2014**, *114*, 1827–1870.

- [4] Liu, L.; Corma, A. Metal Catalysts for Heterogeneous Catalysis: From Single Atoms to Nanoclusters and Nanoparticles. *Chem. Rev.* **2018**, *118*, 4981–5079.
- [5] Seh, Z. W.; Kibsgaard, J.; Dickens, C. F.; Chorkendorff, I.; Nørskov, J. K.; Jaramillo, T. F. Combining theory and experiment in electrocatalysis: Insights into materials design. *Science* **2017**, *355*, eaad4998.
- [6] Chibani, S.; Michel, C.; Delbecq, F.; Pinel, C.; Besson, M. On the key role of hydroxyl groups in platinum-catalysed alcohol oxidation in aqueous medium. *Catal. Sci. Technol.* **2013**, *3*, 339–350.
- [7] Gu, Q.; Sautet, P.; Michel, C. Unraveling the Role of Base and Catalyst Polarization in Alcohol Oxidation on Au and Pt in Water. *ACS Catal.* **2018**, *8*, 11716–11721, Times Cited: 7.
- [8] Carey, S. J.; Zhao, W.; Mao, Z.; Campbell, C. T. Energetics of Adsorbed Phenol on Ni(111) and Pt(111) by Calorimetry. *J. Phys. Chem. C* **2019**, *123*, 7627–7632.
- [9] Bockris, J.; Jeng, K. In-situ studies of adsorption of organic compounds on platinum electrodes. *J. Electroanal. Chem.* **1992**, *330*, 541–581.
- [10] Lu, F.; Salaita, G. N.; Laguren-Davidson, L.; Stern, D. A.; Wellner, E.; Frank, D. G.; Batina, N.; Zapfen, D. C.; Walton, N.; Hubbard, A. T. Characterization of hydroquinone and related compounds adsorbed at Pt(111) from aqueous solutions: electron energy-loss spectroscopy, Auger spectroscopy, LEED, and cyclic voltammetry. *Langmuir* **1988**, *4*, 637–646.
- [11] Michel, C.; Zaffran, J.; Ruppert, A. M.; Matras-Michalska, J.; Jedrzejczyk, M.; Grams, J.; Sautet, P. Role of water in metal catalyst performance for ketone hydrogenation: a joint experimental and theoretical study on levulinic acid conversion into gamma-valerolactone. *Chem. Commun.* **2014**, *50*, 12450–12453.
- [12] Michel, C.; Auneau, E.; Delbecq, F.; Sautet, P. C–H versus O–H Bond Dissociation for Alcohols on a Rh(111) Surface: A Strong Assistance from Hydrogen Bonded Neighbors. *ACS Catal.* **2011**, *1*, 1430–1440.
- [13] Hibbitts, D. D.; Loveless, B. T.; Neurock, M.; Iglesia, E. Mechanistic Role of Water on the Rate and Selectivity of Fischer-Tropsch Synthesis on Ruthenium Catalysts. *Angew. Chem. Int. Ed.* **2013**, *52*, 12273–12278.
- [14] Garcia-Rates, M.; Garcia-Muelas, R.; Lopez, N. Solvation Effects on Methanol Decomposition on Pd(111), Pt(111), and Ru(0001). *J. Phys. Chem. C* **2017**, *121*, 13803–13809.
- [15] Schweitzer, B.; Steinmann, S. N.; Michel, C. Can microsolvation effects be estimated from vacuum computations? A case-study of alcohol decomposition at the H₂O/Pt(111) interface. *Phys. Chem. Chem. Phys.* **2019**, *21*, 5368–5377.

Chapter 2. Solvation Free Energies and Adsorption Energies at the Metal/Water Interface from Hybrid Quantum-Mechanical/Molecular Mechanics Simulations

- [16] Gao, W.; Keith, J. A.; Anton, J.; Jacob, T. Theoretical Elucidation of the Competitive Electro-oxidation Mechanisms of Formic Acid on Pt(111). *J. Am. Chem. Soc.* **2010**, *132*, 18377–18385.
- [17] Behtash, S.; Lu, J.; Mamun, O.; Williams, C. T.; Monnier, J. R.; Heyden, A. Solvation Effects in the Hydrodeoxygenation of Propanoic Acid over a Model Pd(211) Catalyst. *J. Phys. Chem. C* **2016**, *120*, 2724–2736.
- [18] Gu, G. H.; Schweitzer, B.; Michel, C.; Steinmann, S. N.; Sautet, P.; Vlachos, D. G. Group Additivity for Aqueous Phase Thermochemical Properties of Alcohols on Pt(111). *J. Phys. Chem. C* **2017**, 10.1021/acs.jpcc.7b07340, Publisher: American Chemical Society.
- [19] Faheem, M.; Saleheen, M.; Lu, J.; Heyden, A. Ethylene glycol reforming on Pt(111): first-principles microkinetic modeling in vapor and aqueous phases. *Catal. Sci. Technol.* **2016**, *6*, 8242–8256, Publisher: The Royal Society of Chemistry.
- [20] Steinmann, S. N.; Sautet, P. Assessing a First-Principles Model of an Electrochemical Interface by Comparison with Experiment. *J. Phys. Chem. C* **2016**, *120*, 5619–5623, Publisher: American Chemical Society.
- [21] Mathew, K.; Sundararaman, R.; Letchworth-Weaver, K.; Arias, T. A.; Hennig, R. G. Implicit solvation model for density-functional study of nanocrystal surfaces and reaction pathways. *J. Chem. Phys.* **2014**, *140*, 084106.
- [22] Desai, S. K.; Pallassana, V.; Neurock, M. A Periodic Density Functional Theory Analysis of the Effect of Water Molecules on Deprotonation of Acetic Acid over Pd(111). *J. Phys. Chem. B* **2001**, *105*, 9171–9182, Publisher: American Chemical Society.
- [23] Yoon, Y.; Rousseau, R.; Weber, R. S.; Mei, D.; Lercher, J. A. First-Principles Study of Phenol Hydrogenation on Pt and Ni Catalysts in Aqueous Phase. *J. Am. Chem. Soc.* **2014**, *136*, 10287–10298.
- [24] Bellarosa, L.; García-Muelas, R.; Revilla-López, G.; López, N. Diversity at the Water–Metal Interface: Metal, Water Thickness, and Confinement Effects. *ACS Cent. Sci.* **2016**, *2*, 109–116.
- [25] Faheem, M.; Heyden, A. Hybrid Quantum Mechanics/Molecular Mechanics Solvation Scheme for Computing Free Energies of Reactions at Metal–Water Interfaces. *J. Chem. Theory Comput.* **2014**, *10*, 3354–3368, Publisher: American Chemical Society.
- [26] Saleheen, M.; Zare, M.; Faheem, M.; Heyden, A. Computational Investigation of Aqueous Phase Effects on the Dehydrogenation and Dehydroxylation of Polyols over Pt(111). *J. Phys. Chem. C* **2019**, *123*, 19052–19065.

- [27] Steinmann, S. N.; Sautet, P.; Michel, C. Solvation free energies for periodic surfaces: comparison of implicit and explicit solvation models. *Phys. Chem. Chem. Phys.* **2016**, *18*, 31850–31861.
- [28] Bodenschatz, C. J.; Sarupria, S.; Getman, R. B. Molecular-Level Details about Liquid H₂O Interactions with CO and Sugar Alcohol Adsorbates on Pt(111) Calculated Using Density Functional Theory and Molecular Dynamics. *J. Phys. Chem. C* **2015**, *119*, 13642–13651.
- [29] Zhang, X.; DeFever, R. S.; Sarupria, S.; Getman, R. B. Free Energies of Catalytic Species Adsorbed to Pt(111) Surfaces under Liquid Solvent Calculated Using Classical and Quantum Approaches. *J. Chem. Inf. Model.* **2019**, *59*, 2190–2198.
- [30] Spohr, E.; Heinzinger, K. Molecular dynamics simulation of a water/metal interface. *Chem. Phys. Lett.* **1986**, *123*, 218–221.
- [31] Siepmann, J. I.; Sprik, M. Influence of surface topology and electrostatic potential on water/electrode systems. *J. Chem. Phys.* **1995**, *102*, 511–524, Publisher: American Institute of Physics.
- [32] Limmer, D. T.; Willard, A. P.; Madden, P.; Chandler, D. Hydration of metal surfaces can be dynamically heterogeneous and hydrophobic. *Proc. Natl. Acad. Sci. U. S. A.* **2013**, *110*, 4200–4205.
- [33] Heinz, H.; Vaia, R. A.; Farmer, B. L.; Naik, R. R. Accurate Simulation of Surfaces and Interfaces of Face-Centered Cubic Metals Using 12-6 and 9-6 Lennard-Jones Potentials. *J. Phys. Chem. C* **2008**, *112*, 17281–17290.
- [34] Steinmann, S. N.; Ferreira De Morais, R.; Götz, A. W.; Fleurat-Lessard, P.; Iannuzzi, M.; Sautet, P.; Michel, C. Force Field for Water over Pt(111): Development, Assessment, and Comparison. *J. Chem. Theory Comput.* **2018**, *14*, 3238–3251.
- [35] Clabaut, P.; Fleurat-Lessard, P.; Michel, C.; Steinmann, S. N. Ten Facets, One Force Field: The GAL19 Force Field for Water–Noble Metal Interfaces. *J. Chem. Theory Comput.* **2020**, *16*, 4565–4578, Publisher: American Chemical Society.
- [36] Réocreux, R.; Michel, C.; Fleurat-Lessard, P.; Sautet, P.; Steinmann, S. N. Evaluating Thermal Corrections for Adsorption Processes at the Metal/Gas Interface. *J. Phys. Chem. C* **2019**, *123*, 28828–28835.
- [37] Kresse, G. Ab initio molecular dynamics for liquid metals. *J. Non-Cryst. Solids* **1995**, *192-193*, 222–229.
- [38] Kresse, G.; Furthmüller, J. Efficiency of ab-initio total energy calculations for metals and semiconductors using a plane-wave basis set. *Computational Materials Science* **1996**, *6*, 15–50.

Chapter 2. Solvation Free Energies and Adsorption Energies at the Metal/Water Interface from Hybrid Quantum-Mechanical/Molecular Mechanics Simulations

- [39] Case, D. A.; Cheatham, T. E.; Darden, T.; Gohlke, H.; Luo, R.; Merz, K. M.; Onufriev, A.; Simmerling, C.; Wang, B.; Woods, R. J. The Amber biomolecular simulation programs. *J. Comput. Chem.* **2005**, *26*, 1668–1688.
- [40] D.A. Case, R.M. Betz, W. Botello-Smith, D.S. Cerutti, T.E. Cheatham, III, T.A. Darden, R.E. Duke, T.J. Giese, H. Gohlke, A.W. Goetz, N. Homeyer, S. Izadi, P. Janowski, J. Kaus, A. Kovalenko, T.S. Lee, S. LeGrand, P. Li, C. Lin, T. Luchko, R. Luo, B. Madej, D. Mermelstein, K.M. Merz, G. Monard, H. Nguyen, H.T. Nguyen, I. Omelyan, A. Onufriev, D.R. Roe, A. Roitberg, C. Sagui, C.L. Simmerling, J. Swails, R.C. Walker, J. Wang, R.M. Wolf, X. Wu, L. Xiao, D.M. York and P.A. Kollman (2017), AMBER 2017, University of California, San Francisco.
- [41] Rappe, A. K.; Casewit, C. J.; Colwell, K. S.; Goddard, W. A.; Skiff, W. M. UFF, a full periodic table force field for molecular mechanics and molecular dynamics simulations. *J. Am. Chem. Soc.* **1992**, *114*, 10024–10035.
- [42] Hirshfeld, F. L. Bonded-atom fragments for describing molecular charge densities. *Theor. Chim. Acta* **1977**, *44*, 129–138.
- [43] Vilseck, J. Z.; Tirado-Rives, J.; Jorgensen, W. L. Evaluation of CM5 Charges for Condensed-Phase Modeling. *J. Chem. Theory Comput.* **2014**, *10*, 2802–2812.
- [44] Mackerell, A. D. Empirical force fields for biological macromolecules: Overview and issues. *J. Comput. Chem.* **2004**, *25*, 1584–1604.
- [45] Brooks, I., Charles L; Pettitt, B. M.; Karplus, M. Structural and energetic effects of truncating long ranged interactions in ionic and polar fluids. *J. Chem. Phys.* **1985**, *83*, 5897, Publisher: American Institute of Physics.
- [46] Steinbach, P. J.; Brooks, B. R. New spherical-cutoff methods for long-range forces in macromolecular simulation. *J. Comput. Chem.* **1994**, *15*, 667–683.
- [47] Steinmann, S. N.; Fleurat-Lessard, P.; Götz, A. W.; Michel, C.; Ferreira de Moraes, R.; Sautet, P. Molecular mechanics models for the image charge, a comment on “including image charge effects in the molecular dynamics simulations of molecules on metal surfaces”. *J. Comput. Chem.* **2017**, *38*, 2127–2129.
- [48] William L. Jorgensen,; Chandrasekhar, J.; Madura, J. D.; Impey, R. W.; Klein, M. L. Comparison of simple potential functions for simulating liquid water. *J. Chem. Phys.* **1983**, *79*, 926–935.
- [49] Ryckaert, J.-P.; Ciccotti, G.; Berendsen, H. J. Numerical integration of the cartesian equations of motion of a system with constraints: molecular dynamics of n-alkanes. *J. Comput. Phys.* **1977**, *23*, 327–341.

- [50] Ryckaert, J. Special geometrical constraints in the molecular dynamics of chain molecules. *Mol. Phys.* **1985**, *55*, 549–556.
- [51] Berendsen, H. J. C.; Postma, J. P. M.; van Gunsteren, W. F.; DiNola, A.; Haak, J. R. Molecular dynamics with coupling to an external bath. *J. Chem. Phys.* **1984**, *81*, 3684–3690.
- [52] Beutler, T. C.; Mark, A. E.; van Schaik, R. C.; Gerber, P. R.; van Gunsteren, W. F. Avoiding singularities and numerical instabilities in free energy calculations based on molecular simulations. *Chem. Phys. Lett.* **1994**, *222*, 529–539.
- [53] Zacharias, M.; Straatsma, T. P.; McCammon, J. A. Separation-shifted scaling, a new scaling method for Lennard-Jones interactions in thermodynamic integration. *J. Chem. Phys.* **1994**, *100*, 9025–9031.
- [54] Perdew, J. P.; Wang, Y. Accurate and simple analytic representation of the electron-gas correlation energy. *Phys. Rev. B* **1992**, *45*, 13244–13249.
- [55] Perdew, J. P.; Burke, K.; Ernzerhof, M. Generalized Gradient Approximation Made Simple. *Phys. Rev. Lett.* **1996**, *77*, 3865–3868.
- [56] Steinmann, S. N.; Corminboeuf, C. A generalized-gradient approximation exchange hole model for dispersion coefficients. *J. Chem. Phys.* **2011**, *134*, 044117.
- [57] Gautier, S.; N. Steinmann, S.; Michel, C.; Fleurat-Lessard, P.; Sautet, P. Molecular adsorption at Pt(111). How accurate are DFT functionals? *Phys. Chem. Chem. Phys.* **2015**, *17*, 28921–28930.
- [58] Blochl, P. E. Projector augmented-wave method. *Phys. Rev. B* **1994**, *50*, 17953.
- [59] Kresse, G.; Joubert, D. From ultrasoft pseudopotentials to the projector augmented-wave method. *Phys. Rev. B* **1999**, *59*, 1758.
- [60] Monkhorst, H. J.; Pack, J. D. Special points for Brillouin-zone integrations. *Phys. Rev. B* **1976**, *13*, 5188–5192.
- [61] Mathew, K.; Kolluru, V. S. C.; Mula, S.; Steinmann, S. N.; Hennig, R. G. Implicit self-consistent electrolyte model in plane-wave density-functional theory. *J. Chem. Phys.* **2019**, *151*, 234101.
- [62] Neugebauer, J.; Scheffler, M. Adsorbate-substrate and adsorbate-adsorbate interactions of Na and K adlayers on Al(111). *Phys. Rev. B* **1992**, *46*, 16067–16080.
- [63] Marenich, A. V.; Jerome, S. V.; Cramer, C. J.; Truhlar, D. G. Charge Model 5: An Extension of Hirshfeld Population Analysis for the Accurate Description of Molecular Interactions in Gaseous and Condensed Phases. *J. Chem. Theory Comput.* **2012**, *8*, 527–541.

Chapter 2. Solvation Free Energies and Adsorption Energies at the Metal/Water Interface from Hybrid Quantum-Mechanical/Molecular Mechanics Simulations

- [64] Schlick, T. *Molecular Modeling and Simulation: An Interdisciplinary Guide: An Interdisciplinary Guide*, 2nd ed.; Interdisciplinary Applied Mathematics; Springer-Verlag: New York, 2010.
- [65] Steinbrecher, T.; Mobley, D. L.; Case, D. A. Nonlinear scaling schemes for Lennard-Jones interactions in free energy calculations. *J. Chem. Phys.* **2007**, *127*, 214108.
- [66] Staub, R.; Iannuzzi, M.; Khaliullin, R. Z.; Steinmann, S. N. Energy Decomposition Analysis for Metal Surface? @ SAdsorbate Interactions by Block Localized Wave Functions. *J. Chem. Theory Comput.* **2019**, *15*, 265–275.
- [67] Vega, C.; de Miguel, E. Surface tension of the most popular models of water by using the test-area simulation method. *J. Chem. Phys.* **2007**, *126*, 154707, Publisher: American Institute of Physics.
- [68] Singh, N.; Campbell, C. T. A Simple Bond-Additivity Model Explains Large Decreases in Heats of Adsorption in Solvents Versus Gas Phase: A Case Study with Phenol on Pt(111) in Water. *ACS Catal.* **2019**, *9*, 8116–8127.
- [69] Gim, S.; Cho, K. J.; Lim, H.-K.; Kim, H. Structure, Dynamics, and Wettability of Water at Metal Interfaces. *Sci. Rep.* **2019**, *9*, 1–7.
- [70] Fdez Galvan, I.; Sanchez, M.; Martin, M.; Olivares del Valle, F.; Aguilar, M. ASEP/MD: A program for the calculation of solvent effects combining QM/MM methods and the mean field approximation. *Comput. Phys. Commun.* **2003**, *155*, 244–259.
- [71] Kelly, C. P.; Cramer, C. J.; Truhlar, D. G. SM6: A Density Functional Theory Continuum Solvation Model for Calculating Aqueous Solvation Free Energies of Neutrals, Ions, and Solute-Water Clusters. *J. Chem. Theory Comput.* **2005**, *1*, 1133–1152, Publisher: American Chemical Society.
- [72] Singh, N.; Sanyal, U.; Fulton, J. L.; Gutiérrez, O. Y.; Lercher, J. A.; Campbell, C. T. Quantifying Adsorption of Organic Molecules on Platinum in Aqueous Phase by Hydrogen Site Blocking and in Situ X-ray Absorption Spectroscopy. *ACS Catal.* **2019**, *9*, 6869–6881.
- [73] Chaudhary, N.; Hensley, A.; Collinge, G.; Wang, Y.; McEwen, J.-S. Coverage-Dependent Adsorption of Phenol on Pt(111) from First Principles. *J. Phys. Chem. C* **2020**, *124*, 356–362, Publisher: American Chemical Society.
- [74] Bramley, G.; Nguyen, M.-T.; Glezakou, V.-A.; Rousseau, R.; Skylaris, C.-K. Reconciling Work Functions and Adsorption Enthalpies for Implicit Solvent Models: A Pt (111)/Water Interface Case Study. *J. Chem. Theory Comput.* **2020**, *16*, 2703–2715, Publisher: American Chemical Society.

- [75] Ihm, H.; White, J. M. Stepwise Dissociation of Thermally Activated Phenol on Pt(111). *J. Phys. Chem. B* **2000**, *104*, 6202–6211.
- [76] Mark, A. E.; van Gunsteren, W. F. Decomposition of the Free Energy of a System in Terms of Specific Interactions: Implications for Theoretical and Experimental Studies. *J. Mol. Biol.* **1994**, *240*, 167–176.
- [77] Boresch, S.; Karplus, M. The Meaning of Component Analysis: Decomposition of the Free Energy in Terms of Specific Interactions. *J. Mol. Biol.* **1995**, *254*, 801–807.

Investigating water/metal interactions **Part II**

In the following part, three studies of the water/metal interactions are presented. As presented in the previous part, computing accurate adsorption energies at the water/metal interface at a reasonable computational cost requires molecular mechanics computations. The goal of the studies collected in this part was, therefore, to develop a force field to reproduce at best the water/metal interactions. The development of two generations of force fields is presented. The first tackles metallic alloy/water interface in chapter 3, while the second is designed to work for corrugated surfaces and even nanoparticles (chapter 4). These force fields have demonstrated root mean square deviations of only $\sim 1 \text{ kcal}\cdot\text{mol}^{-1}$ for predicting the adsorption energies of a water molecule on diverse metallic surfaces. However, problems were also observed for predicting the interaction of water clusters with metallic surfaces. The synergistic adhesion effect of co-adsorbed water molecule was therefore also investigated in chapter 5 and found mainly due to polarisation and charge transfer. These two effects were quantified for different clusters in a view to understand, and possibly include them in future generations of force fields.

3 Ten Facets, One Force Field: The GAL19 Force Field for Water - Noble Metal Interfaces

This Chapter is based on the following article: Ten Facets, One Force Field: The GAL19 Force Field for Water - Noble Metal Interfaces, *Clabaut, P. and Fleurat-Lessard, P. and Michel, C. and Steinmann, S.N.*, **Journal of Computational and Theoretical Chemistry**, 2020, *10.1021/acs.jctc.0c00091*

abstract: Understanding the structure of the water/metal interfaces plays an important role in many areas ranging from surface chemistry to environmental processes. The size, required phase-space sampling and the slow diffusion of molecules at the water/metal interfaces motivate the development of accurate force-fields. We develop and parametrize GAL19, a novel force-field to describe the interaction of water with two facets (111 and 100) of five metals (Pt, Pd, Au, Ag, Cu). To increase transferability compared to its predecessor GAL17, the water-metal interaction is described as a sum of pair-wise terms. The interaction energy has three contributions: (i) physisorption is described via a Tang and Toennies potential, (ii) chemisorption and surface corrugation relies on an attractive Gaussian term and (iii) the angular dependence is explicitly included as a truncated Fourier series. 13 parameters are used for each metal surface and were fitted on 250 water adsorption energies computed at the PBE+dDsC level. The performance of GAL19 was evaluated on a set of more than 600 DFT adsorption energies for each surface, leading to an average root mean square deviation (RMSD) of only 1 kcal·mol⁻¹, correctly reproducing the adsorption trends: strong on Pt and Pd but weaker on Ag, Au and Cu. This force-field was then used to simulate the water/metal interface for all ten surfaces for 1 ns. Structural analyses reveal similar tendencies for all surfaces: a first, dense water layer that is mostly adsorbed on the metal top sites, and a second layer up

Chapter 3. Ten Facets, One Force Field: The GAL19 Force Field for Water - Noble Metal Interfaces

to around 6 Å, which is less structured. On Pt and Pd, the first layer is strongly organized with water lying flat on the surface. The pairwise additive functional form allows to simulate the water adsorption on alloys, which is demonstrated at the example of Ag/Cu and Au/Pt alloys. The water/Ag-Cu interface is predicted to be disordered with water mostly adsorbed on Cu which should exacerbate the Ag reactivity. On the contrary, incorporating Pt into Au materials leads to a structuring of the water interface. Our promising results make GAL19 an ideal candidate to get representative sampling of complex metal/water interfaces as a first step towards accurate estimation of free energies of reactions in solution at the metal interface.

3.1 Introduction

The metal/water interface is key in many technologically relevant systems, ranging from heterogeneous (electro-)catalysis^{1;2} to tribology³ and corrosion.⁴ Beyond the prototypical monometallic surfaces, alloys are of key importance in the domain of catalysis^{5;6} and active research in corrosion⁷. The atomistic understanding of metal/liquid interfaces remains poor, despite experimental⁸⁻¹⁰ and computational¹¹⁻²⁴ efforts throughout the last 30 years, exclusively devoted to monometallic single-crystal surfaces. The origin of the difficulties to characterize the metal/water interface at an atomistic level comes from its non-crystallinity. In absence of a long-range order, only indirect spectroscopic evidence is available regarding the organization of water at metallic interfaces. Similarly, from a computational perspective, the amorphous nature of the interface requires large simulation cells in combination with thorough phase-space sampling due to the slow equilibration at the interface that features strong interactions with the water molecules.^{18;21}

Large simulation cells and extensive phase-space sampling is routinely applied for biomolecules relying on molecular mechanics (MM), *i.e.*, simple force fields, instead of evaluating the energies and forces from first-principles. These force fields have been optimized over the last sixty years based on a combination of experimental reference data (X-ray structures) and quantum-mechanical computations.²⁵ Experimental benchmark data is nonexistent for alloy surfaces and very limited for monometallic surfaces, which explains the slow development of metal/water force fields.

The motivation for developing a metal/water force field not only lies in gaining an atomistic understanding of the the metal/water interface, but also in being able to account adequately for the solvent effects,

when investigating reactions at these interfaces.²⁶⁻²⁸ Solvent effects have, for instance, been shown to change the relative catalytic activity of metallic catalysts compared to the gas-phase²⁹ and are key for a realistic description of electrocatalysis.³⁰ Today, these investigations mostly rely on microsolvation^{29;31-35} or implicit solvents,³⁶⁻³⁹ where few water molecules or just a dielectric medium is used to represent the solvent, respectively. To overcome the limitations in sampling, molecular dynamics appears as a tool of choice. However, the use of DFT to perform MD simulations of relevant length (~ 500 ps) on systems with a relevant size (~ 200 metal atoms and ~ 200 water molecules) is computationally prohibitive for entire reaction pathways,^{23;40-42} since each ps of such a simulation requires 1'000-10'000 CPUh.²¹

A hybrid approach, where the solvent is described at the MM and the surface at the DFT level, is a promising alternative, provided an accurate force field is available.⁴³⁻⁴⁶ To make such a strategy widely applicable, the metal/water force field should be compatible with established MM water models and standard Lennard-Jones and point-charge description of additional

Chapter 3. Ten Facets, One Force Field: The GAL19 Force Field for Water - Noble Metal Interfaces

molecules and ions. This precludes the use of specialized force fields such as (AI)REBO,^{47–49} COMB3,²² ReaxFF,^{50;51} RexPON⁵² or Neural Networks⁵³ as the corresponding functional form is not compatible with well established force fields available for most organic molecules.

A weak chemisorption⁵⁴ interaction of 5-10 kcal·mol⁻¹ drives the adsorption minimum of water molecules on the top position on closed-packed transition-metal surfaces.¹⁴ Chemisorption interactions are typically treated via fixed topologies in force fields. However, the metal/water interaction is weak and therefore needs to be formed and broken dynamically. For geometric reasons, an atom centered pair-wise potential yields an adsorption minimum in the hollow position as with the METAL¹⁵ or DFT-CES²⁴ force field, in disagreement with the preferred top adsorption. Hence, non-conventional approaches are required to stabilize the top adsorption configuration compared to the hollow site. The use of projectors,¹¹ reactive angular terms,¹² virtual sites¹⁷ or explicit three body terms²² have been proposed to this effect. Our initial force field, GAL17,²¹ standing for Gaussian, Angular and Lennard-Jones, relies on attractive Gaussians which modulate the relative stability of top and hollow sites. In combination with the angular dependence terms and hydrogen repulsion, GAL17 retrieves the qualitative behavior of a single molecule adsorption on Pt(111) as a function of the distance, top/hollow position and angular orientation compared to DFT reference data.²¹ Furthermore, when coupled with an appropriate model for the water–water interaction, ice-like layers are well described as well.

This non-polarizable⁵⁵ force field can be coupled to standard force fields and is compatible with any water–water interaction. However, GAL17 was developed having monometallic, perfectly flat single-crystal surfaces in mind. This allowed to simplify several terms (angular dependence, hydrogen repulsion) into expressions that only depend on the surface position. The extension of the force field from Pt(111) to other noble-metal surfaces also calls for a description of alloy surfaces. An energy expression such as GAL17 that depends on the global surface is not suitable to describe alloys, where the properties of the surface depends on the local configuration, *i.e.*, in an Ag/Pd alloy a locally Pd rich surface configuration will interact more strongly with water than an Ag rich configuration, in analogy to other adsorbates.^{56–58} Hence, we here present a generalized energy expression, called GAL19, that is based on a pair-wise formulation in order to seamlessly treat alloy surfaces. GAL19 is made available in the free, open-source code CP2K.

The next section presents the details of the revamped GAL19 force field and the reference data to fit it for the (111) and (100) surface of Cu, Pd, Ag, Au and Pt. After a short comparison of these different surfaces for water adsorption, we discuss the quality of GAL19 for single molecule adsorption and then move to a comparison of the water structuration at the surface as a function of the metal and the facet. Finally, we investigate the interface of the Ag/Cu and Au/Pt alloys.

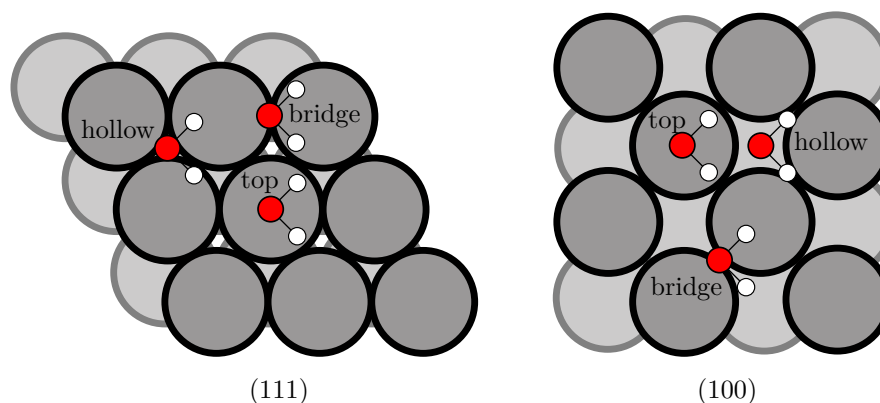


Figure 3.1 – Schematic representation of the top, bridge and hollow site of adsorption on metallic (111) and (100) surfaces.

3.2 Theory

3.2.1 Object definitions and functional form

To define the adsorption of a single water molecule, several geometric descriptors can be distinguished: (i) the distance of the oxygen atom to the surface (ii) the relative position with respect to the surface atoms, *e.g.*, the top, bridge and hollow position (see Fig. 3.1) and, (iii) the relative orientation of the O–H bonds with respect to the surface normal (see Fig. 3.2b).

In GAL19, all these definitions are required to be based on an atom pair-wise description. For instance, the distinction between top/hollow/bridge is well reproduced by sums over interatomic distances in combination with suitable functions to tune the relative interaction energies. The situation becomes more involved for the relative position of the O–H bonds with respect to the surface normal. First, we have to define a surface normal (\vec{n}) based on interatomic pairs. In GAL19, we define a surface normal for each metallic atom M via:

$$\vec{n}(M) = \sum_i \vec{r}_{M_i, M} \quad (3.1)$$

where i runs over all metallic atoms (*i.e.*, including all constituents in the case of an alloy) within a distance cut-off of M (see the green circle in Fig. 3.2a). Due to the symmetry of the surface and the underlying bulk, this vector always points perpendicular to the surface. In our implementation, the cutoff is set independently of the global force field cutoff. A value of 3.0 Å has been used to include all first neighbors of the metallic atom. This is thus large enough to ensure a well behaved surface normal. Note that the very notion of a surface normal restrains the applicability of GAL19 to objects with locally well defined surfaces, *i.e.*, neither to single atoms nor very amorphous or completely irregular nanoparticles with rough cavities etc.

Having defined $\vec{n}(M)$, the orientation of a water molecule is most conveniently expressed

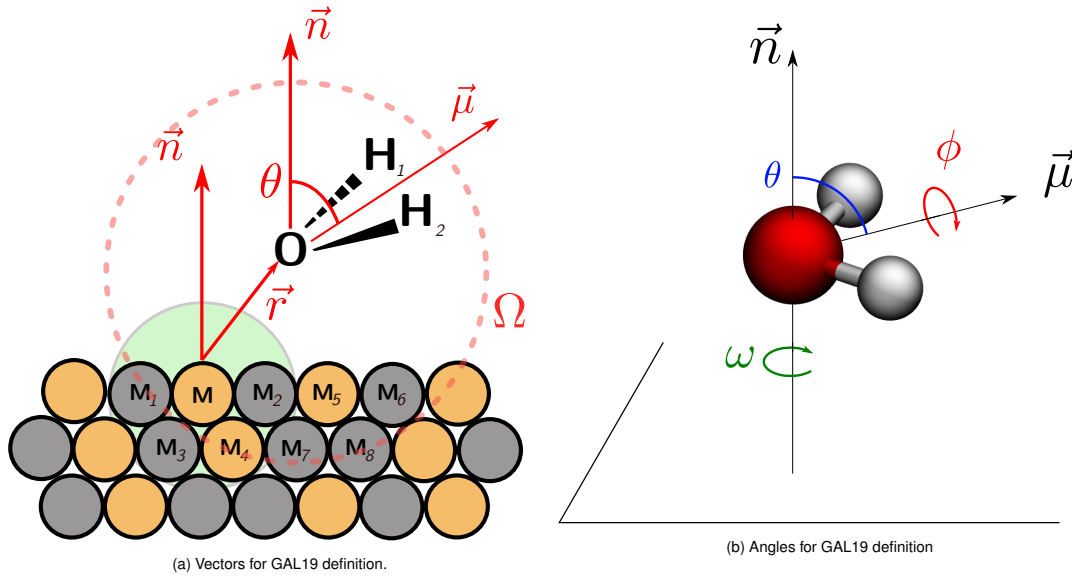


Figure 3.2 – (a) Atoms, vectors and angle used in the definition of the GAL19 force-field for M-OH₂: \vec{r} is the Metal/Oxygen vector; \vec{n} is the surface normal defined by Eq. 3.1 for M using neighbouring metallic atoms within a cutoff distance shown by a green disk; $\vec{\mu}$ is the dipole of the water molecule; Ω is the ensemble of atoms within the cutoff (red dotted circle) which contribute to the overall interaction energy of the water molecule with the metallic surface; and θ is the angle between \vec{n} and $\vec{\mu}$. (b) Schematic representation of the cartwheel angle θ , the propeller angle ϕ , and the helicopter angle ω , defining the orientation of the water molecule with respect to the surface. $\omega = 0$ is arbitrarily defined as a coincidence of the dipole moment vector and the x-axis. At $\phi = 0$ the molecular plane of H₂O is parallel to the surface.

using three angles (see Fig. 3.2b): θ , which is the angle between the dipole moment of the water molecule $\vec{\mu}$ and the surface normal, describes the cartwheel motion. ϕ is related to the propeller motion, defining the rotation of the water plane around the axis of the dipole moment. Finally, the helicopter angle ω describes the rotation of the water molecule around the surface normal.

In agreement with the pair-wise interaction potential, the general functional form of GAL19 reads:

$$V_{\text{GAL19}} = \sum_H \sum_{M \in \Omega(H)} V_{M,H}(\vec{r}_{M,H}) + \sum_O \sum_{M \in \Omega(O)} V_{M,O}(\vec{r}_{M,O}, \theta) \quad (3.2)$$

where Ω represents an ensemble of metallic atoms (indistinct of their nature in the case of an alloy) within a given distance cut-off (red dotted circle in Fig. 3.2a). To simplify the notation below, we will not specify the nature of the metallic atom. In other words, it is implicit that when simulating alloys, the parameters for the corresponding M, O or M, H pair is used.

As shown when developing GAL17, the helicopter angle ω is of negligible importance. In contrast, the propeller motion ϕ is key and is most conveniently described by the hydrogen

repulsion with the metallic surface. In GAL19, this takes the the form of an exponential repulsive wall:

$$V_{M,H}(r_{M,H}) = A_H e^{-r_{M,H}/R_H} \quad (3.3)$$

where r is the norm of \vec{r} , A_H tunes the strength of the repulsion and R_H is the characteristic distance of the exponential decay.

All the other interaction energy terms are collected in the metal oxygen pair:

$$V_{M,O}(\vec{r}_{M,O}, \theta) = V_G(\varepsilon_a, b_{\parallel}, b_{\perp}; \vec{r}_{M,O}) + V_A(R_O, a_{1-4}; r_{M,O}, \theta) + V_{TT}(A, B, C_6; r_{M,O}) \quad (3.4)$$

where V_{TT} is the potential of Tang and Toennies,⁵⁹ V_G is an attractive Gaussian and V_A is the term for the explicit θ angular dependence. Note that for a better readability, the dependence of these expressions on the surface normal and similar ensemble averages that include all metal atoms within the cutoff-distance ($M \in \Omega(O)$) are omitted here. These terms are explicitly described below. A , B , C_6 , ε_a , b_{\parallel} , b_{\perp} , R_O , a_1 , a_2 , a_3 , and a_4 are the respective parameters which are determined as described in section 3.2.2.

Physisorption term: V_{TT}

The physisorption potential V_{TT} is taken from the seminal work of Tang and Toennies,⁵⁹ truncated to the typical (London) dispersion expression $\frac{C_6}{r^6}$:

$$V_{TT}(r) = A e^{-B \cdot r} - \left[1 - \sum_{k=0}^6 \frac{(B \cdot r)^k}{k!} e^{-B \cdot r} \right] \frac{C_6}{r^6} \quad (3.5)$$

where A , B , and C_6 are parameters.

The Tang and Toennies potential is closely related to the Born-Mayer⁶⁰ or Buckingham potential,⁶¹ with which it shares the exponential soft-wall potential and the long-range London attraction. However, in contrast to these earlier potentials, the one of Tang and Toennies damps the diverging $\frac{C_6}{r^6}$ potential in order to have a continuously repulsive potential in the short range. The particularity of the Tang and Toennies damping function is that it does not rely on any additional parameters, but just re-uses the steepness parameter B of the exponentially decaying repulsion. Note that the Tang and Toennies damping function is successfully exploited in dispersion corrections to DFT⁶² and in particular in dDsC,⁶³ which is the one used herein.

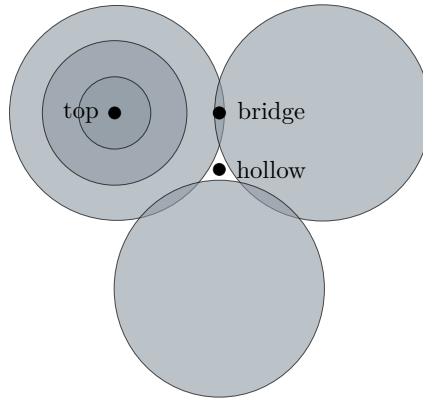


Figure 3.3 – Schematic representation of attractive Gaussian potentials centered on the position of the nuclei. The Gaussians overlap more strongly on bridge sites than on hollow sites. Lines represent isopotential surfaces projected on the surface. Darker colors indicate stronger attractive potential. Metallic atoms are situated at the centre of the circles.

Chemisorption terms: V_G and V_A

DFT computations and surface experiments⁶⁴ agree that the top site is preferred for the adsorption of a water molecule. Hence, in order to stabilize the top site with respect to the hollow site, which would be the low-energy site when only using the physisorption potential (Eq. 3.5), we rely on the polarized attractive Gaussian potential introduced in the GAL17 force field:²¹

$$V_G(\vec{r}_{M,O}) = \varepsilon_a e^{-b_{\parallel} \cdot r_{\parallel}^2} e^{-b_{\perp} \cdot r_{\perp}^2} \quad (3.6)$$

were r_{\parallel} and r_{\perp} are, respectively, the parallel and perpendicular projection of $\vec{r}_{M,O}$ on the surface normal \vec{n} .

The asymmetry introduced by distinguishing the direction perpendicular and parallel to the plane allows to tune independently the contribution of the Gaussian on the top and hollow site (see Fig. 3.3). In a first approximation, the Gaussian of each metallic atom in an alloy surface is taken from the corresponding monometallic surface. To improve the approximation and include at least some fraction of the electronic effects present in alloys, one could introduce atom types that depend on the environment. These atom types would, themselves be parametrized via a cluster expansion, as we have previously done in the context of acetylene adsorption on Ag/Pd alloys.⁵⁸ The introduction of atom types avoids the use of many-body terms to introduce a dependence on the local environment. The explicit many-body terms are, in our case, computationally unnecessarily expensive, since the corresponding atoms do not move during a given computation.

The second chemisorption term of GAL19 is an explicit angular dependence. Indeed, according to DFT, the angle θ of the chemisorption minimum is $\sim 90^\circ$. To reproduce this angular

preference, we rely on a damped, truncated Fourier series of 4 terms:

$$V_A(M_i \in \Omega(O); r, \theta) = \frac{(e^{-r/R_O})^2}{\sum_{M_i \in \Omega(O)} e^{-r_{M_i, O}/R_O}} \sum_{n=1}^4 a_n \cos(n\theta) \quad (3.7)$$

The angular dependence has to vanish for molecules in solution. In GAL17, this was achieved by a global definition of the position of the surface. In GAL19, however, we require a fully pair-wise additive formulation of all terms. Here, we choose an exponential decay with a characteristic distance of R_O . Directly imposing a distance decay for each atom would lead to an unequal description for top, bridge and hollow sites, since they have one, two and three nearest metal neighbours respectively. Squaring the distance dependence and renormalizing it with the sum of contributions within the cutoff $\Omega(O)$ provides a more balanced description across the entire surface.

3.2.2 Fitting method and data set

In total, 13 adjustable parameters are needed for the GAL19 forcefield for each metal: the three parameters for physisorption (Eq. 3.5) A, B and C_6 ; the three parameters of the Gaussian (Eq. 3.6) $\varepsilon_a, b_{\parallel}$ and b_{\perp} ; the five parameters for the angular dependence (Eq. 3.7) R_O, a_1, a_2, a_3 , and a_4 ; and the hydrogen repulsion parameters A_H and R_H of Eq. 3.3.

In order to fit these parameters, a set of 826 configurations is built for each metal. All configurations consist of a single water molecule adsorbed on a $p(3 \times 3)$ metallic slab. The configurations probe various orientations, distances and adsorption sites (top, hollow etc.) of the water molecule. Only a restricted part of the total set (about 250 configurations) is used to fit the data, while the rest is used to validate the model. More details about the set can be found in the appendix chapter B.

The C_6 parameter is the only one that is not fitted but directly extracted from the DFT computations via the use of the dDsC dispersion correction.⁶⁵ A configurational average over the fitting set has been chosen for the final C_6 value. In analogy to the typically adopted united atom approach in water force fields,⁶⁶ we use a single C_6 coefficient for the water molecule, *i.e.*, the combination of the hydrogen and oxygen metal C_6 coefficients.

For the other parameters we distinguish the eight linear ($A, B, a_1, a_2, a_3, a_4, A_H, \varepsilon_a$) from the five non-linear ones (B, b_{\parallel} and b_{\perp}, R_O , and R_H). The non-linear parameters are optimized via a simplex optimizer, distributed via the SIESTA package⁶⁷. In each iteration of the simplex, the optimal solution of the eight linear parameters is obtained via a least square procedure. This process drastically accelerates the optimization of the parameters and is, furthermore, more robust to deal with linear dependencies within the parameter set.

The optimal parameters for the five metals and the two facets are provided in the appendix chapter B.

3.3 Computational details

3.3.1 DFT

All DFT single-point evaluations have been carried out with VASP 5.4.1,^{68;69} using the PBE generalized gradient approximation functional^{70;71} with the dDsC dispersion correction^{63;72} and an energy cutoff of 400 eV for the expansion of the plane-wave basis. The electron-ion interactions are described by the PAW formalism.^{73;74} The interatomic distance of the bulk metals have been optimized and found to be 2.56, 2.78, 2.92, 2.81 and 2.94 Å for Cu, Pd, Ag, Pt and Au, respectively. For all five metals, we have investigated the (100) and (111) facets. Series of 826 configurations of a single water molecule adsorbed on a p(3 x 3) metallic unit cell with 4 metallic layers were built for each of the metal/facet couple. The slabs are separated by a vacuum of 20 Å in order to minimize interactions between periodic images. The diverse set (see appendix chapter B) explores the configurational space characterized by the four main descriptors: The adsorption site, the distance to the surface, the cartwheel angle θ and the propeller angle ϕ as defined in Fig. 3.2b. The Brillouin zone was sampled by a Γ -centered 3 x 3 x 1 Monkhorst-Pack K-point grid.⁷⁵ Idealized geometries (as cut from the bulks) were adopted for the metallic layers, while the water molecule was taken from a DFT optimization in gas phase (O-H: 0.98 Å and a H-O-H angle of 105.32°). The impact of the water geometry on the interaction energy at the Pt(111) interface is depicted in Fig. B.1 and found to be small (0.55 kcal·mol⁻¹ per water molecule on average), so that it barely affects relative energies. Furthermore, choosing a geometry that is not taken from a specific MM water model makes GAL19 less bound to a given water model. Indeed, we combine GAL19 not only with TIP3P, but also perform tests with OPC3⁷⁶ and a polarizable water model⁷⁷.

3.3.2 Molecular Mechanics

All molecular mechanics simulations have been carried out with CP2K 5.1,⁷⁸⁻⁸¹ using the FIST module under periodic boundary conditions. Long-range Coulombic interactions were evaluated through the smooth particle-mesh Ewald summation.⁸² Molecular dynamics were run in the NVT ensemble at 300 K, using the default settings for the Nose-Hoover thermostat.^{83;84} Water molecules interactions were simulated according to the TIP3P model⁶⁶ and inter-atomic distances were accordingly constraint. All metallic atoms were kept frozen. The water/metal interactions were described by our implementation of the GAL19 force-field, which will be released to the public in a future version of the CP2K software.

The interfacial systems contained 192 metal atoms (c(4×6), 4 layers) and 250 water molecules,

yielding a water layer of about 20 Å. A vacuum layer of 20 Å separates the water from the “downside” of the metal slab, see Fig. B.2. Since we do not apply a barostat, this avoids the simulation of a confined water layer.

Finite size effects were tested by running simulations with a larger unit cell (432 metal atoms). As shown in Fig. B.3, these simulations gave nearly identical results for Pt(111) as the smaller unit cell, suggesting a limited dependence on the box size beyond the one adopted herein.

For the simulations of random alloys we used Vegard’s law⁸⁵ to determine the lattice constants, *i.e.*, linear interpolations between the monometallics according to their molar fractions. The random distributions of the 192 atoms were generated such that each metallic layer has the target ratio between the two metals. Just like the monometallics, the alloy surfaces have been kept fixed in their idealized bulk geometries during the simulations. In all simulations, the interfaces were equilibrated for 400 ps and averages were then calculated over 600 ps, giving total simulation lengths of 1 ns.

3.4 Results and discussion

3.4.1 Low-coverage water adsorption

Energy Minima Water adsorption at 1/9 monolayer (ML) on the (111) and (100) facets of Cu, Pd, Ag, Pt and Au has been studied by DFT and used for fitting GAL19 on these ten metallic surfaces.

Water adsorbing flat on top sites ($\theta \approx 90^\circ$, $\phi = 0^\circ$) is the most stable conformation adsorption according to previous DFT optimization and experimental observations⁶⁴. Therefore, Fig. 3.4 reports the distance dependence of this adsorption modes for the 10 facets at the PBE-dDsC level of theory, used herein to fit GAL19. This level of theory has been validated against experimental data on Pt(111) in a previous study.⁷² Furthermore, the comparison of the minimum adsorption energy on the (111) surface with other vdW-inclusive functionals⁸⁶ shows a good agreement, with deviations of about 0.5 kcal·mol⁻¹ and 0.05 Å for minimum adsorption energies and distances.

Starting with the (111) surfaces, which is the lowest energy facet of these fcc metals, Fig. 3.4a shows the (dis)similarities of the studied metals. This analysis agrees well with earlier reports,^{87;88} but sets the stage for the subsequent discussion. Water binds only weakly (5.8 kcal·mol⁻¹) to Au(111) and Ag(111) surfaces at equilibrium distances of 2.8 and 2.75 Å respectively. The third coinage metal, Cu(111), binds water slightly more strongly (6.6 kcal·mol⁻¹) at a shorter distance (2.55 Å), in agreement with its smaller size, reflected in the smaller lattice constant (2.56 Å interatomic distance vs. 2.94 Å for Au). Finally, Pt(111) and Pd(111) bind water the most strongly at the shortest distance (2.5 and 2.45 Å respectively), despite their

Chapter 3. Ten Facets, One Force Field: The GAL19 Force Field for Water - Noble Metal Interfaces

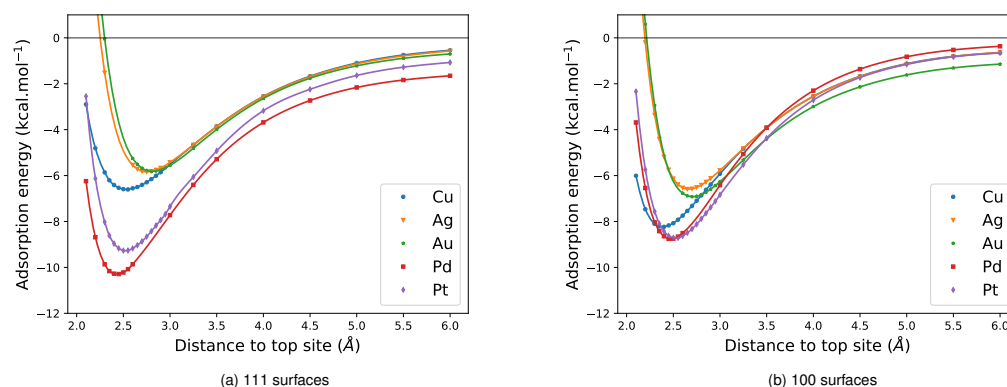


Figure 3.4 – DFT calculated adsorption energy of a water molecule on all the considered metals for their **(111)** facet **(a)**, and **(100)** facet **(b)**, in function of the distance of the water molecule’s oxygen to a top site of the surface, with the angles θ and ϕ (as defined in Fig. 3.2) held at 90° and 0° respectively.

large lattice constant (≈ 2.8 Å interatomic distance). This can be rationalized by the significant chemisorption contribution of water on these surfaces.⁵⁴

Moving to the (100) surfaces (Fig. 3.4b), which are the second most stable ones for these metals, the overall ordering with respect to the energy minimum remains the same as on the (111) facet. However, the coinage metals adsorb water more strongly on the (100) than on the (111) surface, which is most noticeable for Cu(100) (8.23 vs 6.6 kcal.mol⁻¹), while it is the other way round for Pd and Pt. For more strongly adsorbed species such as methyl (CH_3) or CO, a “universal” relationship has been identified,⁸⁹ according to which the more compact facets are interacting less strongly with adsorbates than more open facets due to the higher degree of unsaturation of metallic bonds in the latter. Apparently, this “universal” observation does not necessarily hold for water on (111) vs. (100) and could, therefore, impact the relative stability of the two facets in water compared to computations in vacuum. The preferred shape of large nanoparticles in water compared to vacuum can be determined using Wulff-reconstructions.⁹⁰ Nevertheless, determining the surface free energies of aqueous (100) and (111) surfaces is beyond the scope of this paper: extensive tests with our previous version of the force field, GAL17, have shown that these simulations are technically challenging and we will report on the corresponding results elsewhere. Furthermore, the relative energies of small nanoparticles require also an energy expression for the metal–metal interactions, which is beyond the capabilities of GAL19. For the same reason, surface reconstructions in water cannot be properly described. Overall, we conclude that Pt and Pd surfaces together with Cu(100) bind water strongly, while Cu(111), Au and Ag are significantly less oxophilic.

Fit quality of GAL19 A parity plot of GAL19 compared to the DFT reference data is shown for Au(100) and Pd(111) in Fig. 3.5. These two surfaces are typical for a weak and a strong binding

of H₂O and the corresponding graphs for the other surfaces are available in the appendix chapter B.

The root mean square deviation of the error of GAL19 (see Table B.3 in the appendix chapter B) ranges from 0.8 (for Cu(100)) to 1.4 kcal·mol⁻¹ (Pt(100)) with an average of 1.0 kcal·mol⁻¹. This demonstrates the very satisfying overall performance of GAL19. To test the importance of the training set, we have performed a second parametrization with a randomized training set for Au(111) and Pt(100), which have low (0.75 kcal·mol⁻¹) and high (1.39 kcal·mol⁻¹) RMSDs, respectively. The randomized fit set yields, with 0.98 and 1.19 kcal·mol⁻¹ very similar RMSDs. This similarity is also reflected in the parameters (see Table B.2). This demonstrates that the functional form and optimization method are robust.

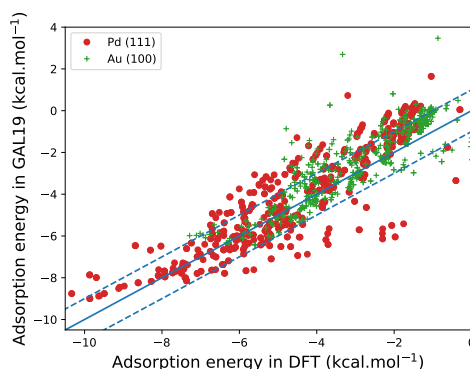


Figure 3.5 – Comparison of the adsorption energy of multiple adsorption conformations of a single water molecule on Pd (111) and Au (100), calculated by DFT and GAL19. All the configurations of the total set (see Supplementary information), resulting in an adsorption energy lower than 0 kcal·mol⁻¹ in DFT are included. The broken lines indicate errors of ± 1 kcal·mol⁻¹.

To analyze the performance of GAL19 more specifically, we first verify the angular dependence, which we previously identified to be a critical point of comparison between different force fields.²¹ Fig. 3.6 shows the θ dependence of the adsorption energy on Pt(111) which is representative of all surfaces. The ϕ dependence and the corresponding graphs for the other surfaces are shown in the appendix chapter B. Overall, the θ dependence shows the success of GAL19 to reproduce the DFT reference data faithfully and in particular the minimum around 90° is reproduced in contrast with the previous generation, where the minimum was shifted to 60°.

The DFT energy minima discussed above are well reproduced by GAL19 (see Fig. 3.7 and Table 3.1 and the additional data in the appendix chapter B). Despite GAL19 being designed to reproduce the chemisorption minimum, Fig. 3.7 evidences the largest errors, up to 1.3 kcal·mol⁻¹ for Pd(111) for the more oxophilic surfaces. Nevertheless, overall the trends are well reproduced, both between metals but also between facets, see Fig. B.4 and B.5. The biggest deviation for the difference between (100) and (111) is obtained for Cu, where it amounts to

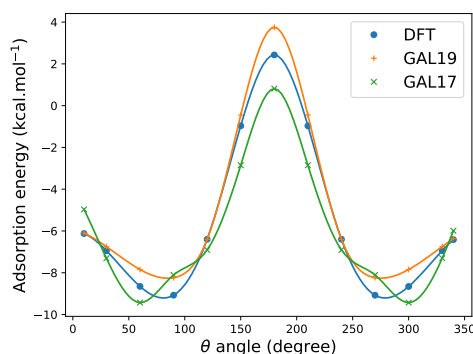


Figure 3.6 – DFT, GAL17 and GAL19 calculated adsorption energy of a water molecule on Pt (111) in function of the cartwheel angle θ , with ϕ held at 0° and at 2.5 \AA from a top site.

$0.8 \text{ kcal}\cdot\text{mol}^{-1}$ in GAL19, while it should be $1.6 \text{ kcal}\cdot\text{mol}^{-1}$ according to DFT.

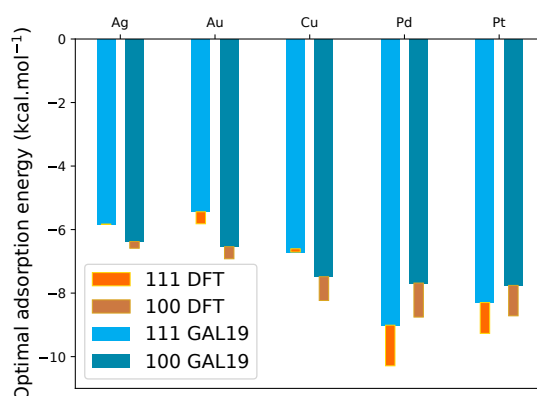


Figure 3.7 – DFT and GAL19 calculated adsorption energy of a single water molecule on different metallic facets, corresponding to the minimum energy found by varying the adsorption distance on top site, with θ and ϕ (as defined above) held at 90° and 0° respectively.

The positions of the top and hollow minima are also compared between DFT and GAL19. The position of the minimum adsorption energy on top and hollow site ($r_{min,top}$ and $r_{min,hlw}$, respectively) and their relative stability ($\Delta E_{top,hlw}$) are available in the appendix chapter B and the deviations ($\Delta_{DFT,GAL19}$) reported in Table 3.1. The low average errors ($\sim 0.1 \text{ \AA}$, and $0.5 \text{ kcal}\cdot\text{mol}^{-1}$) demonstrates the capacity of GAL19 to describe the chemisorption that is different between the hollow and the top site according to DFT. This relative stability of the top site is governed by the anisotropic Gaussian (Eq. 3.6), which counterbalances the physisorption term (Eq. 3.5). The physisorption alone yields an energy minimum for the hollow site, as observed for the METAL force field¹⁵ and the DFT-CES.²⁴ Reproducing the adsorption energy and position away from the top site (*e.g.*, on hollow) is crucial when aiming at a realistic

3.4. Results and discussion

Table 3.1 – Maximum and average deviation of the location of the minimum between DFT and GAL19 (δr_{min}) for top and hollow (hlw) site adsorption and of $\delta \Delta E_{top/hlw}$. δr_{min} is defined as the differences between optimal adsorption distance from the surface in DFT and GAL19 for a single water molecule on the given site and with θ and ϕ at 90° and 0° respectively. Likewise, $\delta \Delta E_{top/hlw}$ is defined by $\delta \Delta E_{top/hlw} = \Delta_{GAL19} E_{top/hlw} - \Delta_{DFT} E_{top/hlw} = (E_{min,hlw,GAL19} - E_{min,top,GAL19}) - (E_{min,hlw,DFT} - E_{min,top,DFT})$ where E_{min} corresponds to the energy minimum.

| | Maximum | Average | Max% | Average% |
|---|---------|---------|------|----------|
| $\delta r_{min,top}$ (Å) | 0.2 | 0.095 | 8.0 | 3.7 |
| $\delta r_{min,hlw}$ (Å) | -0.25 | -0.155 | 9.3 | 5.5 |
| $\delta \Delta E_{top/hlw}$ (kcal·mol ⁻¹) | 1.5 | 0.4 | 87 | 32 |

description of the metal/water interface. If there is no strong preference of water molecules for the top site, one might, for instance, expect a much more disordered interface than when molecules are almost immobilized on the top site.

3.4.2 Ice layers on the (111) facets

In contrast to liquid water/metal interface, the ice water monolayer/metal interface is quite extensively studied⁹¹. In particular, the hexagonal water layer put forward by Doering *et al.*⁹² has been the cornerstone for the understanding of ice monolayers on noble metal surfaces. As a partial validation for more complex adsorption geometries, we have assessed the interaction energy of three typical ice-like layers over the (111) facets over the five metal surfaces. The most stable $\sqrt{3} \times \sqrt{3}$ unit cell, called H_{down}, is a typical honeycomb ice-like layer based on the work by Doering *et al.*⁹². Additionally, we also investigate less regular but more stable $\sqrt{37} \times \sqrt{37}$ and $\sqrt{39} \times \sqrt{39}$ unit cells that have been observed over Pt(111).⁹³

The performance of GAL19 for these ice-like layers depends significantly on the metal studied (see Fig. 3.8). The slope of the GAL19 interaction energy vs. the DFT interaction energy is worst for Cu (almost flat), while for Ag and Pd the results are more acceptable (slope of 0.16 and 0.20). The H_{down} layer, where the water molecules are mostly on top sites, is the one that has the lowest interaction energy, but is also closest to the DFT reference values. For the larger and more complex structures ($\sqrt{37}$ and $\sqrt{39}$) where the water molecules are not situated at high-symmetry positions, the agreement is worse and, moreover, the relative stability from one metal to the other is completely washed out. The two origins for this discrepancy can be found in (i) the uneven description of the top/hollow energetic preference from one metal to the other and (ii) the absence of many-body water–water–metal interactions at the interface, which are non-negligible,⁹⁴ but beyond the scope of the current force field. The good news is, however, that (a) there is a qualitative agreement of which adsorption layer is more stable than the other and (b) the energy difference between them is smaller than at the DFT level. This means that sampling at the MM level and re-evaluating the energy of snapshots at the QM level in a resampling spirit is likely to be successful as the MM energy landscape is flat

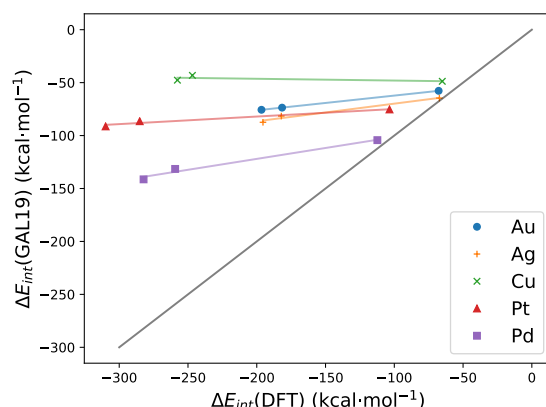


Figure 3.8 – Interaction energies of GAL19 vs DFT for ice-like layers on the (111) facets.

enough to allow a significant ensemble overlap between QM and MM at room temperature.

3.4.3 The mono-metallic/water interface

Molecular dynamics simulations of 1 ns were carried out with GAL19 to evaluate the structure of the metal/water interface for Pt, Pd, Au, Ag, Cu. Due to the slow diffusion of water at the interface, such an extensive phase-space sampling is necessary for obtaining equilibrated results.^{18;21} Fig. B.6 reports the results of a 5 ns trajectory for Pt(111), which shows that 1 ns simulations are well converged. Experimentally, the evidence on the neutral metal/water interface is very scarce: Toney *et al.* have shown that the density in the first layer over Ag(111) is at least 30% higher compared to the bulk and that two to three layers can be distinguished.⁸ The IR data on the Au(111) and Pt(111) is debated⁹⁵ but tends to suggest either flat⁹⁶ or locally ice-like arrangements⁹⁷ for the first layer. Most recent studies heavily rely on theoretical models^{9;10} to interpret the experimental data, but tend not to test many possibilities. As a result, the early ultra-high vacuum data for a water layer on ruthenium⁹² is still frequently used as a reference point to advocate “bilayers” with a $\sqrt{3} \times \sqrt{3}$ unit cell, even though more recent works have shown that the most stable monolayer requires a significantly larger $\sqrt{39} \times \sqrt{39}$ unit cell at least on Pt(111).⁹³ Overall, as a result of the difficulties of the experiments, the (dis-)similarities between noble metal/water interfaces remain largely unaddressed by experiments.

The structuring of the interface can be characterized through the monitoring of various averaged quantities. The planar average density, $d(z) = \frac{\rho(z)}{\rho(wat)} = \frac{n_o(z-dz/2, z+dz/2)}{\Delta X \cdot \Delta Y \cdot \delta z \cdot \rho(wat)}$, as a function of the distance from the topmost metal nuclei (see Fig. 3.9a), is based on the position of the oxygen atoms and compare the number of oxygen atom (n_o) found in each layer of small height (δz) - cut from the complete simulation cell (of volume $\Delta X \cdot \Delta Y \cdot \Delta Z$) - to the

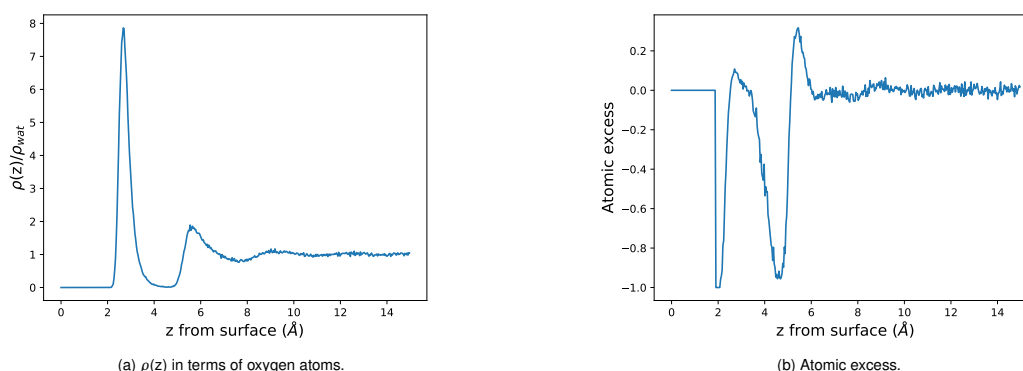


Figure 3.9 – Interface structuring as a function of the distance with respect to the metal surface (z) revealed by **(a)** the molecular density $\rho(z)$ divided by the reference density of water ρ_{wat} and **(b)** the atomic excess $AE(z)$ for the Pt(111)/H₂O interface. AE is held at 0 when neither oxygen or hydrogen are found in the layer. Layers of a thickness of 0.033 Å are used.

standard concentration of aqueous water ($\rho(wat) = 0.33 \text{ \AA}^{-3}$). The “atomic excess” (Fig. 3.9b), $AE(z) = \frac{n_O(z) - 2n_H(z)}{n_O(z) + 2n_H(z)}$, compares the average count of hydrogens (n_H) and oxygens (n_O) in layers parallel to the surface to identify oxygen rich ($AE > 0$) and oxygen poor ($AE < 0$) regions. $AE(z)$ and $\rho(z)$ give complementary information on the layering of the solid/water interface.²⁷ Typical results for this analysis are shown in Fig. 3.9 for Pt(111). As shown in the appendix chapter B (see Fig. B.7 and B.8), all the interfaces feature a very similar structuring, with two distinct layers below 13 Å. Even when using the parametrization from the randomized fit sets, the results remain very comparable (see Fig. B.9).

In order to assess the influence of the adopted water model on the interfacial structuring, we have performed additional simulations with the polarizable water force field from Dang and Chang⁷⁷ for the Pt(111)/water interface. While qualitatively the interfacial structuring is similar to the one obtained with the TIP3P model, the polarizable water model leads to a somewhat longer-ranged structuring: a weakly structured third layer with a flat peak at ~ 9 Å above the surface in the $\rho(z)$ profile (see Fig. B.10) can be distinguished. Interestingly, the OPC3 water model, which is characterized by stronger water–water interactions compared to TIP3P, yields very similar results compared to the polarizable water model (see Fig. B.11).

To gain further insight, we have also analyzed the angular distribution within the two identified layers and the bulk layer. Chosen in the interval 13–15.5 Å above the surface, this bulk layer shows the expected random distribution, demonstrating that it is well-positioned and thick enough to be neither affected by the structuring of the metal/water interface, nor by the water/gas interface. Since also the angular distributions change only subtly between facets and metals, Fig. 3.10 shows the data of the Pt(111) surface, while the corresponding data is available in the appendix chapter B (Fig. B.12 and B.13) for the other facets. Remarkably, the water organization was suggested to be different on Pt(111) and Pt(100) based on the

Chapter 3. Ten Facets, One Force Field: The GAL19 Force Field for Water - Noble Metal Interfaces

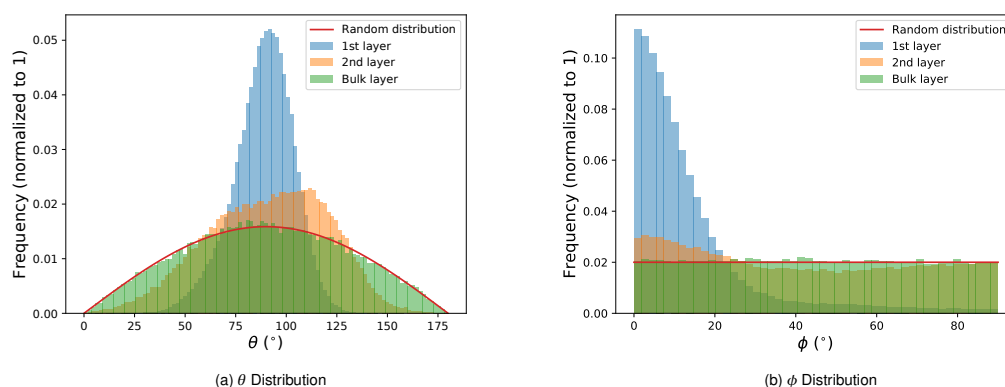


Figure 3.10 – Angular distribution of the (a) the cartwheel angle θ and (b) the propeller angle ϕ of the water molecules on Pt(111) for chemisorption, physisorption, and bulk layer, defined as being water molecule situated between 0 and 4.5, 4.5 and 7, and 13 and 15.5 Å away from the surface respectively. The red line represent an idealized random distribution of the dipoles.

Siepmann-Sprick water/Pt interaction potential.¹⁸ In contrast, GAL19 that uses a facet specific parameterization does not yield a significant difference for interfacial organization between the (100) and the (111) surface.

The first water layer (ending at ~ 4.5 Å) is very dense (about twice as dense as bulk water), in qualitative agreement with the experimental data of Toney *et al.*⁸ This first water layer has a strong preference for $\theta \approx 90^\circ$ as illustrated in Fig. 3.10a. Furthermore, the propeller angle ϕ is close to 0° , which means that in the first layer the molecular plane of water is essentially parallel to the metallic surface in agreement with the experimental data by Ataka *et al.*⁹⁶ This is also in line with the very small positive AE peak at ~ 3 Å, characteristic for compensated hydrogen and oxygen densities. This oxygen rich region is sandwiched between hydrogen rich ($AE < 0$) zones. The first one (~ 2 Å) can be explained by the lower repulsion of hydrogen compared to oxygen, which allows some hydrogen atoms to approach closer to the surface than oxygen. The second one (~ 4.5 Å) is composed of few hydrogen atoms pointing towards the second layer (since most water molecules lay flat according to the θ distribution) and mostly of hydrogen atoms pointing from the second layer to the first layer to maximize the hydrogen bonding, as we will detail in the next paragraph. The first layer might, thus, appear hydrophobic, as previously suggested by Chandler and co-workers based on simulations with the Siepmann-Sprick force field.¹⁸ Note, however, that this conclusion does not hold for the simulations with a polarizable water–water force field, which features a shoulder for H-up configurations ($\theta \approx 60^\circ$, see Fig. B.10). This emphasizes the need for a future validation of the interfacial structuring based on QM/MM resampling techniques.

The second water layer, which is still well distinguishable from the bulk, extends to ~ 7 Å. It is only slightly denser than the bulk and has a much weaker orientational preference. The

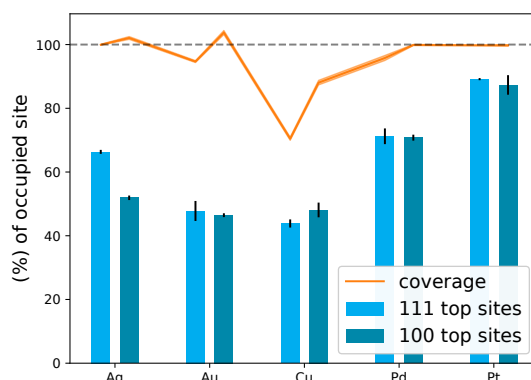


Figure 3.11 – Percentage of the top sites occupied by water molecule and global coverage of the surface for multiple metallic facets. The coverage is defined as the number of oxygen atom in the first layer (between 0 and 4.5 Å from the surface), divided by the number of surface atoms. Errors estimation at 95% confidence interval are depicted by enlarged line for total coverage and black bars for top site occupation.

positive peak of AE at 6 Å, followed by a constant $AE \approx 0$, and the peak at $\theta \approx 120^\circ$ both indicate that water molecules in this second layer are preferentially oriented “H-down” to interact with the first layer, the corresponding H atoms being in excess relative to the oxygen in the H rich region at (~ 4.5 Å). A small population of the second layer is also oriented “H-up” (shoulder at $\theta \approx 60^\circ$). As shown in Fig. B.12 and discussed below in the context of the Pt/Au alloy, such a shoulder is already visible in the first layer for Au(111). The weak orientational preference of this second layer results from the balance between the water/water interaction and the metal/second layer water interaction since the explicit angular dependence (Eq. 3.7) drops to about 40% with respect to its value in the first layer. In summary, the first layer acts as a soft template for the second layer.

Since the interface structuring is very similar for all ten surfaces studied (see Fig. B.14 and B.15), Fig. 3.11 compares the first adsorption layer in terms of coverage and adsorption site preference. The overall coverage (number of water molecules in the first layer divided by the number of surface atoms) reaches 100% for all surfaces but Cu(111). This is higher than the coverage for the famous bilayer structures (67%)⁹², but compatible with the high density of water the the Ag(111)/water interface measured experimentally.⁸ The lower overall coverage on Cu(111) can be traced back to the competition between adsorption ($6.6 \text{ kcal}\cdot\text{mol}^{-1}$ in the minimum) and hydrogen bonding ($\sim 5 \text{ kcal}\cdot\text{mol}^{-1}$) which is particularly fierce on Cu(111) since the Cu–Cu distance of 2.56 Å is too short to accommodate a hydrogen bond (O–H \cdots O of ~ 2.9 Å). However, when determining the proportion of water molecules on top sites (*i.e.*, within 0.4 Å of the formal top site), clear differences emerge between the metal surfaces. On Pt surfaces nearly all the top sites are occupied by water molecules. For Pd, the percentage drops to about 75%, which can be explained by its top/hollow preference being at least 1

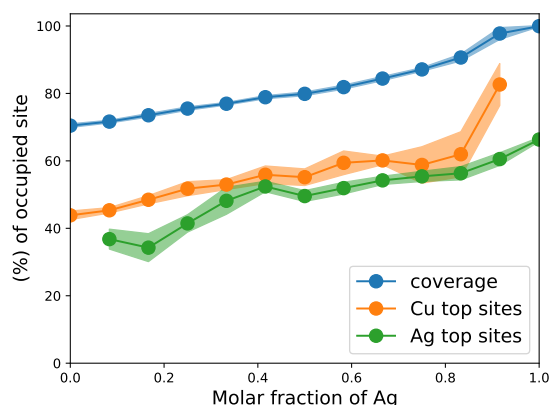


Figure 3.12 – Percentage of the top sites of copper and silver occupied by water molecule and global coverage of the surface for multiple alloy composition of Cu/Ag. The coverage is defined as the number of oxygen atom in the first layer (between 0 and 4.5 Å from the surface), divided by the total number of surface atoms. Confidence interval at 95% are represented as colored band surrounding the data. The corresponding variances were computed by block averaging.¹⁰²

$\text{kcal}\cdot\text{mol}^{-1}$ lower than for Pt. Because of the weaker binding on Ag and Au, only 50-60% of top sites are occupied on these surfaces, clearly demonstrating more disordered interfaces. Such a comparative disordering has already been observed within the short (~ 10 ps) DFT based molecular dynamics simulations of Gross and co-workers.¹⁶ Since the lack of equilibration in the DFT-based MDs and the missing many-body contributions in our GAL19 force field make it difficult to *a priori* judge the relevance of the obtained results, the obtained agreement is reassuring for both approaches. The extent of the preference for top adsorption is expected to manifest when studying the adsorption of molecules on these surfaces, as disordered interfaces can accommodate adsorbates more easily than highly organized ones.

3.4.4 Water structure at the alloy/water interface

GAL19 enables investigations of alloy surfaces at the molecular mechanics level on the basis of accurate water adsorption and orientational preferences on monometallic surfaces. Fig. B.16 and B.17 show that GAL19 is capable of retrieving the major effects of alloying, even though electronic effects cannot be captured for obvious reasons. In the following, we study two families of random alloys to probe two distinct effects: First, the effect of alloying Ag with Cu is assessed. Ag/Cu is a typical example of two surfaces with similar adsorption properties for a single water molecule, but a significant difference in lattice constant, leading to an interatomic distance of 2.56 Å for Cu but 2.92 Å for Ag. Experimentally, Ag/Cu, which forms (metastable) solid solutions,^{98;99} is scrutinized for its anti-bacterial activity¹⁰⁰ and is CO_2 electroreduction properties.¹⁰¹

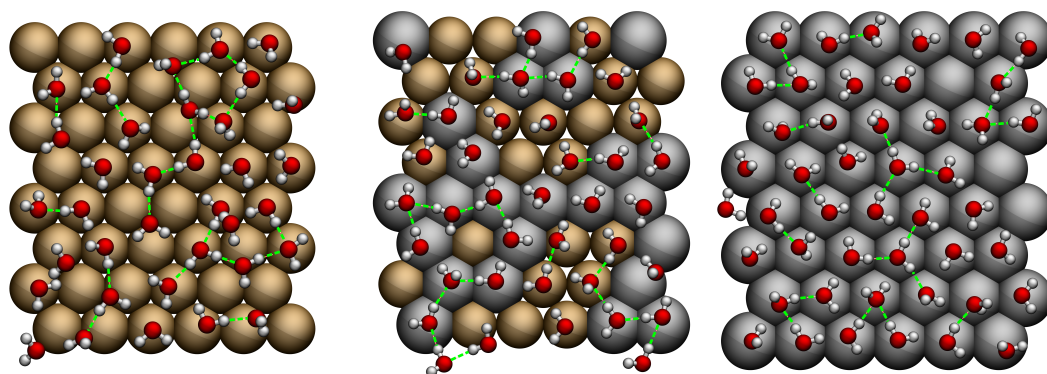


Figure 3.13 – Snapshot extracted from molecular dynamics of water layer on top of Cu (111) (a), $\text{Cu}_{0.5}\text{Ag}_{0.5}$ (111) (b) and Ag (111) (c). Cu is represented in brown, while Ag is shown in grey. Hydrogen bonds (as determined by default settings of VMD) are shown as dashed green lines.

Second, Au/Pt alloy surfaces, typical for nanoparticles with enhanced catalytic properties,^{103–105} are simulated to investigate the impact of mixing a strongly adsorbing metal (Pt) with a weakly interacting one (Au) that have nearly the same lattice constant (2.81 and 2.94 Å interatomic distance, respectively).

As above, we monitor the total coverage and the percentage of occupied top sites to compare the different alloys. Furthermore, for the Au/Pt alloy we also report the angular distributions.

The resulting curves for the Cu/Ag (111) alloy are shown in Fig. 3.12. As expected, the percentage of occupied top sites is quite similar for both constituents, especially around an equimolar mixture. As shown in Fig. B.18, this characteristic still holds when switching from the TIP3P water model to OPC3,⁷⁶ which was found to behave differently at the interface in our previous study.²¹ At large Ag molar fractions, the remaining copper sites show an increased propensity to be occupied, which can be rationalized by the combined effect of a relatively stronger adsorption of water on copper than on silver (see Fig. 3.4a) and the increased lattice constant, which lifts the constraints on the hydrogen bond between adsorbed molecules. Indeed, the numerical experiment where the Cu(111) GAL19 parameters are used for a surface with the Ag lattice constant gives a high percentage of occupied top sites (95%). The effect of the continuously increasing lattice constant is also seen in the smooth and almost linear increase in the overall coverage of the first water layer as the silver content increases. This increase could be experimentally verified adapting the techniques used for Ag(111) surfaces.⁸ Furthermore, the varying total coverage is expected to noticeably impact the solvation energies of adsorbates as a function of the alloy composition. In conclusion, the Ag/Cu(111) alloy interface is expected to be disordered in analogy to the pure coinage metal surfaces (see Fig. 3.13). However, water preferentially adsorbs on copper sites, so that the silver atoms are more available to interact with other adsorbates compared to pure silver.

The corresponding curves for the random Au/Pt (111) alloy are provided in Fig. 3.14 to probe

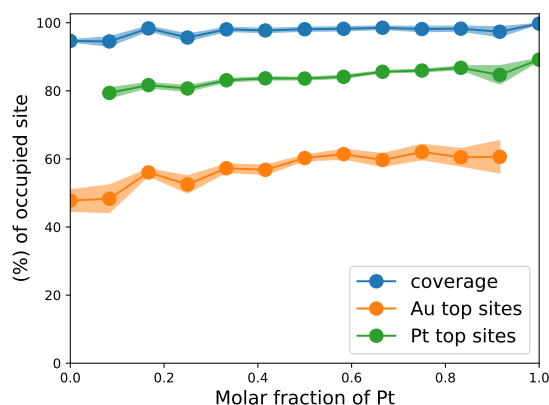


Figure 3.14 – Percentage of the top sites of gold and platinum occupied by water molecule and global coverage of the surface for multiple alloy composition of Au/Pt. The coverage is defined as the number of oxygen atom in the first layer (between 0 and 4.5 Å from the surface), divided by the total number of surface atoms. Confidence interval at 95% are represented as colored band surrounding the data. The corresponding variances were computed by block averaging.¹⁰²

the influence of a contrasted adsorption while keeping a similar inter-metallic distance. In contrast with Ag/Cu, the Au/Pt alloy shows a clear preference for water adsorption on top of the Pt atoms, which is in line with the observations for the monometallic surfaces (Fig. 3.11). Furthermore, the overall coverage is quite constant, again reflecting the behavior of Pt(111) and Au(111) which have similarly dense first layers. Despite the overall nearly constant behavior across the composition, there is a slight increase in the percentage of occupied Au top sites when increasing the Pt molar fraction. This can be rationalized via the templating effect of the surrounding Pt atoms, where water molecules strongly prefer to adsorb on the top position and limit, therefore, the freedom of the water molecules in the vicinity of Au surface atoms. In terms of interface organization, the “constant” behavior of the Au/Pt alloy hides the tuning from a disordered Au(111)-like interface to a highly ordered Pt(111)-like interface. This disordering is, however, visible when analyzing the angular distribution (Fig. 3.15) as a function of the Pt molar fraction. A shoulder at $\theta \approx 60^\circ$ appears when less than $\sim 30\%$ of Pt are on the surface (Fig. 3.15a). Similarly, $\phi = 0$ is lower for these Au rich surfaces at the benefit of $\phi > 50^\circ$ adsorption modes, again attesting the higher disorder for Au rich interfaces. Even though subtle, such a tuning of the interface ordering could influence the solvation energy of molecules on the alloy surface.

In summary, our GAL19 simulations of alloy surfaces are among the first predictions of the interface organization as a function of the alloy composition, revealing subtle effects based on both geometric (lattice constant and its relation to the H-bonding distance) and intrinsic effects (H_2O binding preference).

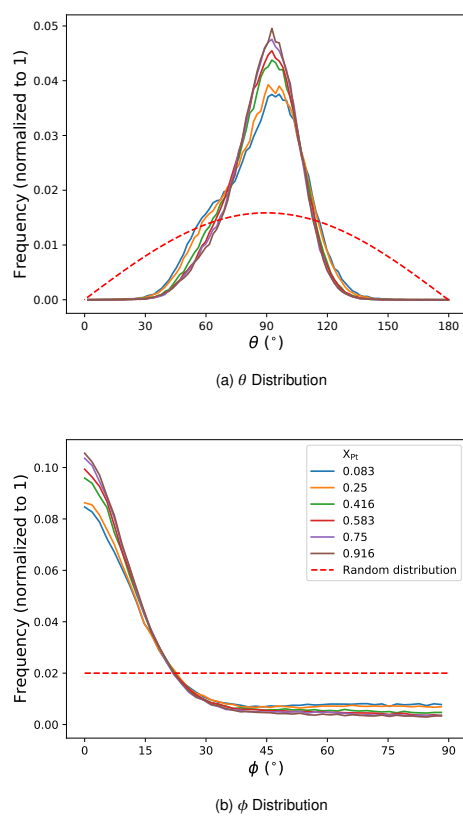


Figure 3.15 – Angular distribution for different molar fraction of Pt (x_{Pt} , given as a number in the legend) within the chemisorption layer (oxygen position $< 4.5 \text{ \AA}$ above the surface) of the (a) the cartwheel angle θ and (b) the propeller angle ϕ of the water molecules on PtAu alloys. The red dashed line represents an ideal random distribution of the dipoles.

3.5 Conclusion

The key ingredient of the metal surface/water force field GAL19 is a locally defined surface normal computed based on atom pairwise sums. As a result of the pairwise nature, the novel force field is directly applicable to alloy surfaces. The 13 parameters have been fitted for 5 metals (Pt, Pd, Au, Ag, Cu) and two facets (111 and 100). For each metal and surface we have used a set of more than 600 configurations of one water molecule interacting with the surface computed at the DFT level. The parametrization leads to low average errors (RMSD ≈ 1.0 kcal·mol⁻¹) for the ten surfaces. Furthermore, the force field qualitatively reproduces the relative adsorption energy between the top and the hollow sites.

Molecular dynamics simulations of 1 ns for each surface show that the structuring of the metal/water interface does not depend a lot on the specific nature of the metal surface. The interface is composed of two layers, followed by the bulk structure of the liquid. The first layer is very dense, with mainly water molecules that are adsorbed flat on the metal surface. On Pt, most of the top sites are occupied while on Au only half of the top sites are occupied due to a lower corrugation between top and hollow sites. We have also studied random alloys, mixing either metals with similar intermetallic distance but contrasted adsorption energy (Au/Pt) or vice versa (Ag/Cu). Keeping in mind the limitations of GAL19 for alloys (absence of electronic effects), our results suggest that while the broad trends in properties of alloy/water interfaces (*e.g.*, water coverages and top sites occupancy) can be inferred from the monometallic interfaces, the details might differ. For instance, when Cu is diluted in Ag, it binds water more strongly since it is not limited anymore by the short Cu-Cu intermetallic distance. Similarly, when Au is diluted in Pt, water will tend to bind more to Au than when it is not as diluted, benefiting from the templating effect of the organized water layer on Pt.

GAL19 shows promising result for mono-molecular water adsorption, even though it does not include interfacial water–water many-body interactions which would be necessary in general. Similarly, the current parametrization is not adapted to ordered surface alloys. Nevertheless, in comparison to DFT, GAL19 allows a much more extensive phase space sampling of the noble metal/water interface. Therefore, our work opens the door to the evaluation of the solvation energy at the metal/water interface using a force field that captures the water–metal interaction with high fidelity.

Bibliography

- [1] Akpa, B. S.; D'Agostino, C.; Gladden, L. F.; Hindle, K.; Manyar, H.; McGregor, J.; Li, R.; Neurock, M.; Sinha, N.; Stitt, E. H.; Weber, D.; Zeitler, J. A.; Rooney, D. W. Solvent effects in the hydrogenation of 2-butanone. *J. Catal.* **2012**, *289*, 30.
- [2] Seh, Z. W.; Kibsgaard, J.; Dickens, C. F.; Chorkendorff, I.; Nørskov, J. K.; Jaramillo, T. F.

- Combining theory and experiment in electrocatalysis: Insights into materials design. *Science* **2017**, 355, eaad4998.
- [3] Shenghua, L.; He, Y.; Yuansheng, J. Lubrication Chemistry Viewed from DFT-Based Concepts and Electronic Structural Principles. *Int. J. Mol. Sci.* **2003**, 5, 13.
- [4] Gece, G. The use of quantum chemical methods in corrosion inhibitor studies. *Corros. Sci.* **2008**, 50, 2981.
- [5] Sinfelt, J. H. Catalysis by alloys and bimetallic clusters. *Acc. Chem. Res.* **1977**, 10, 15–20.
- [6] Wang, D.; Li, Y. Bimetallic Nanocrystals: Liquid-Phase Synthesis and Catalytic Applications. *Adv. Mater.* **2011**, 23, 1044–1060.
- [7] Matzdorf, C.; Grieve, A. US Patent, US 2019/0078179 A1.
- [8] Toney, M. F.; Howard, J. N.; Richer, J.; Borges, G. L.; Gordon, J. G.; Melroy, O. R.; Wiesler, D. G.; Yee, D.; Sorensen, L. B. Voltage-dependent ordering of water molecules at an electrode-electrolyte interface. *Nature* **1994**, 368, 444.
- [9] Schiros, T.; Andersson, K.; Pettersson, L.; Nilsson, A.; Ogasawara, H. Chemical bonding of water to metal surfaces studied with core-level spectroscopies. *J. Electron Spectrosc. Relat. Phenom.* **2010**, 177, 85–98.
- [10] Velasco-Velez, J.-J.; Wu, C. H.; Pascal, T. A.; Wan, L. E.; Guo, J.; Prendergast, D.; Salmeron, M. The structure of interfacial water on gold electrodes studied by x-ray absorption spectroscopy. *Science* **2014**, 346, 831–834.
- [11] Spohr, E.; Heinzinger, K. Molecular dynamics simulation of a water/metal interface. *Chem. Phys. Lett.* **1986**, 123, 218–221.
- [12] Siepmann, J. I.; Sprik, M. Influence of surface topology and electrostatic potential on water/electrode systems. *J. Chem. Phys.* **1995**, 102, 511–524, Publisher: American Institute of Physics.
- [13] Klesing, A.; Labrenz, D.; Santen, R. A. v. Ab initio simulation of ‘liquid’ water on a Pd surface. *J. Chem. Soc., Faraday Trans.* **1998**, 94, 3229–3235, Publisher: The Royal Society of Chemistry.
- [14] Izvekov, S.; Voth, G. A. Ab initio molecular dynamics simulation of the Ag(111)-water interface. *J. Chem. Phys.* **2001**, 115, 7196–7206.
- [15] Heinz, H.; Vaia, R. A.; Farmer, B. L.; Naik, R. R. Accurate Simulation of Surfaces and Interfaces of Face-Centered Cubic Metals Using 12-6 and 9-6 Lennard-Jones Potentials. *J. Phys. Chem. C* **2008**, 112, 17281–17290.

Chapter 3. Ten Facets, One Force Field: The GAL19 Force Field for Water - Noble Metal Interfaces

- [16] Schnur, S.; Groß, A. Properties of metal–water interfaces studied from first principles. *New J. Phys.* **2009**, *11*, 125003.
- [17] Iori, F.; Di Felice, R.; Molinari, E.; Corni, S. GolP: An atomistic force-field to describe the interaction of proteins with Au(111) surfaces in water. *J. Comput. Chem.* **2009**, *30*, 1465–1476, Publisher: Wiley Subscription Services, Inc., A Wiley Company.
- [18] Limmer, D. T.; Willard, A. P.; Madden, P.; Chandler, D. Hydration of metal surfaces can be dynamically heterogeneous and hydrophobic. *Proc. Natl. Acad. Sci. U. S. A.* **2013**, *110*, 4200–4205.
- [19] Sakong, S.; Forster-Tonigold, K.; Groß, A. The structure of water at a Pt(111) electrode and the potential of zero charge studied from first principles. *J. Chem. Phys.* **2016**, *144*, 194701.
- [20] Le, J.; Iannuzzi, M.; Cuesta, A.; Cheng, J. Determining Potentials of Zero Charge of Metal Electrodes versus the Standard Hydrogen Electrode from Density-Functional-Theory-Based Molecular Dynamics. *Phys. Rev. Lett.* **2017**, *119*, 016801.
- [21] Steinmann, S. N.; Ferreira De Moraes, R.; Götz, A. W.; Fleurat-Lessard, P.; Iannuzzi, M.; Sautet, P.; Michel, C. Force Field for Water over Pt(111): Development, Assessment, and Comparison. *J. Chem. Theory Comput.* **2018**, *14*, 3238–3251.
- [22] Antony, A. C.; Liang, T.; Sinnott, S. B. Nanoscale Structure and Dynamics of Water on Pt and Cu Surfaces from MD Simulations. *Langmuir* **2018**, *34*, 11905–11911.
- [23] Le, J.; Cuesta, A.; Cheng, J. The structure of metal-water interface at the potential of zero charge from density functional theory-based molecular dynamics. *J. Electroanal. Chem.* **2018**, *819*, 87–94.
- [24] Gim, S.; Cho, K. J.; Lim, H.-K.; Kim, H. Structure, Dynamics, and Wettability of Water at Metal Interfaces. *Sci. Rep.* **2019**, *9*, 1–7.
- [25] Mackerell, A. D. Empirical force fields for biological macromolecules: Overview and issues. *J. Comput. Chem.* **2004**, *25*, 1584–1604.
- [26] Guo, N.; Caratzoulas, S.; Doren, D. J.; Sandler, S. I.; Vlachos, D. G. A perspective on the modeling of biomass processing. *Energy Environ. Sci.* **2012**, *5*, 6703–6716.
- [27] Réocreux, R.; Michel, C. Rational design of heterogeneous catalysts for biomass conversion - Inputs from computational chemistry. *Curr. Opin. Green Sustain. Chem.* **2018**, *10*, 51–59.
- [28] Xie, T.; Bodenschatz, C. J.; Getman, R. B. Insights into the roles of water on the aqueous phase reforming of glycerol. *React. Chem. Eng.* **2019**, *4*, 383–392.

- [29] Michel, C.; Zaffran, J.; Ruppert, A. M.; Matras-Michalska, J.; Jedrzejczyk, M.; Grams, J.; Sautet, P. Role of water in metal catalyst performance for ketone hydrogenation: a joint experimental and theoretical study on levulinic acid conversion into gamma-valerolactone. *Chem. Commun.* **2014**, *50*, 12450–12453.
- [30] Steinmann, S. N.; Michel, C.; Schwiedernoch, R.; Sautet, P. Impacts of electrode potentials and solvents on the electroreduction of CO₂: a comparison of theoretical approaches. *Phys. Chem. Chem. Phys.* **2015**, *17*, 13949–13963.
- [31] Desai, S. K.; Pallassana, V.; Neurock, M. A Periodic Density Functional Theory Analysis of the Effect of Water Molecules on Deprotonation of Acetic Acid over Pd(111). *J. Phys. Chem. B* **2001**, *105*, 9171–9182, Publisher: American Chemical Society.
- [32] Michel, C.; Auneau, F.; Delbecq, F.; Sautet, P. C–H versus O–H Bond Dissociation for Alcohols on a Rh(111) Surface: A Strong Assistance from Hydrogen Bonded Neighbors. *ACS Catal.* **2011**, *1*, 1430–1440.
- [33] Hibbitts, D. D.; Loveless, B. T.; Neurock, M.; Iglesia, E. Mechanistic Role of Water on the Rate and Selectivity of Fischer-Tropsch Synthesis on Ruthenium Catalysts. *Angew. Chem. Int. Ed.* **2013**, *52*, 12273–12278.
- [34] Garcia-Rates, M.; Garcia-Muelas, R.; Lopez, N. Solvation Effects on Methanol Decomposition on Pd(111), Pt(111), and Ru(0001). *J. Phys. Chem. C* **2017**, *121*, 13803–13809.
- [35] Schweitzer, B.; Steinmann, S. N.; Michel, C. Can microsolvation effects be estimated from vacuum computations? A case-study of alcohol decomposition at the H₂O/Pt(111) interface. *Phys. Chem. Chem. Phys.* **2019**, *21*, 5368–5377.
- [36] Behtash, S.; Lu, J.; Mamun, O.; Williams, C. T.; Monnier, J. R.; Heyden, A. Solvation Effects in the Hydrodeoxygenation of Propanoic Acid over a Model Pd(211) Catalyst. *J. Phys. Chem. C* **2016**, *120*, 2724–2736.
- [37] Heyden, A.; Lin, H.; Truhlar, D. G. Adaptive Partitioning in Combined Quantum Mechanical and Molecular Mechanical Calculations of Potential Energy Functions for Multiscale Simulations. *J. Phys. Chem. B* **2007**, *111*, 2231–2241.
- [38] Gu, G. H.; Schweitzer, B.; Michel, C.; Steinmann, S. N.; Sautet, P.; Vlachos, D. G. Group Additivity for Aqueous Phase Thermochemical Properties of Alcohols on Pt(111). *J. Phys. Chem. C* **2017**, 10.1021/acs.jpcc.7b07340, Publisher: American Chemical Society.
- [39] Steinmann, S. N.; Sautet, P. Assessing a First-Principles Model of an Electrochemical Interface by Comparison with Experiment. *J. Phys. Chem. C* **2016**, *120*, 5619–5623, Publisher: American Chemical Society.

Chapter 3. Ten Facets, One Force Field: The GAL19 Force Field for Water - Noble Metal Interfaces

- [40] Liu, J.; Cao, X.-M.; Hu, P. Density functional theory study on the activation of molecular oxygen on a stepped gold surface in an aqueous environment: a new approach for simulating reactions in solution. *Phys. Chem. Chem. Phys.* **2014**, *16*, 4176–4185.
- [41] Bellarosa, L.; García-Muelas, R.; Revilla-López, G.; López, N. Diversity at the Water–Metal Interface: Metal, Water Thickness, and Confinement Effects. *ACS Cent. Sci.* **2016**, *2*, 109–116.
- [42] de Morais, R. F.; Kerber, T.; Calle-Vallejo, F.; Sautet, P.; Loffreda, D. Capturing Solvation Effects at a Liquid/Nanoparticle Interface by Ab Initio Molecular Dynamics: Pt201 Immersed in Water. *Small* **2016**, *12*, 5312–5319.
- [43] Faheem, M.; Heyden, A. Hybrid Quantum Mechanics/Molecular Mechanics Solvation Scheme for Computing Free Energies of Reactions at Metal–Water Interfaces. *J. Chem. Theory Comput.* **2014**, *10*, 3354–3368, Publisher: American Chemical Society.
- [44] Steinmann, S. N.; Sautet, P.; Michel, C. Solvation free energies for periodic surfaces: comparison of implicit and explicit solvation models. *Phys. Chem. Chem. Phys.* **2016**, *18*, 31850–31861.
- [45] Saleheen, M.; Heyden, A. Liquid-Phase Modeling in Heterogeneous Catalysis. *ACS Catal.* **2018**, *8*, 2188–2194.
- [46] Staub, R.; Steinmann, S. N. Parameter-free coordination numbers for solutions and interfaces. *J. Chem. Phys.* **2020**, *152*, 024124, [_eprint: https://doi.org/10.1063/1.5135696](https://doi.org/10.1063/1.5135696).
- [47] Brenner, D. W. Empirical potential for hydrocarbons for use in simulating the chemical vapor deposition of diamond films. *Phys. Rev. B* **1990**, *42*, 9458–9471.
- [48] Stuart, S. J.; Tutein, A. B.; Harrison, J. A. A reactive potential for hydrocarbons with intermolecular interactions. *J. Chem. Phys.* **2000**, *112*, 6472–6486.
- [49] Brenner, D. W.; Shenderova, O. A.; Harrison, J. A.; Stuart, S. J.; Ni, B.; Sinnott, S. B. A second-generation reactive empirical bond order (REBO) potential energy expression for hydrocarbons. *J. Phys.: Condens. Matter* **2002**, *14*, 783–802.
- [50] van Duin, A. C. T.; Dasgupta, S.; Lorant, F.; Goddard, W. A. ReaxFF: A Reactive Force Field for Hydrocarbons. *J. Phys. Chem. A* **2001**, *105*, 9396–9409.
- [51] van Duin, A. C. T.; Strachan, A.; Stewman, S.; Zhang, Q.; Xu, X.; Goddard, W. A. ReaxFF_{SiO} Reactive Force Field for Silicon and Silicon Oxide Systems. *J. Phys. Chem. A* **2003**, *107*, 3803–3811.
- [52] Naserifar, S.; Goddard, W. A. The quantum mechanics-based polarizable force field for water simulations. *J. Chem. Phys.* **2018**, *149*, 174502.

- [53] Artrith, N.; Behler, J. High-dimensional neural network potentials for metal surfaces: A prototype study for copper. *Phys. Rev. B* **2012**, *85*.
- [54] Staub, R.; Iannuzzi, M.; Khaliullin, R. Z.; Steinmann, S. N. Energy Decomposition Analysis for Metal Surface? @ SAdsorbate Interactions by Block Localized Wave Functions. *J. Chem. Theory Comput.* **2019**, *15*, 265–275.
- [55] Steinmann, S. N.; Fleurat-Lessard, P.; Götz, A. W.; Michel, C.; Ferreira de Morais, R.; Sautet, P. Molecular mechanics models for the image charge, a comment on “including image charge effects in the molecular dynamics simulations of molecules on metal surfaces”. *J. Comput. Chem.* **2017**, *38*, 2127–2129.
- [56] Chen, W.; Schmidt, D.; Schneider, W. F.; Wolverton, C. Ordering and Oxygen Adsorption in Au–Pt/Pt(111) Surface Alloys. *J. Phys. Chem. C* **2011**, *115*, 17915–17924.
- [57] Zhu, B.; Creuze, J.; Mottet, C.; Legrand, B.; Guesmi, H. CO Adsorption-Induced Surface Segregation and Formation of Pd Chains on AuPd(100) Alloy: Density Functional Theory Based Ising Model and Monte Carlo Simulations. *J. Phys. Chem. C* **2016**, *120*, 350–359.
- [58] Vignola, E.; Steinmann, S. N.; Le Mapihan, K.; Vandegheuchte, B. D.; Curulla, D.; Sautet, P. Acetylene Adsorption on Pd–Ag Alloys: Evidence for Limited Island Formation and Strong Reverse Segregation from Monte Carlo Simulations. *J. Phys. Chem. C* **2018**, *122*, 15456–15463.
- [59] Tang, K. T.; Toennies, J. P. An improved simple model for the van der Waals potential based on universal damping functions for the dispersion coefficients. *J. Chem. Phys.* **1984**, *80*, 3726–3741.
- [60] Born, M.; Mayer, J. E. Zur Gittertheorie der Ionenkristalle. *Z. Physik* **1932**, *75*, 1–18.
- [61] Buckingham, R. A.; Lennard-Jones, J. E. The classical equation of state of gaseous helium, neon and argon. *Proc. R. Soc. Lond. A.* **1938**, *168*, 264–283.
- [62] Steinmann, S. N.; Csonka, G.; Corminboeuf, C. Unified Inter- and Intramolecular Dispersion Correction Formula for Generalized Gradient Approximation Density Functional Theory. *J. Chem. Theory Comput.* **2009**, *5*, 2950–2958.
- [63] Steinmann, S. N.; Corminboeuf, C. Comprehensive Benchmarking of a Density-Dependent Dispersion Correction. *J. Chem. Theory Comput.* **2011**, *7*, 3567–3577.
- [64] Zimbitas, G.; Haq, S.; Hodgson, A. The structure and crystallization of thin water films on Pt(111). *J. Chem. Phys.* **2005**, *123*, 174701.
- [65] Steinmann, S. N.; Corminboeuf, C. A generalized-gradient approximation exchange hole model for dispersion coefficients. *J. Chem. Phys.* **2011**, *134*, 044117.

Chapter 3. Ten Facets, One Force Field: The GAL19 Force Field for Water - Noble Metal Interfaces

- [66] William L. Jorgensen,; Chandrasekhar, J.; Madura, J. D.; Impey, R. W.; Klein, M. L. Comparison of simple potential functions for simulating liquid water. *J. Chem. Phys.* **1983**, *79*, 926–935.
- [67] Soler, J. M.; Artacho, E.; Gale, J. D.; García, A.; Junquera, J.; Ordejón, P.; Sánchez-Portal, D. The SIESTA method for *ab initio* order- *N* materials simulation. *J. Phys.: Condens. Matter* **2002**, *14*, 2745–2779.
- [68] Kresse, G. Ab initio molecular dynamics for liquid metals. *J. Non-Cryst. Solids* **1995**, *192-193*, 222–229.
- [69] Kresse, G.; Furthmüller, J. Efficiency of ab-initio total energy calculations for metals and semiconductors using a plane-wave basis set. *Computational Materials Science* **1996**, *6*, 15–50.
- [70] Perdew, J. P.; Wang, Y. Accurate and simple analytic representation of the electron-gas correlation energy. *Phys. Rev. B* **1992**, *45*, 13244–13249.
- [71] Perdew, J. P.; Burke, K.; Ernzerhof, M. Generalized Gradient Approximation Made Simple. *Phys. Rev. Lett.* **1996**, *77*, 3865–3868.
- [72] Gautier, S.; N. Steinmann, S.; Michel, C.; Fleurat-Lessard, P.; Sautet, P. Molecular adsorption at Pt(111). How accurate are DFT functionals? *Phys. Chem. Chem. Phys.* **2015**, *17*, 28921–28930.
- [73] Blochl, P. E. Projector augmented-wave method. *Phys. Rev. B* **1994**, *50*, 17953.
- [74] Kresse, G.; Joubert, D. From ultrasoft pseudopotentials to the projector augmented-wave method. *Phys. Rev. B* **1999**, *59*, 1758.
- [75] Monkhorst, H. J.; Pack, J. D. Special points for Brillouin-zone integrations. *Phys. Rev. B* **1976**, *13*, 5188–5192.
- [76] Izadi, S.; Onufriev, A. V. Accuracy limit of rigid 3-point water models. *J. Chem. Phys.* **2016**, *145*, 074501, Publisher: AIP Publishing LLC.
- [77] Dang, L. X.; Chang, T.-M. Molecular dynamics study of water clusters, liquid, and liquid–vapor interface of water with many-body potentials. *J. Chem. Phys.* **1997**, *106*, 8149–8159, Publisher: American Institute of Physics.
- [78] Schütt, O.; Messmer, P.; Hutter, J.; VandeVondele, J. *Electronic Structure Calculations on Graphics Processing Units*; John Wiley & Sons, Ltd, 2016; pp 173–190.
- [79] Borstnik, U.; VandeVondele, J.; Weber, V.; Hutter, J. Sparse matrix multiplication: The distributed block-compressed sparse row library \textbar Elsevier Enhanced Reader. *Parallel Comput.* **2014**, *40*, 47–58.

- [80] Hutter, J.; Iannuzzi, M.; Schiffmann, E.; VandeVondele, J. CP2K: atomistic simulations of condensed matter systems. *WIREs Comput Mol Sci* **2014**, *4*, 15–25.
- [81] Frigo, M.; Johnson, S. The Design and Implementation of FFTW3. *Proc. IEEE* **2005**, *93*, 216–231.
- [82] Essmann, U.; Perera, L.; Berkowitz, M. L.; Darden, T.; Lee, H.; Pedersen, L. G. A smooth particle mesh Ewald method. *J. Chem. Phys.* **1995**, *103*, 8577–8593.
- [83] Nosé, S. A unified formulation of the constant temperature molecular dynamics methods. *J. Chem. Phys.* **1984**, *81*, 511–519.
- [84] Nosé, S. A molecular dynamics method for simulations in the canonical ensemble. *Mol. Phys.* **1984**, *52*, 255–268.
- [85] Vegard, L. Die Konstitution der Mischkristalle und die Raumfüllung der Atome. *Z. Physik* **1921**, *5*, 17–26.
- [86] Carrasco, J.; Klimeš, J.; Michaelides, A. The role of van der Waals forces in water adsorption on metals. *J. Chem. Phys.* **2013**, *138*, 024708, Publisher: American Institute of Physics.
- [87] Michaelides, A.; Ranea, V. A.; de Andres, P. L.; King, D. A. General Model for Water Monomer Adsorption on Close-Packed Transition and Noble Metal Surfaces. *Phys. Rev. Lett.* **2003**, *90*, 216102.
- [88] Carrasco, J.; Michaelides, A.; Scheffler, M. Insight from first principles into the nature of the bonding between water molecules and 4d metal surfaces. *J. Chem. Phys.* **2009**, *130*, 184707.
- [89] Calle-Vallejo, E.; F de Morais, R.; Illas, E.; Loffreda, D.; Sautet, P. Affordable Estimation of Solvation Contributions to the Adsorption Energies of Oxygenates on Metal Nanoparticles. *J. Phys. Chem. C* **2019**, *123*, 5578–5582.
- [90] Wulff G., XXV. Zur Frage der Geschwindigkeit des Wachstums und der Auflösung der Krystallflächen. *Z. Kri.* **1901**, *34*, 449.
- [91] Carrasco, J.; Hodgson, A.; Michaelides, A. A molecular perspective of water at metal interfaces. *Nat. Mater.* **2012**, *11*, 667–674.
- [92] Doering, D. L.; Madey, T. E. The adsorption of water on clean and oxygen-dosed Ru(011). *Surf. Sci.* **1982**, *123*, 305–337.
- [93] Nie, S.; Feibelman, P. J.; Bartelt, N. C.; Thürmer, K. Pentagons and Heptagons in the First Water Layer on Pt(111). *Phys. Rev. Lett.* **2010**, *105*, 026102.

Chapter 3. Ten Facets, One Force Field: The GAL19 Force Field for Water - Noble Metal Interfaces

- [94] Michel, C.; Goltl, F.; Sautet, P. Early stages of water/hydroxyl phase generation at transition metal surfaces - synergetic adsorption and O-H bond dissociation assistance. *Phys. Chem. Chem. Phys.* **2012**, *14*, 15286–15290.
- [95] Osawa, M.; Tsushima, M.; Mogami, H.; Samjeské, G.; Yamakata, A. Structure of Water at the Electrified Platinum-Water Interface: A Study by Surface-Enhanced Infrared Absorption Spectroscopy. *J. Phys. Chem. C* **2008**, *112*, 4248–4256.
- [96] Ataka, K.-i.; Yotsuyanagi, T.; Osawa, M. Potential-Dependent Reorientation of Water Molecules at an Electrode/Electrolyte Interface Studied by Surface-Enhanced Infrared Absorption Spectroscopy. *J. Phys. Chem.* **1996**, *100*, 10664–10672.
- [97] Iwasita, T.; Xia, X. Adsorption of water at Pt(111) electrode in HClO₄ solutions. The potential of zero charge. *J. Electroanal. Chem.* **1996**, *411*, 95–102.
- [98] Duwez, P.; Willens, R. H.; Klement, W. Continuous Series of Metastable Solid Solutions in Silver-Copper Alloys. *J. Appl. Phys.* **1960**, *31*, 1136–1137.
- [99] Tsaur, B. Y.; Lau, S. S.; Mayer, J. W. Continuous series of metastable Ag-Cu solid solutions formed by ion-beam mixing. *Appl. Phys. Lett.* **1980**, *36*, 823–826.
- [100] Valodkar, M.; Modi, S.; Pal, A.; Thakore, S. Synthesis and anti-bacterial activity of Cu, Ag and Cu-Ag alloy nanoparticles: A green approach. *Mater. Res. Bull.* **2011**, *46*, 384–389.
- [101] Dettelbach, K. E.; He, J.; Johnson, N. J. J.; Huang, A.; Bottomley, A.; Lam, B.; Salvatore, D. A.; Berlinguette, C. P. Kinetic phases of Ag-Cu alloy films are accessible through photodeposition. *J. Mater. Chem. A* **2019**, *7*, 711–715.
- [102] Flyvbjerg, H.; Petersen, H. G. Error estimates on averages of correlated data. *J. Chem. Phys.* **1989**, *91*, 461–466, Publisher: American Institute of Physics.
- [103] Luo, J.; Maye, M. M.; Petkov, V.; Kariuki, N. N.; Wang, L.; Njoki, P.; Mott, D.; Lin, Y.; Zhong, C.-J. Phase Properties of Carbon-Supported Gold-Platinum Nanoparticles with Different Bimetallic Compositions. *Chem. Mater.* **2005**, *17*, 3086–3091.
- [104] Schrunner, M.; Proch, S.; Mei, Y.; Kempe, R.; Miyajima, N.; Ballauff, M. Stable Bimetallic Gold-Platinum Nanoparticles Immobilized on Spherical Polyelectrolyte Brushes: Synthesis, Characterization, and Application for the Oxidation of Alcohols. *Adv. Mater.* **2008**, *20*, 1928–1933.
- [105] Zhang, S.; Shao, Y.; Liao, H.-g.; Liu, J.; Aksay, I. A.; Yin, G.; Lin, Y. Graphene Decorated with PtAu Alloy Nanoparticles: Facile Synthesis and Promising Application for Formic Acid Oxidation. *Chem. Mater.* **2011**, *23*, 1079–1081.



4 Beyond the extended metallic surface/water interface with the GAL21 force field

abstract: This Chapter presents the extension of the GAL19 force field to more complex metallic structures than extended model surfaces. The GAL21 force field uses the Generalised Coordination Numbers to include the under-coordination of surface metallic atoms into the GAL19 functional form and get rid of specific surface parametrisation. The GAL21 force field has been developed and tested on numerous water adsorption configurations featuring diverse metallic surfaces and coordination sites and found to reproduce DFT results with great accuracy ($\approx 1 \text{ kcal}\cdot\text{mol}^{-1}$ of root mean square deviation across 7 metals (Ni, Pt, Pd, Au, Ag, Cu, and Co) and more than 20 000 configurations). Investigation of the resulting structures of nanoparticle/water interfaces is ongoing.

4.1 Introduction

Among the numerous systems that are used as heterogeneous catalysts, metallic nanoparticles have seen a considerable rise in interest in the past 30 years. Indeed, the logic of enhancing the surface-over-volume ratio of catalysts to maximise the exposed surface area while minimising their cost has led to a global augmentation of the dispersion of active catalyst on support surfaces, and thus, to a reduction of the size of the metallic clusters. This reduction of size was pursued up to supported single-atom catalysts,¹ or supported metallic nanoparticle²⁻⁴ Important progress were simultaneously done in the domain of nanoparticle synthesis, primarily focused on the obtention of mono-dispersed particle size distributions with controlled anisotropic shape.^{5,6} Indeed, many chemical but also physical properties of the metallic nanoparticles heavily depend on their morphology and exposed surface area.⁶ Also, metallic nanoparticles have attracted particular attention in the domain of theragnostic because of their ability to both diffuse through the human body to reach the treatment site,⁷ and for their radio-sensitising properties that could be used to selectively kill cancerous cells.⁸ The same care is dedicated to the obtention of precisely controlled nanoparticle shape and size for these biological applications as their diffusivity and optical properties are linked to the morphology of the particles.

Both their usage in the biological environment and in catalytic processes implies interactions between the nanoparticles and liquid water. However, simulating metallic nanoparticles in water is a huge challenge, even compared to the difficult simulation of extended metallic surfaces in water. Indeed, the reduced size of the particles implies that no infinite extended surface model can be used to simulate their surfaces. Complete simulations of the hundreds of atoms constituting the nanoparticles, along with matching water phases are therefore required. Few studies exist that perform such computationally costly simulations. Photo-activated water splitting on Ru clusters⁹ and O₂ dissociation on gold particles¹⁰ were studied, both clusters being supported on immersed oxide surfaces. Such systems require a smaller number of metallic atoms and do not require to sample the diffusion degrees of freedom of the whole cluster as it is immobilised on a support. Other studies investigate directly the nanoparticle/water interface structure with heavy simulation but are limited to structure optimisation,¹¹ implicit solvation,¹² or short sampling duration.¹³ Molecular mechanics (MM) simulations could be employed to lower the cost of the sampling, but again, the choice of an adapted force field is crucial to obtain relevant structures and surface solvation of the nanoparticles. The GAL19 force field, presented in chapter 3 might be a promising candidate. However, it is fitted to reproduce interaction energy between water molecules and metallic atoms from a specific kind of surface (100) or (111). The metallic environment of atoms in such extended surfaces differs from the environment of exposed metallic atoms at the surface of nanoparticles. At the centre of flat exposed portions of the surface, the chemical environment of the metallic atoms might resemble (100) or (111) facets but this does not hold true for edges

or corner atoms. The diversity of surface atoms on nanoparticles makes unfeasible the task of re-parametrising the force field for each atom kind.

However, in 2014 Calle-Vallejo *et al.* introduced the Generalised Coordination Numbers (GCN) to correlate the adsorption energy of small organic molecules on nanoparticles with the metallic environment of the surface atoms.^{14;15} GCN can be seen of second-order coordination number, as they propagate the information of the incomplete coordination sphere of metallic atoms to its first neighbours. GCN are, therefore, much more sensible to the local metallic environment of metallic atoms than standard coordination numbers. Combining GCN with our GAL19 force field, we here introduce the GAL21 forcefield. This force field re-uses the functional form of GAL19 but introduces a continuous dependence of the parameters on the GCN of the metallic atom considered. Therefore, by parametrising the forcefield on a set of interactions between water molecules and metallic atoms featuring different GCN, a global functional form, adapted to any kind of surface or particle was built.

4.2 Theory

4.2.1 Computation of GCN

The generalised coordination number $GCN(i)$ of a metallic atoms i is computed according to the formula introduced by Calle-Vallejo *et al.*¹⁴

$$GCN(i) = \sum_j^n \frac{CN(j)}{CN_{max}} \quad (4.1)$$

where the summation runs on its n closest neighbours, $CN(j)$ is the standard coordination number of the neighbour j , and CN_{max} is the maximum coordination number (CN corresponding to a complete coordination sphere) that could be reached for an atom situated in a bulk metal of the same nature (12 for an fcc metal).

The determination of the neighbours and of their coordination number is not uniquely defined and is here performed by the ASANN algorithm.¹⁶ A visual summary of the method is provided in Fig 4.1.

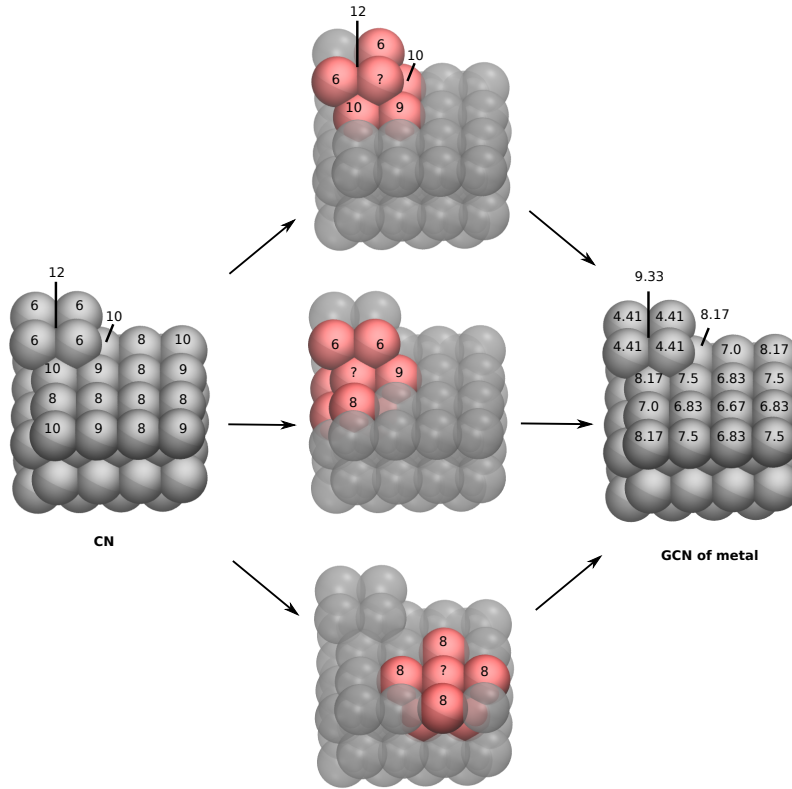


Figure 4.1 – Schematic representation of the GCN determination process. On the left, the standard coordination numbers of the metallic atoms. As a first step, the neighbour of each atom are identified and their standard coordination numbers gathered. In a second step, the formula is applied to compute the GCN of each metallic atom of the slab.

4.2.2 GAL21 functional form

The basic functional form of GAL19 was used:

$$V_{\text{GAL19}} = \sum_H \sum_{M \in \Omega(H)} V_{M,H}(\vec{r}_{M,H}) + \sum_O \sum_{M \in \Omega(O)} V_{M,O}(\vec{r}_{M,O}, \theta) \quad (4.2)$$

where Ω represents an ensemble of metallic atoms (indistinct of their nature in the case of an alloy) within a given distance cut-off.

$$V_{M,H}(r_{M,H}) = A_H e^{-r_{M,H} \cdot B_H} \quad (4.3)$$

where r is the norm of \vec{r} , A_H tunes the strength of the repulsion, and B_H tunes the distance

of the exponential decay. Note that the R_H parameter, homogeneous to a distance was here replaced by a B_H parameter, homogeneous to the inverse of a distance. In the GAL21 functional forms, both A_H and B_H becomes linearly dependant on the GCN of M.

$$V_{M,O}(\vec{r}_{M,O}, \theta) = V_G(\varepsilon_a, b_{\parallel}, b_{\perp}; \vec{r}_{M,O}) + V_A(R_O, a_{1-4}; r_{M,O}, \theta) + V_{TT}(A, B, C_6; r_{M,O}) \quad (4.4)$$

where V_{TT} is the potential of Tang and Toennies,¹⁷ V_G is an attractive Gaussian and V_A is the term for the explicit θ angular dependence.

$$V_G(\vec{r}_{M,O}) = \varepsilon_a e^{-b_{\parallel} r_{\parallel}^2} e^{-b_{\perp} r_{\perp}^2} \quad (4.5)$$

where r_{\parallel} and r_{\perp} are, respectively, the parallel and perpendicular projection of $\vec{r}_{M,O}$ on the surface normal \vec{n} . In the GAL21 functional forms, b_{\parallel} and b_{\perp} become linearly dependant on the GCN of M while ε_a becomes quadratically dependant on the GCN of M.

$$V_A(r, \theta) = \frac{(e^{-r/R_O})^2}{\sum_{M_i \in \Omega(O)} e^{-r_{M_i,O}/R_O}} \sum_{n=1}^4 a_n \cos(n\theta) \quad (4.6)$$

where Ω represents an ensemble of metallic atoms (indistinct of their nature in the case of an alloy) within a given distance cut-off of O.

In the GAL21 functional forms, all a_n becomes quadratically dependant on the GCN of M.

$$V_{TT}(r) = A e^{-B \cdot r} - \left[1 - \sum_{k=0}^6 \frac{(B \cdot r)^k}{k!} e^{-B \cdot r} \right] \frac{C_6}{r^6} \quad (4.7)$$

where A , B , and C_6 are parameters. In the GAL21 functional forms, both A and B become linearly dependant on the GCN of M.

The surface normal definition for each metallic atom M has been slightly adapted compared to GAL19 to behave more smoothly at the surface of highly corrugated objects. It now reads:

$$\vec{n}(M) = \sum_i \frac{\vec{r}_{M_i,M}}{r_{M_i,M}^5} \quad (4.8)$$

Chapter 4. Beyond the extended metallic surface/water interface with the GAL21 force field

where i runs over all metallic atoms (*i.e.*, including all constituents in the case of an alloy) within a distance cut-off of M . The cutoff is defined as the global force field cutoff. The sum cause the resulting vector to point away from the volume containing metallic atoms, and therefore, to the “outside” of the metallic object.

In total, 6 parameters become linearly dependant on the GCN of M : A_H , B_H , b_{\parallel} , b_{\perp} , A , and B ; and 5 parameters becomes quadratically dependant on the GCN of M : ε_a and the four a_n .

Each parameter L depending linearly on the GCN of M is decomposed as:

$$L = L_{(1)} \cdot GCN(M) + L_{(0)} \quad (4.9)$$

and each parameter Q depending quadratically on the GCN of M is decomposed as:

$$Q = Q_{(2)} \cdot GCN(M)^2 + Q_{(1)} \cdot GCN(M) + Q_{(0)} \quad (4.10)$$

The quadratic dependence was chosen base on the observation of the minimum adsorption energy according to DFT among the adsorption configurations of water used as data set to fit and validate the GAL21 force field (see appendix chapter C). The relation between these minimum adsorption energies and the GCN of the atomic adsorption sites is presented in Fig 4.2. Direct fitting of such dependence is out of the question, because the adsorption configurations are different between the presented points and because the interaction between the water molecule and the atomic adsorption site cannot be decorrelated from the interactions between the water molecules and other neighbouring metallic atoms. However, a quadratic trend emerges, advocating for the choice of a quadratic dependence of the parameters in the GCN. Some linear dependences were introduced instead later in the development to reduce the number of fitted parameters.

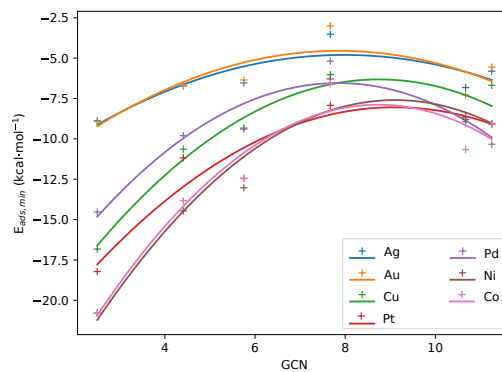


Figure 4.2 – Minimal adsorption energies of water among the configuration set used in this study for each atomic adsorption site in function of the GCN of the atomic adsorption site. Parabolas are fitted on the adsorption energies of water on each metal.

4.2.3 Fitting method and data set

In order to investigate atomic sites for water adsorption presenting a wide range of associated GCN, several surfaces were built. Fig 4.3 presents the different model surfaces and atomic sites considered, along with their associated GCN.

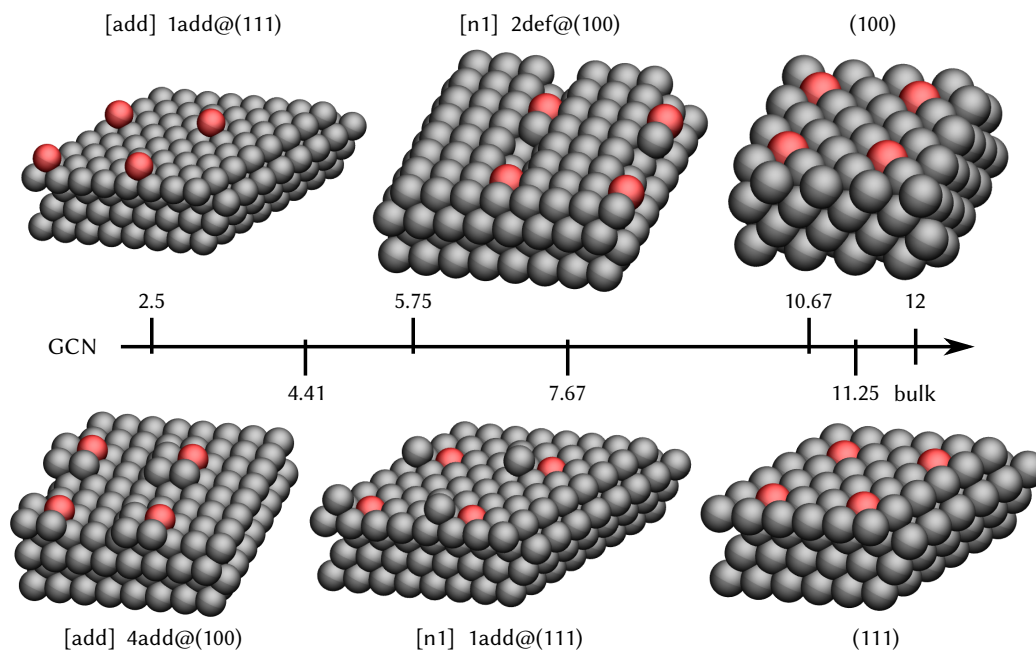


Figure 4.3 – 24×42 representations of the model slabs and atomic adsorption sites chosen for this study. Red atoms represent the atomic sites on top of which water molecules are adsorbed. A Globalised Coordination Number and a name is associated with each of these atoms. Between brackets are the specific names of the atomic sites on the slabs, followed by the designation of the slabs themselves. Atomic site names are not precised when all the surface atoms of a slab are identical. [add] stands for the addatoms, [n1] stands for the first neighbour of an addatom or defect, $n\text{add}@S$ stands for a surface S topped with n addatoms, while $n\text{def}@S$ stands for a surface S for whom n atoms were removed.

In total, 29 adjustable parameters are needed for the GAL19 forcefield for each metal: the five parameters for physisorption (Eq. 4.7): the two parameters of the linear dependence of each A and B , and C_6 ; the seven parameters of the Gaussian (Eq. 4.5): the three parameters of the quadratic dependence of ϵ_a , the two parameters of the linear dependence of each b_{\parallel} and b_{\perp} ; the thirteen parameters for the angular dependence (Eq. 4.6): R_O , and the three parameters of the quadratic dependence of each a_1 , a_2 , a_3 , and a_4 ; and the four hydrogen repulsion parameters: the two parameters of the linear dependence of each A_H and R_H of Eq. 4.3.

In order to fit these parameters, a set of 3458 configurations is built for each metal. All configurations consist of a single water molecule adsorbed on a $p(3 \times 3)$ or $p(4 \times 4)$ metallic slab. The configurations probe various orientations, distances, and adsorption sites (top, hollow, addatom, etc...) of the water molecule. Only a restricted part of the total set (500

Chapter 4. Beyond the extended metallic surface/water interface with the GAL21 force field

configurations) is used to fit the data, while the rest is used to validate the model. More details about the set can be found in the appendix C.

Similarly to GAL 19, the C_6 parameter is the only one that is not fitted but directly extracted from the DFT computations via the use of the dDsC dispersion correction.¹⁸

The same optimisation processes as presented in chapter 3 for the GAL19 force field was used and led to a remarkable speed up of the optimisation procedure, as all linear parameter for which a GCN dependence is introduced can be decomposed into three new linear (and thus, easy to fit) parameters:

$$p(\text{GCN}) \cdot T = (p_2 \cdot \text{GCN}^2 + p_1 \cdot \text{GCN} + p_3) \cdot T = p_2 \cdot \text{GCN}^2 \cdot T + p_1 \cdot \text{GCN} \cdot T + p_3 \cdot T \quad (4.11)$$

where p is a linear parameter, p_n its components in the linear dependence, and T a term of the potential.

The optimal parameters for the seven metals are provided in the appendix chapter C.

4.3 Computational details

All DFT single-point evaluations have been carried out with VASP 5.4.1,^{19;20} using the PBE generalized gradient approximation functional^{21;22} with the dDsC dispersion correction^{23;24} and an energy cutoff of 400 eV for the expansion of the plane-wave basis set. The electron-ion interactions are described by the PAW formalism.^{25;26} The interatomic distances of the bulk metals have been optimized and found to be 2.48, 2.49, 2.56, 2.78, 2.92, 2.81, 2.94 Å for Ni, Co, Cu, Pd, Ag, Pt, and Au respectively. Series of 3458 configurations of a single water molecule adsorbed on a p(3×3) (for (100), (111) surface) or p(4×4) (for all the other surfaces) metallic unit cell with 4 metallic layers were built for each of the metal. The slabs are separated by a vacuum of 20 Å in order to minimize interactions between periodic images. The diverse set (see appendix C) explores the configurational space characterised by the four main descriptors: The adsorption site, the distance to the surface, the cartwheel angle θ and the propeller angle ϕ as defined in Fig. 4.4.

The Brillouin zone was sampled by a Γ -centered 3 x 3 x 1 Monkhorst-Pack K-point grid.²⁷ Idealized geometries (as cut from the bulks) were adopted for the metallic layers, while the water molecule was taken from a DFT optimization in gas phase (O-H: 0.98 Å and a H-O-H angle of 105.32°).

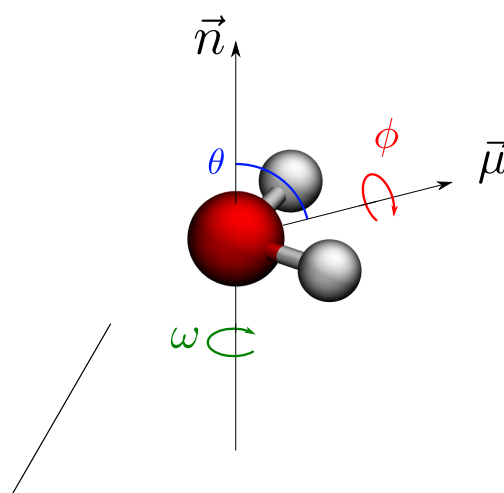


Figure 4.4 – Schematic representation of the cartwheel angle θ , the propeller angle ϕ , and the helicopter angle ω , defining the orientation of the water molecule with respect to the surface. $\omega = 0$ is arbitrarily defined as a coincidence of the dipole moment vector and the x-axis. At $\phi = 0$ the molecular plane of H_2O is parallel to the surface.

4.4 Results

The GAL21 was fitted on single-molecule adsorption configurations and its performances were evaluated on such configurations. Various configurations were used to probe the dependence of the adsorption energy relative to the distance and orientation of the water molecule toward the surface, and on the 6 aforementioned atomic adsorption sites. As an example, resulting plots for the GAL21 force field parametrised for Pd are presented in Fig. 4.5. These results were presented for Pd, for which an average RMSD was found compared to the other metals, as presented in Table 4.1. Similar behaviour, both for DFT and GAL21 dependencies were observed across all investigated metals.

Table 4.1 – Root mean square deviation of the GAL21 predicted adsorption energy compared to the energy predicted by DFT for the configurations of the total set resulting in endothermic adsorption energies in DFT. The number of configurations verifying this criterion is indicated for each metallic facet.

| Metal | RMSD | $N_{\text{configurations}}$ |
|-------|------|-----------------------------|
| Co | 1.54 | 2991 |
| Cu | 1.09 | 3406 |
| Ag | 0.59 | 2706 |
| Au | 0.64 | 2646 |
| Ni | 1.86 | 2742 |
| Pd | 1.25 | 2973 |
| Pt | 1.57 | 3666 |

All ϕ dependences in DFT look rather similar across the adsorption sites. They present a minimum adsorption energy at 0° (the two H at the same distance to the surface), and a

Chapter 4. Beyond the extended metallic surface/water interface with the GAL21 force field

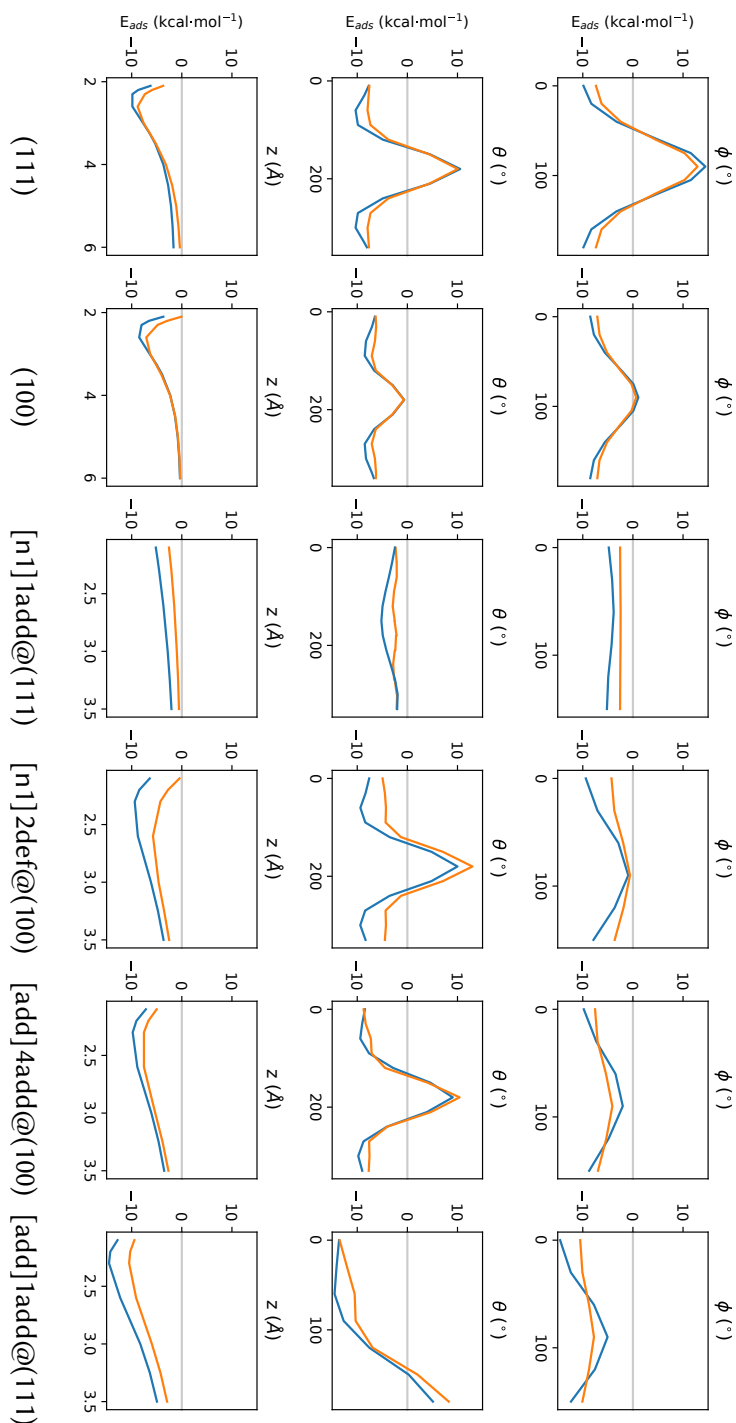


Figure 4.5 – Dependence of the adsorption energies of water molecules on Pd slabs in $\text{kcal}\cdot\text{mol}^{-1}$. DFT adsorption energies are in blue, GAL21 adsorption energies in orange. In columns: the different atomic adsorption sites. In lines: dependence in the ϕ angle (see 4.4), in the θ angle, and in the altitude difference between the oxygen and the higher metallic atom. For each plot, the angles and distances whose dependence are not shown are maintained at the same value as in the optimal adsorption configuration for each atomic adsorption site.

maximum at 90° (one H much closer to the surface). The energy span between the maxima and minima varies as a function of the adsorption site. The biggest span for is found for (111) surface adsorption sites ($24.3 \text{ kcal}\cdot\text{mol}^{-1}$ in DFT), and the smallest for the [n1] site on the 1add@(111) surface ($1.3 \text{ kcal}\cdot\text{mol}^{-1}$ in DFT). The position of the minima and maxima are well reproduced by GAL21, but the spans are slightly underestimated, especially for already small spans, like for the [add] site on the 4add@(111) surface ($7.8 \text{ kcal}\cdot\text{mol}^{-1}$ in DFT versus $3.5 \text{ kcal}\cdot\text{mol}^{-1}$ in GAL21) or the [add] site on the 1add@(111) surface ($0.9 \text{ kcal}\cdot\text{mol}^{-1}$ in GAL21). The θ dependencies are also quite similar across the adsorption sites. They present two maxima: an important one at 180° (the H as close to the surface as possible for a given position of O), and a smaller one at 0° (the H as far to the surface as possible for a given position of O). The optimal adsorption angle is situated between 90° and 60° (close to flat, hydrogen slightly further from the surface than O). However, the adsorption on the [n1] site on the 1add@(111) surface is an exception as the θ dependence is almost insignificant. It must be noticed that the adsorptions on the [add] site on the 1add@(111) surface were not probed for $\theta > 90^\circ$ but should be the same as for $180 - \theta$, for symmetry reasons. All the characteristics (position of the minima and maxima, and energy span) of these dependence curves are well reproduced by GAL21. The exceptions are the positions of the minima that can be slightly displaced (around 30° , the amplitude of our angle step), and the dependence on the [n1] site on the 1add@(111) surface that is too subtle to be properly reproduced. In preliminary results, no difference in adsorption energy between atomic adsorption sites was found beyond 3.5 \AA . The distance dependence in the data set were, therefore, only probed up to 6 \AA for (111) and (100) surfaces and up to 3.5 \AA for other surfaces. The dependences also look similar in DFT, differences between the adsorption sites being found in the position and depth of the adsorption well. The most stable adsorption is found for the [add] site on the 1add@(111) surface ($-14.5 \text{ kcal}\cdot\text{mol}^{-1}$ at 2.3 \AA) and the less stable for the [n1] site on the 1add@(111) surface ($-5.2 \text{ kcal}\cdot\text{mol}^{-1}$ at 2.1 \AA), as already shown in the preliminary DFT results of Fig. 4.2. Once again, GAL21 reproduces quite well the tendencies, with eventual small overestimation of the adsorption position and a general underestimation of the maximum stability brought by adsorption. However, these differences do not exceed $2.9 \text{ kcal}\cdot\text{mol}^{-1}$ (for [n1] site on the 2def@(100) surface) between the most stable structures of DFT and GAL21.

Overall, the GAL21 force field reproduces quite well both the qualitative and quantitative trends described by DFT for the adsorption energy dependence. Small discrepancies can be noticed but the energies are quite consistently accurate across all orientations, distances, and adsorption sites. This accuracy is confirmed by both the parity plot of all GAL21 adsorption energies against all DFT adsorption energies (see appendix C, section C.1) and the excellent root mean square deviation (RMSD) on exothermic adsorption energies ($1.25 \text{ kcal}\cdot\text{mol}^{-1}$ for Pd).

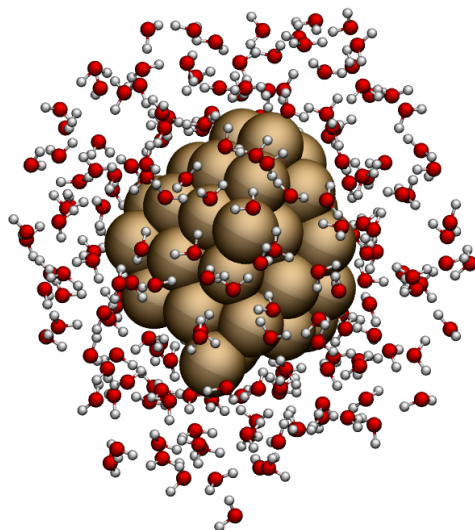


Figure 4.6 – Snapshot extracted from a dynamic of an Au₃₈ nanoparticle in water. Only the closest water molecules to the nanoparticle are shown.

4.5 Discussion and Conclusion

The GAL21 functional form was demonstrated to reproduce accurately the adsorption energy dependence for individual water molecules. In order to go further in the validation of the force-field, dynamic sampling of water phases around diverse nanoparticles should be performed. However, for now, technical limitations hampered such simulations as the lack of a barostat in the CP2K software that would be compatible with frozen-in-position nanoparticles. Fixed volume dynamics were already run, and a snapshot extracted for such dynamic is presented in Fig 4.6. A fixed volume dynamic is not suited for 3-dimensional periodic systems in absence of a vacuum phase. However, we find encouraging that the expected behaviour of the water molecule is reproduced in such dynamics, with molecules flatly adsorbed as a shell around the nanoparticle and a sort of void layer between this first shell and the second.

In the future, we plan to implement an adapted barostat and identify key descriptors to analyse quantitatively the structure of water around the particle. Also, a second step would be to perform Thermodynamic Integration (see chapter 2) on the disappearance of the nanoparticle in the water phase to compute the surface solvation energy of the particle, which might eventually be confronted to experimental values.

Of course, several limitations of the functional form pointed out in the chapter 3 were not addressed, as the lack of a synergistic term between two (or more) co-adsorbed water molecules on the metallic surface. No computation was performed to test this but important errors are expected between the adsorption energy in DFT of an entire water layer around the nanoparticle and the energy predicted by GAL21. But again, the gain in sampling duration brought

by the celerity of MM computation can partly compensate for the lack of accuracy of the functional form for more than one molecule.

Also, in the following chapter 5, leads are investigated to overcome this problem. The synergistic effect is decomposed and studied and even if no technical solution is yet proposed, hopes are that, in the future, the GAL21 force field could be complemented to account for it.

Bibliography

- [1] Qiao, B.; Wang, A.; Yang, X.; Allard, L. F.; Jiang, Z.; Cui, Y.; Liu, J.; Li, J.; Zhang, T. Single-atom catalysis of CO oxidation using Pt-1/FeOx. *Nat. Chem.* **2011**, *3*, 634–641, Place: London Publisher: Nature Publishing Group WOS:000292999100017.
- [2] Schmid, G. Large clusters and colloids. Metals in the embryonic state. *Chem. Rev.* **1992**, *92*, 1709–1727, Publisher: American Chemical Society.
- [3] Dimitratos, N.; Lopez-Sanchez, J. A.; Hutchings, G. J. Selective liquid phase oxidation with supported metal nanoparticles. *Chem. Sci.* **2011**, *3*, 20–44, Publisher: The Royal Society of Chemistry.
- [4] Corma, A.; Serna, P. Chemoselective Hydrogenation of Nitro Compounds with Supported Gold Catalysts. *Science* **2006**, *313*, 332–334, Publisher: American Association for the Advancement of Science Section: Report.
- [5] Brust, M.; Walker, M.; Bethell, D.; Schiffrin, D. J.; Whyman, R. Synthesis of thiol-derivatised gold nanoparticles in a two-phase Liquid–Liquid system. *J. Chem. Soc., Chem. Commun.* **1994**, 801–802, Publisher: The Royal Society of Chemistry.
- [6] Li, N.; Zhao, P.; Astruc, D. Anisotropic Gold Nanoparticles: Synthesis, Properties, Applications, and Toxicity. *Angew. Chem. Int. Ed.* **2014**, *53*, 1756–1789, _eprint: <https://onlinelibrary.wiley.com/doi/pdf/10.1002/anie.201300441>.
- [7] Fan, J.; Cheng, Y.; Sun, M. Functionalized Gold Nanoparticles: Synthesis, Properties and Biomedical Applications. *The Chemical Record* **2020**, *20*, 1474–1504, _eprint: <https://onlinelibrary.wiley.com/doi/pdf/10.1002/tcr.202000087>.
- [8] Roa, W.; Zhang, X.; Guo, L.; Shaw, A.; Hu, X.; Xiong, Y.; Gulavita, S.; Patel, S.; Sun, X.; Chen, J.; Moore, R.; Xing, J. Z. Gold nanoparticle sensitize radiotherapy of prostate cancer cells by regulation of the cell cycle. *Nanotechnology* **2009**, *20*, 375101, Publisher: IOP Publishing.
- [9] Huang, S.; Inerbaev, T. M.; Kilin, D. S. Excited State Dynamics of Ru10 Cluster Interfacing Anatase TiO2(101) Surface and Liquid Water. *J. Phys. Chem. Lett.* **2014**, *5*, 2823–2829, Publisher: American Chemical Society.

Chapter 4. Beyond the extended metallic surface/water interface with the GAL21 force field

- [10] Siemer, N.; Muñoz-Santiburcio, D.; Marx, D. Solvation-Enhanced Oxygen Activation at Gold/Titania Nanocatalysts. *ACS Catal.* **2020**, *10*, 8530–8534, Publisher: American Chemical Society.
- [11] Chan, C.-H.; Poignant, F.; Beuve, M.; Dumont, E.; Loffreda, D. A Water Solvation Shell Can Transform Gold Metastable Nanoparticles in the Fluxional Regime. *J. Phys. Chem. Lett.* **2019**, *10*, 1092–1098, Publisher: American Chemical Society.
- [12] Benedikt, U.; Schneider, W. B.; Auer, A. A. Modelling electrified interfaces in quantum chemistry: constant charge vs. constant potential. *Phys. Chem. Chem. Phys.* **2013**, *15*, 2712–2724, Publisher: The Royal Society of Chemistry.
- [13] Morais, R. F. d.; Kerber, T.; Calle-Vallejo, F.; Sautet, P.; Loffreda, D. Capturing Solvation Effects at a Liquid/Nanoparticle Interface by Ab Initio Molecular Dynamics: Pt201 Immersed in Water. *Small* **2016**, *12*, 5312–5319, _eprint: <https://onlinelibrary.wiley.com/doi/pdf/10.1002/sml.201601307>.
- [14] Calle-Vallejo, F.; Martínez, J. I.; García-Lastra, J. M.; Sautet, P.; Loffreda, D. Fast Prediction of Adsorption Properties for Platinum Nanocatalysts with Generalized Coordination Numbers. *Angew. Chem. Int. Ed.* **2014**, *53*, 8316–8319.
- [15] Calle-Vallejo, F.; F. de Morais, R.; Illas, F.; Loffreda, D.; Sautet, P. Affordable Estimation of Solvation Contributions to the Adsorption Energies of Oxygenates on Metal Nanoparticles. *J. Phys. Chem. C* **2019**, *123*, 5578–5582.
- [16] Staub, R.; Steinmann, S. N. Parameter-free coordination numbers for solutions and interfaces. *J. Chem. Phys.* **2020**, *152*, 024124, _eprint: <https://doi.org/10.1063/1.5135696>.
- [17] Tang, K. T.; Toennies, J. P. An improved simple model for the van der Waals potential based on universal damping functions for the dispersion coefficients. *J. Chem. Phys.* **1984**, *80*, 3726–3741.
- [18] Steinmann, S. N.; Corminboeuf, C. A generalized-gradient approximation exchange hole model for dispersion coefficients. *J. Chem. Phys.* **2011**, *134*, 044117.
- [19] Kresse, G. Ab initio molecular dynamics for liquid metals. *J. Non-Cryst. Solids* **1995**, *192-193*, 222–229.
- [20] Kresse, G.; Furthmüller, J. Efficiency of ab-initio total energy calculations for metals and semiconductors using a plane-wave basis set. *Computational Materials Science* **1996**, *6*, 15–50.
- [21] Perdew, J. P.; Wang, Y. Accurate and simple analytic representation of the electron-gas correlation energy. *Phys. Rev. B* **1992**, *45*, 13244–13249.

- [22] Perdew, J. P.; Burke, K.; Ernzerhof, M. Generalized Gradient Approximation Made Simple. *Phys. Rev. Lett.* **1996**, *77*, 3865–3868.
- [23] Steinmann, S. N.; Corminboeuf, C. Comprehensive Benchmarking of a Density-Dependent Dispersion Correction. *J. Chem. Theory Comput.* **2011**, *7*, 3567–3577.
- [24] Gautier, S.; N. Steinmann, S.; Michel, C.; Fleurat-Lessard, P.; Sautet, P. Molecular adsorption at Pt(111). How accurate are DFT functionals? *Phys. Chem. Chem. Phys.* **2015**, *17*, 28921–28930.
- [25] Blochl, P. E. Projector augmented-wave method. *Phys. Rev. B* **1994**, *50*, 17953.
- [26] Kresse, G.; Joubert, D. From ultrasoft pseudopotentials to the projector augmented-wave method. *Phys. Rev. B* **1999**, *59*, 1758.
- [27] Monkhorst, H. J.; Pack, J. D. Special points for Brillouin-zone integrations. *Phys. Rev. B* **1976**, *13*, 5188–5192.

5 Water adlayers on noble metal surfaces: Insights from energy decomposition analysis

This Chapter is based on the following article: Water adlayers on noble metal surfaces: Insights from energy decomposition analysis, *Clabaut, P. and Staub, R and Galiana, J. and Antonetti, E. and Steinmann, S.N., The Journal of Chemical Physics*, 2020, 10.1063/5.00130409

abstract: Water molecules adsorbed on noble metal surfaces are of fundamental interest in surface science, heterogeneous catalysis and as a model for the metal/water interface. Herein, we analyse 28 water structures adsorbed on five noble metal surfaces (Cu, Ag, Au, Pd, Pt) via density functional theory and energy decomposition analysis based on the block localized wave function technique. The structures, ranging from the monomers to ice adlayers, reveal that the charge-transfer from water to the surface is nearly independent from the charge-transfer between the water molecules, while the polarization energies are cooperative. Dense water-water networks with small surface dipoles, such as the $\sqrt{39} \times \sqrt{39}$ unit cell (experimentally observed on Pt(111)) are favored compared to the highly ordered and popular H^{up} and H^{down} phases. The second main result of our study is that the many-body interactions, which stabilize the water assemblies on the metal surfaces, are dominated by the polarization energies, with the charge-transfer scaling with the polarization energies. Hence, if an empirical model could be found that reproduces the polarization energies, the charge-transfer could be predicted as well, opening exciting perspectives for force field development.

5.1 Introduction

Ice-like water layers over noble metal surfaces are widely studied, both experimentally and theoretically.¹⁻⁴ Due to the sparsity of the characterization of the metal/water interface, they are sometimes considered model systems for the solid/liquid interface,⁵⁻⁹ even though the validity of this extrapolation is far from obvious.^{10;11} Furthermore, the ice adlayers are regularly used to model the metal/liquid interface in (electro-)catalysis.¹²⁻¹⁶ The alternatives for approximate treatments of the solvent are implicit solvents,¹⁷ which do not compete with adsorbates for surface sites,¹⁸ microsolvation^{19;20} which solvates adsorbates only locally, and *ab initio* molecular dynamics, which is computationally very expensive²¹.

The most commonly reported and applied ice adlayers over closed-packed noble-metal surfaces are the $\sqrt{3} \times \sqrt{3}$ H^{up} and H^{down} models, going back to the seminal STM work of Doering on Ru.¹ However, larger unit cells have been observed for Pt(111)² and explained in terms of more disordered ice-like layers featuring ring-structures of various sizes.³

Previous theoretical studies have focused on the bonding mechanism of individual monomers on metal surfaces^{22;23} or on the possibility of water dissociation.²⁴ Herein, we focus on non-dissociated water layers, fully covering the noble metal surfaces. The purpose of this study is, on the one hand, to elucidate the relative stability of these ice-like structures on five noble metal surfaces (Cu, Pd, Ag, Pt, Au) and, on the other hand, to identify the driving force of their formation via energy decomposition analysis (EDA). We rely on dispersion corrected DFT to achieve a balanced description between water–water and water–metal interactions.^{25;26}

Energy decomposition analysis is a powerful tool which is mostly applied in molecular chemistry,²⁷⁻²⁹ but also increasingly in condensed phase³⁰ and at surfaces.³¹⁻³³ EDAs, like most concepts in chemistry, make reference to quantities that are neither observable, nor uniquely defined, just like the definition of an atom in a molecule. Such noumenons are, nevertheless, widely accepted to be useful.³⁴ The lack of unique definition spurs debate in the community,^{35;36} which we interpret as a sign of the importance of the concept and not of its futility. Hence, we herein exploit EDA to gain insight into the role of polarization and charge-transfer for the interaction of water with noble metal surfaces.

We have recently extended the block localized wave function (BLW) technique³⁷⁻³⁹ to metallic surfaces.³³ The BLW based EDA now allows to decompose the adsorption energy into four terms: deformation, frozen, polarization and charge-transfer, which encompasses electron sharing. This energy decomposition not only provides deep insight into the bonding, but also allows to gain information for force field development.⁴⁰ The charge-transfer (chemisorption) is the term that is the most difficult to reproduce, as it is intrinsically a many-body term with no generally applicable analytical expression known for it. The polarization is, on the other hand, a better understood many-body term, which can be modelled via induced dipoles, themselves

modelled according to different techniques. BLW, which includes polarization at the DFT level, also defines the limit of the precision that can be expected from a polarizable force field in the absence of error cancellations between different interaction energy components.

To achieve this detailed insight, the remaining of the work is structured as follows: After describing the computational details, we analyse the stability of the various ice-layers on the five investigated metal surfaces. Next, we perform an EDA for the ice-layers, but also for 23 smaller (monomer to heptamer) clusters (see Fig. D.4 and D.5). According to these computations, the polarization interaction is strongly correlated to the charge-transfer energy, so that the total interaction can be estimated based on the (linear-scaling⁴¹) BLW energy. Furthermore, we quantify the cooperativity between water–water and water–metal polarization interactions and evidence a competition between the water–water and water–metal charge-transfer interactions. Note, that hydrogen bonds are, as attested by various previous studies, not of pure electrostatic origin, but show characteristics of weak covalent bonds,^{30;42;43} which is indistinguishable from charge-transfer in BLW. It is this partial covalent character that is responsible for the synergy or competition with other interactions.

5.2 Methods

We start by defining the total adsorption energy of a given system:

$$\Delta E_{ads} = E_{SCF} - E_{surf^{opt}} - n \cdot E_{W^{opt}} + \Delta E_{BSSE} \quad (5.1)$$

where E_{SCF} is the standard KS-SCF energy of the full system, $E_{surf^{opt}}$ and $E_{W^{opt}}$ are the corresponding energies of the freely optimized surface and water molecule, respectively. n is the number of water molecules in a given system. Since the BLW is only defined in a localized basis set, we have to correct for the basis set superposition error (BSSE), which we do according to the counterpoise procedure of Boys and Bernardi⁴⁴, giving rise to the (by definition positive) energy correction ΔE_{BSSE} .

As common in BLW-EDA,^{27;45;46} we decompose the total adsorption energy ΔE_{ads} into:

$$\Delta E_{ads} = \Delta E_{deform} + \Delta E_{frozen} + \Delta E_{pol} + \Delta E_{CT} \quad (5.2)$$

where ΔE_{deform} is the preparation or deformation energy, ΔE_{frozen} is the frozen energy term that describes the interaction of the isolated fragment densities brought together and covers electrostatic interaction and Pauli repulsion²⁷ as well as dispersion interactions⁴⁶. ΔE_{pol} is the polarization energy which is obtained by variationally optimizing the BLW. ΔE_{CT} is, finally, the charge transfer interaction that includes the covalent bond formation. Note, that the BSSE only affects the charge-transfer term, as all other terms are evaluated using the

Chapter 5. Water adlayers on noble metal surfaces: Insights from energy decomposition analysis

same fragment-decomposed basis set. It is important to note that the distinction between ΔE_{pol} and ΔE_{CT} depends on the choice of the basis set, as in the complete basis set limit the variational optimization at the origin of ΔE_{pol} retrieves the full interaction energy. However, in several previous studies the basis set influence has been found to be rather limited when using “standard” basis sets.^{46;47} Nevertheless, an extension has been proposed to fully overcome this issue if it would severely affect the results.⁴⁸

The following equation summarizes the scheme and different terms. Further details on the computation of these terms are given in the corresponding equations as indicated:

$$\begin{array}{c}
 \begin{array}{ccccccc}
 E_{isolated} & \xrightarrow[\text{Eq. 5.4a}]{\Delta E_{deform}} & E_{fragments} & \xrightarrow[\text{Eq. 5.4b}]{\Delta E_{frozen}} & E_{SFD} & \xrightarrow[\text{Eq. 5.4c}]{\Delta E_{pol}} & E_{BLW} & \xrightarrow[\text{Eq. 5.4d}]{\Delta E_{CT}} & E_{cor} & \xrightarrow{-\Delta E_{BSSE}} & E_{SCF}
 \end{array} \\
 \underbrace{\hspace{10em}}_{\Delta E_{ads}(\text{Eq.5.2})} & & \underbrace{\hspace{10em}}_{\Delta E_{int}(\text{Eq.5.5})} & & \underbrace{\hspace{10em}}_{\Delta E_{int}^{BLW}(\text{Eq.5.6})} & & & & & &
 \end{array} \quad (5.3)$$

where $E_{isolated} = E_{surf^{opt}} + n \cdot E_{W_i^{opt}}$ is the sum of the electronic energy of each fragment optimized separately, $E_{fragments} = E_{surf^{sys}} + \sum_i^n E_{W_i^{sys}}$ is the sum of the energy of each fragment evaluated in its final geometry. The superscript “sys” corresponds to the energy of a fragment in the geometry adopted in the presence of the other fragments. E_{SFD} is the total energy after Superposition of the Fragment Densities, E_{BLW} is the total energy obtained by the Block Localized Wavefunction³³ and E_{cor} corresponds to the final energy of the complete system, corrected for the BSSE, while E_{SCF} is the energy obtained by a standard SCF computation.

This leads to the following definitions for the four terms of the adsorption energy as decomposed in Eq. 5.2:

$$\Delta E_{deform} = E_{surf^{sys}} - E_{surf^{opt}} + \sum_i^n E_{W_i^{sys}} - n \cdot E_{W_i^{opt}} \quad (5.4a)$$

$$\Delta E_{frozen} = E_{SFD} - E_{surf^{sys}} - \sum_i^n E_{W_i^{sys}} \quad (5.4b)$$

$$\Delta E_{pol} = E_{BLW} - E_{SFD} \quad (5.4c)$$

$$\Delta E_{CT} = E_{SCF} - E_{BLW} + \Delta E_{BSSE} \quad (5.4d)$$

Furthermore, we define the interaction energy, ΔE_{int} as the adsorption energy excluding the deformation energy, *i.e.*,

$$\Delta E_{int} = \Delta E_{frozen} + \Delta E_{pol} + \Delta E_{CT} \quad (5.5)$$

Similarly, we define the BLW interaction energy as the interaction energy that excludes the charge-transfer interaction:

$$\Delta E_{BLW} = \Delta E_{frozen} + \Delta E_{pol} \quad (5.6)$$

Since ΔE_{BLW} include all polarization contributions at the DFT level but excludes any charge-transfer, it can be understood as the interaction energy of an “ideal” polarizable force field. Furthermore, computationally its evaluation can be performed with near linear scaling with respect to the number of fragments,⁴¹ which contrasts with the cubic scaling for the computations including the charge-transfer interactions.

For the energy decomposition analysis and its interpretation, each system is either divided into two blocks (one for the metallic surface, one for all the n water molecules together) or into $n + 1$ blocks.

Taking the frozen interaction as an example, we denote the standard decomposition:

$$\Delta E_{frozen} = \Delta E_{frozen}(W_1, \dots, W_n, surf) \quad (5.7)$$

as the situation where every water molecule W_i is treated as a separate subsystem. This contrasts with decomposition into two blocks, the surface and the adlayer:

$$\Delta E_{frozen}^{surf-layer} = \Delta E_{frozen}(\bigcup_i W_i, surf) \quad (5.8)$$

where all the water molecules are treated together as a single block and the surface is a second block.

Finally, in order to assess many-body effects, we also determine the “additive” frozen interaction:

$$\Delta E_{frozen}^{add} = \sum_i^n \Delta E_{frozen}(W_i, surf) \quad (5.9)$$

where we perform n separate computations, one for each water molecule, and then sum the corresponding contributions.

The standard decomposition leads to the most complete interaction while Eq. 5.8 excludes the water–water interaction components and Eq. 5.9 is free of any many-body interactions. It is, therefore, possible to define the missing part of the interaction component

$$\Delta E_{frozen}^{NonAdd} = \Delta E_{frozen} - \Delta E_{frozen}^{add} \quad (5.10)$$

which represent the non-additive part of the interaction.

Analogous equations to Eq. 5.7-5.10 can be written for the polarization and charge-transfer energy.

For the purpose of comparison with experimental estimates, we also compute an approximate surface energy, defined as:

$$\Gamma = \frac{\Delta E_{ads}}{A} \quad (5.11)$$

where ΔE_{ads} is the adsorption energy of the adlayer and A the area of the corresponding surface, *i.e.*, the unit-cell.

5.3 Computational Details

In order to avoid BSSE during geometry optimizations, the adsorbed structures were optimized with the plane-wave code VASP 5.4.1^{49;50} using periodic boundary conditions applying the re-optimized Perdew, Burke and Ernzerhofer functional to make it compatible with the non-local van der Waals (vdW) functional, in short optPBE-vdW⁵¹ functional. An energy cutoff of 400 eV is chosen for the expansion of the plane-wave basis set, which yields converged adsorption energies in agreement with our previous studies^{18;52;53}. The electron-ion interactions are described by the PAW formalism.^{54;55} The unit cells are built from bulk metals (2.821, 2.580, 2.955, 2.943 and 2.797 Å nearest neighbor distance for Pt, Cu, Au, Ag, and Pd, respectively) with four metallic layers, the top two of which are allowed to relax. The out-of-plane vector of the unit cell was chosen to be ~ 20 Å to achieve a negligible interaction between periodic images. Geometries are considered converged when the maximum gradient on all atoms is below 0.05 eV/Å, with the electronic structure being converged to a precision of 10^{-6} eV. Coordinate files for all discussed systems are available in the appendix chapter D. VASP was also used to determine the surface dipole moment and the workfunction of the various systems. Following our previous studies,^{18;56} the dipole moment was determined using the self-consistent dipole correction. The latter not only computes the dipole moment, but also decouples the periodic images, which avoids spurious polarization of the system. The workfunction was, however, computed for a centro-symmetric slab of seven layers, which was found sufficient in our previous study on formic acid decomposition over Pd(111).⁵⁶

In CP2K,^{57;58} which uses atom-centered basis functions as required for the BLW-EDA, the molecular orbitals were represented by a double- ζ Gaussian basis set with one set of polarization functions, called DZVP-MOLOPT-SR-GTH for both BLW-EDA and BSSE corrected SCF DFT simulations.⁵⁹ A cutoff of 400 Ry was used to describe the electron density in agreement with our previous study³³. The exchange-correlation (XC) energy was approximated with the optPBE-vdW⁵¹ functional. Like in VASP, the Brillouin zone was described at the Γ -point. Goedecker, Teter and Hutter (GTH) pseudo-potentials⁶⁰ based on the PBE functional were

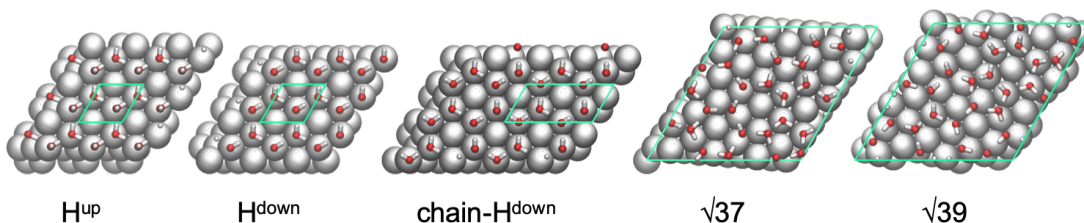


Figure 5.1 – Structures of the ice adlayers on Pt(111) together with their short-hand notation as used herein. The unit cell is indicated in green. For the small unit cells, a supercell is chosen to have comparable sizes for all systems and allow the use of the Γ point only in the DFT computations. The in-plane unit-cell vectors are of following lengths (in Å) for Pt (and accordingly rescaled for the other metals, see sec. 5.3): 14.66×14.66 ; 14.66×14.66 ; 19.54×14.66 ; 17.16×17.16 ; and 17.62×17.62 .

used to describe the interactions between the valence electrons and the ionic cores, and the electronic smearing was approximated by a Fermi-Dirac distribution at 300 K. As discussed in our previous publication³³ the 18 valence electron potential is necessary for Pt to obtain similar results between CP2K and VASP. For Cu and Au the 11 valence electron potential is applied. For the adopted choice, Fig. D.1 provides the comparison between CP2K and VASP, showing a satisfactory correlation for our purposes ($R^2 > 0.99$), indicating good numerical convergence of the results for both codes. We have performed additional tests with the larger TZVP-MOLOPT-(SR)-GTH basis set. As shown in Fig. D.6, ΔE_{pol} increases by about 10% at the expense of ΔE_{CT} , which is similar to the earlier reports.^{46;47}

In order to identify the water molecules in the ice-layers, where the atoms are ordered by elements rather than molecule, we have used our in-house code *imecs*, which is provided in the supplementary information.

5.4 Results and Discussion

5.4.1 Relative Stability of Ice-like Layers

We are comparing five previously reported ice-like layers (depicted in Fig. 5.1) on five metals, which we will denote H^{up} , H^{down} , $chain-H^{down}$, $\sqrt{37}$ and $\sqrt{39}$. The nominal coverage of these structures is 0.67 ML for the first three, 0.70 and 0.72 ML for the last two, where ML stands for monolayer with respect to the surface metal atoms. Figure 5.2 shows that the $\sqrt{39}$ structure leads to the lowest surface energy Γ (see Eq. 5.11) for almost all metals, closely followed by $\sqrt{37}$. Cu(111) is the exception in the sense that it is the only metal investigated herein for which $\Gamma(\sqrt{37}) < \Gamma(\sqrt{39})$. Concomitantly, Cu(111) has the lowest interatomic distance of 2.58 Å followed by 2.80 Å for Pd, the second smallest metal investigated here.

In terms of absolute values, the surface energy of Pt(111) for the $\sqrt{37}$ structure is 1.73 kcal/(mol·Å²), which compares to 0.46 kcal/(mol·Å²) for the adhesion of solid water at ~ 100 K⁶¹ and 3.45

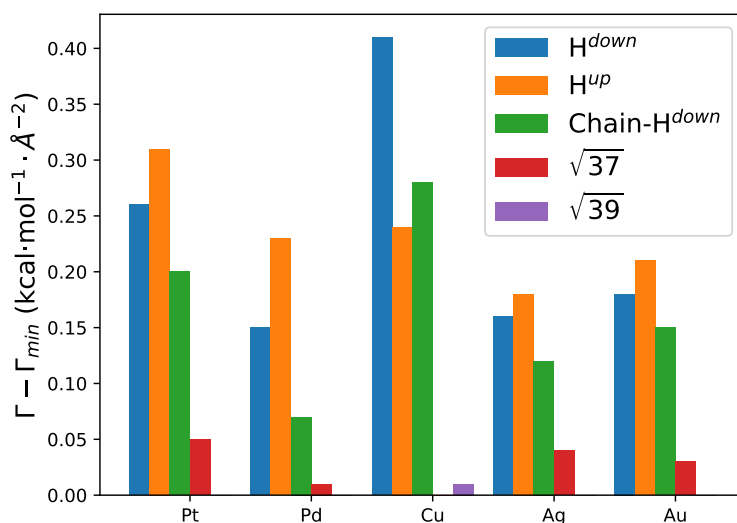


Figure 5.2 – Surface energies Γ in $\text{kcal}\cdot\text{mol}^{-1}/\text{\AA}^2$ relative to the most stable ice adlayer, *i.e.*, $\sqrt{39}$ for all metals except for Cu, where $\sqrt{37}$ is slightly more stable. The higher the bar, the less stable is the corresponding structure.

$\text{kcal}/(\text{mol}\cdot\text{\AA}^2)$ for the Pt/liquid water tension.⁶² For a broader comparison to experiment, Fig. D.2 shows the correlation between the lowest surface energy of each metal and the reported experimental value. Except for Cu, the trends are nicely reproduced. Since, furthermore, the interatomic distance of Cu (2.58 \AA) is less compatible with the ideal H-bond length of ~ 2.8 \AA , this might indicate that liquid water behaves differently on Cu(111) compared to the other noble metal surface.

5.4.2 Electronic Analysis

Before moving to the energy decomposition analysis, we here investigate the electronic nature of the various interfaces by computing the surface dipole moment and the workfunction Φ . The workfunction is intimately connected to the electrochemical potential and it has been argued that the H^{up} and H^{down} phases should co-exist over large potential ranges.^{9;10} However at that time the three other surfaces investigated here have not been assessed.

All ice adlayers taken alone, except H^{up} for all metals and chain- H^{down} on top of Cu(111), feature a positive dipole moment, meaning that there is a positive charge accumulation on the “bottom” and a negative one on the “top” (see the Excel sheet, tab “ComparisonMetals” available in the supporting information of the original article). The maximum (1.4 e \AA) is obtained for $\sqrt{39}$ over Pd(111), while the minimum is found for H^{up} over Cu(111) (-2.7 e \AA). The water layers, when optimized on different metallic surfaces (and hence, on different lattice

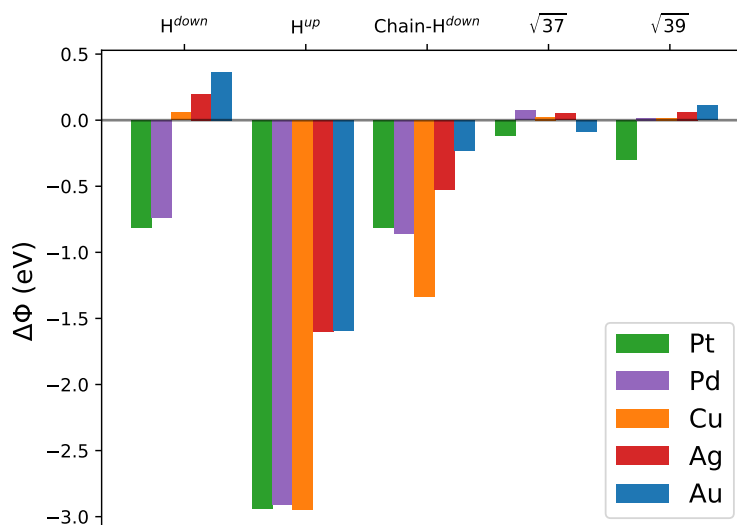


Figure 5.3 – The change of workfunction ($\Delta\Phi$) when an ice adlayer is adsorbed on a (111) noble metal surface.

size), undergo noticeable geometry distortions. A specific layer, evaluated without metallic slab but in the perturbed geometry corresponding to different metals, can exhibit a range of dipole moment up to $1.3 \text{ e}\text{\AA}$. This maximum is obtained for the H^{up} layer optimized on Au(111) ($-1.4 \text{ e}\text{\AA}$) compared to the one from Cu(111) ($-2.7 \text{ e}\text{\AA}$). Since water is adsorbed only slightly stronger on Cu than on Au(111), this shows that it is mostly the lattice mismatch, and not so much the interaction strength with the metal, that affects the electronic structures via geometrical constraints.

Similarly, the change in workfunction upon adsorption of an ice adlayer depends significantly on the metal (larger changes in absolute values for Pt, Pd and Cu than for Ag and Au) and on the ice layer (see Fig. 5.3). In particular, the workfunction is lowered by almost 3 eV when adsorbing the H^{up} layer on Pt, Pd and Cu, but “only” 1.6 V on Au and Ag. Given the very reductive nature of the H^{up} structure,⁹ its stability is doubtful in itself. Even though one could have expected that the H^{down} layer has the opposite effect, this is not the case and the workfunction still drops for Pt and Pd (-0.8 eV), but remains unchanged for Cu and increases slightly (0.2 eV) for Ag and Au. This not only shows that a purely geometric analysis of the structure is not enough to retrieve the trends on the electronic structure, but also that the metal-dependant interaction plays a major role.

As expected based on basic physical principles,⁶³ the surface dipole moments of the hydrated metal surfaces are correlated with the change in workfunction ($\Delta\Phi$), with an intercept of zero (see Fig. D.3). In other words, a positive surface dipole moment is associated with a positive

Chapter 5. Water adlayers on noble metal surfaces: Insights from energy decomposition analysis

change in workfunction and vice versa. Given the generally positive dipole moments for the isolated layers as discussed above, the dominance of negative changes in Φ , and, thus, the negative dipole moments for hydrated surfaces, require additional explanations. Indeed, the change in dipole moment upon adsorption is generally negative (the one exception being H^{up} on Cu(111)), with an average of -0.8 e\AA and a minimum of -1.6 e\AA (chain- H^{down} on Pt(111)). This nicely demonstrates a “universal” interaction between water and noble metal surfaces featuring a net polarization (or charge-transfer) from water to the surface, *i.e.*, the surface becomes more negatively charged and behaves as a more reductive system compared to vacuum. This conclusion is fully confirmed by the analysis of the density reorganization upon adsorption, as shown in see Fig. D.9-D.11, which represent the density difference between the fully relaxed density and the superposition of the density of the surface and the adlayer. The averaged profiles as a function of the out-of-plane distance demonstrate the density accumulation in the region on top of the last metallic layer for all five adstructures. The negative contributions, indicating the origin of the density accumulation, are, however, distinct from one adstructure to the other. In the case of H^{up} , the density comes from the water adlayer. For the other structures, it is a combination of charge transfer from the water-layer and a polarization of the metallic system, down to the second metal layer. The top and side views of the isosurfaces of the density reorganization (Fig. D.9) nicely illustrates the spatial heterogeneity of the $\sqrt{37}$ and $\sqrt{39}$ structures, which can be seen as a low-energy realization of the proposed mixtures of H^{up} and H^{down} structures proposed by Filhol and Doublet.⁹ Note, however, that the arrangements with the lowest surface energy ($\sqrt{39}$ and $\sqrt{37}$) feature a $\Delta\Phi$ close to zero and thus also the smallest surface dipole moments.

In summary, both the energetic and the electronic structure analysis support the idea that the lowest energy arrangement of water on noble metal surfaces might resemble the $\sqrt{39}$ structure, *i.e.*, densely packed, but containing various relative orientations of the water molecules.

5.4.3 Energy Decomposition Analysis

Water–Metal Interaction

The first, fundamental, question addressed herein is how the interaction of water with a given metal surface depends on the arrangement of the water molecules and on the nature of the metal surface. This question is, furthermore, of importance when aiming at the development of a second generation force field, improving over the existing ones that are fitted to monomer interaction energies, *i.e.*, missing all many body terms. Therefore, we start by analyzing the interaction of the preformed adlayers with the metallic surface, *i.e.* $\Delta E_{int}^{surf-layer}$, and each of its components, defined in analogy to Eq. 5.8. This means that the deformation energy is excluded, while the water molecules interact with each other freely, *i.e.*, the water–water charge-transfer associated with the hydrogen bonds is present at all stages of the analysis. As a

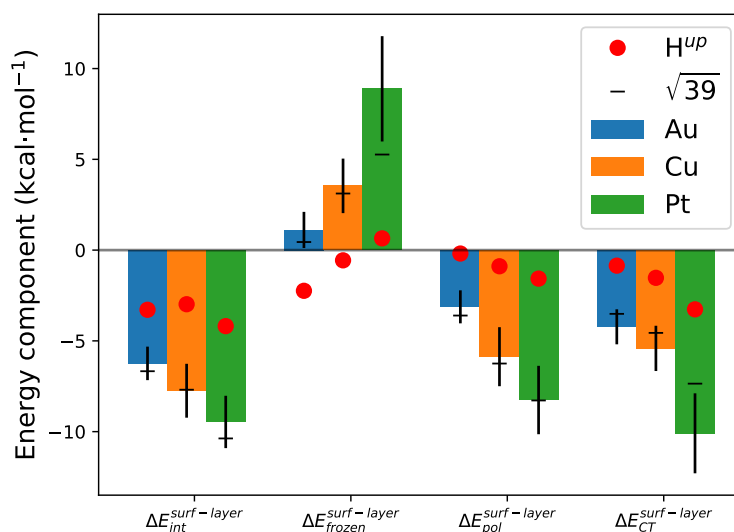


Figure 5.4 – Average (per water molecule) contributions of frozen, polarization, and charge-transfer to the total interaction energy between water structures (oligomer of adlayer) and metal surfaces. The error bar gives the standard deviation among all the 28 considered systems. Red dots give the specific values for the H^{up} layers and horizontal dashes, those for the $\sqrt{39}$ layers.

consequence, the water–water CT does not directly contribute to the studied energy difference: the “frozen” term, $\Delta E_{frozen}^{surf-layer}$, solely accounts for the electrostatic, steric and dispersion interaction between the adlayer and the metal surface. The polarization term $\Delta E_{pol}^{surf-layer}$ is mainly composed of the polarization of the metallic surface and the adlayer, but also contains a response of the water–water interaction due to this polarization. Finally, the charge-transfer contribution $\Delta E_{CT}^{surf-layer}$ captures the charge-transfer between the metal surface and the adlayers and its repercussions on the water–water interaction (see Fig. D.9 for a visualization). To simplify the discussion, we will only discuss the case of three metals: Pt, Cu and Au. Indeed, the corresponding values for Pd resemble Pt very closely and the same is true for the couple Ag and Au. On the other hand, we enrich the discussion by including oligomeric clusters on the surface (see Fig D.4 and D.5), in order to deduce more general trends than just observation of the five ice adlayers. The oligomers offer a larger diversity of structural motives than the five adlayers. Furthermore, compared with the periodic adlayers that need to be stretched or compressed to fit into the unit cell, the oligomers can relax and accommodate more easily the various lattice constants.

Fig. 5.4 reports average energies per water molecule for the interaction energy and its components. As expected based on the single molecule adsorption²⁵, the average interaction energy is largest for Pt ($-9.5 \text{ kcal}\cdot\text{mol}^{-1}$) and smallest for Au ($-6.2 \text{ kcal}\cdot\text{mol}^{-1}$). Note, that this is less than the single molecule adsorption (-10.6 and $-7.5 \text{ kcal}\cdot\text{mol}^{-1}$), indicating that the net effect

Chapter 5. Water adlayers on noble metal surfaces: Insights from energy decomposition analysis

of high coverage is slightly repulsive.

When moving to the components, we can first note a general trend for all components to be, in absolute value, more important for Pt than for Cu, than for Au. For instance, the steric repulsion, at the origin of the positive sign for $\Delta E_{frozen}^{surf-layer}$, is highest for Pt and almost zero for Au. This can be traced back to “geometrical” reasons, with a mean distance Au–O of 3.20 Å vs. Pt–O of 2.98 Å, which is a consequence of the overall stronger adsorption on Pt, which leads to shorter internuclear distances. The origin of this strong difference in geometry, and thus steric repulsion, is mostly found in $\Delta E_{CT}^{surf-layer}$, which is more than twice for Pt compared to Au (-10.1 vs -4.2 kcal·mol⁻¹). The same proportion applies to the polarization energy, but overall, $\Delta E_{pol}^{surf-layer}$ is less stabilizing than $\Delta E_{CT}^{surf-layer}$, except for Cu, where they average to -5.9 and -5.4 kcal·mol⁻¹, respectively.

To give an illustration of the spread of the individual components and the profound difference between H^{up} compared to the other ice adlayers, let us discuss them at the example of Pt(111), even though the observations and conclusions for the other metal surfaces would barely differ. First, many water molecules in the ice adlayers are not adsorbed in the optimal single molecule geometry. This contributes to a lowering of the repulsion ($\Delta E_{frozen}^{surf-layer}$) for the ice adlayers compared to the average (4.6 vs. 8.9 kcal·mol⁻¹). For H^{up} this repulsion is even only 0.6 kcal·mol⁻¹, illustrating the little steric hindrance between the ice-layer and the metal surface. The polarization energy is similarly small for H^{up} (-1.6 kcal·mol⁻¹) while the two H^{down} adlayers feature $\Delta E_{pol}^{surf-layer} \approx -5$ kcal·mol⁻¹. $\Delta E_{pol}^{surf-layer}$ reaches even ~ -8 kcal·mol⁻¹ for the more complex $\sqrt{37}$ and $\sqrt{39}$ structures, a value that compares well to an average of -8.3 kcal·mol⁻¹ for all 28 systems considered. The situation for the charge-transfer, $\Delta E_{CT}^{surf-layer}$, is close to the observations for $\Delta E_{pol}^{surf-layer}$, *i.e.*, H^{up} only marginally benefits from CT ($\Delta E_{CT}^{surf-layer} = -3.3$ kcal·mol⁻¹), while the other structures are, with -7.8 kcal·mol⁻¹ somewhat shy of the average $\Delta E_{CT}^{surf-layer}$ of -10.1 kcal·mol⁻¹. These observations demonstrate that H^{up} behaves differently compared to the other adlayers. However, most of the other ice adlayers, and in particular the $\sqrt{37}$ and $\sqrt{39}$ structures which are the most stable ones, are closely related to adsorption patterns that can be mimicked via oligomers. Indeed, especially on Au and Cu metallic surfaces, the specific value of the energetic components of the surface-layer interaction for the $\sqrt{39}$ structure (for example) is found within the standard deviation among all considered systems. On Pt, however, the $\sqrt{39}$ layer exhibits a lower than average $\Delta E_{frozen}^{surf-layer}$ (5.3 kcal·mol⁻¹ against 8.9 kcal·mol⁻¹). A similar behavior, but with opposite sign, is observed for $\Delta E_{CT}^{surf-layer}$, so that $\Delta E_{int}^{surf-layer}$ is found within the standard deviation. Consequently, the $\sqrt{39}$ structure is a very stable adlayer that is well represented by oligomers.

The comparison of $\sqrt{37}$ and H^{up} based on energetic quantities could not have been deduced from the analysis of the flow of electron density as represented in Figs. D.9-D.11. This is in

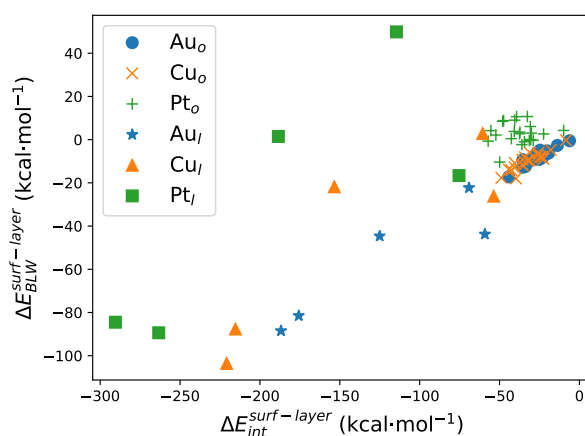


Figure 5.5 – The interaction of the water subsystem with the metal surface at the BLW level, $\Delta E_{BLW}^{surf-layer}$, is plotted against the corresponding total interaction energy, $\Delta E_{int}^{surf-layer}$. The oligomers (o) and adlayers (l) are given by separated symbols. The (l) point most left and right corresponds to $\sqrt{39}$ and H^{up} , respectively.

full agreement with our previous study on molecular complexes, where we demonstrated that the electron flow and the associated interaction strength are not directly related.⁶⁴ In the case of $\sqrt{39}$, the explanation is particularly simple: Even though the overall workfunction is barely affected by the nearly vanishing surface dipole moment, this global property hides the complexity of the local charge rearrangements, associated with the polarization and charge-transfer (see Fig. D.9).

From the perspective of designing a force field, the most important question at this point is if the charge-transfer energy between the ice-like layer and the metallic surface is indeed required. Hence, Fig. 5.5 reports the interaction energy of the water subsystem with the metal surface when charge-transfer is neglected ($\Delta E_{BLW}^{surf-layer}$) as a function of the total interaction energy ($\Delta E_{int}^{surf-layer}$). To better distinguish the behavior of the oligomers (o) and the complete ice adlayers (l), the two groups are depicted with different symbols, but using the same color. For the oligomers (o) Fig. 5.5 it is evident that for Pt (green) there is no relation between the BLW (polarization-only) and the total interaction energy. However, for Cu (orange) and Au (blue), where the role of CT is less important, there is a reasonable correlation between the two quantities, suggesting that relative adsorption energies could already be estimated at the BLW level. The BLW computations could benefit from a significant speedup due to its (near) linear scaling, dramatically reducing the computational cost of sampling phase space at the metal/liquid interface. When considering the ice adlayers (l) we first see a rough correlation for all three metals which supports the suggestion that CT might not be necessary for relative energies at the metal/liquid interface. At a closer look, the value for H^{up} point (rightmost points of the (l) series) does not fit in the correlation for any of the metals.

Chapter 5. Water adlayers on noble metal surfaces: Insights from energy decomposition analysis

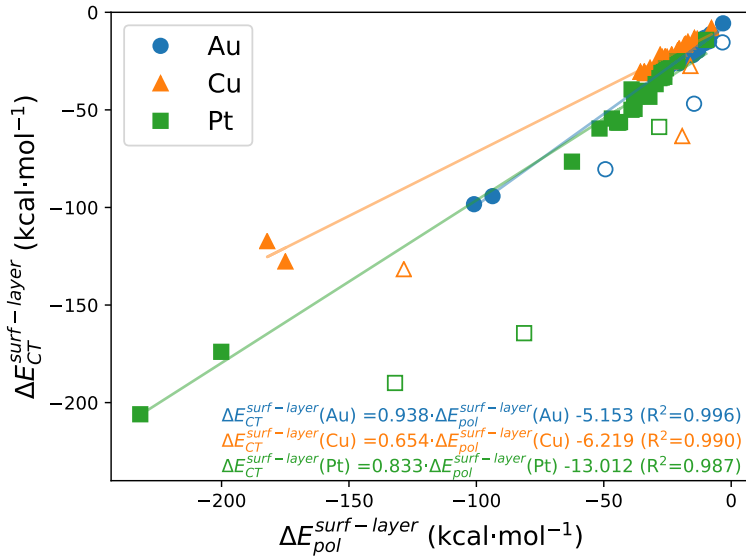


Figure 5.6 – Correlation of $\Delta E_{CT}^{surf-layer}$ with $\Delta E_{pol}^{surf-layer}$. The empty symbols correspond to the three outlier adlayers (H^{up} , H^{down} and chain- H^{down}) which are excluded from the correlation.

Apparently, H^{up} has a non-typical behavior, meaning its properties are significantly different from other water arrangements on noble metal surfaces. We, therefore, advise against its use in practical applications as a model for the water/metal interface.

Even if in the absence of CT a good correlation with $\Delta E_{int}^{surf-layer}$ can be obtained, in absolute terms it cannot be neglected: $\Delta E_{int}^{surf-layer}$ in the absence of CT, *i.e.*, $\Delta E_{BLW}^{surf-layer}$, is not even stabilizing for Pt and only mildly so for Cu and Au (see Fig. 5.5). This demonstrates that $\Delta E_{CT}^{surf-layer}$ is a significant term over all the metals and most important on Pt. Platinum is known to be more oxophilic than Au and Cu, which is also seen in the water monomer binding energy, which is -10.6 for Pt(111) vs -8.5 and -7.5 kcal·mol⁻¹ for Cu and Au, respectively. This oxophilicity can explain the importance of CT over Pt(111). Strikingly, with the exception of the H^{up} , H^{down} and chain- H^{down} adlayers, $\Delta E_{CT}^{surf-layer}$ can be estimated from $\Delta E_{pol}^{surf-layer}$ (see Fig. 5.6). The slope of $\Delta E_{CT}^{surf-layer}$ vs $\Delta E_{pol}^{surf-layer}$ only slightly depends on the metal when excluding the “outliers”, which are H^{up} , H^{down} and chain- H^{down} . The slope is close to unity for Pt and Au, whereas it is only 0.7 for Cu. As shown in Fig. D.6, the basis set dependence of ΔE_{pol} and ΔE_{CT} of about ~ 10% is identical for all metals considered. The slope for Cu rises to 0.9 when excluding all ice adlayers, revealing once again the impact of the lattice mismatch. Hence, if an accurate prediction of the metal/water polarization energy could be found via an empirical force field, the corresponding charge-transfer term could be estimated without a detailed physical model. This possibility opens encouraging perspectives for the

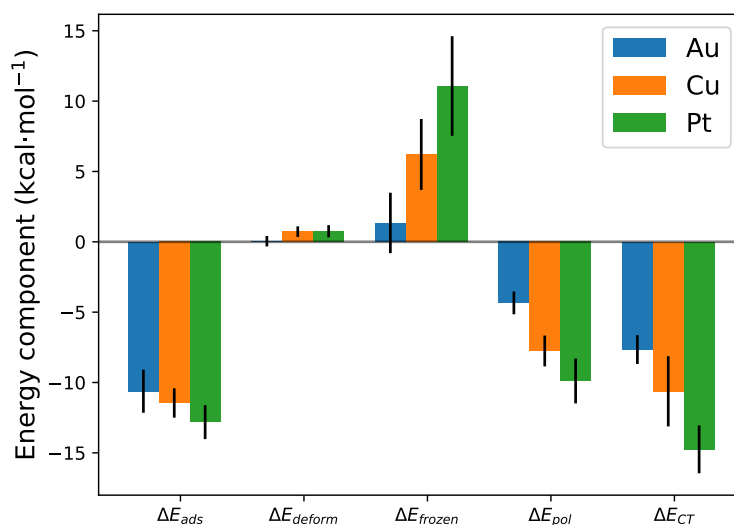


Figure 5.7 – Average (per water molecule) contributions of deformation, frozen, polarization, and charge-transfer to the total adsorption energy of water structures (oligomer of adlayer) on metal surfaces. The error bar gives the standard deviation among all the 28 considered systems.

next generation of water/metal force fields. Indeed, polarizable force fields for metals have been developed in the past,^{65–67} but rarely coupled to polarizable water models,⁶⁸ so that their full potential might not have been reached so far.^{21;69} Furthermore, only our current work quantifies the polarization energy that should be aimed at, an important quantity when fitting an empirical force field.

Adsorption energy of water at noble metal surfaces

Having established that the interaction energy between an ice adlayer, or just a water oligomer, and a noble metal surface can be expressed in terms of the frozen energy and a scaled polarization energy, we now tackle the more general question of the total adsorption energy on metal surface. ΔE_{ads} , (Eq. 5.2) accounts for all the many-body interaction terms, *i.e.*, the water–water many-body interactions that are already present in the absence of a metal surface,⁷⁰ the water–metal many-body interactions at the interface and, moreover, the change of the water–water interaction due to the presence of the metal surface.

To settle the stage, Fig. 5.7 represents the same kind of analysis for ΔE_{ads} , as Fig. 5.4 does for $\Delta E_{int}^{surf-layer}$, *i.e.*, the different interaction energy components per water molecule for each metal. The first, general, comment is that the two Figures look quite similar, with the same increase in absolute value of all terms when going from Au to Cu and then to Pt. The

Chapter 5. Water adlayers on noble metal surfaces: Insights from energy decomposition analysis

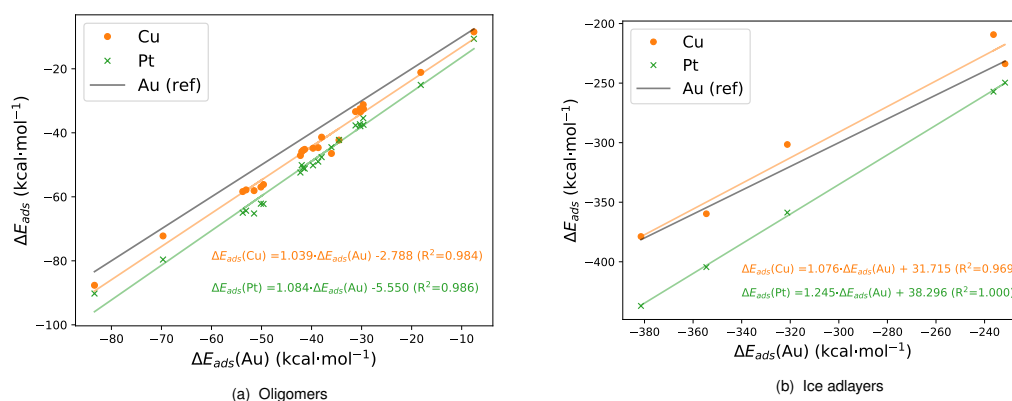


Figure 5.8 – The adsorption energy for oligomers (a) and ice adlayers (b) on Cu(111) and Pt(111) is plotted against the adsorption energy on Au(111).

additional energy contribution, ΔE_{deform} , turns out to be of minor importance overall (<1 kcal·mol⁻¹). Even for Cu(111) the deformation energy is not larger than for Pt, despite the more important lattice mismatch. This can be traced back to the relative rigidity of the water molecules compared to the softer hydrogen bond interactions between them. Hence, while the monomer geometry does not respond much to the unit cell, it is the assembly into an adlayer that has to adapt upon adsorption.

On average, ΔE_{ads} only differs by ~ 2 kcal·mol⁻¹ per water molecule between Au (weakest adsorption) and Pt (strongest adsorption), even though the magnitude of the major adsorption energy components differ by at least a factor of two. In order to uncover if this similarity is only true on average or if it is a “universality” of the interaction of water with any of the noble metal surface, Fig. 5.8 reports the correlation of adsorption energies on Pt(111) and Cu(111) with the more physisorption-like adsorption on Au(111). Due to the large absolute difference between the adsorption energies of oligomers (up to -90 kcal·mol⁻¹) and ice adlayers (up to -380 kcal·mol⁻¹), the two families of systems are separated. The oligomers (Fig. 5.8a) have slope close to unity and the intercept reflects the stronger adsorption of a single water molecule on Cu and Pt compared to Au(111). For the ice adlayers (Fig. 5.8b), Cu(111) is nearly indistinguishable from Au(111). The combination of the two figures clearly shows that even though water oligomers are more strongly bound on Cu(111) than on Au(111), the lattice-mismatch affects the water adlayers significantly. ΔE_{ads} for ice adlayers on Pt(111) is, with a slope of 1.24 against Au(111), stronger and indicative of additional stabilization on Pt(111) compared to the other noble metals and compared to the oligomers. This stabilization is presumably due to a combination of stronger chemisorption and a well-matching metal lattice.

Despite this seemingly simple distinction between adlayers and oligomers when analyzing

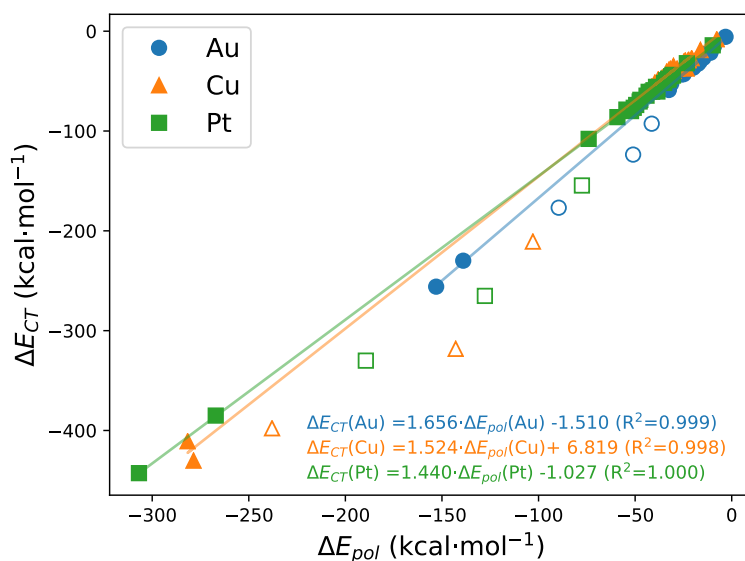


Figure 5.9 – The charge-transfer ΔE_{CT} is correlated to ΔE_{pol} for the adsorption energy. The empty symbols correspond to the three outlier adlayers (H^{up} , H^{down} and chain- H^{down}) which are excluded from the correlation.

the differences between metals, the individual components offer a complementary insight. In Fig. 5.9 we trace ΔE_{CT} as a function of ΔE_{pol} for the three metal surface. When excluding the three “exceptional” and energetically less stable ice adlayers (H^{up} , H^{down} and chain- H^{down}), a correlation with $R^2 > 0.99$ is obtained with slopes of about 1.5 for all three metals. This slope is higher compared to the near unity slope from Fig. 5.6, where only the interaction between the adlayer and the metal surface was analyzed. The origin of the difference is two-fold: first and foremost, the water–water interaction, which is directly present in the scaling of Fig. 5.9, features a comparably stronger CT component with respect to the polarization energy. Second, Fig. 5.9 also contains the full cooperativity between water–water and water–metal interactions, which are quantified in more details in the next subsection. The variation of slope between Fig. 5.9 and Fig. 5.6 nicely illustrates that even though charge-transfer and polarization are related (with the former vanishing in the complete basis set limit), the precise relationship between the two components depends on the nature of the probed interaction. The linear correlation of Fig. 5.9 means that ΔE_{pol} is sufficient to retrieve the complex many-body physics of ΔE_{CT} , even including the water–water interaction. Therefore, modelling the polarization energy in the absence of charge-transfer should be enough to capture the essential features for the full adsorption energies ΔE_{ads} .

Non-Additivity and Cooperativity of Water–Water–Metal Many-Body Interactions

Operationally, modification of the water–water interaction at the metal interface cannot be distinguished from the modification of the water–metal interaction due to the presence of co-adsorbed water molecules. We first quantify and compare the non-additivity of the interaction energy ($\Delta E_{int}^{NonAdd} = \Delta E_{frozen}^{NonAdd} + \Delta E_{pol}^{NonAdd} + \Delta E_{CT}^{NonAdd}$) for oligomers on Pt(111) and Au(111). The non-additivity (Eq. 5.10) measures the difference in the interaction energy between the sum of single water molecules interacting with the surface and the assembly of all water molecules interacting with the metal surface.

For the oligomers, ΔE_{int}^{NonAdd} contributes to more than 30% to the total interaction energy. In other words, the non-additivity is significant for a quantitative understanding of the interactions at the metal/water interface. Fig. D.7 demonstrates, however, that ΔE_{int}^{NonAdd} correlates ($R^2 = 0.93$ and slope of almost unity) between the two extreme metals, Au (weak adsorption) and Pt (strong adsorption), suggesting that it is a “universal” quantity. The components of ΔE_{int}^{NonAdd} do not all behave the same: The repulsive frozen term is very weakly correlated ($R^2 \approx 0.5$), but noticeably smaller for Au than for Pt (roughly one third). This is to be expected since the water molecules are further away from the surface on Au than on Pt. It is the non-additive charge-transfer and polarization energies that correlated between Pt and Au and thus bring about the correlation between the metals.

We now unravel the origin of the non-additivity in terms of contributing components. Overall, $\Delta E_{frozen}^{NonAdd}$ is destabilizing while both the polarization and charge-transfer energies are stabilizing the adlayer and are responsible for $\sim 40\%$ and 60% of $\Delta E_{int}^{NonAdd} - \Delta E_{frozen}^{NonAdd}$ (*i.e.* the stabilizing component), respectively and are correlated with each other ($R^2 = 0.98$). The major exception to this trend is, again, the H^{up} layer for which the frozen interaction is attractive, but the polarization and charge transfer provide less additional stability compared to the average.

Having established the “universal” character of the non-additivity interaction, we now focus on the case of Pt(111) to obtain a geometric understanding of its origin. Since the structures are essentially two-dimensional, we do not simply determine the coordination number,⁷¹ but perform a directional analysis: in each structure, the H-bond (H \cdots O distance below 2.5 Å) acceptors are identified. Then, they are classified according to the Pt–O distance (<3.0 Å for chemisorbed water molecules, > 3.0 Å for physisorbed molecules). Two angles are additionally introduced to describe the water orientation with respect to the surface, namely the cartwheel angle θ and the propeller angle ϕ (see Fig 5.10 for a graphical definition). These angles describe, respectively, the angle between the dipole of water and the normal to the surface, and the rotation of the hydrogen pair around the dipole of water, following our previous studies on the development of water–metal surface force fields.^{21;53} The value of θ is zero when the dipole is pointing away from the surface and rises when the molecule is bending toward the surface. Also, a value of ϕ of 0° indicates that the two hydrogen are equally close to the surface, while a

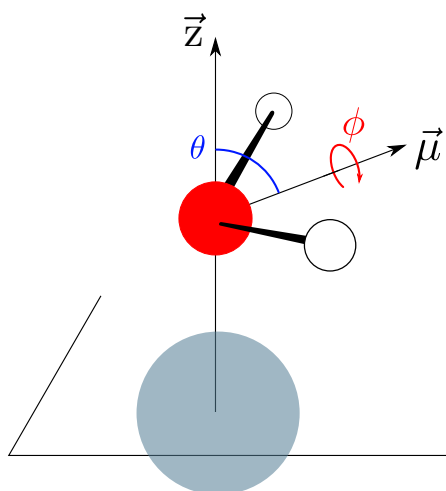


Figure 5.10 – Representation of the cartwheel (θ) and propeller (ϕ) angles used to describe the orientation of water molecules toward the surface. μ is the dipole of the water molecule. $\theta = 0^\circ$ when μ is aligned with the z axis, $\phi = 0^\circ$ when the two hydrogens are at an equal distance to the surface.

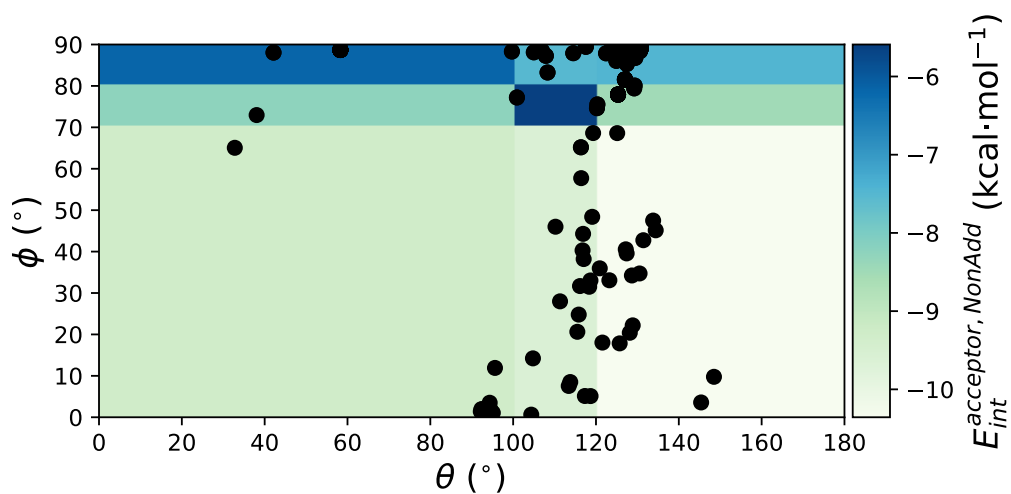


Figure 5.11 – Representation of the non-additive energy contribution of physisorbed H-bond acceptors as a function of their θ and ϕ characteristics. Dots indicate the observed points. The data is also available in Table D.1

Chapter 5. Water adlayers on noble metal surfaces: Insights from energy decomposition analysis

value of 180° indicate that the difference in distance to the surface between the two hydrogen is maximal.

In order to simplify the analysis, the two-dimensional space spanned by θ and ϕ is divided into 9 rectangles for the physisorbed water molecules. The limits of these rectangles are optimized to find the optimal linear model reproducing the non-additivity for all 27 structures, *i.e.*, including the ice adlayers. For the chemisorbed molecules, only two combinations are necessary (see Table D.1). The root mean square error of this linear regression amounts to $1.37 \text{ kcal}\cdot\text{mol}^{-1}$ (see Fig. D.8), demonstrating the good predictive power of this simple model. The advantage of the linear model is that we also identify the geometrical arrangements that are responsible for the non-additivity. The corresponding energy coefficients for chemisorbed molecules (see Table D.1) indicate that the typical adsorption minimum of a single water molecule ($\theta \approx 80^\circ, \phi \approx 0^\circ, \text{Pt-O} \approx 2.5\text{\AA}$) is the worst H-bond acceptor ($\Delta E_{int}^{acceptor, NonAdd} = -3.0 \text{ kcal}\cdot\text{mol}^{-1}$), *i.e.*, does not contribute significantly to the non-additivity. This is compatible with the observation that the oxygen atom is already interacting with the metal surface via its lone-pairs. Therefore, its electrons are less available to interact with a third hydrogen atom. In contrast, the typical building block of the ice-like layers, where the chemisorbed water molecule is tilted so that the hydrogens are pointing away from the surface ($\theta \approx 50^\circ, \phi \approx 0, \text{Pt-O} \approx 2.5\text{\AA}$) is a better H-bond acceptor ($-5.4 \text{ kcal}\cdot\text{mol}^{-1}$). The best H-bond acceptors are, however, not chemisorbed to the surface but physisorbed ($\text{Pt-O} > 3.0$), and present all small ϕ values ($< 70^\circ$), meaning that the two hydrogens are at somewhat similar distances from the surface. The very best region ($-10.4 \text{ kcal}\cdot\text{mol}^{-1}$) is found for $\theta > 120^\circ$, which corresponds to two hydrogens pointing toward the surface, but with a lone pair of the oxygen atom pointing in the direction of the surface, and thus, towards a potential H-bond donor. A more in-depth study on model systems would be necessary in order to deduce clearer trends and adapted functional forms to reproduce these trends in an empirical force field. Nevertheless, based on Fig. 5.11 it is clear that a strategy based on correction maps (CMAPs) as introduced for protein backbone angles,⁷² could successfully retrieve the non-additivity contributions. The only extension to the CMAP approach would be the introduction of a distance dependence, in analogy to the θ dependence introduced in our GAL forcefields.^{21;53}

The synergy between water–water charge transfer and water–metal charge transfer

The synergistic energy can be defined as

$$\Delta E_{CT}^{syn} = \Delta E_{CT}^{NonAdd} - E_{CT} \left(\bigcup_i W_i \right) = \Delta E_{CT} - \sum_i^n \Delta E_{CT}(W_i, surf) - E_{CT} \left(\bigcup_i W_i \right) \quad (5.12)$$

which represents the CT-associated energetic difference between, on one hand, the overall CT and, and on the other hand, the sum of each individual charge transfer between a single water molecule and the surface plus the charge transfer within the isolated water layer. This synergy

is therefore positive (destabilizing) if there is a competition between these charge transfers and negative for (stabilizing) cooperativity. Overall, cooperativity is found with $\Delta E_{CT}^{syn} = -1.37$ kcal·mol⁻¹ per water molecule on average for Pt and -0.57 kcal·mol⁻¹ for Au. For H^{up}, however, ΔE_{CT}^{syn} is positive for both Pt and Au (1.1 and 0.5 kcal·mol⁻¹ per water molecule, respectively). On the opposite, the most stable layers ($\sqrt{37}$, $\sqrt{39}$) are the ones where this cooperation is higher, with also small net dipole moments and large contributions due to polarization.

This observation is in full agreement with our discussion in sec. 5.4.3, where we have highlighted the important density reorganizations of $\sqrt{39}$ that, nevertheless, lead to a small surface dipole moment.

5.5 Conclusion

The detailed analysis of the electronic and geometrical characteristics of 28 diverse water arrangements (from monomer to ice adlayers) over the (111) surface of five noble metals (Cu, Ag, Au, Pd and Pt) has allowed to identify trends and key factors for the stability of water arrangements on metallic surfaces. We identified dense-packed layers to be the most stable structures, like the $\sqrt{39} \times \sqrt{39}$ unit cell for Ag, Au, Pd and Pt and the $\sqrt{37} \times \sqrt{37}$ unit-cell for Cu. This stability was found to correspond to the smallest change of workfunction upon adsorption. The H^{down} and H^{up} structures, which are often cited as model structure for water/metal interfaces, are less stable and lead to workfunction changes up to 3 eV.

The energy decomposition analysis, relying on the block localized wave function (BLW), shows that the charge-transfer from water to the surface is overall nearly independent from the charge-transfer between the water molecules, the latter being key for the H-bonding. ΔE_{CT} , which is the computationally most costly term, is found to be linearly correlated to ΔE_{pol} . Hence, it can be predicted at minimal cost. As a consequence, the polarization energy can be seen as the most important contribution to the adsorption energy.

Remarkably, the polarization energy provides about 40% additional stability at the interface compared to the single water molecule adsorption, and displays a strong correlation with its charge-transfer counterpart ($R^2 = 0.99$ on Pt(111)). This is good news for force field developments, where models for the polarization energy could be included to capture the many-body effects. Alternatively, this cooperativity can be largely reproduced by an additive model based on the geometric parameters of the H-bond acceptor molecule. In summary, our investigation highlights the closely related physics that governs the various noble-metal – water interaction and suggests that polarization energies should be enough to retrieve most of the complex many-body interactions at the metal/water interface.

Bibliography

- [1] Doering, D. L.; Madey, T. E. The adsorption of water on clean and oxygen-dosed Ru(011). *Surf. Sci.* **1982**, *123*, 305–337.
- [2] Glebov, A.; Graham, A. P.; Menzel, A.; Toennies, J. P. Orientational ordering of two-dimensional ice on Pt(111). *J. Chem. Phys.* **1997**, *106*, 9382–9385.
- [3] Nie, S.; Feibelman, P. J.; Bartelt, N. C.; Thürmer, K. Pentagons and Heptagons in the First Water Layer on Pt(111). *Phys. Rev. Lett.* **2010**, *105*, 026102.
- [4] Carrasco, J.; Hodgson, A.; Michaelides, A. A molecular perspective of water at metal interfaces. *Nat. Mater.* **2012**, *11*, 667–674.
- [5] Ogasawara, H.; Brena, B.; Nordlund, D.; Nyberg, M.; Pelmenchikov, A.; Pettersson, L. G. M.; Nilsson, A. Structure and Bonding of Water on Pt(111). *Phys. Rev. Lett.* **2002**, *89*, 276102.
- [6] Rossmeisl, J.; Norskov, J. K.; Taylor, C. D.; Janik, M. J.; Neurock, M. Calculated Phase Diagrams for the Electrochemical Oxidation and Reduction of Water over Pt(111). *J. Phys. Chem. B* **2006**, *110*, 21833–21839.
- [7] Schnur, S.; Groß, A. Properties of metal–water interfaces studied from first principles. *New J. Phys.* **2009**, *11*, 125003.
- [8] Schiros, T.; Andersson, K.; Pettersson, L.; Nilsson, A.; Ogasawara, H. Chemical bonding of water to metal surfaces studied with core-level spectroscopies. *J. Electron Spectrosc. Relat. Phenom.* **2010**, *177*, 85–98.
- [9] Filhol, J.-S.; Doublet, M.-L. An ab initio study of surface electrochemical disproportionation: The case of a water monolayer adsorbed on a Pd(111) surface. *Electrocatalysis* **2013**, *202*, 87–97.
- [10] Vassilev, P.; van Santen, R. A.; Koper, M. T. M. Ab initio studies of a water layer at transition metal surfaces. *J. Chem. Phys.* **2005**, *122*, 054701, Publisher: American Institute of Physics.
- [11] Björneholm, O.; Hansen, M. H.; Hodgson, A.; Liu, L.-M.; Limmer, D. T.; Michaelides, A.; Pedevilla, P.; Rossmeisl, J.; Shen, H.; Tocci, G.; Tyrode, E.; Walz, M.-M.; Werner, J.; Bluhm, H. Water at Interfaces. *Chem. Rev.* **2016**, *116*, 7698–7726.
- [12] Desai, S. K.; Pallassana, V.; Neurock, M. A Periodic Density Functional Theory Analysis of the Effect of Water Molecules on Deprotonation of Acetic Acid over Pd(111). *J. Phys. Chem. B* **2001**, *105*, 9171–9182, Publisher: American Chemical Society.

- [13] Filhol, J.-S.; Neurock, M. Elucidation of the Electrochemical Activation of Water over Pd by First Principles. *Angew. Chem. Int. Ed.* **2006**, *45*, 402–406, _eprint: <https://onlinelibrary.wiley.com/doi/pdf/10.1002/ange.200502540>.
- [14] Skúlason, E.; Karlberg, G. S.; Rossmeisl, J.; Bligaard, T.; Greeley, J.; Jonsson, H.; Norskov, J. K. Density functional theory calculations for the hydrogen evolution reaction in an electrochemical double layer on the Pt(111) electrode. *Phys. Chem. Chem. Phys.* **2007**, *9*, 3241–3250.
- [15] Tian, F.; Jinnouchi, R.; Anderson, A. B. How Potentials of Zero Charge and Potentials for Water Oxidation to OH(ads) on Pt(111) Electrodes Vary With Coverage. *J. Phys. Chem. C* **2009**, *113*, 17484–17492, Publisher: American Chemical Society.
- [16] Hussain, J.; Jónsson, H.; Skúlason, E. Calculations of Product Selectivity in Electrochemical CO₂ Reduction. *ACS Catal.* **2018**, *8*, 5240–5249.
- [17] Mathew, K.; Kolluru, V. S. C.; Mula, S.; Steinmann, S. N.; Hennig, R. G. Implicit self-consistent electrolyte model in plane-wave density-functional theory. *J. Chem. Phys.* **2019**, *151*, 234101.
- [18] Steinmann, S. N.; Sautet, P.; Michel, C. Solvation free energies for periodic surfaces: comparison of implicit and explicit solvation models. *Phys. Chem. Chem. Phys.* **2016**, *18*, 31850–31861.
- [19] Hibbitts, D. D.; Loveless, B. T.; Neurock, M.; Iglesia, E. Mechanistic Role of Water on the Rate and Selectivity of Fischer-Tropsch Synthesis on Ruthenium Catalysts. *Angew. Chem. Int. Ed.* **2013**, *52*, 12273–12278.
- [20] Schweitzer, B.; Steinmann, S. N.; Michel, C. Can microsolvation effects be estimated from vacuum computations? A case-study of alcohol decomposition at the H₂O/Pt(111) interface. *Phys. Chem. Chem. Phys.* **2019**, *21*, 5368–5377.
- [21] Steinmann, S. N.; Ferreira De Moraes, R.; Götz, A. W.; Fleurat-Lessard, P.; Iannuzzi, M.; Sautet, P.; Michel, C. Force Field for Water over Pt(111): Development, Assessment, and Comparison. *J. Chem. Theory Comput.* **2018**, *14*, 3238–3251.
- [22] Carrasco, J.; Michaelides, A.; Scheffler, M. Insight from first principles into the nature of the bonding between water molecules and 4d metal surfaces. *J. Chem. Phys.* **2009**, *130*, 184707.
- [23] Michaelides, A.; Ranea, V. A.; de Andres, P. L.; King, D. A. General Model for Water Monomer Adsorption on Close-Packed Transition and Noble Metal Surfaces. *Phys. Rev. Lett.* **2003**, *90*, 216102.

Chapter 5. Water adlayers on noble metal surfaces: Insights from energy decomposition analysis

- [24] Schiros, T.; Ogasawara, H.; Näslund, L.-Å.; Andersson, K. J.; Ren, J.; Meng, S.; Karlberg, G. S.; Odellius, M.; Nilsson, A.; Pettersson, L. G. M. Cooperativity in Surface Bonding and Hydrogen Bonding of Water and Hydroxyl at Metal Surfaces. *J. Phys. Chem. C* **2010**, *114*, 10240–10248.
- [25] Carrasco, J.; Klimeš, J.; Michaelides, A. The role of van der Waals forces in water adsorption on metals. *J. Chem. Phys.* **2013**, *138*, 024708, Publisher: American Institute of Physics.
- [26] Carrasco, J.; Santra, B.; Klimeš, J.; Michaelides, A. To Wet or Not to Wet? Dispersion Forces Tip the Balance for Water Ice on Metals. *Phys. Rev. Lett.* **2011**, *106*, 026101.
- [27] Mo, Y.; Gao, J.; Peyerimhoff, S. D. Energy decomposition analysis of intermolecular interactions using a block-localized wave function approach. *J. Chem. Phys.* **2000**, *112*, 5530–5538.
- [28] Khaliullin, R. Z.; Bell, A. T.; Head-Gordon, M. Analysis of charge transfer effects in molecular complexes based on absolutely localized molecular orbitals. *J. Chem. Phys.* **2008**, *128*, 184112.
- [29] Steinmann, S. N.; Vogel, P.; Mo, Y.; Corminboeuf, C. The norbornene mystery revealed. *Chem. Commun.* **2011**, *47*, 227–229.
- [30] Elgabarty, H.; Khaliullin, R. Z.; Kuhne, T. D. Covalency of hydrogen bonds in liquid water can be probed by proton nuclear magnetic resonance experiments. *Nat. Commun.* **2015**, *6*.
- [31] Philipsen, P. H. T.; Baerends, E. J. Role of the Fermi Surface in Adsorbate-Metal Interactions: An Energy Decomposition Analysis. *J. Phys. Chem. B* **2006**, *110*, 12470–12479.
- [32] Pecher, L.; Laref, S.; Raupach, M.; Tonner, R. Ethers on Si(001): A Prime Example for the Common Ground between Surface Science and Molecular Organic Chemistry. *Angew. Chem. Int. Ed.* **2017**, *56*, 15150–15154.
- [33] Staub, R.; Iannuzzi, M.; Khaliullin, R. Z.; Steinmann, S. N. Energy Decomposition Analysis for Metal Surface? @ SAdsorbate Interactions by Block Localized Wave Functions. *J. Chem. Theory Comput.* **2019**, *15*, 265–275.
- [34] Parr, R. G.; Ayers, P. W.; Nalewajski, R. F. What Is an Atom in a Molecule? *J. Phys. Chem. A* **2005**, *109*, 3957–3959.
- [35] Bader, R. F. W. Letter to the editor: Quantum mechanics, or orbitals? *Int. J. Quantum Chem.* **2003**, *94*, 173–177.
- [36] Zhao, L.; Hermann, M.; Schwarz, W. H. E.; Frenking, G. The Lewis electron-pair bonding model: modern energy decomposition analysis. *Nat Rev Chem* **2019**, *3*, 48–63.

- [37] Stoll, H.; Wagenblast, G.; Preuss, H. On the use of local basis sets for localized molecular orbitals. *Theor. Chim. Acta* **1980**, *57*, 169–178.
- [38] Mo, Y.; Peyerimhoff, S. D. Theoretical analysis of electronic delocalization. *J. Chem. Phys.* **1998**, *109*, 1687–1697.
- [39] Steinmann, S. N.; Jana, D. F.; Wu, J. I.-C.; Schleyer, P. v. R.; Mo, Y.; Corminboeuf, C. Direct Assessment of Electron Delocalization Using NMR Chemical Shifts. *Angew. Chem. Int. Ed.* **2009**, *48*, 9828–9833.
- [40] Demerdash, O.; Mao, Y.; Liu, T.; Head-Gordon, M.; Head-Gordon, T. Assessing many-body contributions to intermolecular interactions of the AMOEBA force field using energy decomposition analysis of electronic structure calculations. *J. Chem. Phys.* **2017**, *147*, 161721.
- [41] Khaliullin, R. Z.; VandeVondele, J.; Hutter, J. Efficient Linear-Scaling Density Functional Theory for Molecular Systems. *J. Chem. Theory Comput.* **2013**, *9*, 4421–4427.
- [42] Martín Pendás, A.; Blanco, M. A.; Francisco, E. The nature of the hydrogen bond: A synthesis from the interacting quantum atoms picture. *J. Chem. Phys.* **2006**, *125*, 184112, Publisher: American Institute of Physics.
- [43] Arunan, E.; Desiraju, G. R.; Klein, R. A.; Sadlej, J.; Scheiner, S.; Alkorta, I.; Clary, D. C.; Crabtree, R. H.; Dannenberg, J. J.; Hobza, P.; Kjaergaard, H. G.; Legon, A. C.; Mennucci, B.; Nesbitt, D. J. Defining the hydrogen bond: An account (IUPAC Technical Report). *Pure Appl. Chem.* **2011**, *83*, 1619–1636, Publisher: De Gruyter Section: Pure and Applied Chemistry.
- [44] Boys, S. F.; Bernardi, F. The calculation of small molecular interactions by the differences of separate total energies. Some procedures with reduced errors. *Mol. Phys.* **1970**, *19*, 553–566.
- [45] Khaliullin, R. Z.; Cobar, E. A.; Lochan, R. C.; Bell, A. T.; Head-Gordon, M. Unravelling the Origin of Intermolecular Interactions Using Absolutely Localized Molecular Orbitals. *J. Phys. Chem. A* **2007**, *111*, 8753–8765.
- [46] Steinmann, S. N.; Corminboeuf, C.; Wu, W.; Mo, Y. Dispersion-Corrected Energy Decomposition Analysis for Intermolecular Interactions Based on the BLW and dDXDM Methods. *J. Phys. Chem. A* **2011**, *115*, 5467–5477.
- [47] Khaliullin, R. Z.; Bell, A. T.; Head-Gordon, M. Electron Donation in the Water-Water Hydrogen Bond. *Chem. Eur. J.* **2009**, *15*, 851–855.
- [48] Horn, P. R.; Mao, Y.; Head-Gordon, M. Probing non-covalent interactions with a second generation energy decomposition analysis using absolutely localized molecular

Chapter 5. Water adlayers on noble metal surfaces: Insights from energy decomposition analysis


- orbitals. *Phys. Chem. Chem. Phys.* **2016**, *18*, 23067–23079, Publisher: The Royal Society of Chemistry.
- [49] Kresse, G.; Hafner, J. Ab initio molecular dynamics for liquid metals. *Phys. Rev. B* **1993**, *47*, 558.
- [50] Kresse, G.; Furthmüller, J. Efficient iterative schemes for ab initio total-energy calculations using a plane-wave basis set. *Phys. Rev. B* **1996**, *54*, 11169.
- [51] Klimes, J.; Bowler, D. R.; Michaelides, A. Chemical accuracy for the van der Waals density functional. *J. Phys.: Condens. Matter* **2010**, *22*, 022201.
- [52] Gautier, S.; N. Steinmann, S.; Michel, C.; Fleurat-Lessard, P.; Sautet, P. Molecular adsorption at Pt(111). How accurate are DFT functionals? *Phys. Chem. Chem. Phys.* **2015**, *17*, 28921–28930.
- [53] Clabaut, P.; Fleurat-Lessard, P.; Michel, C.; Steinmann, S. N. Ten Facets, One Force Field: The GAL19 Force Field for Water–Noble Metal Interfaces. *J. Chem. Theory Comput.* **2020**, *16*, 4565–4578, Publisher: American Chemical Society.
- [54] Blochl, P. E. Projector augmented-wave method. *Phys. Rev. B* **1994**, *50*, 17953.
- [55] Kresse, G.; Joubert, D. From ultrasoft pseudopotentials to the projector augmented-wave method. *Phys. Rev. B* **1999**, *59*, 1758.
- [56] Wang, P.; Steinmann, S. N.; Fu, G.; Michel, C.; Sautet, P. Key Role of Anionic Doping for H₂ Production from Formic Acid on Pd(111). *ACS Catal.* **2017**, *7*, 1955–1959.
- [57] VandeVondele, J.; Krack, M.; Mohamed, E.; Parrinello, M.; Chassaing, T.; Hutter, J. Quickstep: Fast and accurate density functional calculations using a mixed Gaussian and plane waves approach. *Comput. Phys. Commun.* **2005**, *167*, 103–128, WOS:000228421500005.
- [58] Hutter, J.; Iannuzzi, M.; Schiffmann, F.; VandeVondele, J. CP2K: atomistic simulations of condensed matter systems. *WIREs Comput Mol Sci* **2014**, *4*, 15–25.
- [59] VandeVondele, J.; Hutter, J. Gaussian basis sets for accurate calculations on molecular systems in gas and condensed phases. *J. Chem. Phys.* **2007**, *127*, 114105, WOS:000249667400011.
- [60] Goedecker, S.; Teter, M.; Hutter, J. Separable dual-space Gaussian pseudopotentials. *Phys. Rev. B* **1996**, *54*, 1703–1710, WOS:A1996UZ86100053.
- [61] Rumpitz, J. R.; Campbell, C. T. Adhesion Energies of Solvent Films to Pt(111) and Ni(111) Surfaces by Adsorption Calorimetry. *ACS Catal.* **2019**, *9*, 11819–11825.

- [62] Tyson, W.; Miller, W. Surface free energies of solid metals: Estimation from liquid surface tension measurements. *Surf. Sci.* **1977**, *62*, 267–276.
- [63] Mortensen, J. J.; Hammer, B.; Nørskov, J. K. Alkali Promotion of N_2 Dissociation over Ru(0001). *Phys. Rev. Lett.* **1998**, *80*, 4333–4336.
- [64] Steinmann, S. N.; Piemontesi, C.; Delachat, A.; Corminboeuf, C. Why are the Interaction Energies of Charge-Transfer Complexes Challenging for DFT? *J. Chem. Theory Comput.* **2012**, *8*, 1629–1640.
- [65] Siepmann, J. I.; Sprik, M. Influence of surface topology and electrostatic potential on water/electrode systems. *J. Chem. Phys.* **1995**, *102*, 511–524, Publisher: American Institute of Physics.
- [66] Iori, F.; Corni, S. Including image charge effects in the molecular dynamics simulations of molecules on metal surfaces. *J. Comput. Chem.* **2008**, *29*, 1656–1666.
- [67] Pensado, A. S.; Padua, A. A. H. Solvation and Stabilization of Metallic Nanoparticles in Ionic Liquids. *Angew. Chem. Int. Ed.* **2011**, *50*, 8683–8687.
- [68] Golze, D.; Iannuzzi, M.; Nguyen, M.-T.; Passerone, D.; Hutter, J. Simulation of Adsorption Processes at Metallic Interfaces: An Image Charge Augmented QM/MM Approach. *J. Chem. Theory Comput.* **2013**, *9*, 5086–5097.
- [69] Steinmann, S. N.; Fleurat-Lessard, P.; Götz, A. W.; Michel, C.; Ferreira de Morais, R.; Sautet, P. Molecular mechanics models for the image charge, a comment on “including image charge effects in the molecular dynamics simulations of molecules on metal surfaces”. *J. Comput. Chem.* **2017**, *38*, 2127–2129.
- [70] Reddy, S. K.; Straight, S. C.; Bajaj, P.; Huy Pham, C.; Riera, M.; Moberg, D. R.; Morales, M. A.; Knight, C.; Götz, A. W.; Paesani, F. On the accuracy of the MB-pol many-body potential for water: Interaction energies, vibrational frequencies, and classical thermodynamic and dynamical properties from clusters to liquid water and ice. *J. Chem. Phys.* **2016**, *145*, 194504, Publisher: American Institute of Physics.
- [71] Staub, R.; Steinmann, S. N. Parameter-free coordination numbers for solutions and interfaces. *J. Chem. Phys.* **2020**, *152*, 024124, [_eprint: https://doi.org/10.1063/1.5135696](https://doi.org/10.1063/1.5135696).
- [72] Mackerell, A. D.; Feig, M.; Brooks, C. L. Extending the treatment of backbone energetics in protein force fields: Limitations of gas-phase quantum mechanics in reproducing protein conformational distributions in molecular dynamics simulations. *J. Comput. Chem.* **2004**, *25*, 1400–1415.

Unravelling the link between hydration and adsorption on reactive oxide surfaces

Part III

In the following part, an additional step is taken in the complexity of water/solid interfaces with oxide surfaces. Indeed, such surfaces are subject to surface state changes at the same typical time scales as adsorption. Modeling adsorption on oxide surfaces requires therefore additional effort to sample the phase space of the surface itself. In chapter 6, the effect of an adsorbed xylitol at the γ -alumina/water interface on the hydrolysis mechanism of alumina is investigated. This study proves the major impact of the presence of an adsorbate on the surface state changes of an oxide. To complete this study, the adsorption of alcohols on the surface was studied in chapter 7, which revealed the complexity of the simulation of coupled degrees of freedom like adsorption and surface state changes. The later also compare different interface investigation techniques to highlight their differences and advantages.



6 Reactivity of shape-controlled crystals and metadynamics simulations

This Chapter is based on the following article: Reactivity of shape-controlled crystals and metadynamics simulations locate the weak spots of alumina in water, *Réocreux, R. and Girel, É. and Clabaut, P. and Tuel, A. and Besson, M. and Chaumonnot, A. and Cabiac, A. and Sautet, P. and Michel, C.*, **Nature Communications**, 2020, [10.1038/s41467-019-10981-9](https://doi.org/10.1038/s41467-019-10981-9)

abstract: The kinetic stability of any material in water relies on the presence of surface weak spots responsible for chemical weathering by hydrolysis. Being able to identify the atomistic nature of these sites and the first steps of transformation is therefore critical to master the decomposition processes. This is the challenge that we tackle here: combining experimental and modeling studies we investigate the stability of alumina in water. Exploring the reactivity of shape-controlled crystals, we identify experimentally a specific facet as the location of the weak spots. Using biased *ab initio* molecular dynamics, we recognise this weak spot as a surface exposed tetra-coordinated Al atom and further provide a detailed mechanism of the first steps of hydrolysis. This understanding is of great importance to heterogeneous catalysis where alumina is a major support. Furthermore, it paves the way to atomistic understanding of interfacial reactions, at the crossroad of a variety of fields of research.

6.1 Introduction

The kinetic stability of solids in water is governed by their reactivity at the interface. Being able to understand and control their surface stability and desired properties is therefore at the heart of a variety of research fields: kinetics of drug release¹, corrosion of metals and alloys², lithium batteries³, geochemistry⁴ with in particular the re-equilibration of solid phases in presence of a liquid⁵, water treatment⁶, heterogeneous catalysis^{7;8}, from the preparation^{9;10}, the utilization to the degradation of the catalyst^{11;12}, etc. Several parameters have been identified as key in all these fields: the solid phase (which polymorph)¹³, the nature of the surface exposed (kink, rugosity)⁴, and the species in solutions (additives, ions, pH)¹⁴⁻¹⁶. For instance, alumina is an oxide that is used in catalysis as a support for metallic nanoparticles¹⁷. Its γ allotrope (γ -Al₂O₃) in particular has remarkable properties as a support, long proven in the development of gas phase transformations¹⁸⁻²¹. However, water has detrimental effects on γ -Al₂O₃, either as a liquid¹² or even as steam²². While its polymorph α -Al₂O₃ is stable, γ -Al₂O₃ indeed transforms into various sorts of bulk hydroxides (AlO_xH_y) thereby seriously damaging the catalyst (decrease of surface area, sintering and encapsulation of catalytic particles)²³⁻²⁵. Albeit not fully described at the atomic scale yet, the decomposition of γ -Al₂O₃ was shown to proceed, at the macroscopic scale, through a sequential mechanism involving first dissolution of Al atoms, and then precipitation thereof into the undesired hydroxides^{24;26}. These structural changes can be retarded by tuning the surface chemical composition: silica deposition²⁷, presence of metallic nanoparticles¹², or impregnation with metal ions¹⁶. They are also impacted by the content of the solution: pH²⁴ but also presence of polyols²⁸ or polyphenols²⁵. The mechanism of action of these additives is believed to lie in their chemisorption on the surface that would make γ -Al₂O₃ water-resistant^{28;29}. However little is known on which exposed facet(s) and what site(s) need to be particularly targeted for protection. The optimization of the structure of inhibitors is therefore a challenging task since the exact mechanism of the decomposition of γ -Al₂O₃ in liquid water remains unknown. Whilst the sub-nanometric description of γ -Al₂O₃ is difficult to reach experimentally, molecular simulations have allowed for the development of insightful atomistic models for amorphous³⁰ and nano-crystalline³¹ γ -Al₂O₃. The model proposed by Digne *et al.*³¹, which was obtained from Density Functional Theory (DFT) calculations, has proven to depict properly the reactivity of the surface under various realistic gas phase conditions¹⁹. It is only recently that Ngouana-Wakou *et al.*³² and Réocreux *et al.*³³ have explored the interaction of γ -Al₂O₃ with liquid water, performing *ab initio* Molecular Dynamics (AIMD) simulations. Although these simulations give insights on the relative affinity of water for the different facets and the structuration and dynamics of the liquid at the interface, they cannot capture the details of the decomposition mechanism. Al-O bond formation and scissions are indeed rare events on the time scale achievable today with AIMD. To overcome this limitation and force the system to react along a chosen reaction coordinate, biased AIMD simulations are required. *Ab initio* metadynamics is an example of such methods³⁴, and has been commonly used to model the reactivity between molecules in

homogeneous media^{35;36} or between isolated molecules and a solid surface^{37;38}. Although common using classical force field for crystal growth and dissolution of molecular and ionic crystals^{39;40}, metadynamics has never been used to describe a reactive interface involving bonds with a partial covalent character (typically here Al-O and O-H bonds) hence requiring an *ab initio* description.

Here we combine experiments and theory to provide the atomistic mechanism for the early stage decomposition of γ -Al₂O₃ in liquid water. It was experimentally demonstrated that the decomposition is initiated at the (110) facet by exposing four samples of various shapes of nanoparticles to a hydrothermal treatment in presence of aqueous solution of inhibitors (xylitol and sorbitol) with varying concentrations. Performing *ab initio* metadynamics simulations, we probe the reactivity of the (110)/water interface and identify specific aluminum tetrahedral centers that are particularly reactive with water. We show that interfacial water molecules are involved in the mechanism, both as reactants for the hydration of aluminum and as intermediates for the proton reshuffling required by the decomposition mechanism. We show that the substitution of chemisorbed water molecules on the surface with xylitol locally renders the surface more hydrophobic and pushes water molecules away from the water-sensitive Al sites.

6.2 Methods

6.2.1 Atomistic model.

The model of γ -Al₂O₃/water interface was taken from our previous study on the characterization of interfacial water in contact with γ -Al₂O₃.³³ This model was built using the surface model proposed by Digne *et al.*⁴¹ (and further improved by Wischert *et al.*⁴²) and has been used for about 15 years to rationalize efficiently experimental data.¹⁹ The simulation cell consists of a 10 Å thick 2x2 unit cell of γ -Al₂O₃ (110), which is surmounted with a 20 Å thick water layer and another 10 Å thick layer of void to avoid spurious confinement effects⁴³.

6.2.2 Molecular simulations.

All *ab initio* molecular dynamics simulations (AIMD) reported here were performed using density functional theory (DFT) with the Gaussian and Plane Wave combined approach as implemented in CP2K/Quickstep⁴⁴⁻⁴⁷ using the same model and set of parameters as in our previous work on the γ -Al₂O₃(110)/water interface³³. The electrons were treated using the exchange correlation PBE functional⁴⁸ with a Grimme D3⁴⁹ correction. Core electrons were described using the Goedecker-Teter-Hutter (GTH) pseudo-potentials⁵⁰⁻⁵² and the valence density was developed on a double-zeta DZVP basis set along with an auxiliary plane wave basis set with cut-off energy of 400 Ry. During AIMD, nuclei were treated within the Born-

Oppenheimer approximation with a time step of 0.5 fs for the integration of the equations of motion. The temperature of the simulation was maintained at 330 K using the Canonical Sampling through Velocity Rescaling (CSVR) thermostat coupled to the system with a time constant of 100 fs⁵³. All the systems presented here were thermalized for at least 5 ps before production of about 30 ps for statistical analysis. For the well-tempered *ab initio* metadynamics simulations⁵⁴, Gaussian hills of 0.04 width and 3.3 kJ·mol⁻¹ initial height were added in a two-dimensional set of collective variables, described by coordination numbers (CN) as defined in Plumed 2.0⁵⁵. For each collective variable, the chosen CN gives the average number on a set of oxygen atoms coordinated to the probed Al atom. We used two different sets. In the first one (CN_a), the oxygen atoms belong to the surface structure of dry alumina. The second one includes all the other oxygen atoms of the simulations (CN_w or CN_{w+p}, with w for water oxygens and p for polyol oxygens respectively). The error associated with this procedure is lower than 2 kJ·mol⁻¹.

6.2.3 Theoretical aspects of Metadynamics

During *ab initio* molecular dynamics (AIMD), various geometries are sampled as a function of simulation time t and can be described using a generalised coordinate $q(t)$. In metadynamics, a bias potential is, on top of that, added to the unknown free energy surface $F(q)$ along a few chosen geometric parameters (distance, angles, or any sort of quantities that depend on q) called collective variables s_i . For the sake of simplicity, the ensemble of the selected d collective variables will be referred to as the vector \vec{s} . The bias potential is progressively built during AIMD through the periodic addition (stride τ) of small amounts of free energy that takes the form of Gaussians. This history-dependent potential $V(\vec{s}, t)$ then writes:

$$V(\vec{s}, t) = \sum_{k < \frac{t}{\tau}} W(k\tau) \exp\left(-\sum_i \frac{(s_i - s_i(q(k\tau)))^2}{2\sigma_i^2}\right) \quad (6.1)$$

where W is the height of the Gaussians and σ the width along the direction of collective variable s_i . For standard metadynamics W is a constant, but for well-tempered metadynamics, W decreases as a function of the amount of Gaussians previously added locally:

$$W(k\tau) = W_0 \exp\left(-\frac{V(\vec{s}(q(k\tau), k\tau), t)}{k_B \Delta T}\right) \quad (6.2)$$

The decay is controlled using the parameter ΔT . This procedure allows for a smoother convergence of the bias potential. In the limit of long simulation times, the bias potential

converges and is related to the free energy surface projected along the selected collective variables.

$$V(\vec{s}, t \rightarrow \infty) = \frac{-\Delta T}{T + \Delta T} F(\vec{s}) + \text{constant} \quad (6.3)$$

Practically, we do not choose directly ΔT when using Plumed/CP2K but rather the bias factor γ :

$$\gamma = \frac{T + \Delta T}{T} \quad (6.4)$$

The bias factor was set to 100. The details of the set-up (collective variables and parameters) of the metadynamics simulations are given in the Methods section in the main article. The collective variables we chosen are based on coordination numbers. To describe the coordination of aluminium Al_j with a set of oxygens O_{set} CN is defined by:

$$CN(Al_j, O_{set}) = \sum_{i \in O_{set}} s_{ij}(r_{ij}) = \sum_{i \in O_{set}} \frac{1 - \left(\frac{r_{ij} - d_0}{r_0}\right)^n}{1 - \left(\frac{r_{ij} - d_0}{r_0}\right)^m} \quad (6.5)$$

with r_{ij} the inter-atomic distance between atom i and atom j , $s_{ij}(r_{ij})$ the switching function describing the coordination between atom i and j , d_0 the central value of the switching function ($s_{ij}(d_0) = 1$), r_0 the acceptance distance of the switching function, and with n and m two integer exponents with $n \leq m$. The switching function s_{ij} is plotted for a given value of r_0 and various ratios n/m to illustrate the effect of those parameters on its shape in Figure 6.1. d_0 is chosen to match the Al-O equilibrium distance (1.5Å). r_0 can be seen as an acceptance distance which, coupled with the n/m ratio, controls at which distance the O atom is not anymore considered as bonded to Al. At $d_0 + r_0$, the switching function s_{ij} is equal to n/m . The n/m ratio can be seen as the swiftness of decrease of the function away from the equilibrium distance d_0 . Here, a ratio of 2/5 ($n=4$, $m=10$) and a r_0 of 0.9 Å has been chosen and we can, therefore, observe that this switching function has a value of about zero for an interatomic distance greater than 3 Å.

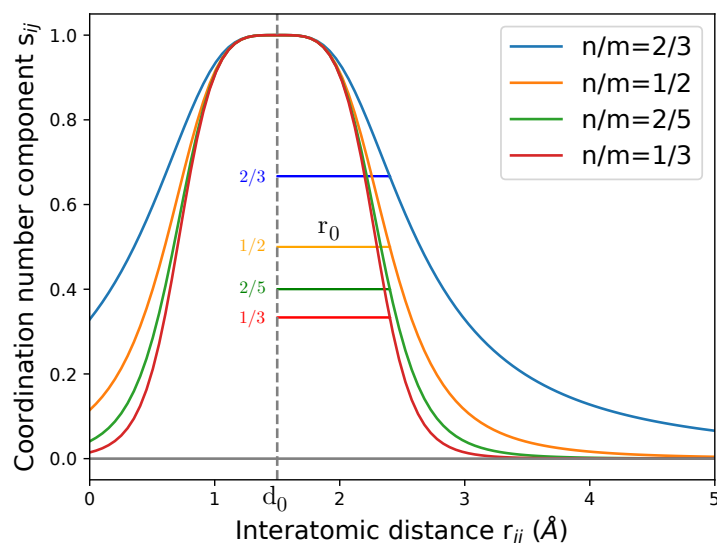


Figure 6.1 – Switching function s_{ij} for $r_0 = 0.9$ Å and n/m ratio with $n = 4$. The corresponding mathematical definition is given in the text.

6.3 Results and Discussion

6.3.1 Identification of the facet whence the decomposition initiates.

γ - Al_2O_3 particles mainly expose three facets commonly referred to with their set of Miller indices: the predominant and hydrophilic (110) facet, the less hydrophilic (100) facet and the (111) facet (see Fig. 6.2a). In order to identify the facet(s) involved in the decomposition of γ - Al_2O_3 , four samples containing particles of different shapes were prepared (see Fig. 6.2 g-j). These four samples therefore showed four distinct proportions of facet areas, which were quantified using X-Ray Diffraction (XRD) (see appendix table E.2). They underwent hydrothermal treatment (*i.e.* 200°C, 2 h, 14 bar autogeneous pressure) using various aqueous solutions of sorbitol (represented in Fig. 6.2b), a known inhibitor, and xylitol (represented in Fig. 6.2c), a shorter sugar polyol. A very strong alumina stabilization was observed in the presence of both sorbitol or xylitol suggesting that the minimal $-(\text{CHOH})_5$ - sequence, common to those two polyols, is essential to protect alumina from water. This is consistent with the work by Ravenelle *et al.* showing that sorbitol is a good inhibitor while glycerol (C3-polyol) is not as efficient²⁸. To go beyond this qualitative statement, the minimum surface coverage of polyol for each sample at which the decomposition of alumina gets inhibited was determined, that is no hydroxides could be detected by XRD after hydrothermal treatment (see appendix section E.3.1). This quantity, referred to as *inhibiting coverage*, was reached for concentrations of 4 g/L of polyols for 2 g of alumina in 50 mL of solution and varied from 0.15 to 0.30 nm^{-2} for xylitol, and from 0.20 to 0.35 nm^{-2} for sorbitol, depending on the shape of the nanoparticles

(see appendix table E.4). This strong variation of the *inhibiting coverages* with the distribution of facet surface areas (up to a factor of two in the case of xylitol) indicates that each facet does not interact equally with the two polyols. In the case of a specific adsorption on one facet only, the so-determined *inhibiting coverage* increases linearly with the fractional surface area of this facet with a zero-intercept (see appendix section E.3.3). As shown in Fig. 6.2d-f, this is only with the fractional surface area of the hydrophilic (110) facet that the *inhibiting coverage* of both sorbitol and xylitol correlates with a zero-intercept function. No such correlations could be established with the other fractional surface areas. Following the same kind of reasoning, we show in appendix chapter E that edges and kinks are unlikely to be involved as major active sites for hydrolysis. Therefore, the adsorption of sorbitol or xylitol is specific to the (110) facet and allows for the total inhibition of the decomposition of γ - Al_2O_3 in liquid water at similar partial coverage of 0.36 and 0.44 nm^{-2} of (110) facet for xylitol and sorbitol respectively (slopes on Fig. 6.2d). As a corollary, we can infer that the (110) facet must exhibit sites responsible for the hydrolysis of γ - Al_2O_3 and that the reactivity of these sites with water can be limited or even suppressed upon the adsorption of sorbitol or xylitol.

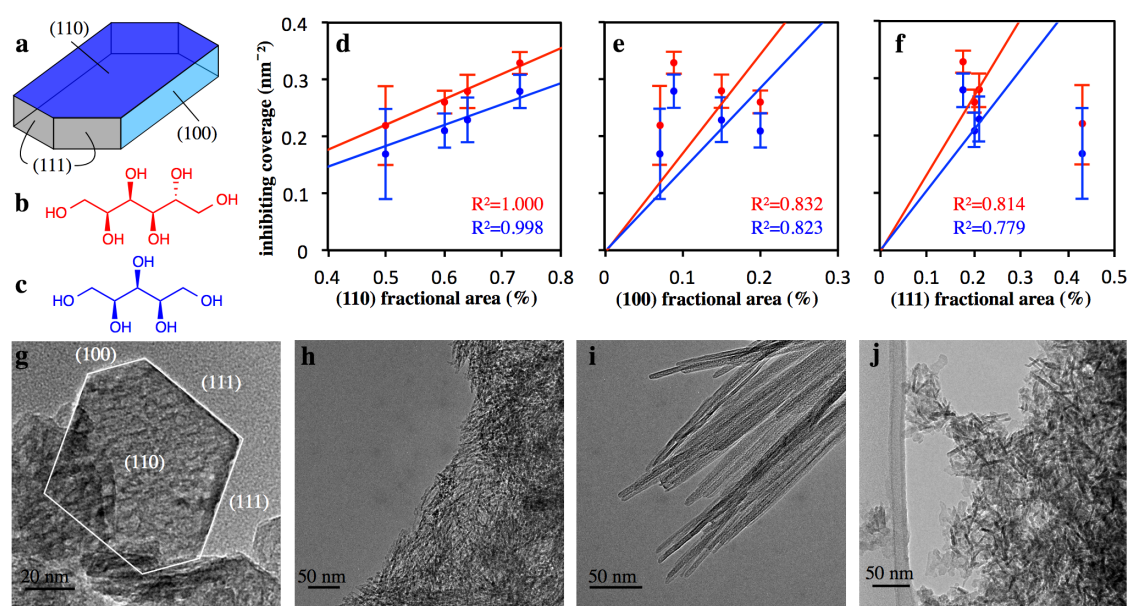


Figure 6.2 – **Implication of the (110) facet in the decomposition of γ - Al_2O_3** **a**, General topology of a γ - Al_2O_3 nanoparticle exhibiting three major facets: (110) in dark blue, (100) in light blue and (111) in grey. **b,c**, Structures of two inhibitors: **b**, sorbitol (red) and **c**, xylitol (blue). **d,e,f**, Comparisons between the *inhibiting coverage* (sorbitol in red, xylitol in blue) and the fraction of exposed (110) (**d**), (111) (**e**) and (100) (**f**) surface areas. The experimental data sets are fitted to the zero-intercept linear model derived in appendix chapter E. The fitted curves are represented as straight lines. A correlation could only be established in the case of the (110) surface (**d**) with slopes of 0.367 ± 0.009 and $0.443 \pm 0.005 \text{ nm}^{-2}$ for xylitol and sorbitol respectively ($R^2 > 0.99$). **g,h,i,j**, Transmission Electronic Microscopy images of the four differently shaped γ - Al_2O_3 nanoparticles ordered in increasing (110) fractional area: plates (**g**), fibres (**h**), rods (**i**) and commercial γ - Al_2O_3 (**j**).

6.3.2 Identification of the atomic sites on the (110) facet whence the decomposition initiates.

To gain atomistic insight and identify the sites involved in the decomposition of γ - Al_2O_3 on the (110) facet, we performed *ab initio* simulations using our recently developed model for γ - Al_2O_3 /water interfaces³³. The primitive cell of the model of the γ - Al_2O_3 (110) surface shows four different surface Al sites: two octahedral and two tetrahedral sites, referred to as $\text{Al}_{(1)}$ and $\text{Al}_{(2)}$ for the former and Al_α and Al_β for the latter (see Fig. 6.4a-b). This surface is fully hydrated with five chemisorbed water fragments, the oxygen atoms of which are represented in blue in Fig. 6.4a-b. Some of these water molecules are dissociated, generating hydroxyl surface groups. Repeating the surface unit cell in the x and y directions, the resulting p(2x2) slab is surmounted by a 20 Å thick layer of liquid water that is not represented here for clarity. The iso-electric point of alumina being close to 8, we consider pure neutral water.^{56;57} Since the decomposition of γ - Al_2O_3 transforms tetrahedral Al sites into octahedral Al centers, we have focused on the tetrahedral sites, Al_α and Al_β , and their reactivity with water (see Fig. 6.4a). Both of them have a coordination number to alumina oxygen atoms (CN_a) of three and a coordination number to water oxygen atoms (CN_w) of one. Performing *ab initio* metadynamics, we made each tetrahedral Al center specifically react along these two variables (see details in Methods, section 6.2). The statistical analysis of the variations of CN_w and CN_a allows for the construction of free energy landscapes (like the one given in Fig. 6.4c), the local depth of which assesses for the stability of the intermediates, transition states and products encountered along the course of the simulation (see details in Method, section 6.2.3). Obtaining this mechanistic information is a key achievement in the quest of a better understanding of reactive interfaces and kinetic stability of solids in water. In the case of Al_α , the free energy landscape mainly shows one deep minimum at $(\text{CN}_a, \text{CN}_w)=(3,1)$, that is the initial structure (see Fig. 6.3). Even within a span of $200 \text{ kJ}\cdot\text{mol}^{-1}$, no transition state to escape that deep well towards other minima could have been identified. This suggests that Al_α is very unlikely to react with liquid water.

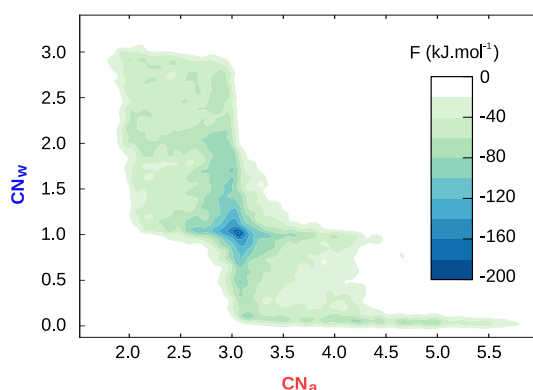


Figure 6.3 – Free energy surface of Al_α computed from the metadynamics simulation using two collective variables, CN_a that represents the Al coordination to alumina oxygen atoms and CN_w the one to water oxygen atoms.

Conversely, the free energy landscape for Al_β shows, over a span of $180 \text{ kJ}\cdot\text{mol}^{-1}$, a variety of minima spread over the nodes of a well-defined checkered pattern and associated with a decreased number of bonds to surface oxygen atoms and increased number with water oxygens (see Fig. 6.4c). Al_β therefore progressively detaches from the oxygen network of γ - Al_2O_3 and is hydrated with the surrounding water molecules. A more detailed look at the free energy surface indicates that this hydration is sequential and follows an addition/elimination mechanism. It is only when Al_β has reached a total coordination number of 5 that an Al_β -O-Al bond cleavage occurs. Noticeably, five-coordinated species appear to be key intermediates in the decomposition of alumina as in the water-induced de-alumination of zeolites⁵⁸. This holds true until $(\text{CN}_a, \text{CN}_w)=(1,4)$ where Al_β readily guests a water molecule to achieve an octahedral structure with $(\text{CN}_a, \text{CN}_w)=(1,5)$. This last structure obtained from the simulation is represented in Fig. 6.4e and shows how Al_β has been extracted from its initial position. Among the water molecules in the first coordination sphere, three of them were initially present on the surface as chemisorbed water molecules and the two others were physisorbed water molecules. Proton transfers are not included in the general reaction coordinates we designed. Nevertheless, the inspection of the trajectory shows that these early-stage steps of the hydration are accompanied with the deprotonation of some of the coordinated water molecules and a widespread reshuffling of surface protons over about 1 nm (compare Fig. 6.4a and 6.4d). The amphoteric character of the hydrated material allows γ - Al_2O_3 to offer the proper local protonation level for the intermediates involved in its own decomposition into AlO_xH_y . In this respect, the trajectory reveals that physisorbed water molecules are involved, *via* a Grotthus mechanism, in this redistribution of surface protons. Physisorbed water molecules do therefore not only react but also help accommodating the protonation state of the surface to guest the final octahedral intermediate. This is particularly striking for the water fragments bound to the octahedral $\text{Al}_{(1)}$ and $\text{Al}_{(2)}$, which need to be deprotonated to coordinate the fleeing tetrahedral Al_β . This study highlights the key role of water as a reactant and as a solvent in the stability of an oxide and pre-figures the role of the pH in the interface transformation. *Ab initio* metadynamics can hence provide a complete atomistic picture of the alteration mechanism of an iono-covalent solid in contact with a reactive solvent.

6.3.3 Xylitol/water interface

Three additional *ab initio molecular dynamics* (AIMD) simulations were performed to study the water/ γ -alumina interface in presence of an adsorbed xylitol. We used, as a reference, our recently published AIMD simulation on the γ - Al_2O_3 (110)/water interface³³, with the same simulation set-up. Starting from this equilibrated interface, we substituted 5 water molecules (2 chemisorbed H_2O , 1 chemisorbed OH and 2 physisorbed water molecules) with xylitol as illustrated in Fig. 6.5.

We considered three different tridentate geometries. The choice of these tridentate geometries

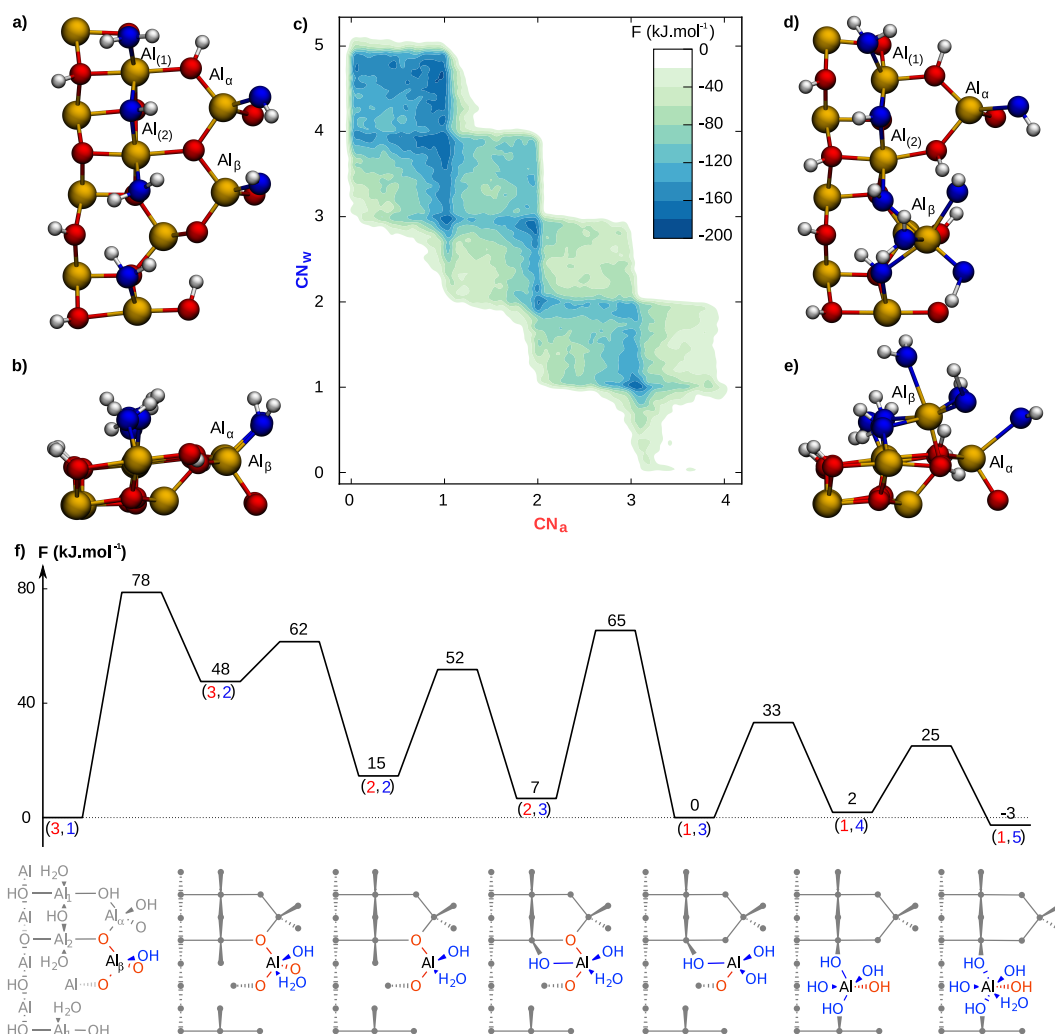


Figure 6.4 – **Exploration of the reactivity of tetrahedral Al_β on $\gamma\text{-Al}_2\text{O}_3$ (110) from *ab initio* metadynamics.** **a,b**, Structure of the initial surface with chemisorbed water molecules or fragments (the oxygen atoms of which are shown in blue) adsorbed on tetrahedral Al_α and Al_β and octahedral $\text{Al}_{(1)}$ and $\text{Al}_{(2)}$. **c**, Free energy surface obtained from the metadynamics simulation on Al_β using the coordination numbers to alumina oxygen atoms (CN_a) and to water molecules and fragments (CN_w) as variables. The simulation starts from the point of coordinates $(\text{CN}_a, \text{CN}_w) = (3, 1)$. **d,e**, Structure of the last intermediate obtained from the hydration of tetrahedral Al_β with $(\text{CN}_a, \text{CN}_w) = (1, 5)$. **f**, Projected free energy profile with the structure of each intermediate and the corresponding $(\text{CN}_a, \text{CN}_w)$. Yellow and white balls represent aluminum and hydrogen atoms respectively. The color red is used for alumina oxygen atoms and the associated CN_a . The color blue is used for water oxygen atoms and the associated CN_w .

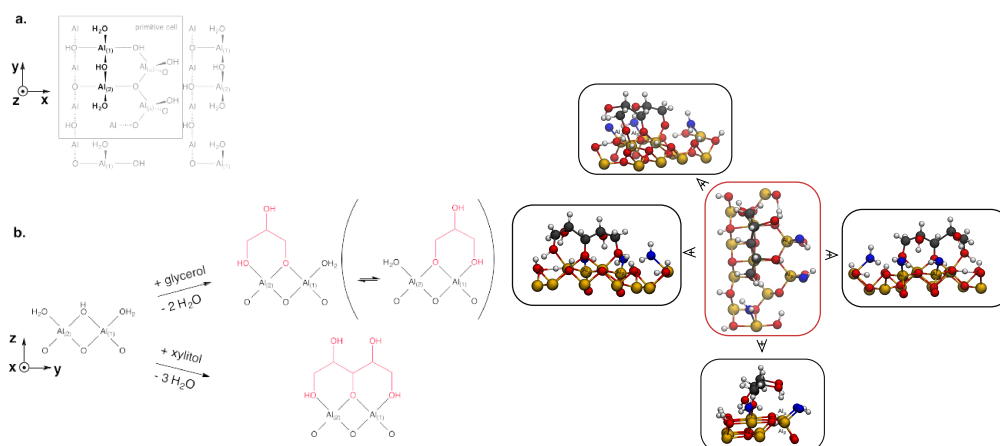


Figure 6.5 – Adsorption of glycerol and xylitol through the substitution of water molecules. **a**, Structure of γ - Al_2O_3 (110) surface saturated with water molecules. **b**, Substitution of chemisorbed water molecules with glycerol (structure proposed by Copeland *et. al.*²⁹) and xylitol (geometry proposed in the present work) and various views of a snapshot of xylitol at the γ - Al_2O_3 -water interface (O in red except O from water in blue, Al in yellow, C in black and H in white)

is motivated by both literature and the present work:

- We show in the appendix section E.3.2 that sorbitol and xylitol reach a saturation of adsorption for about 1/4 to 1/3 of a monolayer. If the interaction with the surface was driven by non-specific interaction, we should in principle be able to saturate the surface. This low coverage saturation thus suggests that the adsorption relies on specific interaction rather than non-specific physisorption. The corresponding free energy of adsorption is moderate for chemisorption ($-20 \text{ kJ}\cdot\text{mol}^{-1}$ according to our Langmuir constant) but is consistent with a substitution of water molecules with alcohol moieties on the surface.
- The only polyols for which the adsorption geometry on γ - Al_2O_3 (110) has been studied in the literature is glycerol, which happens to adsorb with a bidentate geometry^{29;59}. We can infer that xylitol and sorbitol would also have a multi-dentate adsorption mode. Considering the local geometry of γ - Al_2O_3 (110), it is possible to propose a tridentate adsorption geometry for those C5 and C6 polyols. Moreover, it is worth noting that glycerol is also an inhibitor of the decomposition of γ - Al_2O_3 ²⁸. Since all three are polyols, we can assume that they inhibit the decomposition via similar mechanisms. Glycerol however is only able to slow down the decomposition, whereas sorbitol and xylitol totally inhibit the decomposition. The latter must therefore interact more with the surface, which is consistent with a tridentate geometry.
- The present work shows the importance of chemisorbed water molecules in the decomposition mechanism of γ - Al_2O_3 in liquid water. With its partial substitution of

water molecule on the surface, glycerol leaves some water molecules behind that can potentially react with the leaching Al atoms. With a tridentate adsorption mode, the probability of having such chemisorbed water molecules in the vicinity of the particularly water-sensitive Al centre vanishes.

We performed one AIMD simulation for each adsorption mode of xylitol. After 10 ps of thermalisation, we ran the simulations for 25 ps for production. We compared the structuration of the free water molecules around the water-sensitive Al_β with the reference interface using radial distribution functions (see Fig. 6.6). When the two OH moieties of xylitol point toward the tetrahedral Al atoms (Fig. 6.6a-b), the structuration of free water molecules is highly impacted: the second coordination shell (the first being the chemisorbed OH group on Al_β) either has a smaller concentration (Fig. 6.6d) or is pushed further to larger radii (Fig. 6.6e). The OH group indeed induce bulk hindrance that makes those second coordination shell water molecules less accessible to Al_β . For the last geometry (Fig. 6.6c) with the OH moieties opposite to the tetrahedral centres, the effect can also be detected, albeit to a lesser extent.

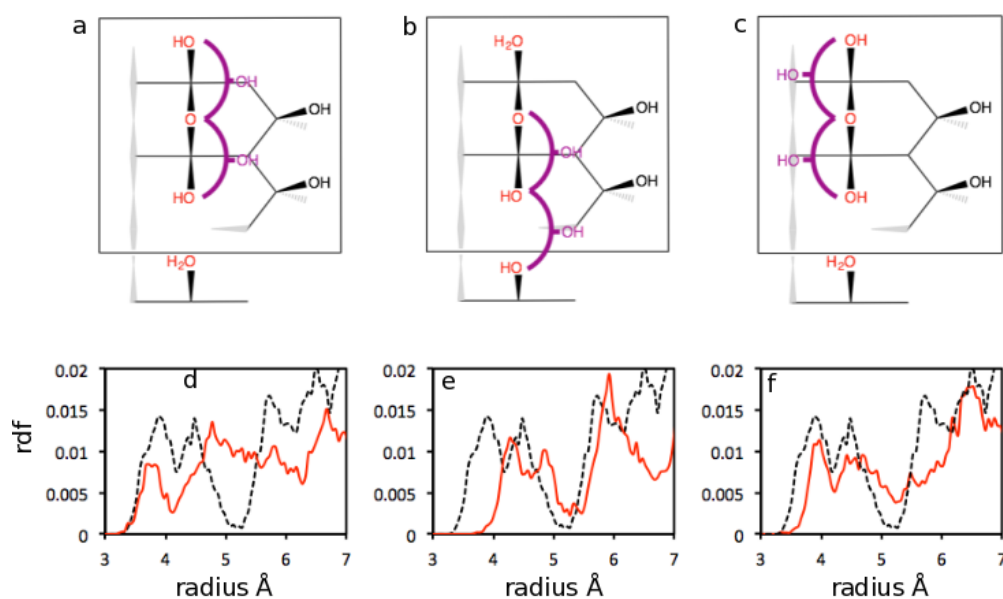


Figure 6.6 – γ - $Al_2O_3(111)$ /water interface including adsorbed xylitol in three different geometries (a, b and c). The radial distribution of Al_β with free water molecules is given in absence (dash black) and in presence (solid red) of xylitol to show the influence of its adsorption on the structuration of the interface depending on the adsorption mode (d, e and f).

6.3.4 Reactivity with chemisorbed xylitol.

We performed the same metadynamics as the first one used to study the reactivity of Al_β , but substituting the water fragments bound to the octahedral $Al_{(1)}$ and $Al_{(2)}$, which are in close

vicinity to the water-sensitive tetrahedral Al_β , with xylitol. The reactivity of Al_β is described using again the coordination number of Al_β to alumina oxygen atoms (CN_a) as a variable. Since now, oxygen atoms are also found in xylitol, we considered, as a second variable, the coordination number to all other oxygen atoms that are external to alumina (oxygen atoms of water molecules and polyol) and referred to as CN_{w+p} . The resulting free energy landscape in the presence of xylitol (Fig. 6.7c) is profoundly modified compared to the uncoated case (Fig. 6.4c). Despite the exploration of a $200 \text{ kJ}\cdot\text{mol}^{-1}$ energy span, the sampled $(\text{CN}_a, \text{CN}_{w+p})$ space is reduced, meaning that Al_β is more constrained near its initial geometry at $(\text{CN}_a, \text{CN}_{w+p})=(3,1)$. A detailed look at the free energy landscape shows nevertheless that Al_β is able to react with some surrounding oxygen atoms (CN_{w+p} goes up to 4). The exact mechanism is however very different from that described above. With xylitol adsorbed, CN_a first decreases from 3 to 2 and CN_{w+p} increases from 1 to 2, without any clear minimum in-between. This corresponds to a $\text{S}_\text{N}2$ mechanism with a strong $\text{S}_\text{N}1$ character where the Al_β leaches first from alumina to the outer surface (CN_a decreases) before gaining an Al-O bond with water or xylitol (CN_{w+p} increases). As discussed above, the hydration of Al_β follows an addition/elimination mechanism in the absence of xylitol. In other words, while a water molecule could easily reach the Al_β and perform a nucleophilic addition in absence of xylitol, it has become more difficult in presence of xylitol. The nucleophile must therefore either be immobilized or have difficulties to approach Al_β . This is indeed confirmed by the inspection of the trajectories: Al_β does not react with physisorbed water molecules but rather with the chemisorbed alcohol moieties of xylitol. This frustrated extraction of Al_β out of the alumina surface is highly activated and shows a barrier of $161 \text{ kJ}\cdot\text{mol}^{-1}$, consistent with the experimentally observed inhibiting power of xylitol for hydroxides formation.

To better understand why Al_β reacts with xylitol rather than water, we performed a 25 ps long regular *ab initio* molecular dynamics simulation of the interface with xylitol adsorbed and compared to our recently published study work on the $\gamma\text{-Al}_2\text{O}_3/\text{water}$ interface³³. The volume visited by physisorbed water molecules around Al_β is greatly impacted by the presence of xylitol as shown in Fig. 6.7a and b. This is further confirmed by the radial distribution functions of Al_β with physisorbed water molecules: the probabilities of finding physisorbed water molecules in the second coordination shell are indeed reduced and shifted to larger distances (Fig. 6.6). This clearly evidences an important steric hindrance induced by xylitol, which is at the origin of the inhibition. Once Al_β sees its coordination number to alumina oxygen atoms diminished by one unit, it directly coordinates to two alcohol groups because of the constrained adsorption mode of xylitol (CN_{w+p} increases by two units). The resulting square-based pyramidal structure readily captures a water physisorbed molecule to gain a saturated octahedral geometry, reaching $(\text{CN}_a, \text{CN}_{w+p})=(2,4)$.

We have already mentioned in section 6.3.3 that the adsorption geometries **a** and **b** for xylitol show a similar influence on the structure of water molecules around Al_β (second coordination shell). This results in an analogous reactivity towards water as shown by the very similar

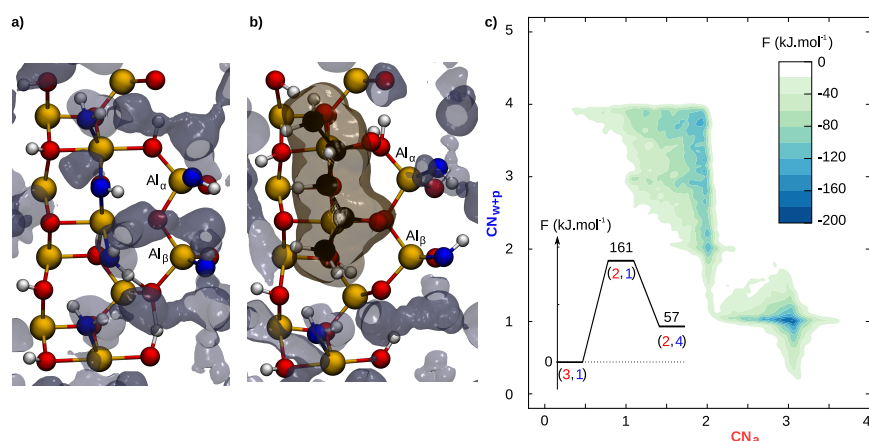


Figure 6.7 – **Inhibition of the decomposition of $\gamma\text{-Al}_2\text{O}_3$ in the presence of chemisorbed xylitol evidenced by *ab initio* metadynamics.** **a.** $\gamma\text{-Al}_2\text{O}_3(110)$ /water interface with the average occupation volume of water in grey. **b.** Geometry of adsorbed xylitol at the $\gamma\text{-Al}_2\text{O}_3(110)$ /water interface with the iso-surface of the average occupation volume of xylitol in ochre, and the average occupation volume of water in grey. The iso-surfaces were computed from an extra regular *ab initio* molecular dynamics simulation. More details can be found in Section 6.3.3 **c.** Free energy surface obtained from the metadynamics simulation on Al_β in presence of xylitol. CN_a is the coordination number of Al_β to alumina oxygen atoms. CN_{w+p} is the coordination number of Al_β to water and polyols oxygens. Yellow and white balls represent aluminum and hydrogen atoms respectively. The color red is used for alumina oxygen atoms and the associated CN_a . The color blue is used for water oxygen atoms and the associated CN_w .

free energy surfaces displayed in Fig. 6.7 and Fig. 6.8a. Second coordination shell water molecules cannot access Al_β and the mechanism therefore switches from a two-step addition and elimination mechanism to a $\text{S}_\text{N}2$ mechanism with a strong $\text{S}_\text{N}1$ character. Al_β reacts with xylitol instead of water, upon the de-coordination from one oxygen atom belonging to alumina. There is therefore no need for extra physisorbed water molecule to come to saturate the octahedral structure of the product. In the last structure Fig. 6.6c), which has the two uncoordinated alcohol moieties opposite to the tetrahedral centres, the reactivity is different (Fig. 6.8b). As expected, xylitol cannot chelate the leaching Al_β in the same manner. Al_β is able to de-coordinate from one oxygen atom of alumina and to coordinate with one alcohol moiety of xylitol (product at (2,2)) through a $\text{S}_\text{N}2$ mechanism. The barrier is higher than in absence of xylitol ($95 \text{ kJ}\cdot\text{mol}^{-1}$ to compare with $78 \text{ kJ}\cdot\text{mol}^{-1}$ in absence of xylitol). In addition, no other minimum can be observed for a span of free energies of $180 \text{ kJ}\cdot\text{mol}^{-1}$, probably because of the constraint and hindrance induced by the C-H bonds of xylitol. In short, all three adsorption modes show that physisorbed water molecules cannot react anymore with Al_β directly. The only reactivity observed is limited with that involving xylitol and does not allow the dissolution of Al centres.

Noticeably, for all adsorption modes, the inhibitor does not directly interact with the weak spot, but with a neighboring site, thereby modifying the interfacial structure of the liquid. It substitutes the water molecules that are involved in the first hydration steps and prevents the necessary proton re-shuffling to generate AlO_xH_y and therefore provides a strong stabilization

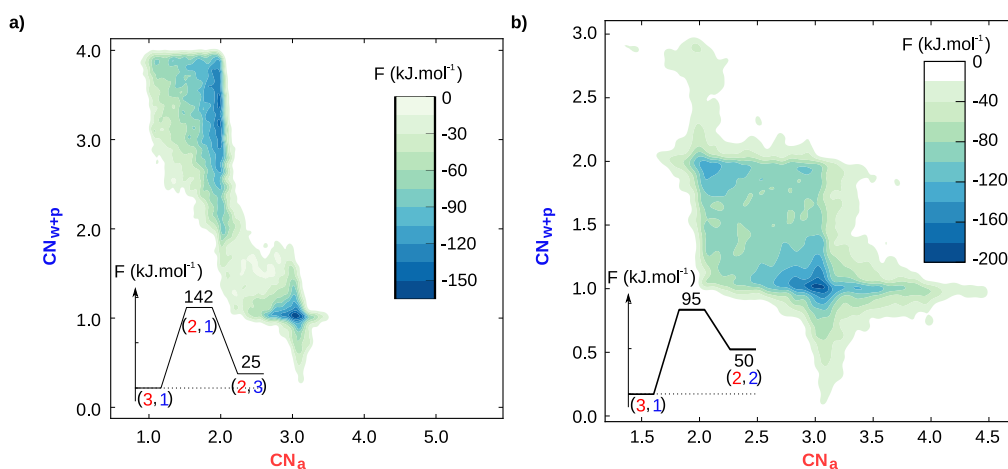


Figure 6.8 – Free energy surface obtained from the metadynamics simulation on Al_β in presence of xylitol adsorbed as in Fig. 6.6b (a) and Fig. 6.6c (b). CN_a is the coordination number of Al_β to alumina oxygen atoms. CN_{w+p} is the coordination number of Al_β to water and polyol oxygen atoms.

of the surface of alumina. This is attributed to the γ -pentanetriol backbone of xylitol, a structural feature shared with sorbitol (a known good inhibitor) but not with glycerol (a known weak inhibitor)²⁸. Our study therefore opens the road to a rational design of the structure of coating agents able to prevent γ - Al_2O_3 from decomposing in water.

6.4 Conclusions

The combined experimental and theoretical study presented here provides an atomistic mechanistic picture of the initial steps of the decomposition of γ - Al_2O_3 in water. The weak spot is a tetrahedral surface Al of the (110) surface. It undergoes successive addition of water/scission of Al-O, yielding to AlO_xH_y . This process is accompanied by proton reshuffling. The chemisorption of a polyol on a neighbor site inhibits this hydrolysis by replacing the water molecules that initiate the process and by limiting the access of water to this weak spot. Noticeably, the weak spot of this oxide is not located at kink or edges but at the heart of a given facet. This understanding opens the road to further improvement of inhibitors. Since γ - Al_2O_3 is an ionic-covalent oxide and water potentially reacts during the process and may dissociate into (OH^- , H^+), gaining such an atomistic understanding is a rather challenging task, especially regarding computational chemistry where the use of biased *ab initio* molecular dynamic is necessary. The present achievement thus constitutes an unprecedented milestone in the understanding of solid/liquid interface transformation. The approach that we propose here could be insightfully applied to various other relevant systems in electrochemistry, geochemistry or material science, where the reactivity of the solid with water and possibly other liquids plays a crucial role.

Bibliography

- [1] Sato, H.; Miyagawa, Y.; Okabe, T.; Miyajima, M.; Sunada, H. Dissolution mechanism of diclofenac sodium from wax matrix granules. *J. Pharm. Sci.* **1997**, *86*, 929–934, WOS:A1997XP65700009.
- [2] Maurice, V.; Marcus, P. Progress in corrosion science at atomic and nanometric scales. *Prog. Mater. Sci.* **2018**, *95*, 132–171, WOS:000431163100003.
- [3] Chen, Z.; Amine, R.; Ma, Z.-F.; Amine, K. Interfacial reactions in lithium batteries. *Journal of Physics D-Applied Physics* **2017**, *50*, 303001, WOS:000415293600001.
- [4] Fischer, C.; Kurganskaya, I.; Schaefer, T.; Luetge, A. Variability of crystal surface reactivity: What do we know? *Appl. Geochem.* **2014**, *43*, 132–157, WOS:000334315500012.
- [5] Putnis, A.; Putnis, C. V. The mechanism of reequilibration of solids in the presence of a fluid phase. *J. Solid State Chem.* **2007**, *180*, 1783–1786, WOS:000246892800034.
- [6] Pirkanniemi, K.; Sillanpaa, M. Heterogeneous water phase catalysis as an environmental application: a review. *Chemosphere* **2002**, *48*, 1047–1060, WOS:000177824800006.
- [7] Chheda, J. N.; Huber, G. W.; Dumesic, J. A. Liquid-phase catalytic processing of biomass-derived oxygenated hydrocarbons to fuels and chemicals. *Angew. Chem. Int. Ed.* **2007**, *46*, 7164–7183, WOS:000249967100004.
- [8] Sievers, C.; Noda, Y.; Qi, L.; Albuquerque, E. M.; Rioux, R. M.; Scott, S. L. Phenomena Affecting Catalytic Reactions at Solid-Liquid Interfaces. *ACS Catal.* **2016**, *6*, 8286–8307, WOS:000389399400033.
- [9] Skorina, T.; Allanore, A. Aqueous alteration of potassium-bearing aluminosilicate minerals: from mechanism to processing. *Green Chem.* **2015**, *17*, 2123–2136, WOS:000352724200012.
- [10] Chen, G.; Wang, Y.; Wei, Y.; Zhao, W.; Gao, D.; Yang, H.; Li, C. Successive Interfacial Reaction-Directed Synthesis of CeO₂@Au@CeO₂-MnO₂ Environmental Catalyst with Sandwich Hollow Structure. *ACS Appl. Mater. Interfaces* **2018**, *10*, 11595–11603, WOS:000430156000024.
- [11] Zhang, X.; Sewell, T. E.; Glatz, B.; Sarupria, S.; Getman, R. B. On the water structure at hydrophobic interfaces and the roles of water on transition-metal catalyzed reactions: A short review. *Catal. Today* **2017**, *285*, 57–64, WOS:000397684500007.
- [12] Ravenelle, R. M.; Copeland, J. R.; Kim, W.-G.; Crittenden, J. C.; Sievers, C. Structural Changes of gamma-Al₂O₃-Supported Catalysts in Hot Liquid Water. *ACS Catal.* **2011**, *1*, 552–561, WOS:000290426600016.

- [13] Hilfiker, R. *Polymorphism: in the Pharmaceutical Industry*, John Wiley & Sons, Ltd, 2006; pp I–XIX, _eprint: <https://onlinelibrary.wiley.com/doi/pdf/10.1002/3527607889.fmatter>.
- [14] Siegfried, M. J.; Choi, K.-S. Elucidating the effect of additives on the growth and stability of Cu₂O surfaces via shape transformation of pre-grown crystals. *J. Am. Chem. Soc.* **2006**, *128*, 10356–10357, WOS:000239618700005.
- [15] Pedreira-Segade, U.; Michot, L. J.; Daniel, I. Effects of salinity on the adsorption of nucleotides onto phyllosilicates. *Phys. Chem. Chem. Phys.* **2018**, *20*, 1938–1952, WOS:000423019600062.
- [16] Abi Aad, J.; Courty, P.; Decottignies, D.; Michau, M.; Diehl, F.; Carrier, X.; Marceau, E. Inhibition by Inorganic Dopants of γ -Alumina Chemical Weathering under Hydrothermal Conditions: Identification of Reactive Sites and their Influence in Fischer–Tropsch Synthesis. *ChemCatChem* **2017**, *9*, 2106–2117, _eprint: <https://chemistry-europe.onlinelibrary.wiley.com/doi/pdf/10.1002/cctc.201700140>.
- [17] Busca, G. *Advances in Catalysis*; Elsevier, 2014; Vol. 57; pp 319–404.
- [18] Trueba, M.; Trasatti, S. P. gamma-Alumina as a support for catalysts: A review of fundamental aspects. *Eur. J. Inorg. Chem.* **2005**, 3393–3403, WOS:000231995500001.
- [19] Raybaud, P.; Chizallet, C.; Mager-Maury, C.; Digne, M.; Toulhoat, H.; Sautet, P. From gamma-alumina to supported platinum nanoclusters in reforming conditions: 10 years of DFT modeling and beyond. *J. Catal.* **2013**, *308*, 328–340, WOS:000329881700030.
- [20] Busca, G. The surface of transitional aluminas: A critical review. *Catal. Today* **2014**, *226*, 2–13, WOS:000332407200002.
- [21] Mager-Maury, C.; Chizallet, C.; Sautet, P.; Raybaud, P. Platinum Nanoclusters Stabilized on gamma-Alumina by Chlorine Used As a Capping Surface Ligand: A Density Functional Theory Study. *ACS Catal.* **2012**, *2*, 1346–1357, WOS:000306297900006.
- [22] Sakwa-Novak, M. A.; Jones, C. W. Steam Induced Structural Changes of a Poly(ethylenimine) Impregnated gamma-Alumina Sorbent for CO₂ Extraction from Ambient Air. *ACS Appl. Mater. Interfaces* **2014**, *6*, 9245–9255, WOS:000338184500041.
- [23] Lefevre, G.; Duc, M.; Lepeut, P.; Caplain, R.; Fedoroff, M. Hydration of gamma-alumina in water and its effects on surface reactivity. *Langmuir* **2002**, *18*, 7530–7537, WOS:000178300200042.
- [24] Carrier, X.; Marceau, E.; Lambert, J.-F.; Che, M. Transformations of gamma-alumina in aqueous suspensions 1. Alumina chemical weathering studied as a function of pH. *J. Colloid Interface Sci.* **2007**, *308*, 429–437, WOS:000244841500019.

Chapter 6. Reactivity of shape-controlled crystals and metadynamics simulations

- [25] Jongerius, A. L.; Copeland, J. R.; Foo, G. S.; Hofmann, J. P.; Bruijninx, P. C. A.; Sievers, C.; Weckhuysen, B. M. Stability of Pt/ γ -Al₂O₃ Catalysts in Lignin and Lignin Model Compound Solutions under Liquid Phase Reforming Reaction Conditions. *ACS Catal.* **2013**, *3*, 464–473, WOS:000315707700025.
- [26] Aad, J. A.; Casale, S.; Michau, M.; Courty, P.; Diehl, F.; Marceau, E.; Carrier, X. Chemical Weathering of Alumina in Aqueous Suspension at Ambient Pressure: A Mechanistic Study. *ChemCatChem* **2017**, *9*, 2186–2194, WOS:000412338800017.
- [27] Liu, F.; Okolie, C.; Ravenelle, R. M.; Crittenden, J. C.; Sievers, C.; Bruijninx, P. C. A.; Weckhuysen, B. M. Silica deposition as an approach for improving the hydrothermal stability of an alumina support during glycerol aqueous phase reforming. *Appl. Catal., A* **2018**, *551*, 13–22, WOS:000425555600002.
- [28] Ravenelle, R. M.; Copeland, J. R.; Van Pelt, A. H.; Crittenden, J. C.; Sievers, C. Stability of Pt/ γ -Al₂O₃ Catalysts in Model Biomass Solutions. *Top. Catal.* **2012**, *55*, 162–174.
- [29] Copeland, J. R.; Santillan, I. A.; Schimming, S. M.; Ewbank, J. L.; Sievers, C. Surface Interactions of Glycerol with Acidic and Basic Metal Oxides. *J. Phys. Chem. C* **2013**, *117*, 21413–21425, Publisher: American Chemical Society.
- [30] Adiga, S. P.; Zapol, P.; Curtiss, L. A. Atomistic simulations of amorphous alumina surfaces. *Phys. Rev. B* **2006**, *74*, 064204, WOS:000240238500030.
- [31] Krokidis, X.; Raybaud, P.; Gobichon, A. E.; Rebours, B.; Euzen, P.; Toulhoat, H. Theoretical study of the dehydration process of boehmite to gamma-alumina. *J. Phys. Chem. B* **2001**, *105*, 5121–5130, WOS:000169232800008.
- [32] Ngouana-Wakou, B. E.; Cornette, P.; Valero, M. C.; Costa, D.; Raybaud, P. An Atomistic Description of the gamma-Alumina/Water Interface Revealed by Ab Initio Molecular Dynamics. *J. Phys. Chem. C* **2017**, *121*, 10351–10363, WOS:000402024200012.
- [33] Réocreux, R.; Jiang, T.; Iannuzzi, M.; Michel, C.; Sautet, P. Structuration and Dynamics of Interfacial Liquid Water at Hydrated γ -Alumina Determined by ab Initio Molecular Simulations: Implications for Nanoparticle Stability. *ACS Appl. Nano Mater.* **2018**, *1*, 191–199.
- [34] Laio, A.; Gervasio, F. L. Metadynamics: a method to simulate rare events and reconstruct the free energy in biophysics, chemistry and material science. *Rep. Prog. Phys.* **2008**, *23*.
- [35] Michel, C.; Laio, A.; Mohamed, F.; Krack, M.; Parrinello, M.; Milet, A. Free energy ab initio metadynamics: A new tool for the theoretical study of organometallic reactivity? Example of the C-C and C-H reductive eliminations from platinum(IV) complexes. *Organometallics* **2007**, *26*, 1241–1249, WOS:000244248900020.

- [36] Blumberger, J.; Ensing, B.; Klein, M. L. Formamide hydrolysis in alkaline aqueous solution: Insight from ab initio metadynamics calculations. *Angew. Chem. Int. Ed.* **2006**, *45*, 2893–2897, WOS:000237518600014.
- [37] Moors, S. L. C.; De Wispelaere, K.; Van der Mynsbrugge, J.; Waroquier, M.; Van Speybroeck, V. Molecular Dynamics Kinetic Study on the Zeolite-Catalyzed Benzene Methylation in ZSM-5. *ACS Catal.* **2013**, *3*, 2556–2567, WOS:000326615200018.
- [38] Munoz-Santiburcio, D.; Camellone, M. F.; Marx, D. Solvation-Induced Changes in the Mechanism of Alcohol Oxidation at Gold/Titania Nanocatalysts in the Aqueous Phase versus Gas Phase. *Angew. Chem. Int. Ed.* **2018**, *57*, 3327–3331, WOS:000427235600006.
- [39] Stack, A. G.; Raiteri, P.; Gale, J. D. Accurate Rates of the Complex Mechanisms for Growth and Dissolution of Minerals Using a Combination of Rare-Event Theories. *J. Am. Chem. Soc.* **2012**, *134*, 11–14, WOS:000301084200004.
- [40] Salvalaglio, M.; Vetter, T.; Giberti, E.; Mazzotti, M.; Parrinello, M. Uncovering Molecular Details of Urea Crystal Growth in the Presence of Additives. *J. Am. Chem. Soc.* **2012**, *134*, 17221–17233, WOS:000309854700048.
- [41] Digne, M.; Sautet, P.; Raybaud, P.; Euzen, P.; Toulhoat, H. Hydroxyl Groups on γ -Alumina Surfaces: A DFT Study. *J. Catal.* **2002**, *211*, 1–5.
- [42] Wischert, R.; Laurent, P.; Coperet, C.; Delbecq, F.; Sautet, P. gamma-Alumina: The Essential and Unexpected Role of Water for the Structure, Stability, and Reactivity of “Defect” Sites. *J. Am. Chem. Soc.* **2012**, *134*, 14430–14449, WOS:000308283200031.
- [43] Bellarosa, L.; García-Muelas, R.; Revilla-López, G.; López, N. Diversity at the Water–Metal Interface: Metal, Water Thickness, and Confinement Effects. *ACS Cent. Sci.* **2016**, *2*, 109–116.
- [44] VandeVondele, J.; Krack, M.; Mohamed, F.; Parrinello, M.; Chassaing, T.; Hutter, J. Quickstep: Fast and accurate density functional calculations using a mixed Gaussian and plane waves approach. *Comput. Phys. Commun.* **2005**, *167*, 103–128, WOS:000228421500005.
- [45] VandeVondele, J.; Hutter, J. Gaussian basis sets for accurate calculations on molecular systems in gas and condensed phases. *J. Chem. Phys.* **2007**, *127*, 114105, WOS:000249667400011.
- [46] Lippert, G.; Hutter, J.; Parrinello, M. A hybrid Gaussian and plane wave density functional scheme. *Mol. Phys.* **1997**, *92*, 477–487, WOS:A1997YC60700017.
- [47] Hutter, J.; Iannuzzi, M.; Schiffmann, F.; VandeVondele, J. CP2K: atomistic simulations of condensed matter systems. *WIREs Comput Mol Sci* **2014**, *4*, 15–25.

Chapter 6. Reactivity of shape-controlled crystals and metadynamics simulations

- [48] Perdew, J. P.; Burke, K.; Ernzerhof, M. Generalized Gradient Approximation Made Simple. *Phys. Rev. Lett.* **1996**, *77*, 3865–3868.
- [49] Grimme, S.; Antony, J.; Ehrlich, S.; Krieg, H. A consistent and accurate *ab initio* parametrization of density functional dispersion correction (DFT-D) for the 94 elements H-Pu. *J. Chem. Phys.* **2010**, *132*, 154104.
- [50] Goedecker, S.; Teter, M.; Hutter, J. Separable dual-space Gaussian pseudopotentials. *Phys. Rev. B* **1996**, *54*, 1703–1710, WOS:A1996UZ86100053.
- [51] Hartwigsen, C.; Goedecker, S.; Hutter, J. Relativistic separable dual-space Gaussian pseudopotentials from H to Rn. *Phys. Rev. B* **1998**, *58*, 3641–3662, WOS:000075616800043.
- [52] Krack, M. Pseudopotentials for H to Kr optimized for gradient-corrected exchange-correlation functionals. *Theor. Chem. Acc.* **2005**, *114*, 145–152, WOS:000232053800020.
- [53] Bussi, G.; Donadio, D.; Parrinello, M. Canonical sampling through velocity rescaling. *J. Chem. Phys.* **2007**, *126*, 014101, WOS:000243380000005.
- [54] Barducci, A.; Bussi, G.; Parrinello, M. Well-Tempered Metadynamics: A Smoothly Converging and Tunable Free-Energy Method. *Phys. Rev. Lett.* **2008**, *100*.
- [55] Tribello, G. A.; Bonomi, M.; Branduardi, D.; Camilloni, C.; Bussi, G. PLUMED 2: New feathers for an old bird. *Comput. Phys. Commun.* **2014**, *185*, 604–613, WOS:000329537500020.
- [56] SPRYCHA, R. ELECTRICAL DOUBLE-LAYER AT ALUMINA ELECTROLYTE INTERFACE .1. SURFACE-CHARGE AND ZETA POTENTIAL. *J. Colloid Interface Sci.* **1989**, *127*, 1–11, WOS:A1989R707500001.
- [57] Kosmulski, M. The pH-dependent surface charging and points of zero charge V. Update. *J. Colloid Interface Sci.* **2011**, *353*, 1–15, WOS:000283825300001.
- [58] Silaghi, M.-C.; Chizallet, C.; Sauer, J.; Raybaud, P. Dealumination mechanisms of zeolites and extra-framework aluminum confinement. *J. Catal.* **2016**, *339*, 242–255, WOS:000378453700025.
- [59] Copeland, J. R.; Shi, X.-R.; Sholl, D. S.; Sievers, C. Surface Interactions of C₂ and C₃ Polyols with γ -Al₂O₃ and the Role of Coadsorbed Water. *Langmuir* **2013**, *29*, 581–593.



7 Adsorption study of ethanol at the γ -alumina/water interface

The following chapter is a follow-up to the previous study of the inhibiting ability of polyols on the hydrolysis of γ -alumina in water. It has not yet been published in the form of an article.

abstract: Predicting adsorption free energies and adsorption modes of alcohols at the alumina/water interface is required to study their inhibiting capacities of γ -alumina hydrolysis. The adsorption of ethanol is here investigated as a test-case for the future study of polyols adsorption. Three different methods are used: metadynamics, MMSolv (introduced in chapter 2), and thermodynamic integration. We observed an alternate surface state to the one established in the literature. This state is found to be more stable than the reference state in presence of a bidentate adsorbed ethanol. The desorption mechanism is proven to imply the coordination of an additional water molecule close to the adsorption site prior to the desorption of ethanol. If a qualitative agreement about the desorption mechanism is found between the three methods, no quantitative agreement could be found for the desorption free energies. This work evidences the issues of the three methods that remain to be fixed, but also demonstrates that their combination can already lead to a better understanding of the desorption mechanism.

7.1 Introduction

In the precedent chapter (chapter 6), following experimental evidence of inhibition of the hydrolysis of γ -alumina in presence of xylitol, we investigated the water/alumina interface. We demonstrated the responsibility of the modification of the interfacial water structure by an adsorbed xylitol in the inhibition process. However, interestingly, very close alcohols like ribitol (a diastereomer of xylitol, as shown in Fig 7.1 **b**) were demonstrated in a preliminary study to have little to no effect on the hydrolysis of alumina. We conducted the exact same metadynamics as proposed in chapter 6 but replacing the adsorbed xylitol by ribitol. Surprisingly, as depicted in Fig. 7.1, the hydrolysis Free Energy Surface (FES) obtained in presence of ribitol was very close to the FES obtained in presence of xylitol, despite their different inhibiting capacities. Both of them presented a high free energy barrier ($\geq 150 \text{ kJ}\cdot\text{mol}^{-1}$) associated with the first step of the hydrolysis mechanism. These results would therefore suggest that their inhibiting power was similar. To explain the discrepancy between these results and the experimental evidence, we emitted the hypothesis of different adsorption capabilities between xylitol and ribitol. Indeed, ribitol could have a theoretical inhibiting effect if adsorbed but would actually adsorb in very low quantity at the water/alumina interface.

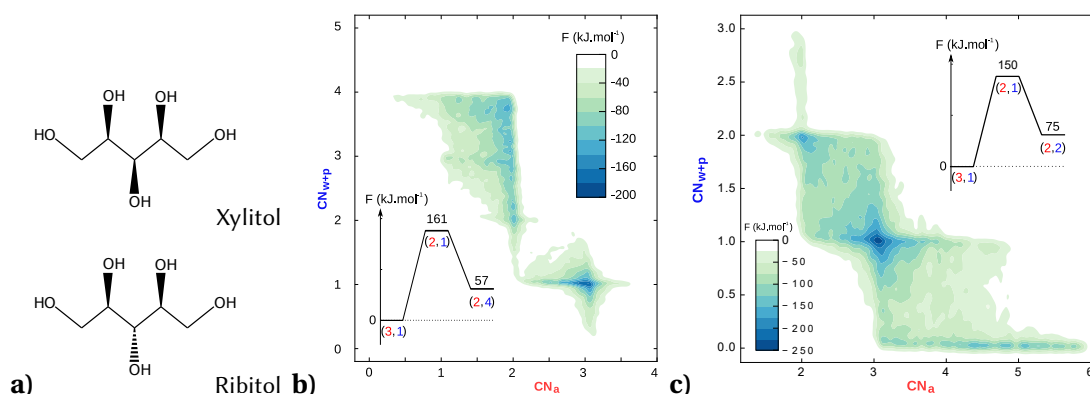


Figure 7.1 – **a**) topological representation of xylitol and ribitol. **b**) and **c**) Free energy surface (FES) corresponding to the hydrolysis of alumina in water, following the same method and conventions as in chapter 7. **b**) FES in presence of an adsorbed xylitol (taken from our previous study). **c**) FES in presence of an adsorbed ribitol.

However, as extensively demonstrated in the precedent chapters of this manuscript, the theoretical description and understanding of the adsorption or desorption of various molecules at the water/solid interface are very challenging. Especially, interfaces between water and oxophilic metallic surfaces or oxide surfaces feature very strong interactions between surface atoms and water molecules that can be responsible for dissociative adsorption of water^{1;2} or surface reconstructions, as highlighted in chapter 6. The resulting surface state can also depend on the presence of molecules adsorbed at the water/solid interface. These surface state modifications should therefore also be accurately sampled to conduct this adsorption study.

Moreover, both xylitol and ribitol are flexible molecules, with numerous alcohol functions, and thus, possible adsorption modes. This flexibility adds considerable complexity to the study of adsorption by enhancing the number of degrees of freedom of the system. As a first test case to both determine the efficiency of the different adsorption investigation methods and to better grasp the difficulties of adsorption studies at such water/alumina interface, we decided to study the adsorption of ethanol instead of xylitol or ribitol. Ethanol stands as a convenient model, small enough to avoid too much sampling, but able to mimic the reactivity of alcohols at the surface of alumina.

Therefore, we investigate herein the adsorption process of ethanol on γ -alumina in water with a panel of different methods to unravel all the important processes involved in the adsorption. This comparison assesses the efficiency of two standard methods for determining reaction free energies from first principles (thermodynamic integration^{3;4} and metadynamics^{5;6}) but also of our simplified hybrid quantum mechanics, molecular mechanics scheme.⁷

Two different adsorption configurations of ethanol were considered, built similarly to the adsorption modes of xylitol proposed in chapter 6: a single-bond non-dissociative mode, where ethanol substitutes a non dissociated water molecule, chemisorbed on an octahedral aluminum atom of the surface (here Al₍₁₎, following Copeland's denomination)⁸, and a bridging dissociative mode, where ethanol is found as a formal ethoxy, bridging between the two octahedral aluminum atoms of the surface (Al₍₁₎ and Al₍₂₎), and replacing a hydroxyl group from a dissociated water molecule (see Fig 7.2). These two modes are dubbed μ_1 and μ_2 , respectively, following the analogous notation for ligands binding to 1 or 2 metallic centers.

At first, this study focuses on the exploration of desorption mechanisms by metadynamics. Then, free energy differences between the key geometries identified by metadynamics are established at different approximated solvation levels. Finally, a thermodynamic integration is employed to refined the activation barriers associated with desorption.

7.2 Computational details

7.2.1 Initial structures

Hydrated γ -alumina (110) initial surface geometries and water structure were taken from our previous study⁹ and referred to as S_{ref} . For dynamics including a water phase, our previous pre-equilibrated water box of approximately 16 Å height was used, complemented with a 14 Å vacuum. For gas-phase static computations, a vacuum phase of 30 Å was used. A second stable hydrated surface geometry is identified during the study and referred to a S_{diss} . A visual comparison of S_{ref} and S_{diss} can be found in the metadynamics section (section 7.3.1, Fig 7.5).

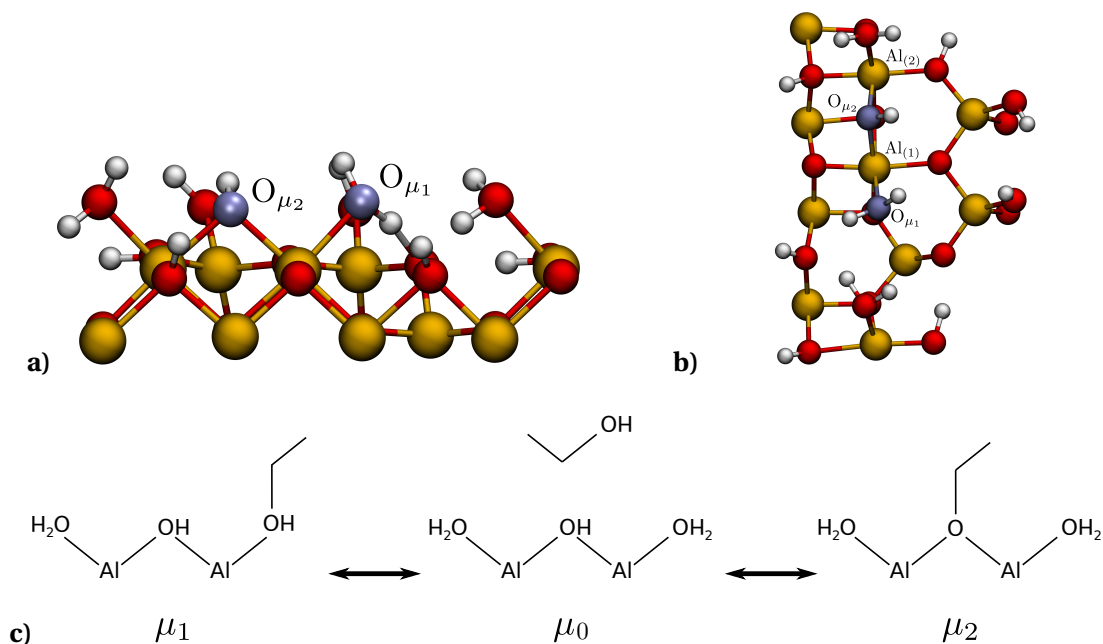


Figure 7.2 – a side and b) top view of the model γ -alumina surface used as hydrated reference surface. Light blue oxygens labeled O_{μ_1} and O_{μ_2} are the two atoms that are substituted to build the μ_1 and μ_2 adsorption mode respectively. c) Schematic representation of the adsorption from a free ethanol (dubbed μ_0) to the μ_1 or μ_2 adsorption mode.

7.2.2 General parameters for DFT dynamics

Following our previous studies, all DFT dynamics were conducted using the CP2K-Quickstep^{10–13} implementation of DFT with Gaussian Plane Wave (GPW) combined approach, with the Perdew-Burke-Ernzerhof (PBE) functional¹⁴ to describe electron interactions, supplemented by Grimme D3 correction¹⁵. Goedecker-Teter-Hutter (GTH) pseudo-potentials^{16–18} for core electrons and a combination of double-zeta (DZVP) basis set and auxiliary plane waves up to 400 Ry for valence density were used. The Self-Consistent Field convergence criterium was set to $5 \cdot 10^{-6}$ Hartree. Dynamic samplings were performed in the NVT thermodynamic ensemble, with a temperature held constant at 330 K *via* a Canonical Sampling through Velocity Rescaling (CSVR) thermostat.¹⁹ The two bottommost layers of alumina were held frozen during dynamics. An integration time step of 0.5 fs was chosen for runs associated with thermodynamic integration, while 1 fs was preferred for metadynamics runs, associated with an increase tripled atomic weight for hydrogen.

7.2.3 Free energy differences

Free energy differences between portions of the Free Energy Surfaces (FES) were computed following the method of Ciacchi and co-workers²⁰:

$$\Delta F = -RT \cdot \ln \left(\frac{c_1}{c_2} \right) \quad (7.1)$$

were c_1 and c_2 are averaged population of two region of the FES (1 and 2) defined by their boundaries ($CV_{i,max}$ and $CV_{i,min}$ for each collective variable i). c are defined as:

$$c(CV_{i,min}, CV_{i,max}, i = 1..N_{CV}) = \frac{1}{\prod_{CV_i} (CV_{i,max} - CV_{i,min})} \int_{CV_{1,min}}^{CV_{1,max}} \dots \int_{CV_{N,min}}^{CV_{N,max}} \exp \left(-\frac{F(x_{CV}^N)}{RT} \right) dx_{CV}^N \quad (7.2)$$

with x_{CV}^N being the coordinate of the system in the N-space defined by the CV. Integration of the free energy along a dimension as used for the representations in section 7.3.1 was obtained using the same equation applied on one CV only.

7.2.4 Specific parametrization for the metadynamics study (section 7.3.1)

For metadynamics,^{5;6} PLUMED²¹ implementation of collective variables was used in combination with CP2K. All coordinations between groups of atoms are considered as defined in plumed with the numerical parameters detailed in Table 7.1. Three collective variables were used.

| type | d_0 | r_0 | n | m |
|------|-------|-------|---|----|
| Al-O | 2.0 | 0.8 | 4 | 10 |
| O-H | 1.9 | 0.4 | 4 | 10 |

Table 7.1 – Numerical parameters used to define the coordination between atoms. Type designs the type of bonds considered for the coordination. d_0 is the central value of the coordination function ($C(d_0) = 1$), r_0 is the acceptance distance of the coordination function, and n and m are two integer exponents with $n \leq m$. At d_0+r_0 , the coordination function is equal to n/m . A visual interpretation of these parameters can be found in Fig. 6.1

The ‘‘Coordination’’ CV was chosen as the coordination between the ethanol’s oxygen and the adsorption site of alumina: $Al_{(1)}$ for the metadynamics starting from μ_1 (see Fig. 7.2) and $Al_{(1)}$ and $Al_{(2)}$ for the metadynamics starting from μ_2 (see Fig. 7.2).

Chapter 7. Adsorption study of ethanol at the γ -alumina/water interface

The “Solvation” CV is designed to account for H-bonds between water molecules and either the anchor aluminum(s) of the surface or with the hydroxyl group of ethanol. It is defined as follow:

$$Solvation = C(O_{ethanol}, H_{water}) + C(H_{ethanol}, O_{water}) + C(Al_n, O_{water})$$

were $C(A, B)$ stands for the coordination between two groups of atoms (A and B). $O_{ethanol}$ stands for ethanol’s oxygen. H_{water} stands for every hydrogen originating from water molecules (free, adsorbed, or dissociated). $H_{ethanol}$ stands for the O–H hydrogen of the adsorbed ethanol (therefore, only for the coordination mode μ_1). O_{water} stands for every oxygen originating from water molecules (free, adsorbed, or dissociated). Al_n stands for $Al_{(1)}$ in the μ_1 metadynamics, and for $Al_{(1)}$ and $Al_{(2)}$ in the μ_2 metadynamics.

Finally, the “Height” CV was chosen as the absolute coordinate of ethanol’s oxygen in the out-of-plane direction.

The biasing potential component added were isotropic Gaussians (along each collective variable) of 0.04 width and deposited at a 10 fs rate. Their height was determined following the well-tempered metadynamics²² scheme, starting from $3.3 \text{ kJ}\cdot\text{mol}^{-1}$ with a bias factor of 100 and a temperature of 330 K.

7.2.5 General parameters for static DFT computations with VASP

For static DFT computations, including these conducted for the MMSolv method, gas-phase adsorption energies were computed using plane-wave DFT as implemented in VASP 5.4.1^{23;24}. The PBE functional was used to describe electron interactions,^{14;25} supplemented by the dDsC dispersion correction^{26;27}. The electron-ion interactions were described by the PAW formalism^{28;29}. The plane-wave energy cutoff was set to 400 eV. Entropic differences associated with adsorptions were estimated following the method exposed in chapter 1.

$$\Delta_{ads}S = S_{aq,rot}(EtOH) + S_{aq,trans}(EtOH) - S_{aq,rot}(water) - S_{aq,trans}(water) \quad (7.3)$$

The experimental value of liquid phase entropy for a water molecule ($S_{aq}(water)$) was used and liquid phase entropic contributions of ethanol were estimated from the gas phase entropic estimates by the empiric relation:³⁰

$$S_{aq}(EtOH) = 0.54 \cdot S_{gas}(EtOH) + 2.759 \cdot 10^{-2} (\text{kJ} \cdot \text{mol}^{-1} \cdot \text{K}^{-1}) \quad (7.4)$$

For implicit solvent computations, the Polarisable Continuum Model (PCM) implemented in the VASPsol module³¹ was used. The default settings for cavitation energy were used.

7.2.6 Molecular mechanics computations with AMBER

For the classical computations of MMSolv, the same computational setup was used as described in chapter 2. However, Lennard-Jones parameters for γ -alumina atoms were taken from the CLAYFF forcefield.³² An additional gaussian attraction between water's oxygen and surface aluminum atoms was also added as described in our previous work.³³ Chemisorbed water molecules (dissociated or not) were also frozen, their Lennard-Jones parameters taken from the UFF forcefield³⁴ and their partial charges extracted from DFT static computations of the hydrated slab, following our method described in chapter 2

7.2.7 Specific parametrization for the Thermodynamic integration study (section 7.3.3)

For the Thermodynamic integration (TI)^{3;4} study, the free energy differences ΔF were calculated by integration of the gradient of F over the parameter z representing the absolute height of the oxygen atom of the ethanol molecule. The free energy gradient was computed along a discretised reaction path with around 20 constrained runs, for z increasing from an initial value just below the equilibrium position of the chemisorbed molecule to $z = 18 \text{ \AA}$, near the zone the bulk water⁹. The starting geometries of each run were obtained *via* a preliminary slow-growth.³⁵ The free energy gradient is given by the ensemble average of the Lagrange multiplier associated with the constraint on z_O in the constrained run. Standard errors on free energies are deduced, after integration, from the standard errors on the gradient by block averaging.³⁶ The first 5 ps of each run were considered necessary for equilibration and thus discarded for the analysis, leaving production times of at least 10 ps each. Some runs ($z = 15.5$ and 17.0 \AA) were extended. In a few cases ($z \geq 13 \text{ \AA}$), preliminary slow growth simulations were performed to displace a water molecule in the space left vacant by the alcohol, in order to decrease the equilibration duration. At distances $z > 14 \text{ \AA}$ from the surface (which correspond to ethanol being further from the surface than the physisorbed water layer,⁹ the structures originating from desorption modes $\mu_1@S_{ref}$ and $\mu_2@S_{ref}$ have been considered to be equivalent, with a free ethanol molecule in liquid water, and only the data gathered in the TI run starting from $\mu_2@S_{ref}$ were used. In the same manner, at distances $z > 12.5 \text{ \AA}$, the windows of the TI originating from $\mu_2@S_{diss}$ are similar to the windows of the TI originating from $\mu_2@S_{ref}$ as the surface has undergone spontaneous reconstruction. Only the data originating from the $\mu_2@S_{ref}$ are therefore used for windows featuring $z > 12.5 \text{ \AA}$.

7.3 Results

7.3.1 Metadynamics

Following our recent studies of alumina hydrolysis, we performed an investigation of the desorptions from two configurations (μ_1 and μ_2) by using metadynamics to enhance the sampling of the desorption free energy surface (FES). The biasing of the FES along three collective variables (CV) was identified as necessary to accelerate the desorption event. The first natural CV to be considered is the relative height of the ethanol compared to the average position of the upper layer of alumina. This CV ensures that the alcohol will move away from the surface and be pushed into the bulk solvent. Besides, the coordination between the alcohol's O and its anchoring(s) Al atom(s) was also found to be an important descriptor of the system because it allows distinguishing a situation where the bond(s) is(are) already broken but the alcohol has not drifted away from the surface. It is of particular importance for the desorption from the μ_2 state where only one of the Al-O bonds can be broken without changing the altitude of the alcohol. Additionally, this coordination cannot simply replace the height CV because a bias along the coordination variable would not push the molecule away from the surface toward the bulk solution and could let it trapped into the physisorbed water layer evidence by Réocreux *et al.*⁹ Last but not least, a solvation coordinate was designed that describes the number of H-bond shared between the alcohol and the water molecules but also the number of water molecules adsorbed on the surface. This CV allows a quick reorganisation of the water structure upon desorption. During this reorganisation, water molecules complete the hydration sphere of the ethanol but also fill the vacant coordination site of the former anchoring Al. The metadynamics of the desorption from the two states were therefore conducted along these three degrees of freedom: the coordination of the alcohol with the surface, the solvation of both the ethanol and the surface, and the altitude of the alcohol's oxygen.

In the free energy surface FES_1 corresponding to the desorption of the ethanol from its μ_1 adsorption mode (see Fig 7.3), two portions are highlighted using different colour scales, corresponding to the desorbed (μ_0 , in green) and adsorbed (μ_1 , in blue) state of the ethanol. As depicted in the solvation/height representation, the portion of the phase space corresponding to μ_1 is quite narrow, constraint to a small absolute height (12 Å at maximum, approximately *i.e.* 2 Å away from to the surface), but also to small solvation value (≤ 4 corresponding to one water molecule co-adsorbed on $Al_{(1)}$, and one hydrogen bond formed between ethanol's oxygen and a water molecule). On the contrary, the μ_0 portion is quite large and the full sampling of the corresponding phase space cannot be successfully achieved because the height can rise up indefinitely which is a problem in a finite size simulation box. Also, the solvation value in this portion is higher (from 4 to 8), because after desorption of the alcohol, water molecules can replace the alcohol to complete $Al_{(1)}$ coordination and at the same time, the ethanol can form more H-bonds with neighbouring water molecules. The second representation allows

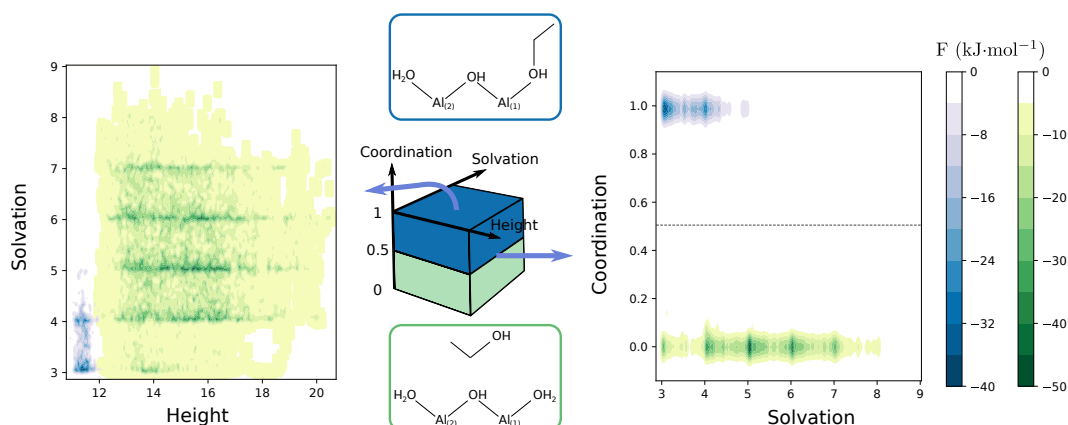


Figure 7.3 – 2D representations of the 3D free energy surface FES_1 of the desorption of ethanol from its μ_1 adsorption mode on the alumina surface. Two portions of phase spaces are represented by two different colour scales: in blue for the adsorbed μ_1 ethanol (Coordination > 0.5) and in green for the desorbed μ_0 ethanol (Coordination < 0.5). The grey line represents the boundaries of the colour scales. The **middle** schematics depicts the cubic 3-dimensional FES and a schematic representation of μ_0 and μ_1 . On the **left**, the FES in function of the solvation and absolute height, obtained by integrating out the surface/ethanol coordination variable (see 7.2). On the **right**, the FES in function of the surface/ethanol coordination and the solvation degrees of freedom, obtained by integrating out the solvation variable (see 7.2). Both representations share the same energy scales.

a better understanding of this μ_0 portion, by integrating the multiple close local minima depending on the height in a more limited number of solvation-dependant minima. Based on the analysis of F in the well corresponding to the adsorbed state (see Eq. 7.2) a free energy barrier of $\Delta_{desorption}F^\ddagger(\mu_1) = 35 \text{ kJ}\cdot\text{mol}^{-1}$ was found, assorted with a desorption energy of $\Delta F_{desorption}(\mu_1) = -9 \text{ kJ}\cdot\text{mol}^{-1}$. The desorption would therefore be slightly exothermic and kinetically easy which implies a very low amount of adsorbed ethanol as μ_1 on the surface. Also, noticeably, prior to desorption from the μ_1 state, an increase in solvation is observed, suggesting the necessity of adsorption of an additional water molecule on $\text{Al}_{(1)}$ to trigger the desorption of ethanol. This mechanistic clue is not only important to better understand the global desorption process, but it also rationalises the necessity of the solvation CV, as free energy barriers of approximately $30 \text{ kJ}\cdot\text{mol}^{-1}$ are observed along this coordinate. Indeed, because of the bias imposed along the solvation CV, additional water molecules will be pulled to the aluminum site, thus allowing a new desorption path that could have been missed in absence of this bias.

However, while the free energy barriers can be considered as relatively reasonable, less confidence can be put in the free energy difference with the μ_0 state. Indeed, as mentioned early, the upper bound of the height variable is ill-defined which implies an incomplete sampling of the μ_0 state which could be more stabilised than these results suggest.

To compare the desorption from μ_1 to the desorption from μ_2 , another metadynamics was used, resulting in FES_2 (see Fig 7.4). FES_2 was divided into three sub-portions, to distinguish the fully adsorbed state μ_2 , the half-desorbed state $\mu_{1,bis}$ where only one Al-O bond still

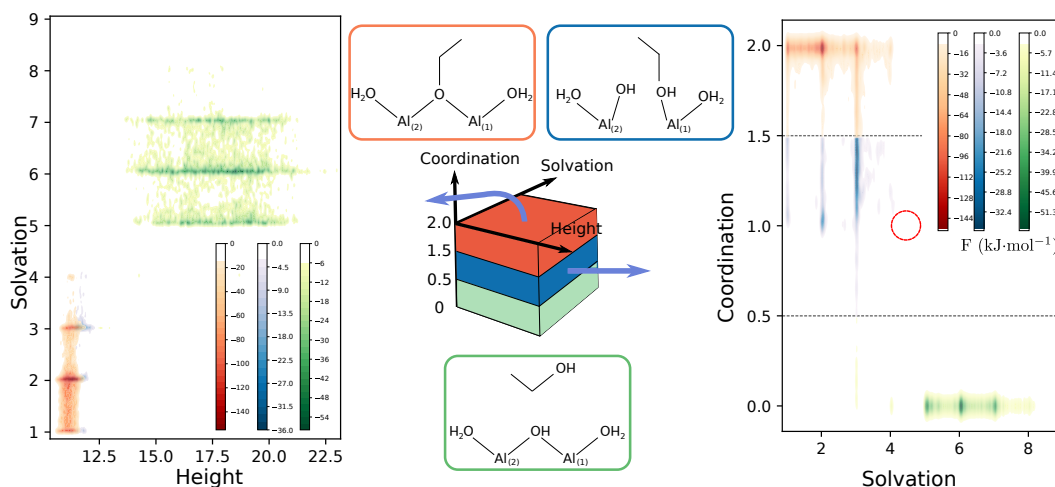


Figure 7.4 – 2D representations of the 3D free energy surface FES_2 of the desorption of ethanol from its μ_2 adsorption mode on the alumina surface. Three portions of phase spaces are represented by three different colour scales: in orange for the fully adsorbed μ_2 ethanol (Coordination > 1.5), in blue for the partially desorbed ethanol $\mu_{1,bis}$, only linked by one bond to the surface aluminum ($1.5 > \text{Coordination} > 0.5$), and in green for the desorbed μ_0 ethanol (Coordination < 0.5). The grey line represents the boundaries of the colour scales. The **middle** schematics depicts the cubic 3-dimensional FES and a schematic representation of μ_0 , $\mu_{1,bis}$, and μ_2 . On the **left**, the FES in function of the solvation and absolute height, obtained by integrating out the surface/ethanol coordination variable (see 7.2). On the **right**, the FES in function of the surface/ethanol coordination and the solvation degrees of freedom, obtained by integrating out the solvation variable (see 7.2). The red circle stands for the approximate coordinates of the μ_1 geometry used in the study of FES_1 , but here evaluated with the CV used in the study of FES_2 .

connects the ethanol to the surface, and the fully desorbed state μ_0 . The mono-coordinate state of ethanol $\mu_{1,bis}$ explored in FES_2 differs from the μ_1 state of the previous FES_1 . Indeed, if both these modes feature mono-adsorbed ethanol on $Al_{(1)}$, they are distinguished by the position of the ethanol relative to $Al_{(2)}$. In the μ_1 adsorption mode, ethanol is placed away from $Al_{(2)}$, while it is closer in $\mu_{1,bis}$. Once again, we retrieve a very narrow phase space, confined around 11.3 Å for the μ_2 and $\mu_{1,bis}$ and a wide one at a higher distance for μ_0 . The path taken during the desorption (from μ_2 , at the coordinate (2,2)) is evidenced in the representation on the right. Direct desorption, at constant solvation, only leads to a dead-end as $\mu_{1,bis}$ in (2,1) that does not lead to a fully desorbed μ_0 state. Actual desorption instead requires a prior increase in the solvation of one of the anchoring aluminum atom to μ_2 in (3,2) before the breaking of the two Al-O bonds (to $\mu_{1,bis}$ in (3,1) and to μ_0 in (3,0)). Afterward, the solvation rises again with the constitution of the solvation sphere of ethanol and the replacement of the ethanol by a water molecule on the surface. In Fig 7.4, the red circle indicates the coordinates of μ_1 as evaluated in the CV space of FES_2 (which differs slightly from its coordinates in FES_1 as the CV are not exactly similar). It can be observed that this position of the FES is not explored during the metadynamics starting from μ_2 and that it is not part of the desorption path. This difference in the spatial arrangement between μ_1 and $\mu_{1,bis}$, therefore is reflected on the CV coordinates. Mechanistically, it means that the μ_1 state studied in the first metadynamics is not an intermediate state in the desorption from μ_2 .

Another important feature of the system encountered during the metadynamics was the spontaneous modification of the surface state of the alumina that was experienced only when ethanol was adsorbed as μ_2 . Indeed, in presence of the bidentate alcohol, a nearby chemisorbed water molecule underwent dissociation. Such dissociation was never observed in presence of a μ_1 adsorbed ethanol, nor in absence of the ethanol. It is possible that the adsorbed ethoxy acts as a pivot to allow hydrogen hopping between surface oxygen, enabling fast exchanges that can conduct to other stable states. Consequently, even after the desorption of the ethoxy, during the metadynamics run, no spontaneous return to the initial surface state was observed. This means that μ_1 and μ_2 cannot be linked to a common μ_0 configuration by these two metadynamics as the final surface state of alumina differs between the two simulations because of the water dissociation. From now on, the standard reference surface state, as evidenced in our previous study of γ -alumina in water is dubbed S_{ref} while the novel surface state, presenting an additional dissociated water molecule is dubbed S_{diss} . Both are represented in Fig. 7.5. This dissociation is invisible in the CV space of the metadynamics, and therefore cannot be observed in the represented FES. This evidences a critical problem of standard metadynamics because only the starting geometry of the simulation is imposed and it may be difficult to connect it to a reference state.

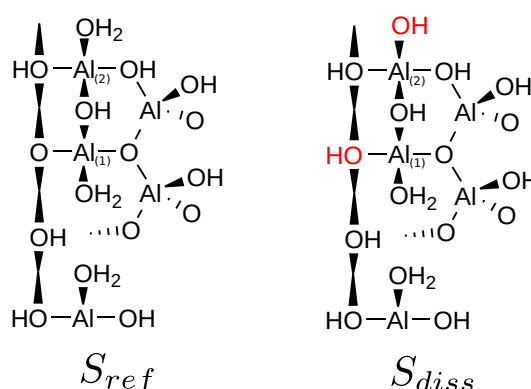


Figure 7.5 – Schematic representation of the two surfaces S_{ref} and S_{dis} . The red atoms underline the difference between the two surfaces.

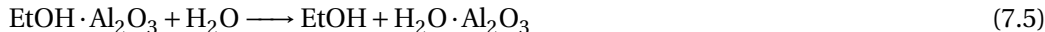
In FES₂, no local free energy minimum was observed for $\mu_{1,bis}$ in (3,1), suggesting that the mono-adsorbed state is not stable and that only one transition state exists between μ_2 in (3,2) and μ_0 in (3,0), that is situated around (3,0.5). A total barrier of $\Delta F^\ddagger = 149 \text{ kJ}\cdot\text{mol}^{-1}$ was found (from μ_2 to μ_0), assorted with a total desorption energy of $\Delta F = 97 \text{ kJ}\cdot\text{mol}^{-1}$. This difference can hardly be interpreted in comparison to the one associated with μ_1 as it is coupled with the free energy of dissociation of a nearby water molecule. Hence, here $\Delta F = F(\mu_0 + S_{diss}) - F(\mu_2@S_{ref})$.

Overall, the metadynamics has proven itself useful for exploring the mechanism of desorption from the μ_1 mode and allowed an evaluation of the associated desorption free energy barrier

$\Delta_{desorption}F^\ddagger(\mu_1)$. However, because of the unbounded nature of our height CV, our estimation of the desorption free energy difference $\Delta_{desorption}F(\mu_1)$ is questionable. Interestingly, in the case of desorption from μ_2 , a different desorbed state as the reference one was found, even if the free energy difference computed by metadynamics is related to S_{diss} whose stability compared to our reference state S_{ref} is unknown. However, metadynamics has allowed us to understand that the surface state was of importance in the adsorption mechanism, that the two mono-adsorbed states μ_1 and $\mu_{1,bis}$ were not equivalent, and provided us with configurations for these chemically relevant surface states that can be exploited by static methods. Metadynamics also proved the importance of an increase of the surface solvation prior to any desorption. Therefore, the metadynamics study has provided us a meaningful mechanistic insight even if its energetic evaluation must be completed by other methods.

7.3.2 Thermodynamic differences

Based on the information and structures gathered by metadynamics, we performed a thermodynamic study of the desorption from the two μ_1 and μ_2 adsorption modes, combined with the two different surface states S_{diss} and S_{ref} . In this part, free energy differences are computed based on the two following substitution reactions for μ_1 and μ_2 adsorption mode respectively:



At first, a pure gas-phase approach, completely neglecting solvent effects, has been adopted in order to provide an estimate of the interaction energy between ethanol and the hydrated aluminum surface. We chose to consider substitution reactions of water molecules by ethanol on a fully hydrated surface, *i.e.* covered by chemisorbed water molecules (some dissociated) as proposed by Reocreux *et al.* The standard energy substitution difference is also supplemented by an approximated entropy difference, deduced from rotational and translational entropy of ethanol and water (see computational details). The result are here presented in Fig. 7.6 (middle). It appears that in absence of solvent, the reference surface model S_{ref} established in the literature⁹ is less stable by 9 $\text{kJ} \cdot \text{mol}^{-1}$ than the surface state S_{diss} presenting an additional dissociated water molecule adsorbed on its surface. S_{diss} is even more stabilised in presence of an adsorbed ethanol in μ_2 by 10 $\text{kJ} \cdot \text{mol}^{-1}$. However, if ethanol is adsorbed in μ_1 , this surface state is destabilised by 17 $\text{kJ} \cdot \text{mol}^{-1}$, thus becoming less stable than S_{ref} . Therefore, the only

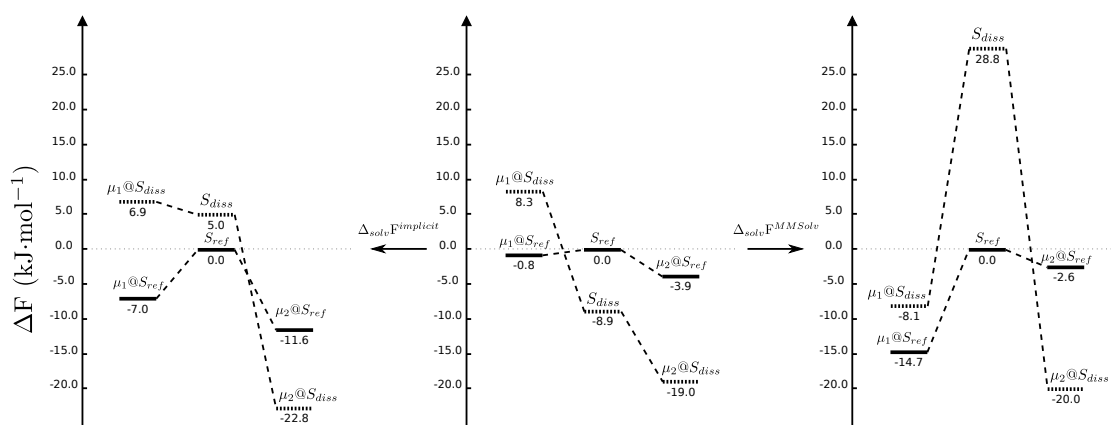


Figure 7.6 – Free energy level of the two adsorption mode μ_1 and μ_2 on the two considered surface S_{ref} and S_{diss} . The gas phase free energies are presented in the **middle** plot, the free energy level in implicit solvent are presented on the **left**, and the free energy level computed in the MMSolv scheme are presented on the **right**. All free energies are given in $\text{kJ}\cdot\text{mol}^{-1}$ relatively to S_{ref} for each different method.

situation where S_{ref} is the most stable surface state is when ethanol is adsorbed in μ_1 , and even in this case, it is less stable by $9 \text{ kJ}\cdot\text{mol}^{-1}$ than a raw S_{diss} , meaning that the adsorption of ethanol in μ_1 is quite limited.

Upon the inclusion of an implicit solvent, the relative stability of these surface states and adsorption modes is modified as pictured in Fig. 7.6 (left). Indeed, in absence of adsorbed ethanol, S_{ref} is found slightly more stable than S_{diss} (by $5 \text{ kJ}\cdot\text{mol}^{-1}$). However, the relative stability of S_{ref} and S_{diss} when ethanol is adsorbed (as either μ_1 or μ_2) is not strongly impacted by the inclusion of the implicit solvent. Their relative stability is only reduced by $4 \text{ kJ}\cdot\text{mol}^{-1}$ under μ_2 adsorption and increased by $5 \text{ kJ}\cdot\text{mol}^{-1}$ under μ_1 adsorption. Noticeably also, $\mu_1@S_{ref}$ becomes more stable than any bare surface (S_{ref} or S_{diss}), meaning that adsorption as μ_1 is possible. Overall, these results tell us that the better stability of S_{ref} compared to S_{diss} in absence of ethanol is due to solvent effects (that are partially reproduced here by implicit solvation), which is compatible with the surface model of alumina in water established by Réocreux and co-workers.⁹ These observations are also in line with the result observed in our metadynamics, as the S_{diss} state is only observed to be more stable than S_{ref} in presence of an adsorbed ethanol as μ_2 .

However, if the implicit solvent is well suited to describe indirect solvation effects like long-range electrostatic interactions modification, it cannot provide a proper estimate of another massive enthalpic contribution: the rearrangement of the hydrogen bonding network. In order to overcome this problem, we used the MMSolv technique introduced in chapter 2 to compute solvation free energy difference between the different adsorption modes and surfaces. This technique proceeds by freezing the surface and adsorbate in a given geometry and conducting a full sampling of the water phase *via* Molecular mechanics (MM) in order to determine the solvation difference between two states. MMSolv can therefore be considered

as a static method, even if it implies a dynamic sampling of the water phase, as it computes free energy difference between fixed conformations of the surface and adsorbates.

The inclusion of this explicit solvation contribution to the free energy differences aforementioned modifies again the relative stability of the adsorption modes and surface state as depicted in Fig. 7.6 (right). Some of the solvation effects already observed upon the inclusion of the implicit solvent are even enhanced, as the reduced stability of S_{diss} compared to S_{ref} that peaks at $29 \text{ kJ}\cdot\text{mol}^{-1}$, or the increased stability of the adsorption mode μ_1 , on both S_{diss} and S_{ref} compared to the raw surfaces. However, for μ_2 adsorption mode, almost no change in stability is observed compared to gas phase adsorption, contrasting with the increased stability predicted by the implicit solvent method for the $\mu_2@S_{ref}$ adsorption. As a result, if similar trends as in implicit solvation are observed (S_{ref} surface state is favoured over S_{diss} except for μ_2 adsorption, that is the most stable adsorption mode), several important energy differences are reduced, as the difference between $\mu_1@S_{ref}$ and $\mu_2@S_{diss}$ of $5 \text{ kJ}\cdot\text{mol}^{-1}$ that falls into the estimated uncertainty level of the method (estimated around $4 \text{ kJ}\cdot\text{mol}^{-1}$).⁷

Overall, a few qualitative trends emerge from those computations with both solvation models: (i) S_{ref} is the most stable bare surface state, (ii) $\mu_1@S_{ref}$ is consistently more stable than $\mu_1@S_{diss}$, while (iii) $\mu_2@S_{diss}$ is more stable than $\mu_2@S_{ref}$. These three observations are consistent with the result from our metadynamics study but also with S_{ref} being the standard surface state model for alumina under water. More important differences are found between the two solvation models in the free energy differences between the surface state model and the different adsorption modes. The most noticeable of these differences is the much more exothermic adsorption from S_{ref} to $\mu_1@S_{ref}$ predicted by MMSolv than in an implicit solvent, which is also in contradiction with the metadynamics results that predicted an endothermic adsorption. In order to confirm these trends, but also to complete these thermodynamic differences with kinetic information, the Thermodynamic Integration method was employed.

7.3.3 Thermodynamic Integration

Thermodynamic integrations (TI) were used to investigate the complete desorption pathway from μ_1 and μ_2 , and determine the free energy barrier hindering the desorption or adsorption. The free energy profile along the altitude of ethanol's oxygen was investigated starting from three initial geometries: $\mu_2@S_{diss}$, $\mu_2@S_{ref}$, and $\mu_1@S_{ref}$.

As presented in Fig 7.7, the three desorption profiles determined by TI are rather similar. They all present a transition state in the area of the physisorbed water layer around 12.5 \AA . Also, it must be noticed that the tails of the profiles are here merged above a certain z threshold (see computational details), as ethanol can be considered as μ_0 , which does not depend anymore on the initial geometry. Indeed, oppositely to metadynamics, for TI windows with $z > 12.5 \text{ \AA}$, the surface underwent a spontaneous reconstruction from S_{diss} to S_{ref} during the TI starting

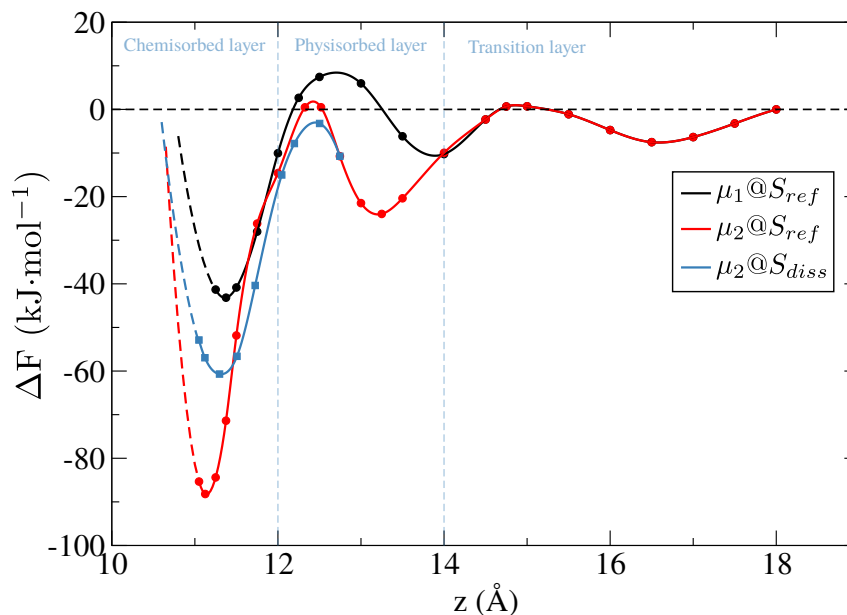


Figure 7.7 – Free energy profiles $\Delta F(z)$ computed with thermodynamic integrations for the desorption from $\mu_2@S_{diss}$, $\mu_2@S_{ref}$, and $\mu_1@S_{ref}$. The dashed parts of the profiles represent an extrapolation at small z determined by a quadratic fit. The light blue vertical lines represent the limit of the structured water layers of water evidenced by Réocreux and co-workers⁹

from $\mu_2@S_{diss}$. All surface states are therefore similar (S_{ref}) above 12.5 Å, thus justifying the merging of the tails. Noticeably, the tails of the profiles continue to oscillate even at long distances. This behaviour indicates that the sampling of the μ_0 region is not totally sufficient. Indeed, given the large space associated with this system, unreasonable sampling time would be required to sample all the degrees of freedom that would affect the forces applied on the ethanol (like diffusion in the in-plane direction for example).

Based on these profiles, desorption free energy and associated activation barriers were determined (see Fig 7.8), following the same averaging method as described in computational details but along a single dimension. These levels indicate that according to this method, $\mu_2@S_{ref}$ is actually more stable than $\mu_2@S_{diss}$, which contradicts both previous metadynamics predictions and static thermodynamic differences. Moreover, both the predicted stability and desorption barrier from $\mu_1@S_{ref}$ are very different between the TI results and the metadynamics ones. However, because of the fluctuation in the tail of the profile, the resulting level of μ_0 is again uncertain. However, the desorption mechanism observed is here different, as, in all of these simulations, the desorption happens prior to any co-adsorption of a water molecule on the anchoring Al atom or atoms, a consequence of using z as the only CV. It was even often necessary to manually pull water molecules at the adsorption site after the desorption (and therefore to cross the approximately 30 kJ·mol⁻¹ barriers evidenced with metadynamics). Oppositely, the building of additional H-bonds between the ethanol and

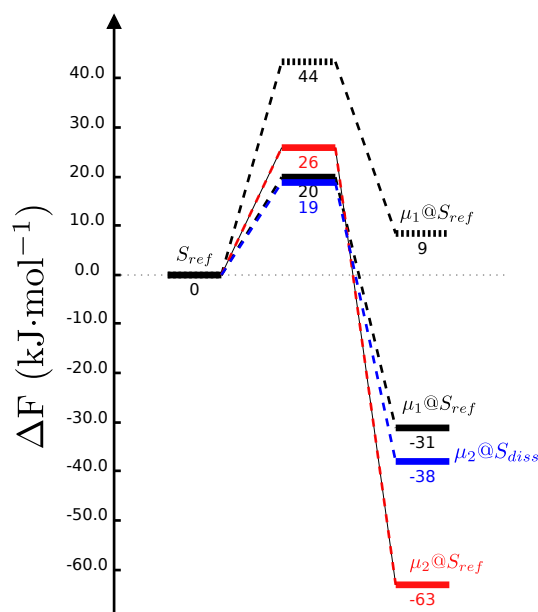


Figure 7.8 – Free energy level $\Delta F(z)$ computed with thermodynamic integrations (full lines) or metadynamics (dashed line) for the desorption from $\mu_2@S_{diss}$, $\mu_2@S_{ref}$, and $\mu_1@S_{ref}$. All free energy levels are determined by the weighted average method described in computational details with $z_0 = 12.5$ Å taken as boundary between the two region of the curve (adsorbed for $z < z_0$, desorbed for $z > z_0$). Figures are given within a $3 \text{ kJ}\cdot\text{mol}^{-1}$ uncertainty.

surrounding water molecules and also the reprotonation of the ethanol in μ_2 were observed before the desorption itself. It must therefore be considered that the desorption path observed here is different from the one of metadynamics. In both pathways, the solvation must be raised prior to desorption but in the TI one, this increase is due to stronger solvation of ethanol, while in metadynamics the solvation raise is due to the coordination of more water molecules on the surface aluminum atom. These differences could explain the divergences between the free energy profiles as the activation barrier of all these transverse degrees of freedom are invisible in these results.

Overall, the results of TI are difficult to interpret in relation to the previous ones. Independently considered, they stand as perfectly reasonable but they are not consistent with our previous findings. However, they highlighted again the importance of the transverse motion in the rare events methods study as these invisible hindered degrees of freedom can change the shape of the desorption free energy profile.

7.4 Conclusion and discussion

We investigated the desorption of the ethanol from the γ -alumina/water interface, as a test-case to study the desorption of xylitol and ribitol. The desorptions from two kinds of adsorption modes were investigated: μ_1 , a monodentate adsorption mode, and μ_2 a dissociative bidentate

mode. Because direct sampling of the desorptions cannot be achieved in a reasonable time, we used three complementary approximate methods, with different underlying assumptions. Metadynamics was used to compare the desorption mechanism between μ_1 and μ_2 and pointed out the predominance of an alternative surface state S_{diss} (compared to S_{ref} , evidence by Réocreux *et al.*⁹) in presence of an adsorbed ethanol as μ_2 . Also, during the metadynamics runs an increase of the surface solvation of the alumina was observed prior to desorption from both μ_1 and μ_2 . Only the desorption free energy associated to the μ_1 adsorption mode was determined and found to be slightly negative ($\Delta F_{desorption}(\mu_1) = -9 \text{ kJ}\cdot\text{mol}^{-1}$), associated with a relatively small desorption free energy barrier ($\Delta_{desorption}F^\ddagger(\mu_1) = 35 \text{ kJ}\cdot\text{mol}^{-1}$). Two methods of thermodynamic free energy differences (featuring implicit or explicit solvation) confirmed the increased stability of S_{diss} in presence of ethanol adsorbed as μ_2 but predicted a positive desorption free energy from the μ_1 adsorption mode ($7 \text{ kJ}\cdot\text{mol}^{-1}$ for implicit solvation, and $15 \text{ kJ}\cdot\text{mol}^{-1}$ for explicit solvation). Thermodynamic Integration runs, however, predicted an even more stable μ_1 adsorption mode with an associated desorption free energy of $31 \text{ kJ}\cdot\text{mol}^{-1}$ and a more important desorption free energy barrier compared to metadynamics ($\Delta_{desorption}F^\ddagger(\mu_1) = 51 \text{ kJ}\cdot\text{mol}^{-1}$). Also, according to thermodynamic integration, S_{ref} is more stable than S_{diss} upon the adsorption of ethanol as μ_2 ($\Delta F_{desorption}(\mu_2@S_{ref}) = 63 \text{ kJ}\cdot\text{mol}^{-1}$ against $\Delta F_{desorption}(\mu_2@S_{diss}) = 38 \text{ kJ}\cdot\text{mol}^{-1}$). Overall, the three methods reached the same qualitative conclusion about the more important stability of the μ_2 adsorption mode compared to μ_1 . However, it remains unclear if the surface state S_{diss} is more stable than S_{ref} in presence of an adsorbed ethanol as μ_2 , as only two of the three methods agree on this point. The importance of solvation and the difficulty to sample the reorganisation of the water structure at the interface was evidenced in the mechanism of metadynamics and the difficulty to re-adsorb water molecules after the desorption of ethanol during TI.

The remaining uncertainties about the desorption free energies still advocate against the direct application of these methods to the desorption of xylitol and ribitol as even more conformation sampling problems are expected. However, several leads can be proposed to enhance the quality of each method individually. Metadynamics could use an additional CV to bias the dissociation of the water molecule distinguishing S_{diss} from S_{ref} in order to explore the transition between these two surface states. The MMSolv method used to compute the direct free energy differences could be improved by the use of a better force field to describe the interactions between water and the surface without freezing chemisorbed molecules. Thermodynamic Integration results could also be improved by increasing the equilibration phase conducted for each window (possibly at the molecular mechanics level). Disposing of these three methods could thus be a benefit to assess the continuous improvement of each of them until they converge to similar conclusions not only qualitatively but also quantitatively.

Bibliography

- [1] Digne, M.; Sautet, P.; Raybaud, P.; Euzen, P.; Toulhoat, H. Hydroxyl Groups on γ -Alumina Surfaces: A DFT Study. *J. Catal.* **2002**, *211*, 1–5.
- [2] Wischert, R.; Laurent, P.; Coperet, C.; Delbecq, F.; Sautet, P. gamma-Alumina: The Essential and Unexpected Role of Water for the Structure, Stability, and Reactivity of “Defect” Sites. *J. Am. Chem. Soc.* **2012**, *134*, 14430–14449, WOS:000308283200031.
- [3] Kirkwood, J. G. Statistical Mechanics of Fluid Mixtures. *J. Chem. Phys.* **1935**, *3*, 300–313.
- [4] Martins, S. A.; Sousa, S. F.; Ramos, M. J.; Fernandes, P. A. Prediction of Solvation Free Energies with Thermodynamic Integration Using the General Amber Force Field. *J. Chem. Theory Comput.* **2014**, *10*, 3570–3577.
- [5] Laio, A.; Parrinello, M. Escaping free-energy minima. *PNAS* **2002**, *99*, 12562–12566, Publisher: National Academy of Sciences Section: Physical Sciences.
- [6] Laio, A.; Gervasio, F. L. Metadynamics: a method to simulate rare events and reconstruct the free energy in biophysics, chemistry and material science. *Rep. Prog. Phys.* **2008**, *23*.
- [7] Clabaut, P.; Schweitzer, B.; Götz, A. W.; Michel, C.; Steinmann, S. N. Solvation Free Energies and Adsorption Energies at the Metal/Water Interface from Hybrid Quantum-Mechanical/Molecular Mechanics Simulations. *J. Chem. Theory Comput.* **2020**, *16*, 6539–6549.
- [8] Copeland, J. R.; Santillan, I. A.; Schimming, S. M.; Ewbank, J. L.; Sievers, C. Surface Interactions of Glycerol with Acidic and Basic Metal Oxides. *J. Phys. Chem. C* **2013**, *117*, 21413–21425, Publisher: American Chemical Society.
- [9] Réocreux, R.; Jiang, T.; Iannuzzi, M.; Michel, C.; Sautet, P. Structuration and Dynamics of Interfacial Liquid Water at Hydrated γ -Alumina Determined by ab Initio Molecular Simulations: Implications for Nanoparticle Stability. *ACS Appl. Nano Mater.* **2018**, *1*, 191–199.
- [10] VandeVondele, J.; Krack, M.; Mohamed, F.; Parrinello, M.; Chassaing, T.; Hutter, J. Quickstep: Fast and accurate density functional calculations using a mixed Gaussian and plane waves approach. *Comput. Phys. Commun.* **2005**, *167*, 103–128, WOS:000228421500005.
- [11] VandeVondele, J.; Hutter, J. Gaussian basis sets for accurate calculations on molecular systems in gas and condensed phases. *J. Chem. Phys.* **2007**, *127*, 114105, WOS:000249667400011.
- [12] Lippert, G.; Hutter, J.; Parrinello, M. A hybrid Gaussian and plane wave density functional scheme. *Mol. Phys.* **1997**, *92*, 477–487, WOS:A1997YC60700017.

- [13] Hutter, J.; Iannuzzi, M.; Schiffmann, F.; VandeVondele, J. CP2K: atomistic simulations of condensed matter systems. *WIREs Comput Mol Sci* **2014**, *4*, 15–25.
- [14] Perdew, J. P.; Burke, K.; Ernzerhof, M. Generalized Gradient Approximation Made Simple. *Phys. Rev. Lett.* **1996**, *77*, 3865–3868.
- [15] Grimme, S.; Antony, J.; Ehrlich, S.; Krieg, H. A consistent and accurate *ab initio* parametrization of density functional dispersion correction (DFT-D) for the 94 elements H-Pu. *J. Chem. Phys.* **2010**, *132*, 154104.
- [16] Goedecker, S.; Teter, M.; Hutter, J. Separable dual-space Gaussian pseudopotentials. *Phys. Rev. B* **1996**, *54*, 1703–1710, WOS:A1996UZ86100053.
- [17] Hartwigsen, C.; Goedecker, S.; Hutter, J. Relativistic separable dual-space Gaussian pseudopotentials from H to Rn. *Phys. Rev. B* **1998**, *58*, 3641–3662, WOS:000075616800043.
- [18] Krack, M. Pseudopotentials for H to Kr optimized for gradient-corrected exchange-correlation functionals. *Theor. Chem. Acc.* **2005**, *114*, 145–152, WOS:000232053800020.
- [19] Bussi, G.; Donadio, D.; Parrinello, M. Canonical sampling through velocity rescaling. *J. Chem. Phys.* **2007**, *126*, 014101, WOS:000243380000005.
- [20] Schneider, J.; Colombi Ciacchi, L. Specific Material Recognition by Small Peptides Mediated by the Interfacial Solvent Structure. *J. Am. Chem. Soc.* **2012**, *134*, 2407–2413.
- [21] Tribello, G. A.; Bonomi, M.; Branduardi, D.; Camilloni, C.; Bussi, G. PLUMED 2: New feathers for an old bird. *Comput. Phys. Commun.* **2014**, *185*, 604–613, WOS:000329537500020.
- [22] Barducci, A.; Bussi, G.; Parrinello, M. Well-Tempered Metadynamics: A Smoothly Converging and Tunable Free-Energy Method. *Phys. Rev. Lett.* **2008**, *100*.
- [23] Kresse, G. Ab initio molecular dynamics for liquid metals. *J. Non-Cryst. Solids* **1995**, *192-193*, 222–229.
- [24] Kresse, G.; Furthmüller, J. Efficiency of ab-initio total energy calculations for metals and semiconductors using a plane-wave basis set. *Computational Materials Science* **1996**, *6*, 15–50.
- [25] Perdew, J. P.; Wang, Y. Accurate and simple analytic representation of the electron-gas correlation energy. *Phys. Rev. B* **1992**, *45*, 13244–13249.
- [26] Steinmann, S. N.; Corminboeuf, C. Comprehensive Benchmarking of a Density-Dependent Dispersion Correction. *J. Chem. Theory Comput.* **2011**, *7*, 3567–3577.
- [27] Gautier, S.; N. Steinmann, S.; Michel, C.; Fleurat-Lessard, P.; Sautet, P. Molecular adsorption at Pt(111). How accurate are DFT functionals? *Phys. Chem. Chem. Phys.* **2015**, *17*, 28921–28930.

Chapter 7. Adsorption study of ethanol at the γ -alumina/water interface

- [28] Blochl, P. E. Projector augmented-wave method. *Phys. Rev. B* **1994**, *50*, 17953.
- [29] Kresse, G.; Joubert, D. From ultrasoft pseudopotentials to the projector augmented-wave method. *Phys. Rev. B* **1999**, *59*, 1758.
- [30] Wertz, D. H. Relationship between the gas-phase entropies of molecules and their entropies of solvation in water and 1-octanol. *J. Am. Chem. Soc.* **1980**, *102*, 5316–5322.
- [31] Mathew, K.; Sundararaman, R.; Letchworth-Weaver, K.; Arias, T. A.; Hennig, R. G. Implicit solvation model for density-functional study of nanocrystal surfaces and reaction pathways. *J. Chem. Phys.* **2014**, *140*, 084106.
- [32] Skelton, A. A.; Fenter, P.; Kubicki, J. D.; Wesolowski, D. J.; Cummings, P. T. Simulations of the Quartz(101 $\bar{1}$)/Water Interface: A Comparison of Classical Force Fields, Ab Initio Molecular Dynamics, and X-ray Reflectivity Experiments. *J. Phys. Chem. C* **2011**, *115*, 2076–2088.
- [33] Rey, J.; Blanck, S.; Clabaut, P.; Loehlé, S.; Steinmann, S.; Michel, C. Transferable Gaussian Attractive Potentials for Organic/oxide Interfaces. **2021**, Publisher: ChemRxiv.
- [34] Rappe, A. K.; Casewit, C. J.; Colwell, K. S.; Goddard, W. A.; Skiff, W. M. UFF, a full periodic table force field for molecular mechanics and molecular dynamics simulations. *J. Am. Chem. Soc.* **1992**, *114*, 10024–10035.
- [35] Margl, P.; Lohrenz, J. C. W.; Ziegler, T.; Blöchl, P. E. A Dynamical Density Functional Study on the Reaction of Ethylene with $\text{Cp}_2\text{Zr}(\text{C}_2\text{H}_5)^+$. *J. Am. Chem. Soc.* **1996**, *118*, 4434–4441.
- [36] Flyvbjerg, H.; Petersen, H. G. Error estimates on averages of correlated data. *J. Chem. Phys.* **1989**, *91*, 461–466, Publisher: American Institute of Physics.



Conclusions and Outlook

In the present Ph.D. thesis, we investigated the relations between adsorption and solvation at the water/solid interface. Many tools required to conduct these investigations were either missing from the literature or lack accuracy and/or transferability across solvents and solids. We developed several tools to fill these gaps, by combining ideas and methods from previous studies, and refining or adapting them to water/solid interfaces. Using these tools, we demonstrated the impact of solvation on adsorption energies, but also the effect of the presence of adsorbates at the water/solid interface and the structuration of the water phase and the surface state of solids.

In the first part, we have built the MMSolv method and implemented it as in an easy-to-use computational tool, SolvHybrid, to determine the adsorption free energy of compounds on Pt (111) surfaces. We benchmarked this method against experimental values and an implicit solvation model. Based on experimental reference data, we have shown the greater and more realistic impact of explicit molecular mechanics solvation (around $10 \text{ kcal}\cdot\text{mol}^{-1}$ error to experimental) compared to implicit solvation (around $40 \text{ kcal}\cdot\text{mol}^{-1}$ error to experimental). In the future, the MMSolv method could be expanded to other surfaces and even solvents. The main requirement for wider applicability is for accurate force fields, able to reproduce realistically interactions between a solid and liquid molecules.


This is why, in the second part, interactions between water molecules and diverse metallic surfaces were investigated. Two generations of force fields were built to remedy two deficits from the literature: water/metallic alloy interactions, and water/nanoparticle interactions. These two force fields demonstrated an accuracy of about $1 \text{ kcal}\cdot\text{mol}^{-1}$ in reproducing the adsorption energies of single water molecules on diverse metallic surfaces. However, the problem of a lack of synergistic adsorption term between several co-adsorbed water molecules was also found quantitatively important. Therefore, a decomposition of the adsorption energies of water clusters on metallic surfaces was performed to identify and characterise this synergy. It was found to be mainly due to polarisation and charge transfer. Moreover, charge transfer and polarisation are highly correlated in the studied adsorption energies. This means that an interesting lead to improve the quality of additive force fields would be, at first, to include polarisation effects by mimicking some already existing solutions from other force fields, and

then, to scale the effect of polarisation to remedy the lack of charge transfer. These new-generation force fields could then open the path to routine water/metal interface simulations at the molecular mechanics level.

In the third part, we focused on oxide surfaces/water interfaces. Oxides differ greatly from metal surfaces in the sense that their surface state can vary in water at similar time scales as adsorption. Because of that, other methods are required to investigate adsorption processes at the water/oxide interface. We used *ab initio* metadynamics, a rare event method widely used for biological system investigation but scarcely employed at solid/liquid interfaces. Thanks to the full description of surface reactivity provided by metadynamics, we unraveled the hydrolysis mechanism of γ -alumina in water and its inhibition in presence of an adsorbed xylitol. In order to complete this study, we investigated the adsorption of alcohols at the oxide/water interface, which combines all aforementioned aspects of adsorption study at the water/solid interface: the surface reactivity of alumina, the costly sampling of the reorganisation of the interfacial water structure, and the substitution of a strongly adsorbed water molecule at the surface of alumina. Several tools were applied to investigate the adsorption of ethanol at the γ -alumina/water interface: metadynamics, MMSolv, and thermodynamic integrations. The three methods delivered numerous information about the adsorption/desorption mechanism but did not converge to a common answer as for the free energy profile of the desorption. This study revealed that, if several tools are now available to conduct these investigations, improvements are still required to accurately understand the difficult process of adsorption. MMSolv can be improved by the usage of better force fields for alumina/water interactions, while rare events methods could benefit from longer sampling durations, but also for a better overall knowledge of interfacial mechanism to choose relevant variables to bias.

Overall, this work allowed us to better understand the issues of adsorption at the water/solid interface. We learned about the impact of the explicit water structure on adsorption energies, which is far more important than a simple screening of electrostatic interactions. We observed the delicate interactions between co-adsorbed water molecules on metallic surfaces, either as a cluster or a model water layer, and how the smallest perturbation of this network was impacting all interactions between the molecules and the surface. We understood the importance of the surface state at the oxide/water interface, and how this surface state could change and affect the adsorption of compounds. We conceived and used numerous tools that helped us overcome the impossibly high cost of phase-space sampling at such interfaces. We gathered knowledge about the triangular interactions between water, adsorbates, and surfaces. But also, we gain a better understanding of the tools themselves, ours and previously existing ones. Thanks to this knowledge, we have leads for future improvements. The science of water/solid interface can only progress through these two axes of method development and a better understanding of interfacial relations, that feed on each other. With this work, we hoped to have participated in both these directions.

Appendix Part



A Solvation Free Energies and Adsorption Energies at the Metal/Water Interface: Appendix

This appendix is provided as the supplementary information corresponding to chapter 2

A.1 Thermodynamic integration: The principle

Thermodynamic Integration (TI) is a very general methodology,¹⁻⁴ which allows to compute free energy differences based on the numerical integration of the gradient of the potential energy V with respect to the path-variable typically called λ . This gradient, $\frac{\partial V(\lambda)}{\partial \lambda}$ is evaluated at discrete points, also called windows. Provided that the sampling is sufficient in each window and that the integration error is low (sufficient number of windows) the free energy difference between the two states (A and B) converges to :

$$\Delta_{A \rightarrow B} G = \int_A^B \langle \frac{\partial V(\lambda)}{\partial \lambda} \rangle_{\lambda} d\lambda \quad (\text{A.1})$$

where $\langle \frac{\partial V(\lambda)}{\partial \lambda} \rangle_{\lambda}$ is the ensemble average of the partial derivative of the potential energy of the system with respect to λ , at a given value of λ .

In the context of MM solvation energies or (relative) binding strengths of ligands to receptors, TI is most often applied in conjunction with an alchemical transformation. During alchemical transformations, the two physical states are connected without a physically meaningful path between them, exploiting the fact that free energies are state functions. The path is formulated in terms of the abstract variable λ which goes from 0 (initial state A) to 1 (final state B), interpolating the potential energy of the two systems in-between:²

$$V(\lambda) = (1 - \lambda) V_A + \lambda V_B \quad (\text{A.2})$$

where V_A and V_B are the potential energies of state A and B , respectively. In practice, this allows, for instance, to compute the solvation energy difference between phenol and benzene by gradually and simultaneously replacing the OH of phenol by the H of benzene. These alchemical transformations come, however, with one caveat: the change along the path should not be too strong. While in principle increasing the number of windows is supposed to alleviate this issue, in practice large changes are difficult to converge, with meta-stable regions in phase-space leading to hysteresis and thus unreliable predictions of the free energy change.

A.2 Logarithmic spacing for TI windows

These spacings have been determined in order to reflect the variations of the free energy gradient of each step of the transformation, (see Fig A.2).

A.2. Logarithmic spacing for TI windows

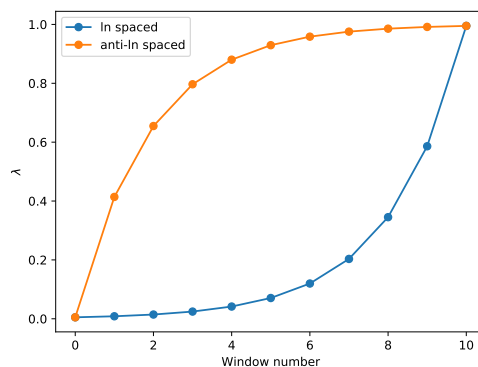


Figure A.1 – Lambda values used for the TI windows of the GAL17 softening transformation and its unsoftening (anti-In spaced and In spaced, respectively).

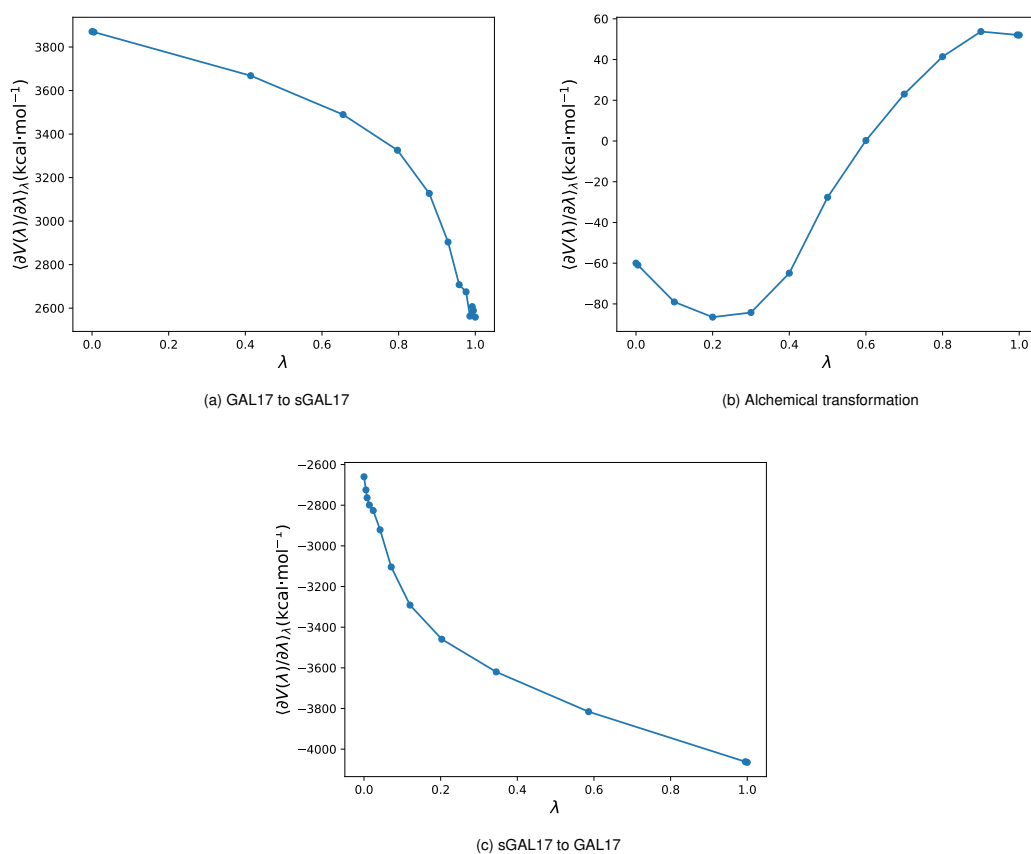


Figure A.2 – Typical evolution of the average value of the free energy gradient in function of λ , i.e., $\langle \frac{\partial V(\lambda)}{\partial \lambda} \rangle_{\lambda} = f(\lambda)$ during (a) the softening (c) and unsoftening of GAL17, and (b) alchemical steps of the process. The data are taken from the annihilation of $\text{H}_2\text{O}^{\text{DFT}}$ at a distance of 2.5 Å away from the surface.

A.3 Comparison with Particle Mesh Ewald Electrostatics

The particle mesh Ewald (PME) scheme for the electrostatics is incompatible with the proposed short range Coulomb correction. However, we have compared the shifted Coulomb potential with the standard PME scheme of Amber for the adsorption free energy of water in Fig. A.3. We confirm that PME gives quite similar results as the direct space, shifted Coulomb potential. In particular, the short range peak at 3 Å is conserved at 12 kcal·mol⁻¹ while it was reduced to 8 kcal·mol⁻¹ by the inclusion of the short range correction. At longer distances, given the 1 kcal·mol⁻¹ uncertainty, the $\Delta_a G^{solv}$ can be considered as similar for all three schemes. Overall, PME seems to perform on par with the real-space, shifted Coulomb interaction for $\Delta_a G^{solv}$ of water in water.

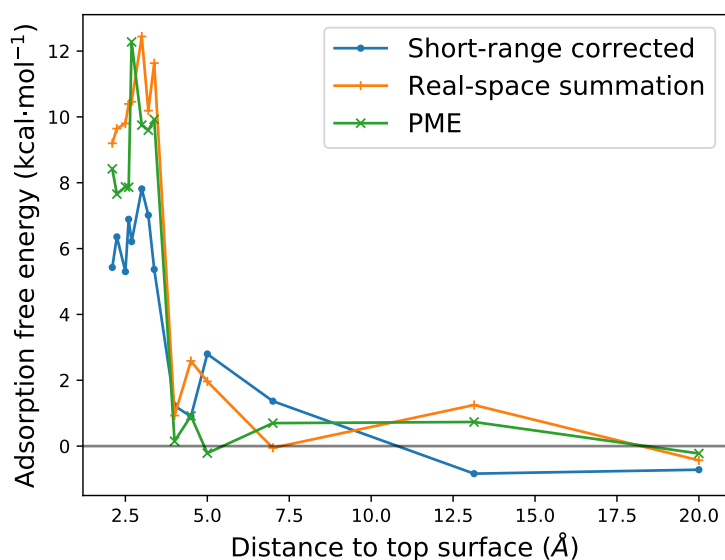


Figure A.3 – Adsorption free energy $\Delta_a G^{solv}$ for a frozen water molecule on a 4 layers slab of Pt(111) using a p(4x4) cell as a function of the distance of the oxygen to the surface. Its interactions with the slab are described at DFT level. Corrected refers to free energies computed with the coulombic correction proposed, in opposition to the uncorrected energies which use standard real space summation, and PME refers to particle mesh Ewald summation. Free energies are given an estimated ± 1.0 kcal·mol⁻¹ accuracy (See SI A.4 for details).

A.4 Error Estimates for Adsorption Free Energies

Statistical errors on adsorption energy were estimated by block averaging⁵ (pyblock, James Spencer, <http://github.com/jsspencer/pyblock>) on each λ windows combined with squared error propagation for each transformations and then over the whole computation of the MMSolv contribution.

A.5 Details for Surface Energy Computation

In order to compute the solvation surface free energy, which necessitates a converged alchemical creation of the solid phase, additional steps have been introduced. Indeed, the transformation is much stronger than what is usually done for TI. The scheme has, therefore, been adapted to conduct smoother transformations and divided into four steps : (i) Discharge of the whole Pt slab, (ii) Switch from GAL17 to sGAL17 (with no charge on the slab), (iii) Turning off of all sGAL17 terms except the Lennard-Jones interactions (with no charge on the slab) (iv) Alchemical change corresponding to the disappearance of the slab (with no charge on the slab, and only LJ interaction between the metal and the water). Additionally, the heating phase duration were doubled (400 ps). Furthermore, the slab presents two interfaces with water, but only one interface is actually described by the GAL17 force field. Due to technical limitations, the other one is treated only by the LJ interactions included in GAL17. The appearance of the slab, thus implies the creation of two interfaces, one being poorly described and undesired. In order to get rid of this contribution, another computation has been performed, not with the complete GAL17 forcefield but only its LJ terms in order to get the solvation surface free energy at an interface governed only by these interactions. It has then been subtracted from the first one to determine only the surface free energy of the GAL17 interface. This is summarized in the following equation:

$$\Gamma_{surf} = \frac{1}{A} \left(\Delta_{(i)}G - \frac{\Delta_{(i)'}G}{2} + \Delta_{(ii)}G - \frac{\Delta_{(ii)'}G}{2} + \Delta_{(iii)}G + \Delta_{(iv)}G - \frac{\Delta_{(iv)'}G}{2} \right) \quad (\text{A.3})$$

where A is the area of the Pt(111) slab , i to iv are the aforementioned steps and $'$ is used to designate the same step performed for the LJ-only treated interface. Please note that the $(ii)'$ step consists, indeed, only in a smoothing of the LJ interactions while $(iii)'$ is unnecessary as the interface is already treated only by LJ interactions. Also, (iv) and $(iv)'$ are strictly identical.

A.6 Most Stable Adsorption Configuration for Phenol on Pt(111)

Appendix A. Solvation Free Energies and Adsorption Energies at the Metal/Water Interface: Appendix

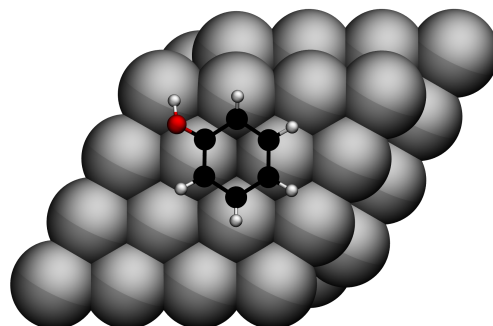


Figure A.4 – Most stable adsorption configuration for phenol on a Pt (111) 4x4 slab, named Brg30°C2, according to Chaudhary *et.al.* nomenclature⁶

A.7 Study of the of Local Coverages

To evaluate the tendency for island-formation, we minimize the following function :

$$E_{ads}^{mean} = \sum_i^{coverages} E_{ads,i} \cdot p_i \quad \text{with} \quad \theta^{mean} = \sum_i^{coverages} \theta_i \cdot p_i \quad \text{being constant} \quad (\text{A.4})$$

where E_{ads}^{mean} is the average adsorption (free) energy over all adsorbed benzene or phenol molecules in the system, $E_{ads,i}$ is the adsorption (free) energy of a single molecule at a given coverage indexed by i , p_i is the percentage of the molecules that are adsorbed at that coverage, θ^{mean} is the global coverage value for all molecules that is fixed to study a given situation, and θ_i is actual coverage corresponding to the index i .

With the data gathered for the four coverages tested, Fig. A.5 shows the proportions p_i for each of these coverages that are expected for global coverages θ^{mean} in the range between 0.03 and 0.1 ML.

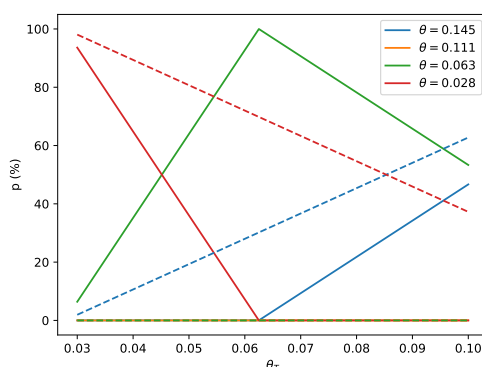


Figure A.5 – Evolution of the proportions p_i of phenols that are adsorbed at each different local coverage as a function of the global coverage θ_T . Filled lines are generated with adsorption free energies computed with SolvHybrid, while dashed lines are generated with gas-phase adsorption energies.

As depicted in Fig. A.5, despite the limited number of considered local coverages, trends emerge clearly, pointing out a rapid decay of the proportion of the lowest coverages (0.028 ML, red) when the global coverage increases, along with a rapid increase of the next highest coverage 0.063 ML (green), themselves replaced at higher coverage by 0.145 ML (blue). However, 0.111 ML cells never contribute to the low energy arrangements. Interestingly, at a global coverage of 0.054, which is considered in Campbell's work⁷), the dominant local coverage is 0.063 ML ($\approx 70\%$ of the phenols), followed by 0.028 ML. This trend is in moderate support of his hypothesis of local highly concentrated islands (0.063 ML), surrounded by low-coverage area (0.028 ML). However, in gas phase, at the same global coverage, a local coverage of 0.028 ML is found to be dominant ($\approx 75\%$ of the phenols), completed by 0.145 ML, which suggest an even more pronounced heterogeneity of coverage on the surface, incompatible with the

corresponding experimental observations.⁸

Overall, this approach seems therefore promising in principle, but a much larger number of local coverages (and maybe DFT results that are better converged in terms of K-points, number of metallic layers etc.) would be necessary to achieve definite results.

A.8 Decomposition Analysis

The decomposition of the free energy in electrostatic and non-electrostatic terms depends on the chosen path for the alchemical transformation.^{9;10} We here provide the “standard” decomposition of $\delta\Delta_h G$ into the electrostatic and non-electrostatic contributions in Table A.1, resulting from our choice of the path (electrostatic decoupling fully separated from the change in topology).

| Component | Benzene | Phenol |
|-----------------------------|---------|--------|
| $\delta\Delta_h G_{el}$ | -14.5 | -17.7 |
| $\delta\Delta_h G_{non-el}$ | 38.4 | 39.1 |
| $\delta\Delta_h G$ | 23.9 | 21.4 |

Table A.1 – Components (in kcal·mol⁻¹) for the solvation free energy change of benzene and phenol adsorption on Pt(111) at a coverage of 1/9 ML. The electrostatic component encompasses the removal of charges on S and the appearance of charges on M@S. The non-electrostatic component consists in the actual alchemical transformation and the (un-)softening of GAL19 necessary for a smooth alchemical transformation.

Bibliography

- [1] Kirkwood, J. G. Statistical Mechanics of Fluid Mixtures. *The Journal of Chemical Physics* **1935**, *3*, 300–313.
- [2] Martins, S. A.; Sousa, S. F.; Ramos, M. J.; Fernandes, P. A. Prediction of Solvation Free Energies with Thermodynamic Integration Using the General Amber Force Field. *Journal of Chemical Theory and Computation* **2014**, *10*, 3570–3577.
- [3] Steinbrecher, T.; Mobley, D. L.; Case, D. A. Nonlinear scaling schemes for Lennard-Jones interactions in free energy calculations. *The Journal of Chemical Physics* **2007**, *127*, 214108.
- [4] Gao, Y.; Zhu, T.; Chen, J. Exploring drug-resistant mechanisms of I84V mutation in HIV-1 protease toward different inhibitors by thermodynamics integration and solvated interaction energy method. *Chemical Physics Letters* **2018**, *706*, 400–408.
- [5] Flyvbjerg, H.; Petersen, H. G. Error estimates on averages of correlated data. *J. Chem. Phys.* **1989**, *91*, 461–466, Publisher: American Institute of Physics.

- [6] Chaudhary, N.; Hensley, A.; Collinge, G.; Wang, Y.; McEwen, J.-S. Coverage-Dependent Adsorption of Phenol on Pt(111) from First Principles. *The Journal of Physical Chemistry C* **2020**, *124*, 356–362, Publisher: American Chemical Society.
- [7] Singh, N.; Campbell, C. T. A Simple Bond-Additivity Model Explains Large Decreases in Heats of Adsorption in Solvents Versus Gas Phase: A Case Study with Phenol on Pt(111) in Water. *ACS Catalysis* **2019**, *9*, 8116–8127.
- [8] Ihm, H.; White, J. M. Stepwise Dissociation of Thermally Activated Phenol on Pt(111). *The Journal of Physical Chemistry B* **2000**, *104*, 6202–6211.
- [9] Mark, A. E.; van Gunsteren, W. F. Decomposition of the Free Energy of a System in Terms of Specific Interactions: Implications for Theoretical and Experimental Studies. *Journal of Molecular Biology* **1994**, *240*, 167–176.
- [10] Boresch, S.; Karplus, M. The Meaning of Component Analysis: Decomposition of the Free Energy in Terms of Specific Interactions. *Journal of Molecular Biology* **1995**, *254*, 801–807.



B The GAL19 Force Field for Water - Noble Metal Interfaces: Appendix

This appendix is provided as the supplementary information corresponding to chapter 3

B.1 Configuration set

B.1.1 Complete set

The set of configurations that was used both to fit and validate the force-field was built as follow:

- Configurations were built on top, hollow and bridge site for both (100) and (111) facets.
- For the top, hollow and bridge sites of each facet, an ensemble of 13 values of the θ angle ranging from 10° to 340° were combined with different distances to the surface, as follow (442 configurations per facet):
 - For top site on Pt and other metals: 2.1, 2.2, 2.3, 2.6, 3.0, 3.25, 3.5, 4.0, 4.5, 5, 5.5 and 6.0 Å
 - For hollow and bridge site on Pt: 2.3, 2.4, 2.5, 2.8, 3.25, 3.5, 4.0, 4.5, 5, 5.5 and 6.0 Å
 - For hollow and bridge site on other metals: 2.1, 2.2, 2.3, 2.6, 3.0, 3.25, 3.5, 4.0, 4.5, 5 and 5.5 Å

For these configurations, the ϕ angle was held at 0° .

- For the top site only, an ensemble of 10 values of the ϕ angle ranging from 20° to 180° were combined with 3 values of the θ angle (30° , 90° and 120°), and with the same 12 distances to the top sites as presented above for the top site of every metals and added to the set (360 configurations per facet).
- Configurations were built between the top and hollow site of each facet with a fixed ϕ angle at 0° and θ angle at 90° . They were build as a combination of 4 distances to the surface (2.6, 3.0, 3.5 and 4.0 Å) and 3 proportion of the top/hollow distance (10%, 25% and 50%) (12 configurations).
- The exact same configurations as those between top and hollow sites were built between the top and the bridge site (12 configurations).

A total of 826 configurations were thus generated for each facet.

For the Cu (111) facets, an ensemble of 207 configurations were added on top, hollow and bridge site for the short distances of 1.8, 1.9 and 2.0 Å and built as described above by varying ϕ and θ . A total of 1033 configurations were thus generated for this facet. These distances ensure a good description of the repulsive wall on this metal that has a smaller atomic radius compared to the other elements considered herein.

The whole set of configurations can be found in the attached archive in a the VASP-style formatting.

B.1.2 Fitting set

For the fitting of the force-field, only a restricted part of the configuration set was used. It was chosen as follow:

- All configurations on hollow and bridge sites presenting $\theta = 90^\circ$.
- All configurations built between top and hollow or top and bridge site.
- On top site, all configurations presenting $\phi = 0^\circ$ with a distance comprise between 2.3 and 5 Å included.
- On top site again, all configurations presenting $\phi \neq 0^\circ$ with a distance comprise between 2.3 and 3.25 Å included.

Configurations with endothermic $E_{ads} > 1 \text{ kcal}\cdot\text{mol}^{-1}$ are removed from the fit set to focus on the most relevant region in configurational space.

B.2 Force-field parameters

| | Ag 100 | Ag 111 | Au 100 | Au 111 | Cu 100 | Cu 111 | Pd 100 | Pd 111 | Pt 100 | Pt 111 |
|---|--------|--------|--------|--------|--------|--------|--------|--------|--------|--------|
| R_O (Å) | 2.38 | 2.39 | 2.03 | 2.10 | 2.20 | 2.48 | 2.70 | 2.51 | 2.47 | 2.41 |
| b_\perp (Å ⁻²) | 0.58 | 0.63 | 0.52 | 0.70 | 0.78 | 4.66 | 0.62 | 0.64 | 0.90 | 0.89 |
| b_\parallel (Å ⁻²) | 0.13 | 0.15 | 0.13 | 0.09 | 0.15 | 0.13 | 0.20 | 0.10 | 0.12 | 0.13 |
| R_H (Å) | 0.36 | 0.36 | 0.34 | 0.33 | 0.37 | 0.33 | 0.30 | 0.33 | 0.33 | 0.35 |
| B (Å ⁻¹) | 3.93 | 3.18 | 3.48 | 4.42 | 3.05 | 3.7 | 3.99 | 3.74 | 3.70 | 3.72 |
| a_1 (kcal·mol ⁻¹) | 21.08 | 20.97 | 22.42 | 18.51 | 30.34 | 17.47 | 15.53 | 24.93 | 29.43 | 35.25 |
| a_2 (kcal·mol ⁻¹) | 6.58 | 6.27 | 11.56 | 9.74 | 7.13 | 8.56 | 7.42 | 8.52 | 13.05 | 12.87 |
| a_3 (kcal·mol ⁻¹) | -3.33 | -2.94 | -5.79 | -4.26 | -2.60 | -2.70 | -3.02 | -3.55 | -6.64 | -5.58 |
| a_4 (kcal·mol ⁻¹) | 1.49 | 1.61 | 4.72 | 4.07 | 0.87 | 0.17 | 2.71 | 3.17 | 2.91 | 3.13 |
| ϵ_a (kcal·mol ⁻¹) | 14.44 | 18.52 | 14.73 | 7.95 | 14.54 | 7.99 | 23.26 | 13.44 | 13.29 | 17.39 |
| A (kcal·mol ⁻¹) | 61736 | 12872 | 25890 | 273900 | 2114 | 21289 | 67507 | 22099 | 18141 | 26446 |
| A_H (kcal·mol ⁻¹) | 2056 | 210 | 3305 | 3313 | 1326 | 2290 | 5468 | 3179 | 3653 | 3010 |
| C (Å ⁶ ·kcal·mol ⁻¹) | 930 | 930 | 918 | 918 | 899 | 899 | 872 | 872 | 917 | 917 |

Table B.1 – Fitted parameters.

Appendix B. The GAL19 Force Field for Water - Noble Metal Interfaces: Appendix

| | Au(111) ^{std} | Au(111) ^{rand} | Pt(100) ^{std} | Pt(100) ^{rand} |
|---|------------------------|-------------------------|------------------------|-------------------------|
| RMSD | 0.75 | 0.98 | 1.39 | 1.19 |
| R_O (Å) | 2.10 | 2.03 | 2.47 | 2.50 |
| b_{\perp} (Å ⁻²) | 0.70 | 1.83 | 0.90 | 0.80 |
| b_{\parallel} (Å ⁻²) | 0.09 | 0.08 | 0.12 | 0.10 |
| R_H (Å) | 0.33 | 0.30 | 0.33 | 0.29 |
| B (Å ⁻¹) | 4.42 | 4.50 | 3.70 | 4.18 |
| a_1 (kcal·mol ⁻¹) | 18.51 | 16.51 | 29.43 | 30.19 |
| a_2 (kcal·mol ⁻¹) | 9.74 | 5.06 | 13.05 | 4.59 |
| a_3 (kcal·mol ⁻¹) | -4.26 | -1.28 | -6.64 | -2.36 |
| a_4 (kcal·mol ⁻¹) | 4.07 | 4.07 | 2.91 | 2.76 |
| ε_a (kcal·mol ⁻¹) | 7.95 | 6.35 | 13.29 | 10.64 |
| A (kcal·mol ⁻¹) | 273900 | 295414 | 18141 | 81250 |
| A_H (kcal·mol ⁻¹) | 3313 | 6831 | 3653 | 7453 |
| C (Å ⁶ ·kcal·mol ⁻¹) | 918 | 918 | 917 | 917 |

Table B.2 – Comparison of the parameters with the standard fit set and the randomized fit set for two selected facets.

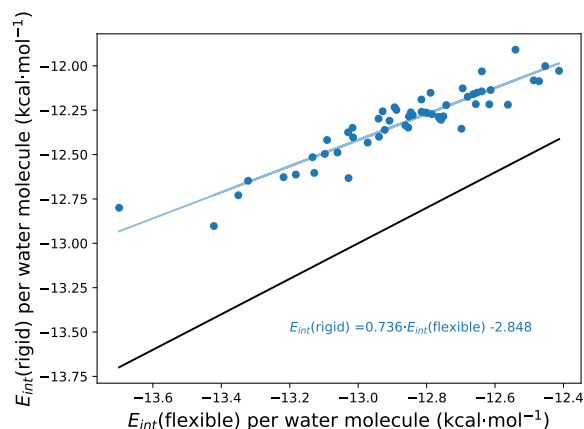


Figure B.1 – Parity representation of the interaction energy of 55 snapshots extracted from an AIMD, re-evaluated at DFT level with the TIP3P water geometry instead of the flexible DFT geometry.

B.3 Additional Tables and Figures

Table B.3 – Root mean square deviation of the GAL19 predicted adsorption energy compared to the energy predicted by DFT for the configurations of the total set resulting in an adsorption energy lower than $1 \text{ kcal}\cdot\text{mol}^{-1}$ in DFT. The number of configurations verifying this criterion is indicated for each metallic facet.

| facet | RMSD | $N_{\text{configurations}}$ |
|--------|------|-----------------------------|
| Cu 100 | 0.81 | 742 |
| Cu 111 | 0.96 | 747 |
| Ag 100 | 0.78 | 698 |
| Ag 111 | 0.73 | 669 |
| Au 100 | 0.94 | 675 |
| Au 111 | 0.75 | 662 |
| Pd 100 | 1.13 | 745 |
| Pd 111 | 1.15 | 744 |
| Pt 100 | 1.39 | 700 |
| Pt 111 | 1.36 | 720 |

Bibliography

- [1] Dang, L. X.; Chang, T.-M. Molecular dynamics study of water clusters, liquid, and liquid–vapor interface of water with many-body potentials. *J. Chem. Phys.* **1997**, *106*, 8149–8159.
- [2] Izadi, S.; Onufriev, A. V. Accuracy limit of rigid 3-point water models. *J. Chem. Phys.* **2016**, *145*, 074501.

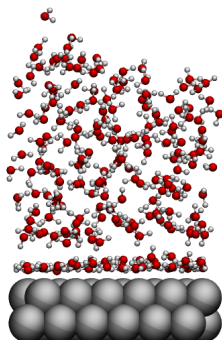
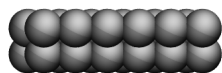


Figure B.2 – Typical unit cell for the metal/water interface simulated.

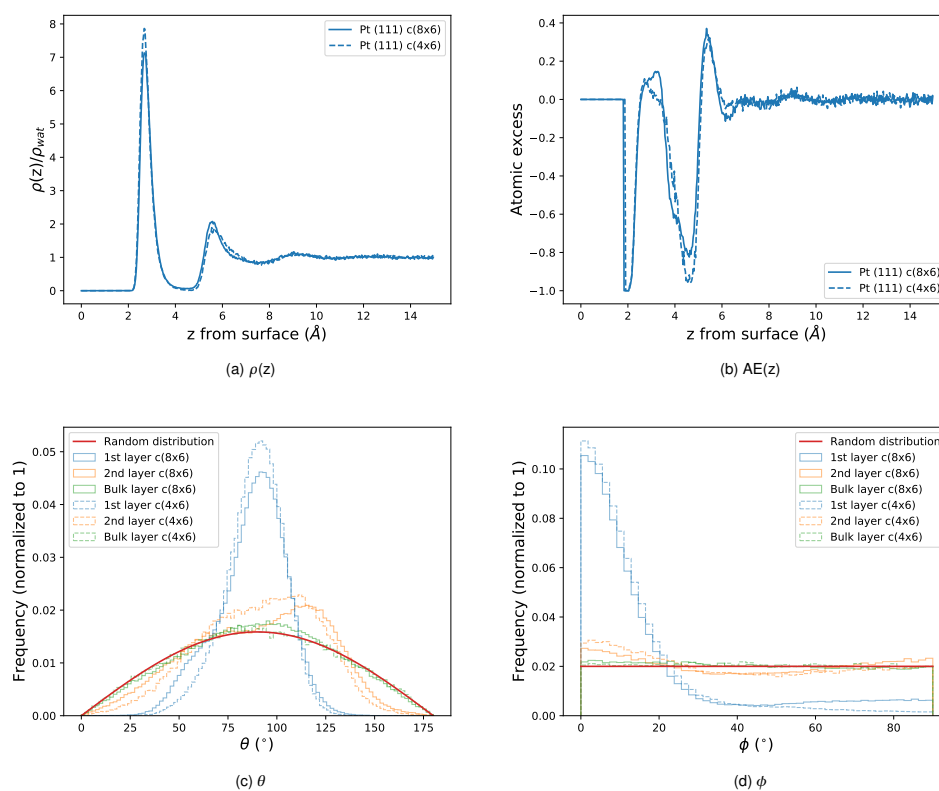


Figure B.3 – Comparison of the structure at the Pt(111)/water interface obtained with the $c(4 \times 6)$ (dashed lines) and the $c(8 \times 6)$ unit cell (full lines).

Appendix B. The GAL19 Force Field for Water - Noble Metal Interfaces: Appendix

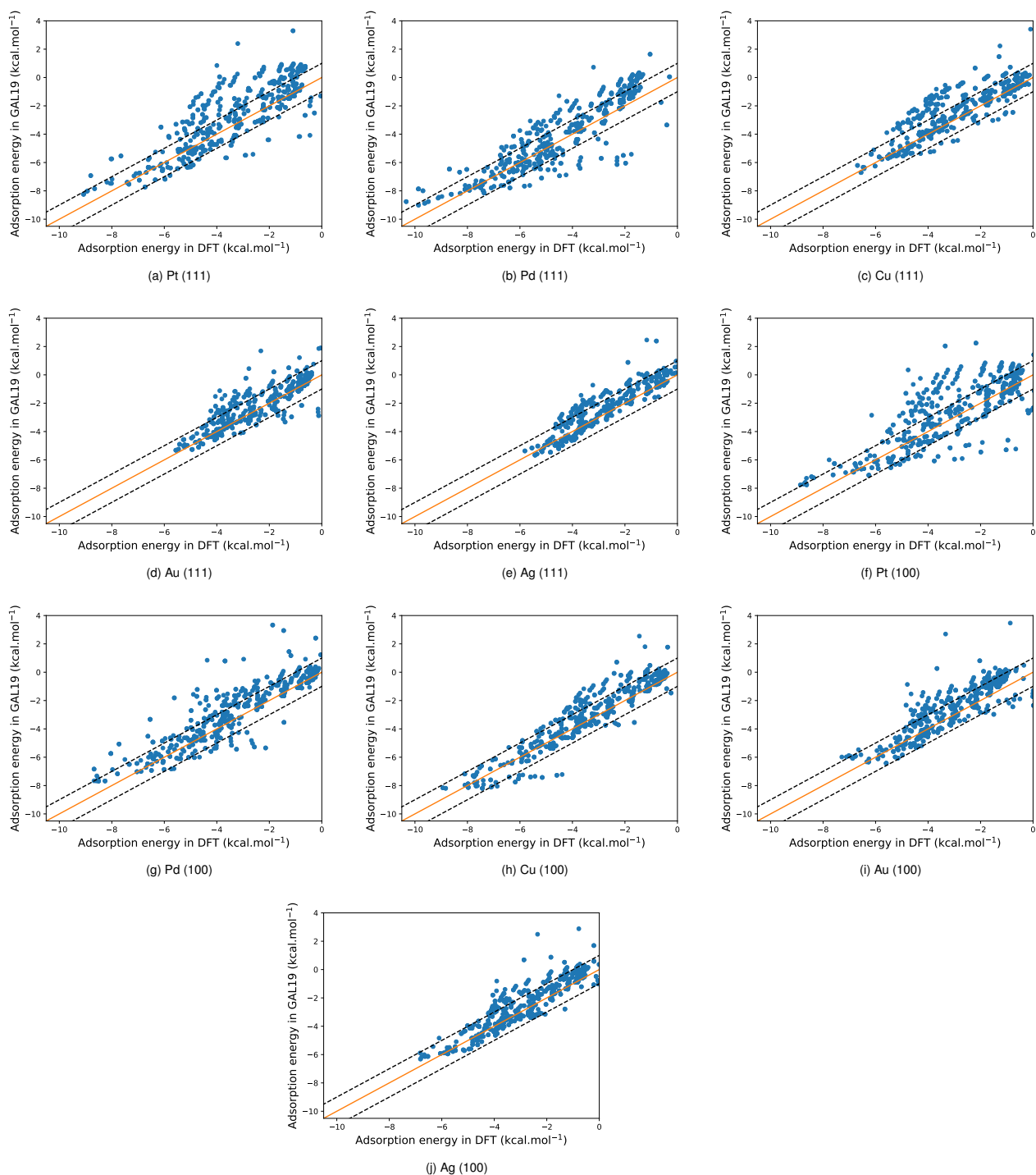


Figure B.4 – Comparison of the adsorption energy of multiple adsorption conformations of a single water molecule on each metallic facet, calculated by DFT and GAL19. All the configurations of the total set, resulting in an adsorption energy lower than 1 kcal.mol^{-1} in DFT are included. The broken lines indicates errors of $\pm 1 \text{ kcal.mol}^{-1}$.

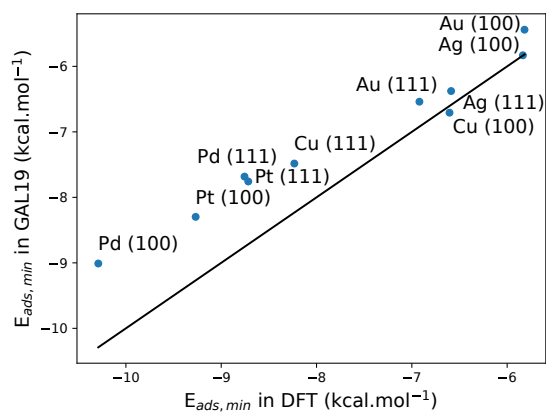


Figure B.5 – Parity representation of the optimal adsorption energy of water on each metallic facets obtained with GAL19 compared to the one obtained in DFT. Each minimum is the effective minimum of the functional form by which it is evaluated, therefore, a dot can represent the energy obtained for different configurations in DFT or with GAL19.

Appendix B. The GAL19 Force Field for Water - Noble Metal Interfaces: Appendix

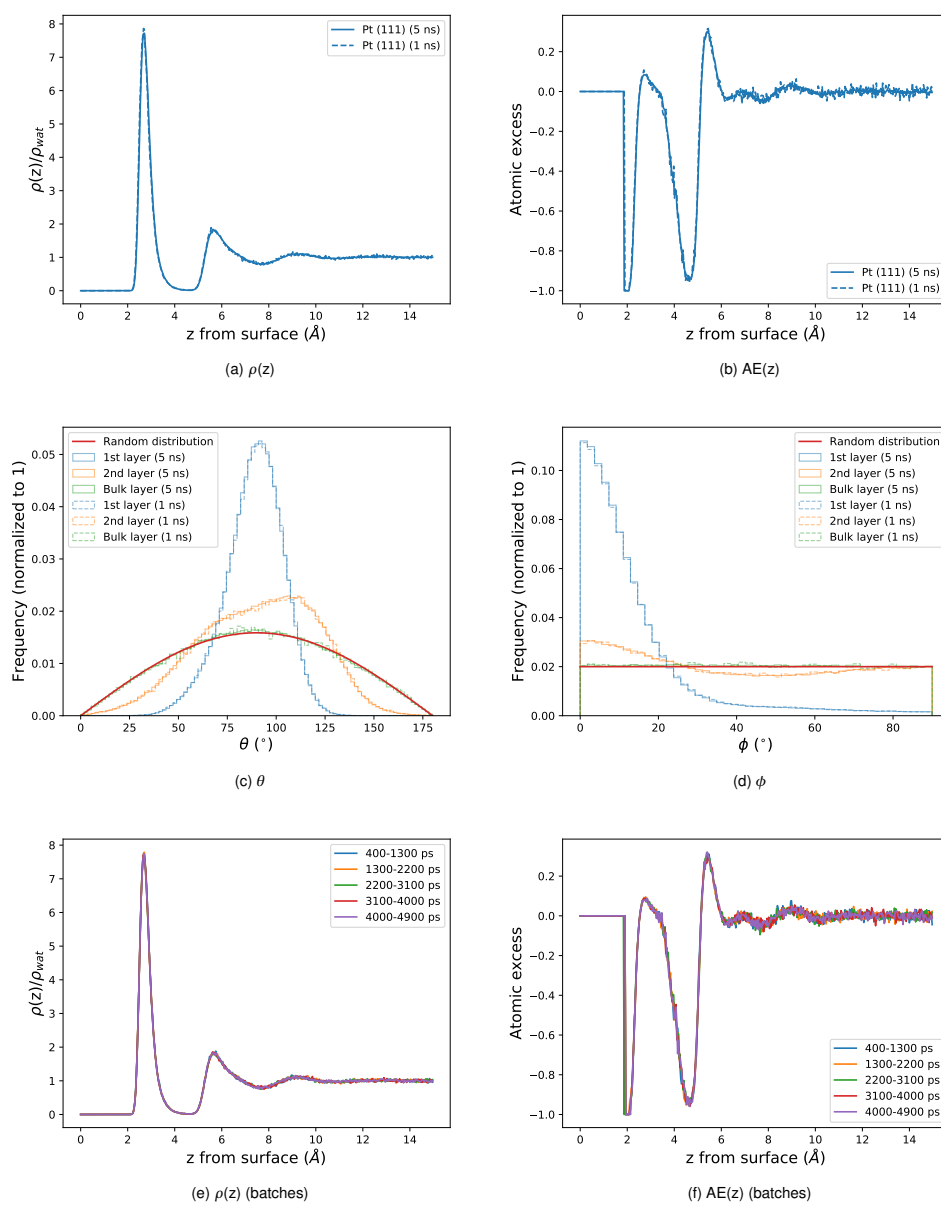


Figure B.6 – Comparison of the structure at the Pt(111)/water interface obtained with the 1 ns simulations (600 ps of production), a single 5 ns simulation (4.6 ps of production). For the $\rho(z)$ and AE(z), we also show the results for 5 blocks of the 5 ns trajectory, each one being 900 ps long, which illustrates the small statistical variations.

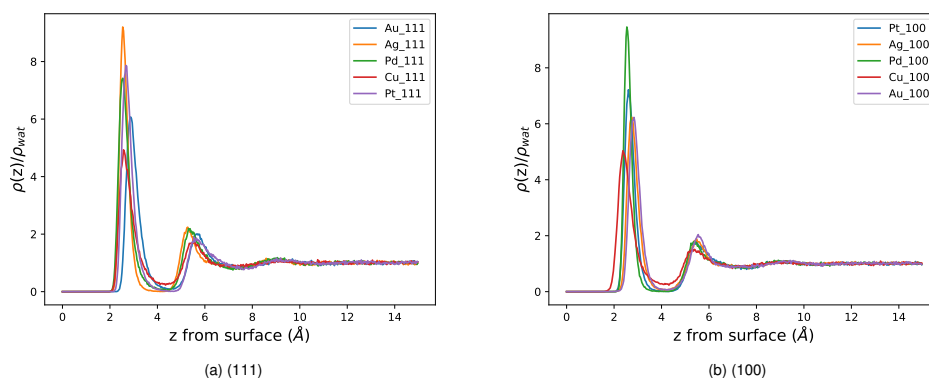


Figure B.7 – Molecular density of water above the surface for different metallic facets, defined by the number of oxygen found in 0.033 thick layer of water at different distance from the surface, then divided by the reference density of water, chosen at 0.033 \AA^{-3} . A density superior to one indicate a denser water layer than in the bulk.

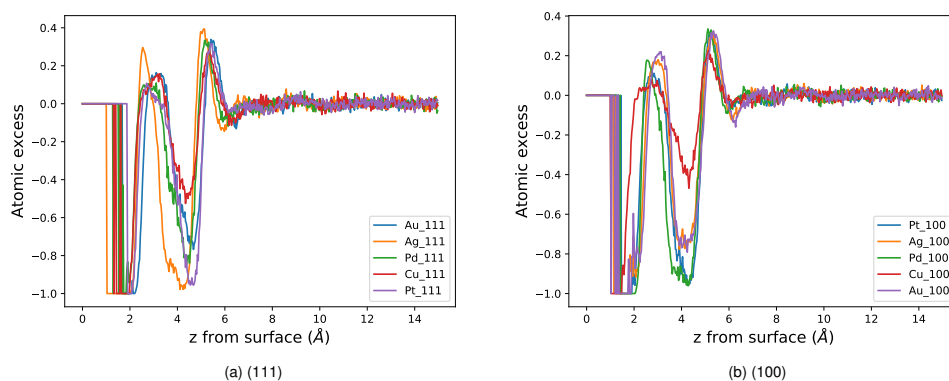


Figure B.8 – Atomic excess of water above the surface for different metallic facets, defined by $AE = ([O] - 2 \cdot [H]) / ([O] + 2 \cdot [H])$ for densities of oxygen and hydrogen computed on 0.033 thick layer of water at different distance from the surface. A positive atomic excess then implies an overrepresentation of oxygen compared to the stoichiometry of water while a negative value implies an excess of hydrogen. AE is held at 0 when neither oxygen or hydrogen are found in the layer

Appendix B. The GAL19 Force Field for Water - Noble Metal Interfaces: Appendix

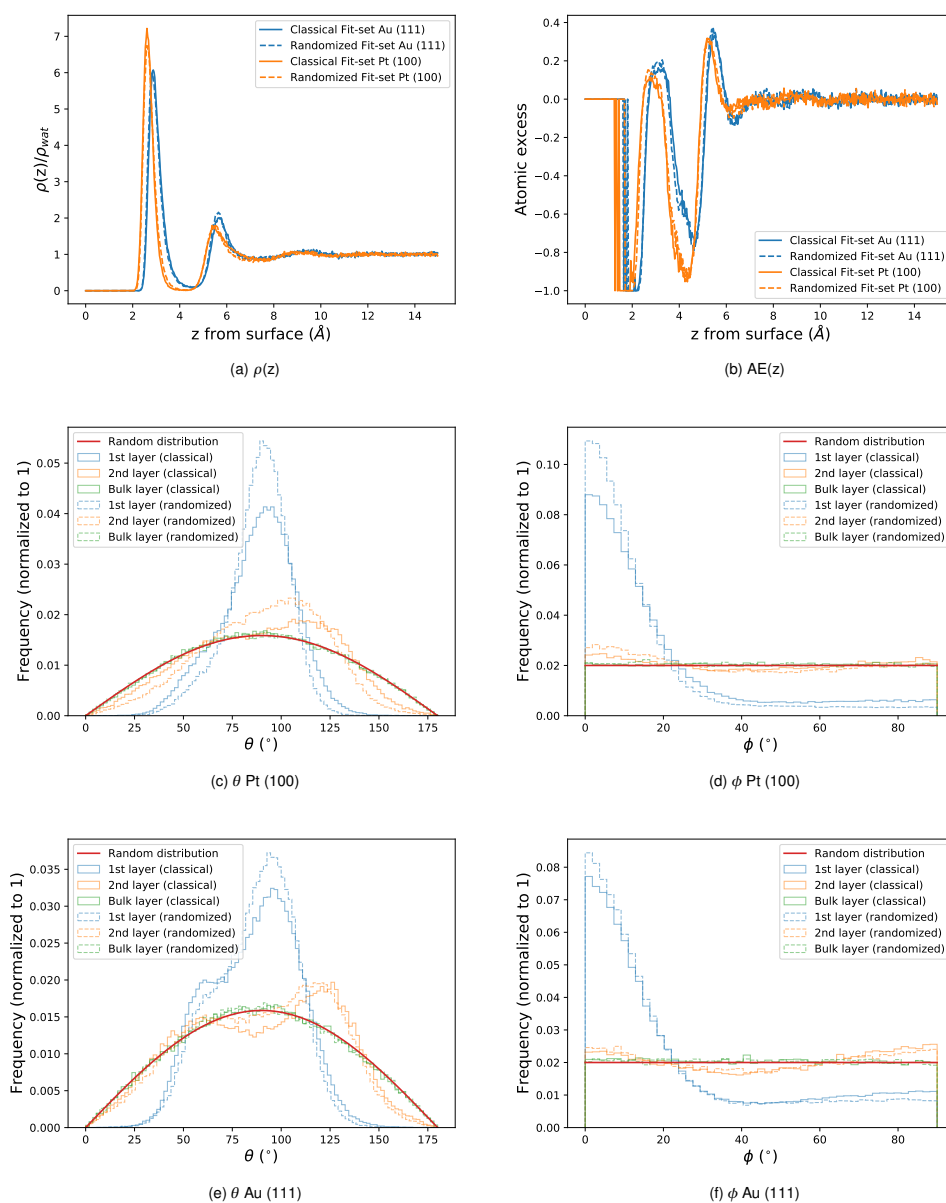


Figure B.9 – Comparison of the interfacial structuration obtained with the parameters from the “standard” fit set (full lines) and the randomized fit set (dashed lines).

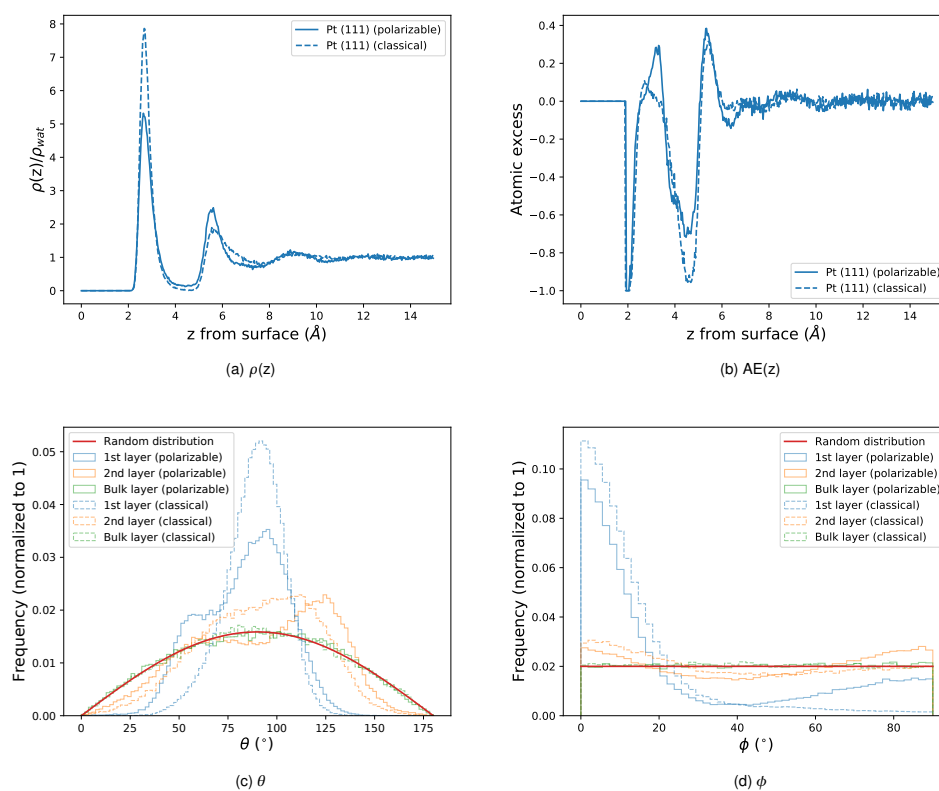


Figure B.10 – Comparison of the structure at the Pt(111)/water interface obtained with the TIP3P water model (dashed lines) and the polarizable water model by Dang and Chang¹ (full lines).

Appendix B. The GAL19 Force Field for Water - Noble Metal Interfaces: Appendix

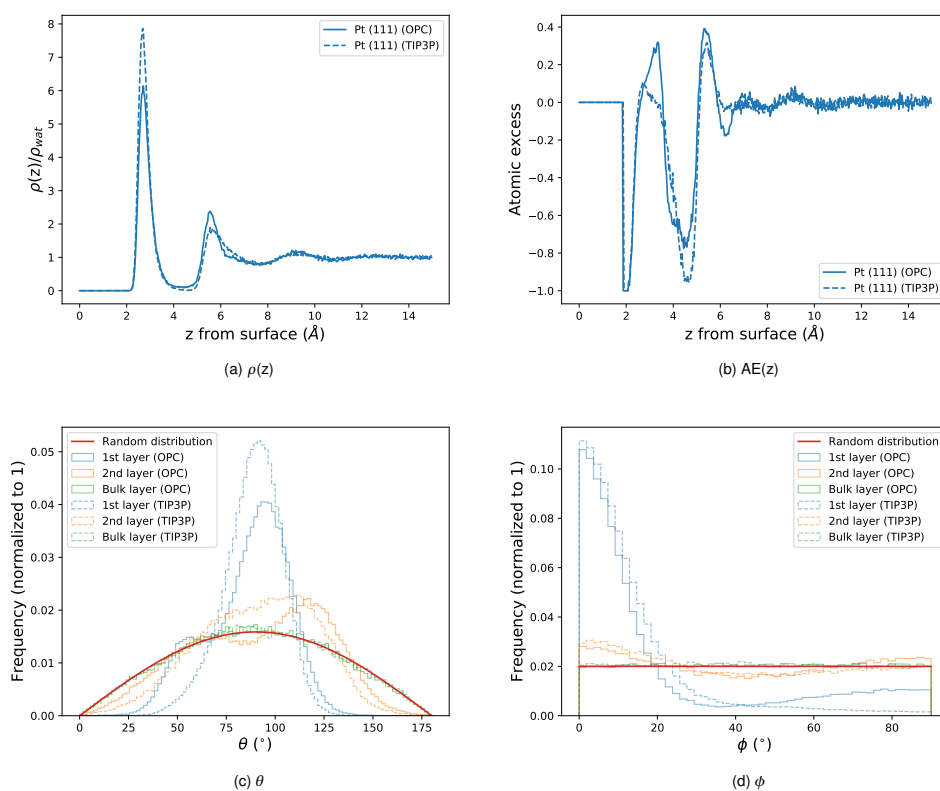


Figure B.11 – Comparison of the structure at the Pt(111)/water interface obtained with the TIP3P water model (dashed lines) and the OPC3 water model by Izadi and Onufriev² (full lines).

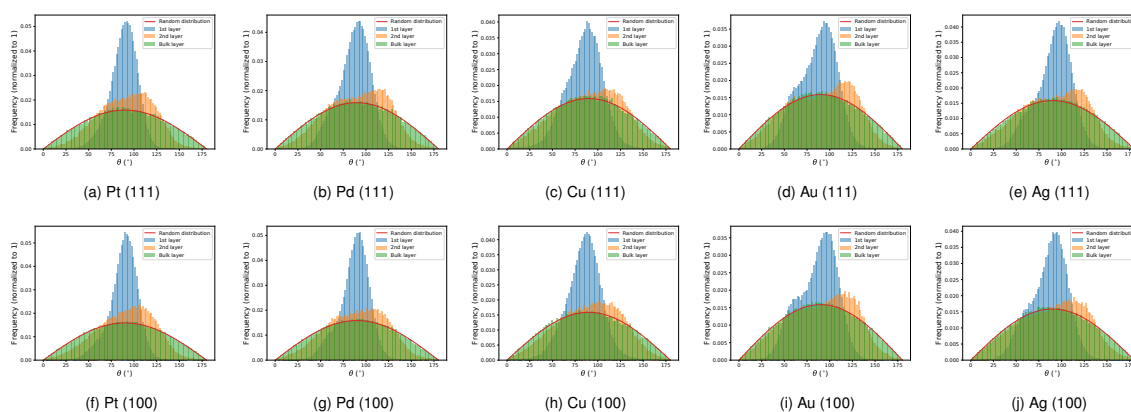


Figure B.12 – Angular distribution of the cartwheel θ angle of the water dipoles different metallic facets for chemisorption, physisorption, and bulk layer, defined as being water molecule situated between 0 and 4.5, 4.5 and 7, and 13 and 15.5 \AA away from the surface respectively. The red line represent an idealized random distribution of the dipoles, defined as a normalized sinusoidal distribution

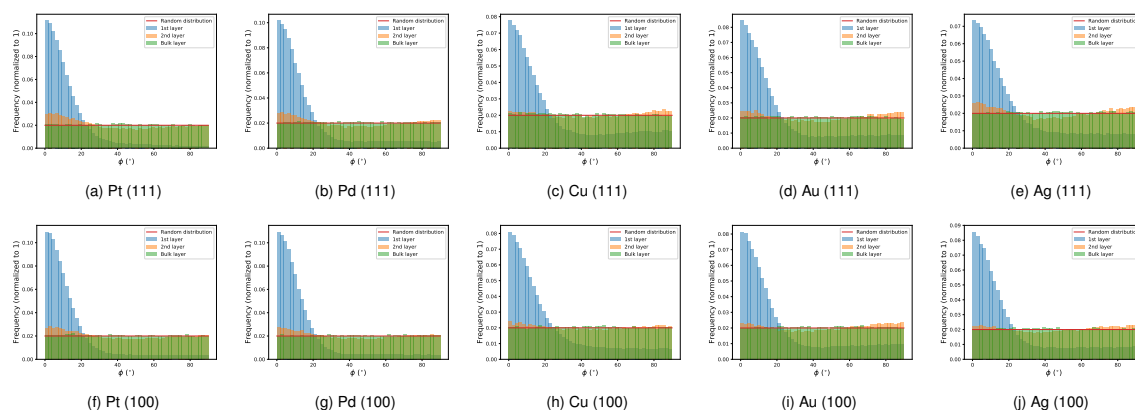


Figure B.13 – Angular distribution of the propeller ϕ angle of the water dipoles different metallic facets for chemisorption, physisorption, and bulk layer, defined as being water molecule situated between 0 and 4.5, 4.5 and 7, and 13 and 15.5 Å away from the surface respectively. The red line represent an idealized random distribution of the dipoles, defined as a normalized uniform distribution

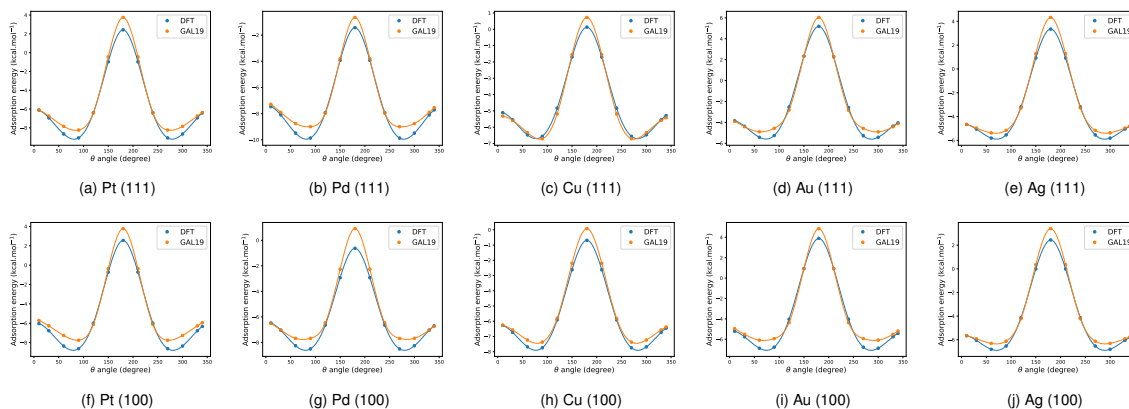


Figure B.14 – DFT and GAL19 calculated adsorption energy of a water molecule on different facets in function of the cartwheel angle θ , with ϕ held at 0° and at 2.5 Å from a top site

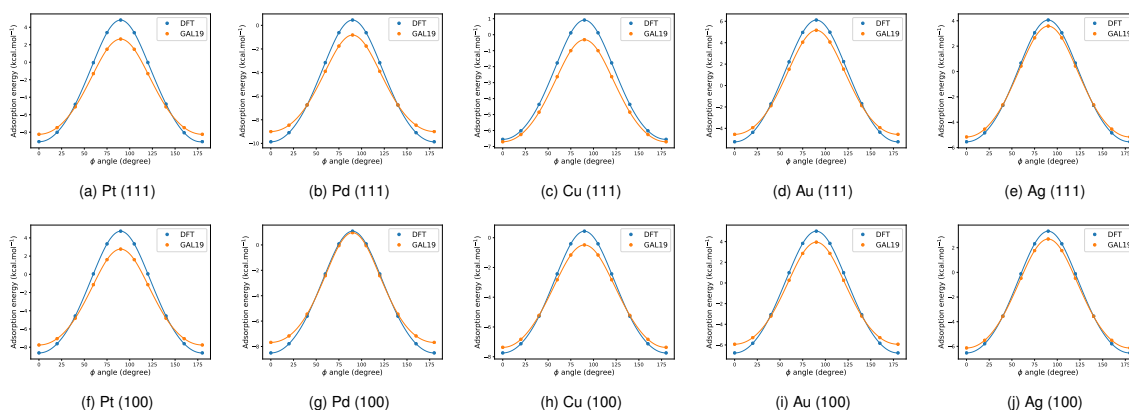


Figure B.15 – DFT and GAL19 calculated adsorption energy of a water molecule on different facets in function of the propeller angle ϕ , with θ held at 90° and at 2.5 Å from a top site

Appendix B. The GAL19 Force Field for Water - Noble Metal Interfaces: Appendix

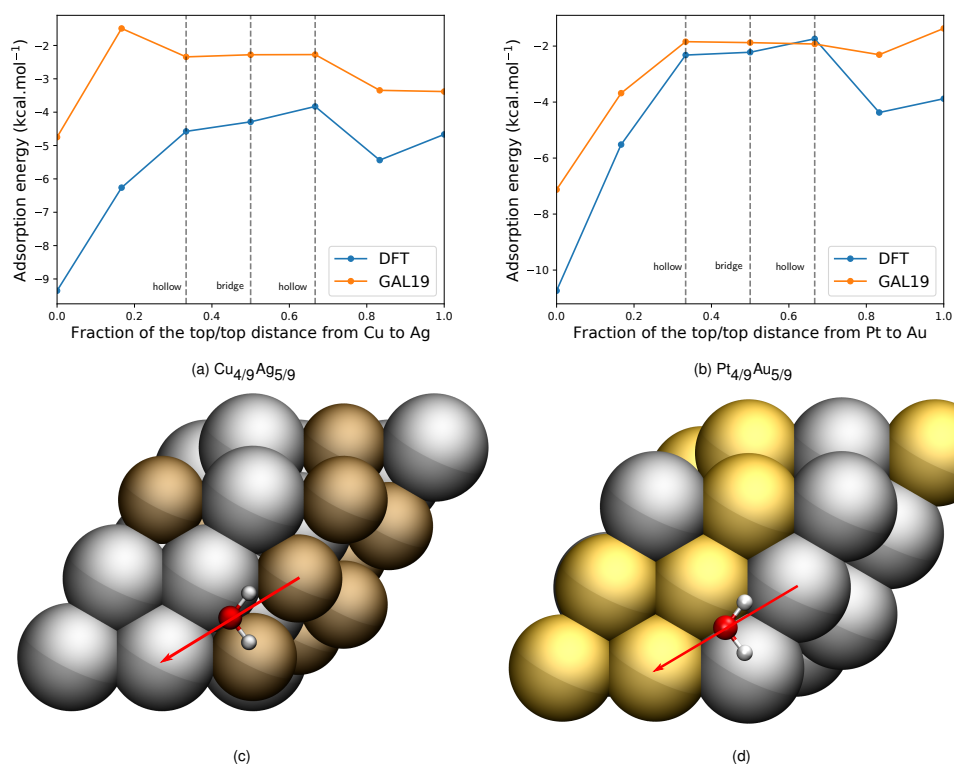


Figure B.16 – Adsorption energy in DFT and GAL19 of a single water molecule in function of the portion of the top-top distance between the two different metallic site of a (111) alloy. The distance to the surface is held at 2.5 Å, and the θ and ϕ angles, at 90 and 0° respectively. Corresponding trajectories are represented above

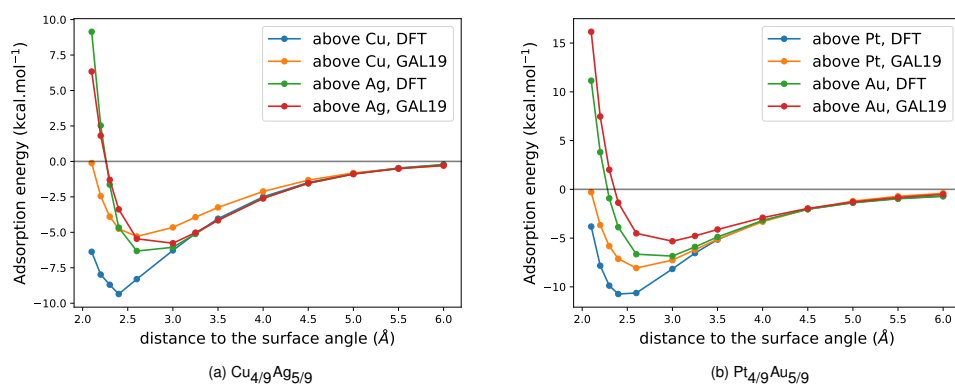


Figure B.17 – Adsorption energy in DFT and GAL19 of a single water molecule in function of the distance to the two different metallic top site of a (111) alloy. The θ and ϕ angles are held at 90 and 0° respectively.

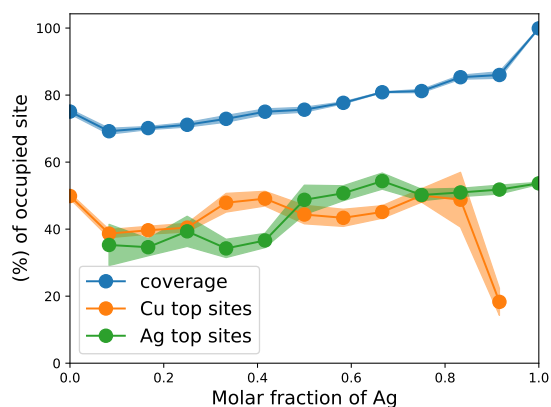


Figure B.18 – Percentage of the top sites of copper and silver occupied by OPC3 water molecules and global coverage of the surface for multiple alloy composition of Cu/Ag. The coverage is defined as the number of oxygen atom in the first layer (between 0 and 4.5 Å from the surface), divided by the total number of surface atoms. Confidence interval at 95% are represented as colored bands surrounding the data. The corresponding variances were computed by block averaging.



C The GAL21 force field: Appendix

This appendix is provided as the supplementary information corresponding to chapter 4

C.1 Configuration set

C.1.1 Complete set

The set of configurations that was used both to fit and validate the force-field was built as follow:

- Configurations were built on top, hollow and bridge site for both (100) and (111) facets.
- For the top, hollow and bridge sites of each facet, an ensemble of 13 values of the θ angle ranging from 10° to 340° were combined with different distances to the surface, as follow (442 configurations per facet):
 - For top site on Pt and other metals: 2.1, 2.2, 2.3, 2.6, 3.0, 3.25, 3.5, 4.0, 4.5, 5, 5.5 and 6.0 Å
 - For hollow and bridge site on Pt: 2.3, 2.4, 2.5, 2.8, 3.25, 3.5, 4.0, 4.5, 5, 5.5 and 6.0 Å
 - For hollow and bridge site on other metals: 2.1, 2.2, 2.3, 2.6, 3.0, 3.25, 3.5, 4.0, 4.5, 5 and 5.5 Å

For these configurations, the ϕ angle was held at 0° .

- For the top site only, an ensemble of 10 values of the ϕ angle ranging from 20° to 180° were combined with 3 values of the θ angle (30° , 90° and 120°), and with the same 12 distances to the top sites as presented above for the top site of every metals and added to the set (360 configurations per facet).
- Configurations were built between the top and hollow site of each facet with a fixed ϕ angle at 0° and θ angle at 90° . They were build as a combination of 4 distances to the surface (2.6, 3.0, 3.5 and 4.0 Å) and 3 proportion of the top/hollow distance (10%, 25% and 50%) (12 configurations).
- The exact same configurations as those between top and hollow sites were built between the top and the bridge site (12 configurations).
- Configurations were built on top of the different atomic sites presented in Fig 4.3. An ensemble of 12 values of the θ angle ranging from 0° to 330° (except for the configurations built on top of [add] of 1add@(111) were only 7 values of the θ angle ranging from 0° to 180° were used) were combined with 6 values of the ϕ angle ranging from 0° to 150° , and with different distances to the surface: 2.1, 2.2, 2.3, 2.6, 3.0, 3.25, and 3.5 Å (in total 504 configurations per sites except [add] of 1add@(111) with 294 configurations):

A total of 3458 configurations were thus generated for each metal.

For the Cu facets, an ensemble of 901 configurations was added on all adsorption sites for the short distances of 1.8, 1.9, and 2.0 Å and built as described above by varying ϕ and θ . A total of 4439 configurations were thus generated for this facet. These distances ensure a good description of the repulsive wall on this metal that has a smaller atomic radius compared to the other elements considered herein.

C.1.2 Fitting set

For the fitting of the force-field, only a restricted part of the configuration set was used. 500 hundred configurations were chosen among those featuring an endothermic E_{ads} : 100 randomly chosen for each of the following sites: [add] of 1add@(111), [n1] of 1add@(111), and [add] of 4add@(111); plus 100 randomly chosen on both the (100) and (111) facets. [n2] of 2def@(100) configurations were deliberately let aside as they were found to result in a worse overall fitting.

C.2 Force-field parameters

Appendix C. The GAL21 force field: Appendix

| | Ag | Au | Co | Cu | Ni | Pd | Pt |
|---|---------|----------|-----------|---------|---------|----------|---------|
| R_O (Å) | 2.02 | 2.04 | 1.99 | 2.00 | 1.99 | 2.03 | 2.01 |
| $b_{\perp,0}$ (Å ⁻²) | 0.38 | 0.43 | 0.61 | 0.63 | 0.21 | 0.46 | 0.57 |
| $b_{\perp,1}$ (Å ⁻²) | 0.00 | 0.00 | 0.00 | 0.00 | 0.00 | 0.01 | 0.01 |
| $b_{\parallel,0}$ (Å ⁻²) | 0.13 | 0.09 | 0.13 | 0.23 | 0.28 | 0.26 | 0.22 |
| $b_{\parallel,1}$ (Å ⁻²) | -0.00 | 0.00 | 0.00 | 0.00 | 0.00 | -0.00 | 0.00 |
| B_0 (Å ⁻¹) | 3.45 | 3.49 | 3.24 | 3.25 | 3.23 | 3.24 | 3.26 |
| B_1 (Å ⁻¹) | -0.10 | -0.09 | 0.16 | -0.08 | 0.15 | -0.18 | -0.01 |
| $B_{H,0}$ (Å ⁻¹) | 3.05 | 4.69 | 3.89 | 4.02 | 3.79 | 3.94 | 3.33 |
| $B_{H,1}$ (Å ⁻¹) | 0.03 | -0.18 | -0.04 | -0.02 | -0.06 | -0.07 | 0.09 |
| $a_{1,0}$ (kcal·mol ⁻¹) | -136.67 | -122.35 | -459.60 | -234.36 | -334.81 | -150.34 | 49.82 |
| $a_{1,1}$ (kcal·mol ⁻¹) | 45.33 | 43.43 | 134.32 | 70.10 | 107.09 | 46.85 | -17.70 |
| $a_{1,2}$ (kcal·mol ⁻¹) | -3.18 | -3.20 | -8.66 | -4.56 | -7.59 | -3.06 | 1.89 |
| $a_{2,0}$ (kcal·mol ⁻¹) | 8.17 | 10.64 | 12.17 | 46.69 | 16.16 | 12.07 | 55.91 |
| $a_{2,1}$ (kcal·mol ⁻¹) | 2.16 | -1.50 | -0.14 | -9.71 | -5.61 | -2.78 | -18.02 |
| $a_{2,2}$ (kcal·mol ⁻¹) | -0.38 | 0.07 | -0.07 | 0.50 | 0.63 | 0.21 | 1.50 |
| $a_{3,0}$ (kcal·mol ⁻¹) | -20.36 | -13.00 | -21.48 | -47.26 | -25.22 | -35.32 | -92.20 |
| $a_{3,1}$ (kcal·mol ⁻¹) | 1.68 | -0.26 | -0.54 | 10.90 | -1.03 | 4.23 | 12.11 |
| $a_{3,2}$ (kcal·mol ⁻¹) | 0.19 | 0.26 | 0.37 | -0.58 | 0.37 | -0.02 | 0.06 |
| $a_{4,0}$ (kcal·mol ⁻¹) | -2.52 | 0.58 | 9.02 | -10.75 | 16.89 | -6.92 | 6.40 |
| $a_{4,1}$ (kcal·mol ⁻¹) | -0.00 | 0.00 | -0.00 | -0.00 | -0.00 | -0.00 | 0.00 |
| $a_{4,2}$ (kcal·mol ⁻¹) | 0.06 | -0.01 | -0.14 | 0.20 | -0.32 | 0.11 | -0.10 |
| $\varepsilon_{a,0}$ (kcal·mol ⁻¹) | 8.53 | 0.54 | -17.34 | 37.83 | 137.58 | 0.40 | 55.60 |
| $\varepsilon_{a,1}$ (kcal·mol ⁻¹) | 1.82 | 3.47 | 16.06 | -0.12 | -38.61 | 29.59 | -3.63 |
| $\varepsilon_{a,2}$ (kcal·mol ⁻¹) | -0.20 | -0.28 | -1.65 | 0.14 | 2.71 | -3.39 | 0.03 |
| A_0 (kcal·mol ⁻¹) | 8278.92 | 7553.69 | -49271.02 | 3928.51 | 2702.40 | 6082.77 | 301.57 |
| A_1 (kcal·mol ⁻¹) | -587.78 | -175.69 | 16707.66 | 25.42 | 4253.73 | -662.05 | 1742.28 |
| $A_{H,0}$ (kcal·mol ⁻¹) | 2517.03 | 32286.66 | 10171.40 | 8578.84 | 7048.14 | 11756.76 | 9856.14 |
| $A_{H,1}$ (kcal·mol ⁻¹) | 370.92 | -3619.43 | 2.84 | 869.16 | -395.93 | -816.35 | 1166.11 |
| C (Å ⁶ ·kcal·mol ⁻¹) | 930 | 918 | 907 | 899 | 903 | 872 | 917 |

Table C.1 – Fitted parameters

C.3 Additional Tables and Figures

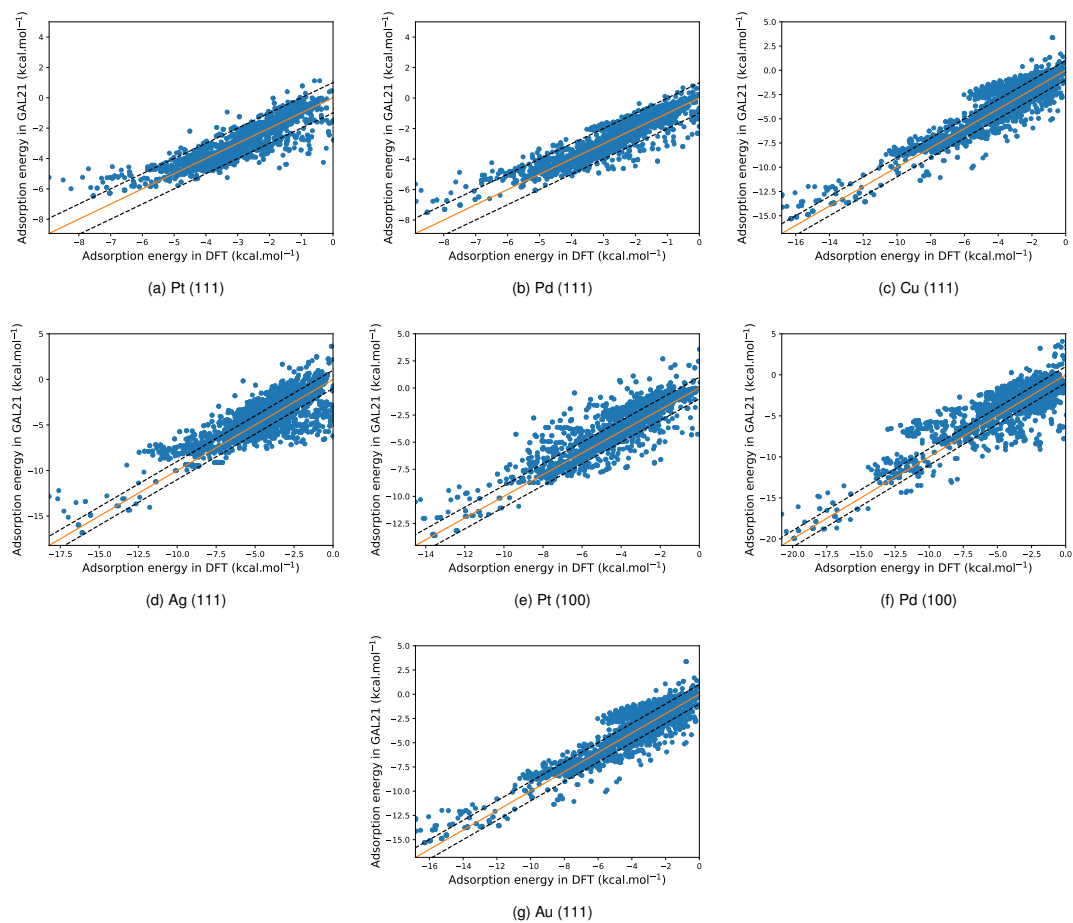


Figure C.1 – Comparison of the adsorption energy of multiple adsorption conformations of a single water molecule on each metals, calculated by DFT and GAL21. All the configurations of the total set, resulting in endothermic adsorption energies in DFT are included. Broken lines indicate errors of $\pm 1 \text{ kcal.mol}^{-1}$.

Appendix C. The GAL21 force field: Appendix

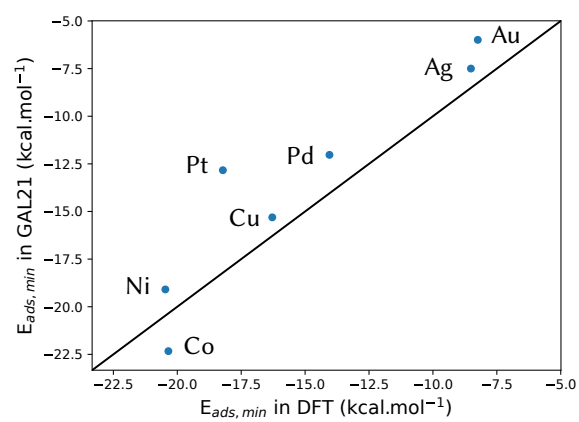


Figure C.2 – Parity representation of the optimal adsorption energy of water on each metal obtained with GAL21 compared to the one obtained in DFT. Each minimum is the effective minimum of the functional form by which it is evaluated, therefore, a dot can represent the energy obtained for different configurations in DFT or with GAL21.



D Water adlayers on noble metal surfaces: Appendix

This appendix is provided as the supplementary information corresponding to chapter 5

D.1 Additional Analysis

D.1.1 Water–Water interaction

The water–water interaction as assessed in the absence of the metal surfaces amounts to -4 (Pt) to -5 (Au) kcal·mol⁻¹ per water molecule, indicating that the chemisorption on Pt(111) imposes stronger constraints on the water geometries than the weaker interaction with Au(111).

In other words, the chemisorption on Pt leads to water layers that adopt less favorable geometries than on Au, with the deformation energy at the single molecule level being negligible. Interestingly, Cu is, in this respect, closer to the behavior of Pt than of Au. This is likely a coincidence, with the lattice mismatch on Cu(111) playing the role of the chemisorption on Pt(111).

The water–water interaction is, in magnitude, dominated by the ΔE_{CT} , which contributes -4.0 kcal·mol⁻¹ per water molecule over Pt(111), close to the -4.2 kcal·mol⁻¹ average total stabilization.

The water–water interaction contributes -10 kcal·mol⁻¹ per water molecule, more than twice as much as on average, to the stability of the H^{up} add-layer. In contrast, the $\sqrt{37}$ and $\sqrt{39}$ structures benefit “only” from a stabilization of about -6 kcal·mol⁻¹ per molecule, once again pointing to the fact that the H^{up} layer is “peculiar” and not a typical case for the interaction of water with metal surfaces.

D.2 Additional Tables and Figures

| $\theta(^{\circ})/\phi(^{\circ})$ | [0 – 100] | [100 – 120] | [120 – 180] |
|-----------------------------------|-----------|-------------|-------------|
| [80 – 90] | -6.2 | -7.5 | -7.4 |
| [70 – 80] | -8.2 | -5.6 | -8.5 |
| [0 – 70] | -9.3 | -9.6 | -10.4 |

Table D.1 – $E_{ads}^{acceptor}$ (kcal·mol⁻¹) for acceptor with a distance to the surface $z > 3.0 \text{ \AA}$

For chemisorbed acceptors (with a distance to the surface $z < 3.0 \text{ \AA}$), $E_{ads}^{acceptor} = -5.4 \text{ kcal}\cdot\text{mol}^{-1}$ if $\theta < 60^{\circ}$ and -3.0 kcal·mol⁻¹ else.

Bibliography

- [1] Heinz, H.; Vaia, R. A.; Farmer, B. L.; Naik, R. R. Accurate Simulation of Surfaces and Interfaces of Face-Centered Cubic Metals Using 12-6 and 9-6 Lennard-Jones Potentials. *J. Phys. Chem. C* **2008**, *112*, 17281–17290.

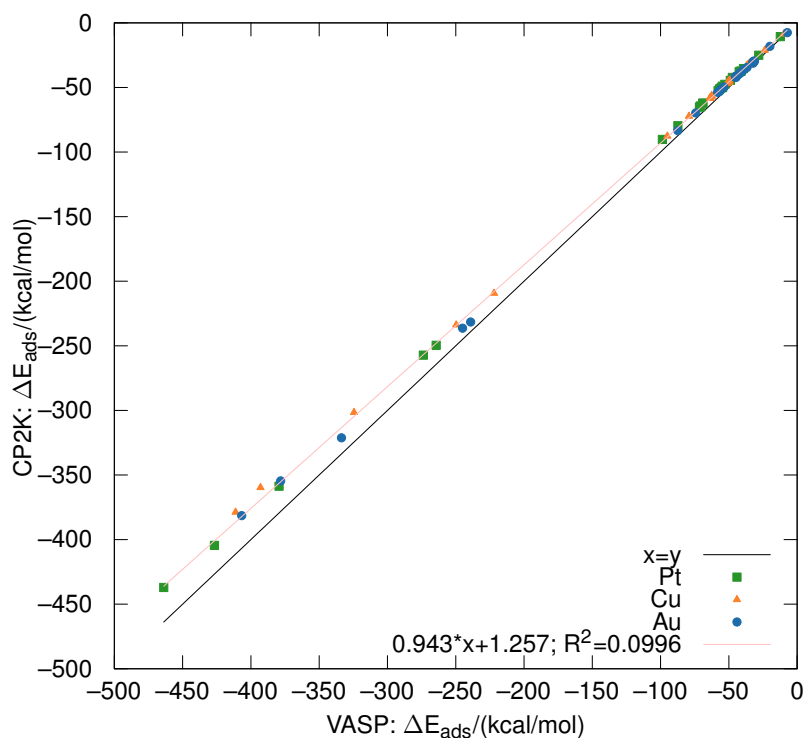


Figure D.1 – Interaction energies obtained with CP2K plotted against the ones from VASP. The black line corresponds to the bisector.

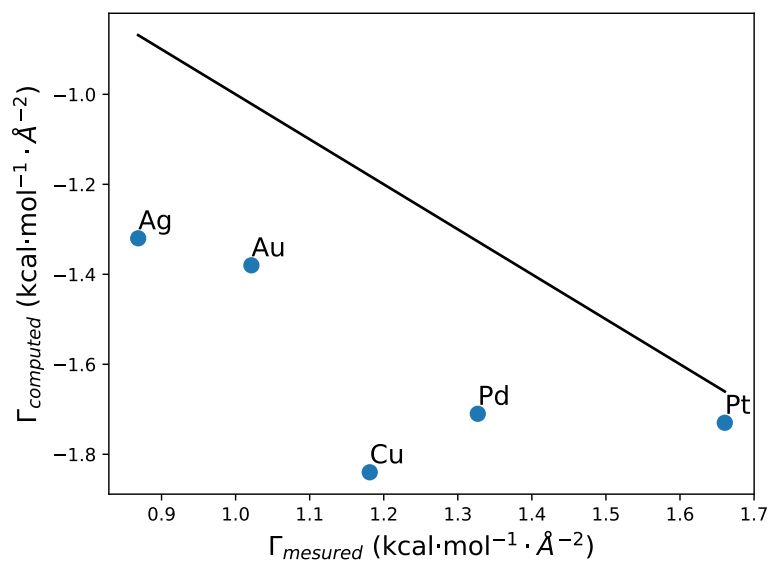


Figure D.2 – Surface energies in $\text{kcal}\cdot\text{mol}^{-1}\cdot\text{\AA}^2$ of the most stable ice-like water layer as a function of the experimental metal/liquid tension (retrieved from ref 1). The black line corresponds to the bisector.

Appendix D. Water adlayers on noble metal surfaces: Appendix

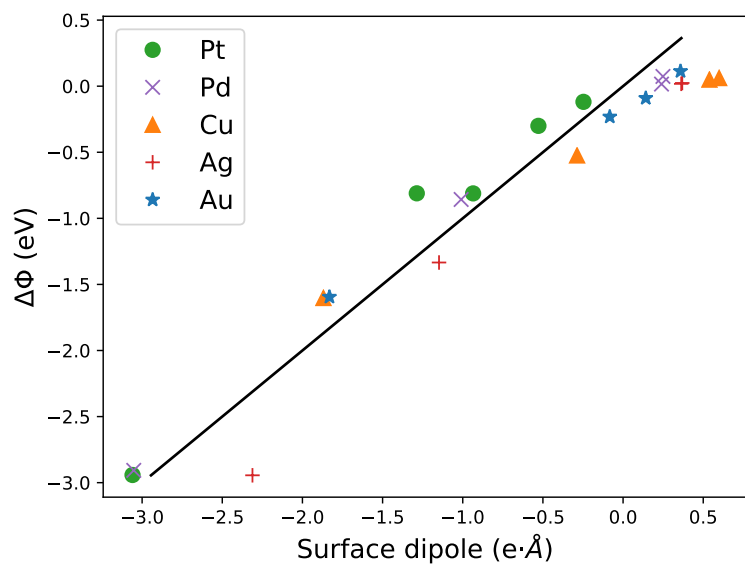


Figure D.3 – The correlation between the surface dipole moment and the change in workfunction $\Delta\Phi$ upon adsorption of ice add-layers.

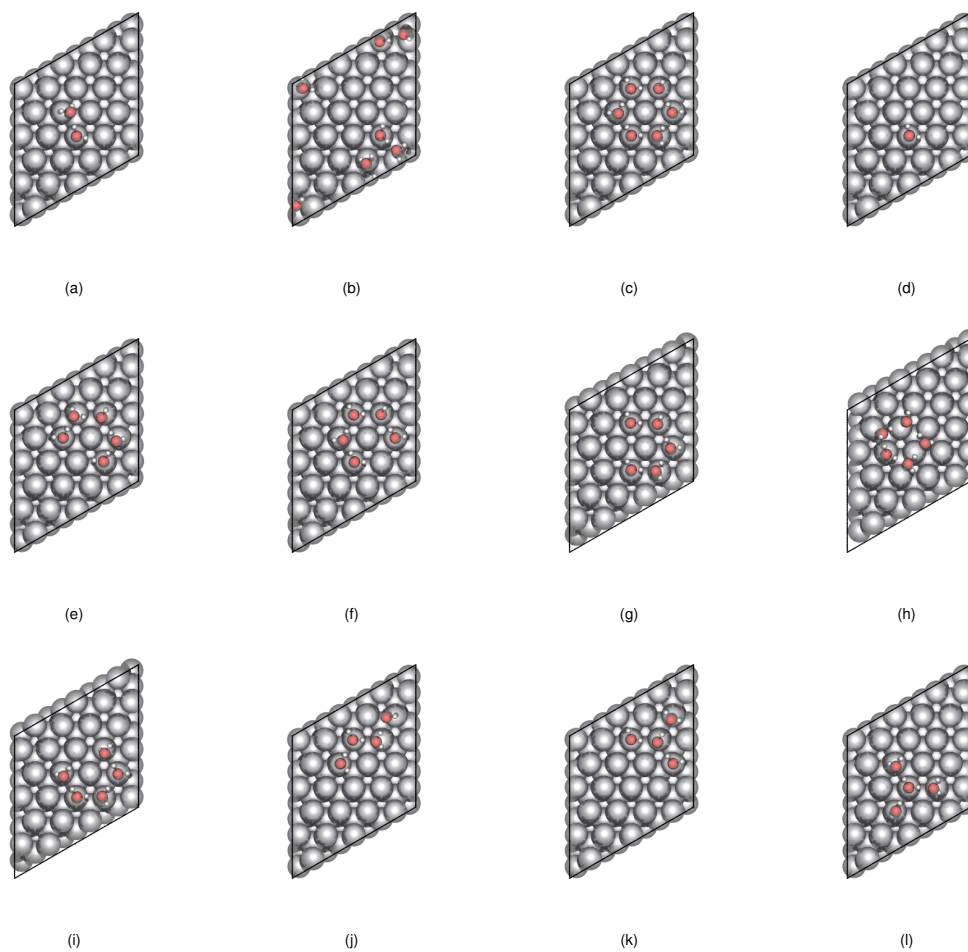


Figure D.4 – Visualization of the different discussed water oligomers. The cell and slab used were similar to those used for H^{up} and H^{down} water layers on each metal ($3\sqrt{3}\times 3\sqrt{3}$ (111)). (1^{st} part)

Appendix D. Water adlayers on noble metal surfaces: Appendix

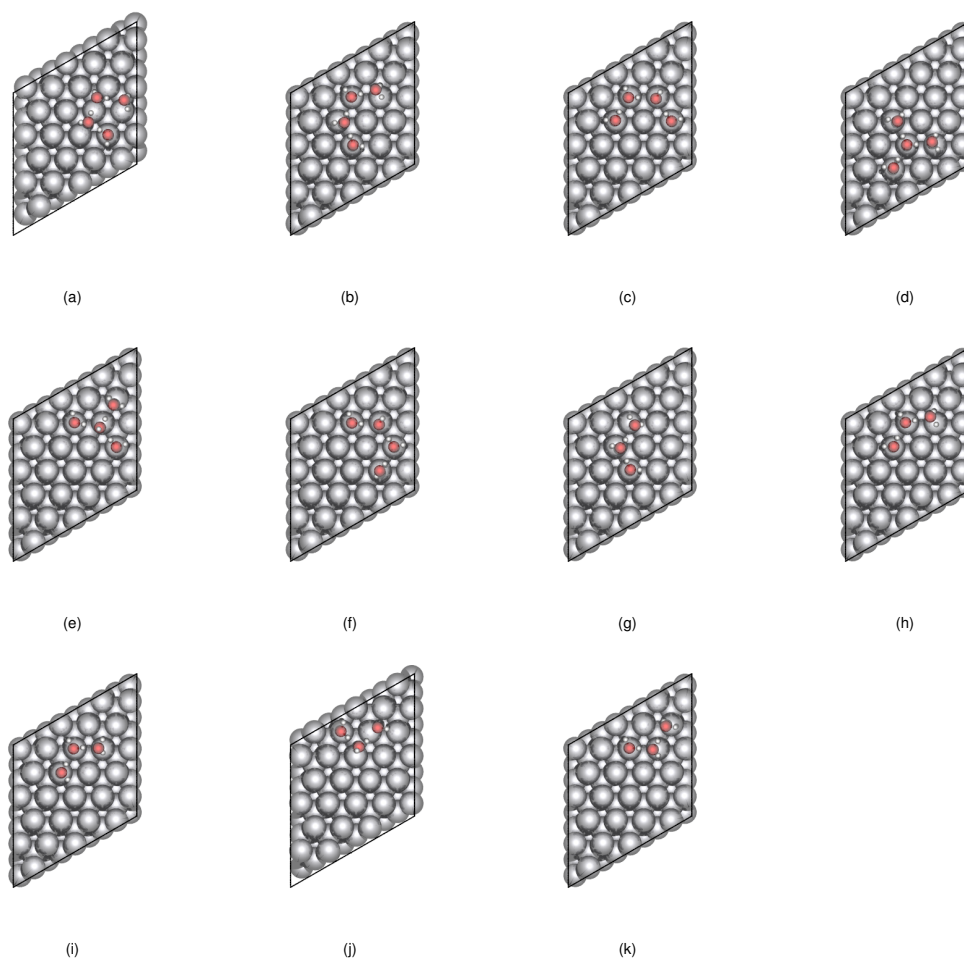


Figure D.5 – Visualization of the different discussed water oligomers. The cell and slab used were similar to those used for H^{up} and H^{dp} water layers on each metal ($3\sqrt{3}\times 3\sqrt{3}$ (111)). (2^{nd} part)

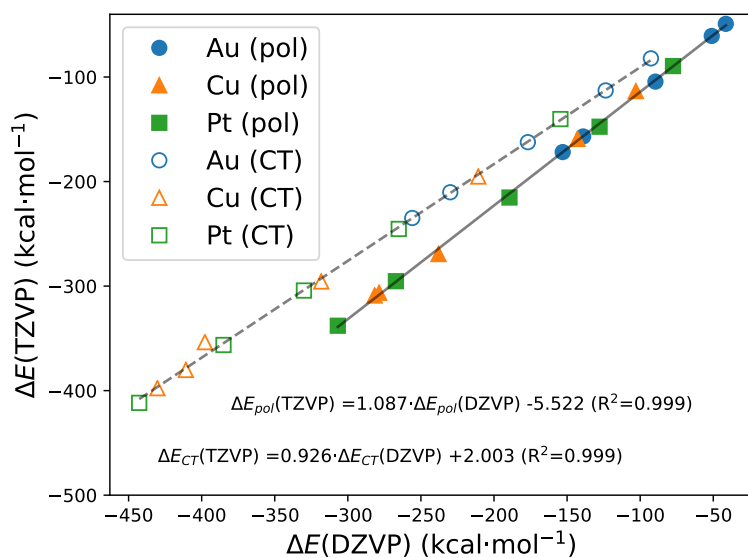


Figure D.6 – Correlation between DZVP basis set based computation and TZVP computations for ΔE_{pol} and ΔE_{CT} of water layers on Au(111), Cu(111), and Pt(111). The black continuous line corresponds to the fitted trend for polarisation energy and the dashed one to the fitted trend of charge transfer energy.

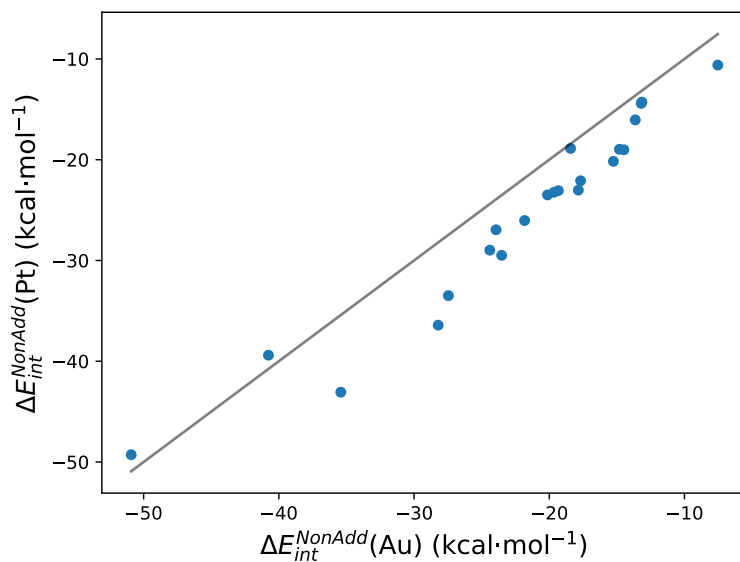


Figure D.7 – Correlation between ΔE_{int}^{NonAdd} for oligomers on Pt(111) vs Au(111). The black line corresponds to the bisector.

Appendix D. Water adlayers on noble metal surfaces: Appendix

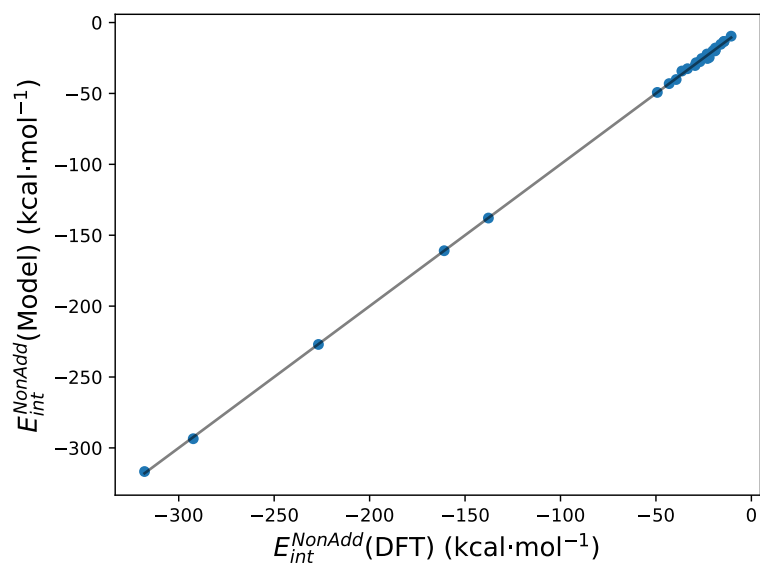


Figure D.8 – Parity plot for the linear regression model based on the H-bond acceptor type for the 27 investigated systems. Eleven variables are used (see Table D.1), leading to a root mean squared error of $1.37 \text{ kcal}\cdot\text{mol}^{-1}$. The black line represent the parity line.

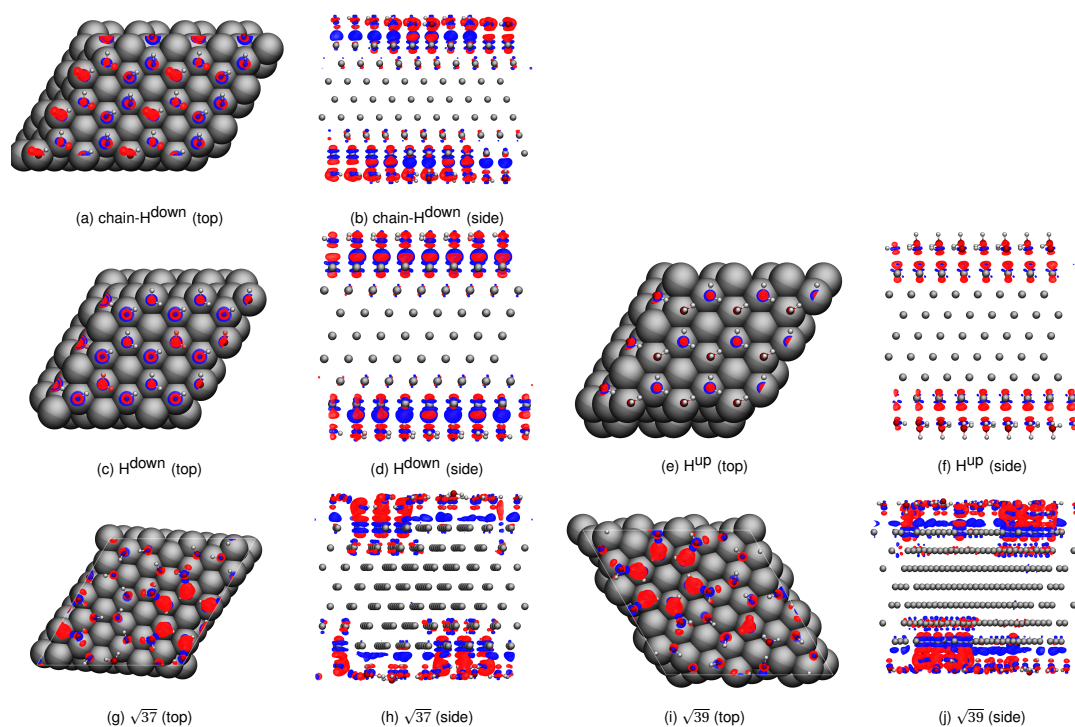


Figure D.9 – Visualization of the spatial distribution of the electronic density from water layers. Isosurfaces are plotted at -0.02 eV (?)

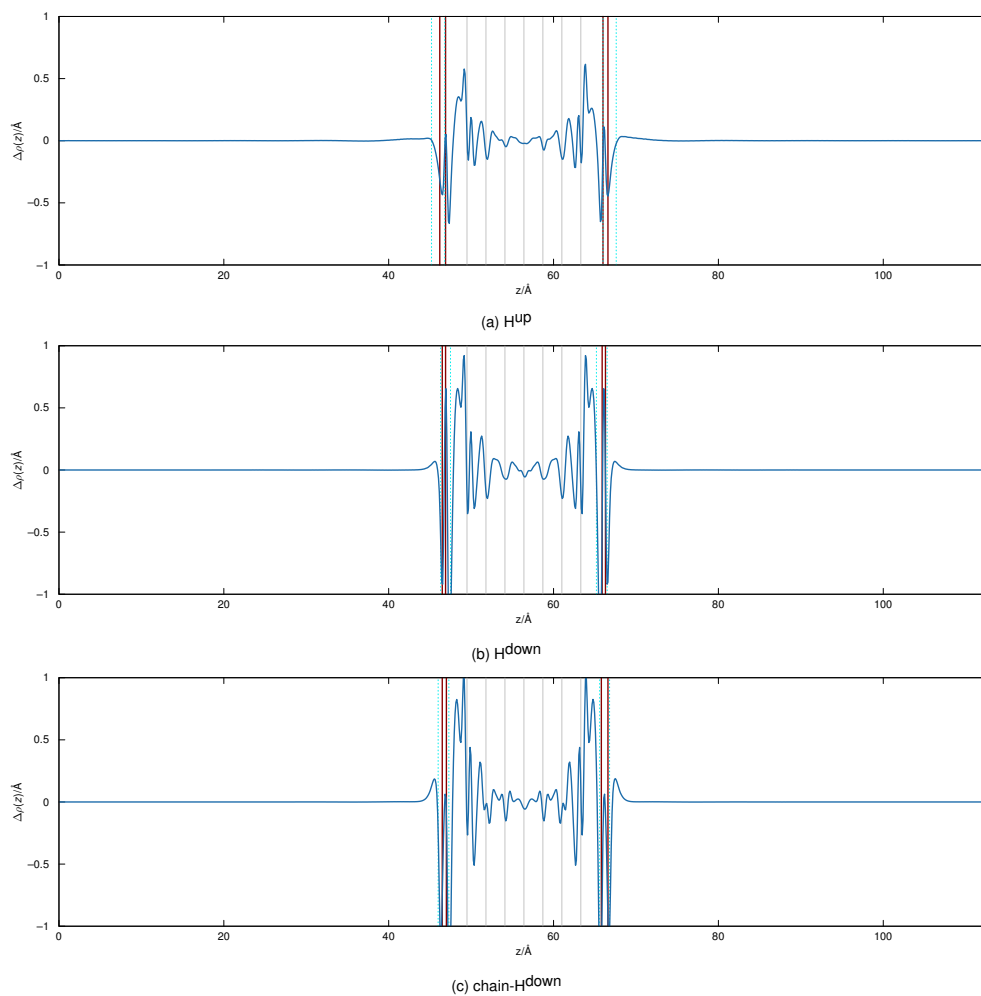


Figure D.10 – Averaged density difference ($\rho(\text{SCF}) - \rho(\text{surface, adlayer})$) profiles along the out-of-plane unit-cell direction (1^{st} part). Density accumulations are positive, while density depletion with respect to the sum of the densities of the surface and the adlayer is negative. Grey vertical lines indicate the position of the Pt metal layers. Dark red and broken cyan lines indicate the top-most and lowest position of the oxygen and hydrogen atoms, respectively.

Appendix D. Water adlayers on noble metal surfaces: Appendix

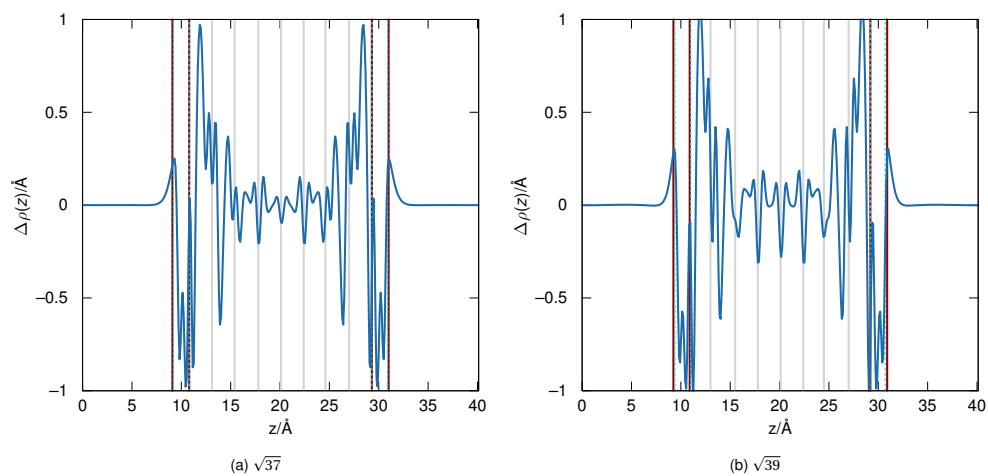



Figure D.11 – Averaged density difference ($\rho(\text{SCF}) - \rho(\text{U}_{\text{surface,adlayer}})$) profiles along the out-of-plane unit-cell direction (2^{nd} part). Density accumulations are positive, while density depletion with respect to the sum of the densities of the surface and the adlayer is negative. Grey vertical lines indicate the position of the Pt metal layers. Dark red and broken cyan lines indicate the top-most and lowest position of the oxygen and hydrogen atoms, respectively.



E **Reactivity of shape-controlled crystals and metadynamics simulations: Appendix**

This appendix is provided as the supplementary information corresponding to chapter 6

E.1 Experimental methods

Alumina materials syntheses. Alumina C (for Commercial) was obtained by calcination of commercial boehmite (Sasol PURAL SB3) at 600°C for 4 hours. Alumina F (for Fibers) was synthesized by precipitation of aluminum nitrate ($\text{Al}(\text{NO}_3)_3 \cdot 9\text{H}_2\text{O}$, 0.1 mol.L^{-1}) in acidic medium according to the method described by Chiche *et al.*¹ and Jolivet *et al.*² Alumina P (for Plates) and R (for Rods) were obtained by an hydrothermal treatment of alumina C in water (alumina P) or in acidified water with acetic acid (alumina R). Typically, 15 g of alumina C were dispersed in 100 mL of water or acidified water (pH=2). The mixture was heated at 200°C for 10 h under mechanical stirring and autogeneous pressure in a stainless steel autoclave. During this step, alumina was dissolved and boehmite precipitation occurred. Boehmite nanoparticles properties (size, morphology, texture, etc.) are depending on the experimental conditions (pH, temperature, concentrations...) ^{2,3}. In an acidic medium, boehmite precipitates as rod-like nanoparticles. In neutral medium, nanoparticles adopt a plate-like morphology. After cooling at RT, the solid phase was recovered by centrifugation, dried at 100°C overnight and calcinated at 600°C for 4 h.

Material characterization. XRD analyses were performed on powders with a Bragg-Brentano diffractometer (PANalytical X'Pert PRO MDP) using $\text{Cu K}\alpha$ radiation. Diffractograms were obtained from $2\theta = 4-74^\circ$ with a step of 0.033° and 5 s per step. Textural properties of aluminas were determined by N_2 sorption studies at 77 K using a Micromeritics ASAP 2000 instrument. The BET method was applied to determine the specific surface area. Transmission electron microscopy (TEM) images were obtained on a JEOL 2010 LaB₆ microscope operating at 200kV. A dispersion of the sample crushed in ethanol was deposited on standard holey carbon-covered copper TEM grids.

Adsorption experiments. Polyol adsorption isotherms were performed on three alumina materials exhibiting different morphologies in a 100 mL stainless steel autoclave equipped with a mechanical stirring rod (Top Industrie). Aqueous solutions of xylitol and sorbitol (0.5 g.L^{-1} , 1 g.L^{-1} , 2 g.L^{-1} , 4 g.L^{-1} , 6 g.L^{-1} and 8 g.L^{-1}) were prepared using commercial polyols (Sigma Aldrich) and deionized water. Typically, 2 g of alumina were dispersed in 50 mL of an aqueous solution of polyol. After 2 h at 200°C under autogeneous pressure (14 bar) and vigorous stirring, a sample of the liquid phase was taken and the solid phase was recovered by centrifugation. Final concentration was determined by HPLC analysis using a Shimadzu Rezex RXM-Monosaccharide Ca^{2+} 8% column connected to a differential refraction detector (Shimadzu RID10A). The amount of polyol adsorbed was calculated from the difference between initial and final concentrations.

E.2 $\gamma\text{-Al}_2\text{O}_3$ nanoparticles with different shapes

All nanoparticles were synthesised from the calcination of boehmite nanoparticles (see details in Experimental methods section E.1). The morphology (distribution of fractional facet areas) of the particles was determined from the diffractograms of boehmite before the calcination step since calcination is topotactic and does not modify the shape. Therefore, there is an unequivocal relationship between the shape of boehmite precursors and $\gamma\text{-Al}_2\text{O}_3$. Boehmite nanoparticles were considered as lamellar crystals (Fig. 6.2a and appendix Fig. E.1) using a geometry that is frequently observed.⁴ The α angle (see definition in appendix Fig. E.1) can be measured from TEM data. Its value is comprised between 95 and 110° , in good agreement with the 104° calculated by Lippens from boehmite lattice parameter⁵. This latter value was then chosen for the calculations. Boehmite diffractograms were deconvoluted in the $2\theta \in [10^\circ; 70^\circ]$ domain. In this range of setting, 15 characteristic diffraction lines are indexed in international tables of crystallography (ICDD PDF-2 Database (2016), n°021-1307). The deconvolution was realised using 15 pseudo-Voigt functions positioned on the indexed position of the diffraction lines. A liberty of $\Delta(2\theta) = 0.5^\circ$ on the left and on the right of the referenced position of the peak was tolerated. Typical dimensions of interest in a boehmite particle are defined in appendix Fig. E.1. Scherrer equation is used to estimate the average thickness e and the dimensions a and c of the boehmite particles. These lengths correspond to the diffraction by the (020), (200) and (002) planes at $2\theta \approx 14.5^\circ$, $2\theta \approx 49.2^\circ$, and $2\theta \approx 65.0^\circ$ respectively. x and y values are then determined using equations E.1 and E.2. With these lengths, the proportion of each facet area ((010), (001) and (101)) can be easily calculated. Similar method was used by Alphonse *et al.* to provide an estimation of boehmite nanoparticles morphologies.⁶ Since the $\text{AlOOH}/\gamma\text{-Al}_2\text{O}_3$ transition is topotactic, the morphologies of alumina nanoparticles are directly deduced by applying contraction rates⁷ in dimensions x , y and e (appendix Table E.1). Sizes and shapes of the nanoparticles in alumina P, C and F (resp. plates, commercial and fibres) as determined from XRD analysis (appendix Table E.2) are in good agreement with the TEM observations (Fig. 6.2g-j). However, this is not the case for alumina R (rods). According to TEM pictures, this alumina should present a very high proportion of lateral (100) facets (*i.e.* dimension $y \gg x$ and e) and a small proportion of (111) facets. This difference indicates that boehmite R platelets at the origin of alumina R are most likely polycrystalline. The polycrystallinity of such boehmite nanorods has already been observed by Mathieu *et al.*⁸ More generally, the morphologies obtained in the current work are in good agreement with the recent work by Lee *et al.*⁹ that determined the morphologies of boehmite platelets using TEM images.

Equations:

$$y = c - \left(\frac{a}{\tan(\pi\alpha/360)} \right) \quad (\text{E.1})$$

**Appendix E. Reactivity of shape-controlled crystals and metadynamics simulations:
Appendix**

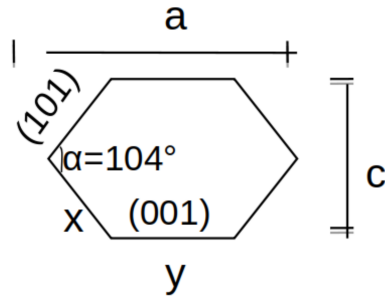


Figure E.1 – Schematics of the top view of a boehmite AlOOH nanoparticle. Dimensions of interest in that plane are indexed (see details in text). In addition, the e dimension corresponds to the thickness of the particle

Table E.1 – Unequivocal relationship between facets upon the topotactic calcination of boehmite into γ -Al₂O₃. The variation is given as a contraction rate for each directions^{7;10}

| Direction | | Contraction rate |
|-----------|--|------------------|
| Boehmite | γ -Al ₂ O ₃ | (%) |
| (010) | (110) | 31 |
| (001) | (100) | -6 |
| (101) | (111) | -1.6 |

$$x = \sqrt{\left(\frac{c-y}{2}\right)^2 + \left(\frac{a}{2}\right)^2} \quad (\text{E.2})$$

Scherrer equation :

$$\epsilon_{hkl} = \frac{K.k.\lambda}{\sqrt{(b_{hkl}^2 - b^2).cos(\theta)}} \quad (\text{E.3})$$

K is the shape factor of the particle (we chosed 1), k is a corrective factor due to the utilization of the full-width half maximum of the peaks, b_{hkl} is the full-width half maximum of the (hkl) line, b is the intrumental width, θ is the (hkl) line Braag angle.

Relations between γ -Al₂O₃ and boehmite (AlOOH) e, x and y dimensions:

$$e_{Al_2O_3} = 0.69e_{AlOOH} \quad (\text{E.4})$$

E.3. Adsorption of Sorbitol and Xylitol and Inhibition of Decomposition

Table E.2 – Characterisation of the morphology of the four samples of γ - Al_2O_3 consisting of nanoparticles with different edge lengths and facet surface area distributions. S_{BET} is the specific surface area. F, R, P and C respectively stand for fibres, rods, plates and commercial alumina.

| | S_{BET} (m^2/g) | $e_{\text{Al}_2\text{O}_3}$ (nm) | $x_{\text{Al}_2\text{O}_3}$ (nm) | $y_{\text{Al}_2\text{O}_3}$ (nm) | (110) (%) | (100) (%) | (111) (%) |
|------------------|--|-------------------------------------|-------------------------------------|-------------------------------------|--------------|--------------|--------------|
| Alumine F | 250 | 1.9 | 2.5 | 5.7 | 60 | 21 | 19 |
| Alumine R | 179 | 4.8 | 8.4 | 11.5 | 64 | 15 | 22 |
| Alumine P | 78 | 16.9 | 21.4 | 6.4 | 50 | 7 | 43 |
| Alumine C | 212 | 2.2 | 6.6 | 3.7 | 73 | 9 | 18 |

$$x_{\text{Al}_2\text{O}_3} = 1.06x_{\text{AlOOH}} \quad (\text{E.5})$$

$$y_{\text{Al}_2\text{O}_3} = 1.016y_{\text{AlOOH}} \quad (\text{E.6})$$

E.3 Adsorption of Sorbitol and Xylitol and Inhibition of Decomposition

E.3.1 Adsorption isotherms

Appendix Fig. E.2 shows adsorption isotherms of sorbitol (a) and xylitol (b) using three aluminas with different morphologies (C, P and F). For all aluminas, the amount of polyol adsorbed increases rapidly with the concentration to a value between 2 and 4 g.L^{-1} . At this concentration and for concentrations above, no boehmite was detected by XRD after the hydrothermal treatment and no Al_3^+ was detected in the liquid phase (measured with ICP AES). On the other hand, for concentrations lower than 4 g.L^{-1} , alumina dissolution and boehmite precipitation occurred. This is illustrated in appendix Fig. E.3 in the case of xylitol and alumina C: boehmite phase is always detected for concentrations lower than 4 g.L^{-1} . The same behaviour was observed in the case of sorbitol and with other aluminas. For concentrations higher than 4 g.L^{-1} , the amount of polyol adsorbed increases slower, indicating that primary adsorption sites become saturated, and that saturation of all those sites is not required to effectively protect alumina from dissolution. Appendix Fig. E.2 shows also that the isotherm profiles are the same for all aluminas but the amount of primary adsorption sites seems to be significantly different. This is confirmed by the fitted Langmuir isotherm parameters (appendix Table E.3). Indeed, the Langmuir constant is of the same order of

Appendix E. Reactivity of shape-controlled crystals and metadynamics simulations: Appendix

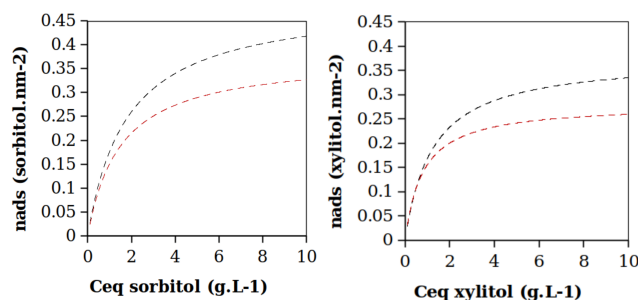


Figure E.2 – Adsorption isotherms at 200°C of sorbitol (a) and xylitol (b) on alumina C (black), F (red) and P (blue). Dashed lines correspond to the fit with the Langmuir model (see equation E.7). Conditions: 2 g Al₂O₃, 50 mL polyol/H₂O solution, 200°C, autogeneous pressure, 2 h.

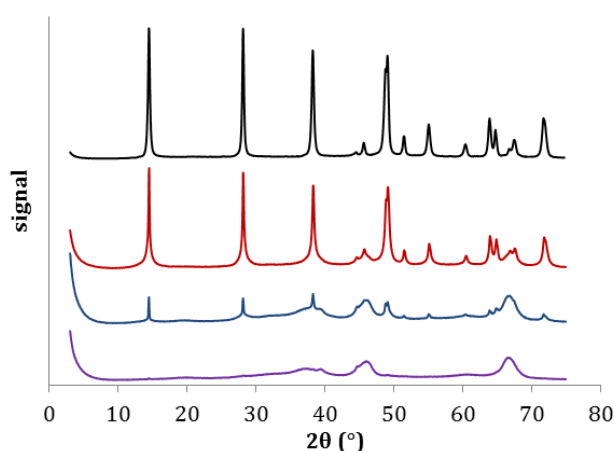


Figure E.3 – XRD patterns of alumina C after a 2h hydrothermal treatment at 200°C in aqueous solution of xylitol at 4 g.L⁻¹ (purple), 2 g.L⁻¹ (blue), 1 g.L⁻¹ (red), and 0 g.L⁻¹ (black).

magnitude for all aluminas indicating that the adsorption sites involved are the same. The monolayer constant value is however significantly different from one alumina to another. Thus, the number of primary adsorption sites is different from one alumina to the other. We note that after all the treatment performed here, only xylitol or sorbitol was detected in the liquid phase indicating that the polyols did not react under these conditions.

Langmuir equation:

$$\frac{n_{ads}}{n_{\infty}} = \frac{kC_{eq}}{1 + kC_{eq}} \quad (E.7)$$

k is the Langmuir constant (L.mol⁻¹), n_{∞} is the monolayer constant (molecule.nm⁻²), n_{ads} is the amount of polyol adsorbed (molecule.nm⁻²), C_{eq} is the equilibrium concentration.

E.3. Adsorption of Sorbitol and Xylitol and Inhibition of Decomposition

Table E.3 – Fitted Langmuir parameters from the experimental curves plotted in appendix Fig. E.2

| | Xylitol | | | Sorbitol | | |
|---|---------|------|------|----------|------|------|
| | C | F | P | C | F | P |
| n_{∞} (molecule.nm ⁻²) | 0.37 | 0.29 | 0.24 | 0.49 | 0.38 | 0.31 |
| k (L.mol ⁻¹) | 125 | 181 | 94 | 101 | 121 | 102 |

Table E.4 – Sorbitol and xylitol inhibiting coverages for the four alumina samples used in this study. Inhibiting coverages are determined from the amount of polyol adsorbed during a 200°C hydrothermal treatment in a polyol solution at 4 g.L⁻¹. Specific surface areas were determined with N₂ sorption isotherms at 77 K. The concentration of the remaining polyol in solution was determined by HPLC.

| Alumina | Sorbitol inhibiting coverage (sorbitol.nm ⁻²) | Xylitol inhibiting coverage (xylitol.nm ⁻²) |
|---------|--|--|
| C | 0.33±0.02 | 0.28±0.03 |
| F | 0.26±0.02 | 0.21±0.06 |
| P | 0.22±0.07 | 0.17±0.08 |
| R | 0.28±0.03 | 0.23±0.04 |

E.3.2 Inhibition of decomposition and inhibiting coverage

The inhibition coverage is defined as the amount of polyol adsorbed on the alumina surface at a polyol concentration of 4 g.L⁻¹. This is so because all alumina samples were found to require 4 g.L⁻¹ as the minimum polyol concentration to reach full protection. This defined concentration was also used for alumina R, without performing any further isotherm analysis. We note that using this concentration of 4 g.L⁻¹, no boehmite was detected after a hydrothermal treatment at 200°C for 10 hours (not shown here). In fact, there was no difference between the amount of polyol adsorbed after a high temperature treatment of 2 hours or 10 hours indicating that the adsorption equilibrium is quickly reached.

Under the assumption that both sorbitol and xylitol adsorb specifically to edges, one can also define a lineal inhibiting coverage. To do so, we can first determine the total length D of edges for one particle in each sample using the dimensions given in appendix Table E.2 (see equation E.8). From these dimensions, one can also determine the surface area of one particle $S_{particle}$. The amount N of particles in each sample can then be estimated from the BET specific surface area, the mass of the alumina sample m and $S_{particle}$ (see equation E.9). Dividing the amount n_{ads} of polyol adsorbed by the product $N \times D$ we obtain the lineal coverage.

$$D = 8x + 6e + 4y \quad (E.8)$$

**Appendix E. Reactivity of shape-controlled crystals and metadynamics simulations:
Appendix**

Table E.5 – Lineal inhibiting coverage for sorbitol and xylitol for each sample of alumina.

| Alumina | Sorbitol inhibiting coverage (sorbitol.nm ⁻²) | Xylitol inhibiting coverage (xylitol.nm ⁻²) |
|----------|--|--|
| C | 1.06±0.08 | 0.90±0.12 |
| P | 2.76±0.89 | 1.92±1.30 |
| R | 1.41±0.15 | 1.18±0.25 |
| F | 0.51±0.04 | 0.42±0.06 |

$$N = \frac{S_{BET}m}{S_{particle}} \quad (E.9)$$

$$\Lambda = \frac{n_{ads}}{N \times D} \quad (E.10)$$

In appendix Tables E.4 and E.4 errors have been calculated from High Performance Liquid Chromatography (HPLC) measurement of C_{eq} (equation E.11). HPLC standard deviation (ΔC_{eq} value has been determined to be 5% for a concentration range of 0.1 to 1 g.L⁻¹ and 2% for the range of 1 to 10 g.L⁻¹. Errors due to weight measurement, initial concentration, specific surface area and dimensions of edges have been neglected.

$$\Delta n_{ads} = n_{ads} \frac{\Delta C}{C_i - C_{eq}} \quad (E.11)$$

E.3.3 Relation between inhibiting coverages and the morphology of the nanoparticles.

The total number of adsorbed molecules N (say polyol) writes as the sum over the number of adsorbed molecules on each surface:

$$N = N_{111} + N_{110} + N_{100} \quad (E.12)$$

Dividing by the area of the entire surface accessible to adsorbates S_{tot} , we can write the total

E.3. Adsorption of Sorbitol and Xylitol and Inhibition of Decomposition

coverage:

$$\Theta = \frac{N}{S_{tot}} = \frac{N_{111}}{S_{tot}} + \frac{N_{110}}{S_{tot}} + \frac{N_{100}}{S_{tot}} \quad (\text{E.13})$$

We can then introduce the area of each facets S_{111} , S_{110} and S_{100} :

$$\Theta = \frac{N}{S_{tot}} = \frac{S_{111}}{S_{tot}} \frac{N_{111}}{S_{111}} + \frac{S_{110}}{S_{tot}} \frac{N_{110}}{S_{110}} + \frac{S_{100}}{S_{tot}} \frac{N_{100}}{S_{100}} \quad (\text{E.14})$$

The total coverage simply writes as a sum over the fractional area x_i of each surface times its partial coverage θ_i :

$$\Theta = \frac{N}{S_{tot}} = \theta_{111}x_{111} + \theta_{110}x_{110} + \theta_{100}x_{100} \quad (\text{E.15})$$

In the ideal situation where adsorbates only cover one surface specifically (say the (110) facet), the equation reduces to:

$$\Theta = \frac{N}{S_{tot}} = \theta_{110}x_{110} \quad (\text{E.16})$$

Similarly one can derive the same equation assuming that polyols only adsorb on edges. In the particular and ideal case of specific adsorption on one edge i , the total lineal inhibiting coverage Λ writes as the product of the partial lineal coverage λ on edge i with the fraction x_i of edge i : $\Lambda = \lambda_i x_i$

E.3.4 Can kinks and edges be involved in the decomposition mechanism of alumina?

First, the amount of kinks is much smaller than the amount of polyol required to inhibit the decomposition of alumina. It is therefore very unlikely that they play a major role in the decomposition mechanism of alumina. As for the edges, the situation is a bit more delicate. In a polydentate configuration, the size of either xylitol or sorbitol is about 1 nm, meaning that lineal coverages cannot go beyond 1 nm⁻¹. This corresponds to the order of magnitude of

Appendix E. Reactivity of shape-controlled crystals and metadynamics simulations: Appendix

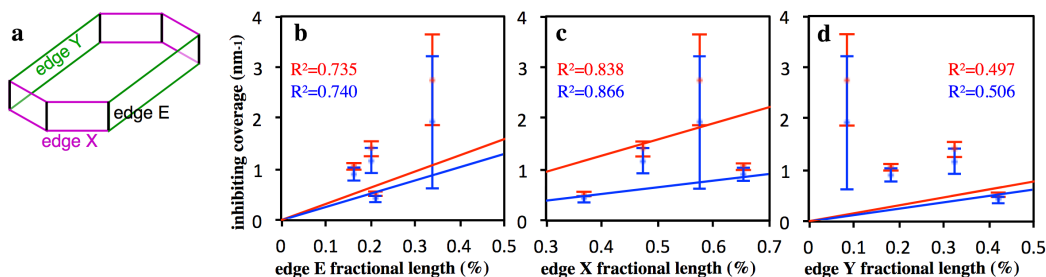


Figure E.4 – Non-implication of edges in the inhibiting adsorption of polyols on the four alumina samples. **a**, General topology of a γ - Al_2O_3 nanoparticle exhibiting three major edges: E in black, X in purple and Y in green. **b,c,d**, Comparisons between the *lineal inhibiting coverage* (sorbitol in red, xylitol in blue) and the fraction of exposed E (**d**), X (**e**) and Y (**f**) edge lengths. The experimental data sets are fitted to the zero-intercept linear model derived in appendix Section E.3.3. The fitted curves are represented as straight lines. No correlation could be established for any edges ($R^2 < 0.9$).

lineal inhibiting coverages determined experimentally and given in appendix Table E.5. The fact that lineal coverages can experimentally exceed 1 nm^{-1} is already a bit suspicious but could be explained with a certain amount of monodentate species at the edges. We thus need to analyse edges in more details.

To understand the potential role of edges, we have followed the same analysis as that carried out for the facets and described in Fig. 6.2. We assume in this paragraph that the weak spots are on the edges, *i.e.* decomposition is initiated at the edges and polyols preferably interact with the edges thereby providing protection of the nanoparticles. First, it is worth noting that the lineal inhibiting coverages vary between 0.51 and 2.76 nm^{-1} and 0.42 and 1.92 nm^{-1} for sorbitol and xylitol respectively. From one sample to another, only the shape of the nanoparticles changes: the three types of edges (namely E, X and Y see appendix Fig. E.4) are present in different proportions (see appendix Table E.2). The strong variation of the lineal inhibiting coverages (up to a factor of 5) therefore suggests that adsorption might occur more preferably at one specific edge. When we plot the lineal inhibiting coverage as a function of the fractional length, we see however no correlations ($R^2 < 0.9$). This means that there are no such things as specific interaction with one edge in particular. The shape effect evidenced by the strong variation of (lineal) inhibiting coverage can seemingly be solely explained for polyol molecules interacting specifically with the (110) facet, as shown in Fig. 6.2.

This is consistent with previous work by Copeland *et al.*¹¹ and Larmier *et al.*^{12,13} who were able to explain the properties of moderately hydrated alumina regarding the spectroscopy and reactivity of alcohols/polyols without invoking edges and kinks. It is very likely that the Lewis acid and basic sites at edges and kinks are almost instantaneously saturated with water at the early stage of water adsorption. The resulting aluminol groups are most probably strongly bound to the edges/kinks and cannot be displaced with alcohol/polyol molecules.

Bibliography

- [1] Chiche, D.; Digne, M.; Revel, R.; Chaneac, C.; Jolivet, J.-P. Accurate determination of oxide nanoparticle size and shape based on X-ray powder pattern simulation: Application to boehmite AlOOH. *Journal of Physical Chemistry C* **2008**, *112*, 8524–8533, WOS:000256492500007.
- [2] Jolivet, J. P.; Froidefond, C.; Pottier, A.; Chaneac, C.; Cassaignon, S.; Tronc, E.; Euzen, P. Size tailoring of oxide nanoparticles by precipitation in aqueous medium. A semi-quantitative modelling. *Journal of Materials Chemistry* **2004**, *14*, 3281–3288, WOS:000224735700028.
- [3] He, T.; Xiang, L.; Zhu, S. Different nanostructures of boehmite fabricated by hydrothermal process: effects of pH and anions. *Crystengcomm* **2009**, *11*, 1338–1342, WOS:000267920400029.
- [4] Busca, G. The surface of transitional aluminas: A critical review. *Catalysis Today* **2014**, *226*, 2–13, WOS:000332407200002.
- [5] Aad, J. A.; Casale, S.; Michau, M.; Courty, P.; Diehl, F.; Marceau, E.; Carrier, X. Chemical Weathering of Alumina in Aqueous Suspension at Ambient Pressure: A Mechanistic Study. *Chemcatchem* **2017**, *9*, 2186–2194, WOS:000412338800017.
- [6] Alphonse, P.; Courty, M. Structure and thermal behavior of nanocrystalline boehmite. *Thermochimica Acta* **2005**, *425*, 75–89.
- [7] Lippens, B. C. Structure and texture of aluminas. **1961**, Publisher: Waltman.
- [8] Mathieu, Y.; Lebeau, B.; Valtchev, V. Control of the Morphology and Particle Size of Boehmite Nanoparticles Synthesized under Hydrothermal Conditions. *Langmuir* **2007**, *23*, 9435–9442, Publisher: American Chemical Society.
- [9] Lee, J.; Jang, E. J.; Jeong, H. Y.; Kwak, J. H. Critical role of (100) facets on γ -Al₂O₃ for ethanol dehydration: Combined efforts of morphology-controlled synthesis and TEM study. *Applied Catalysis A: General* **2018**, *556*, 121–128.
- [10] Digne, M.; Sautet, P.; Raybaud, P.; Euzen, P.; Toulhoat, H. Use of DFT to achieve a rational understanding of acid–basic properties of γ -alumina surfaces. *Journal of Catalysis* **2004**, *226*, 54–68.
- [11] Copeland, J. R.; Shi, X.-R.; Sholl, D. S.; Sievers, C. Surface Interactions of C₂ and C₃ Polyols with γ -Al₂O₃ and the Role of Coadsorbed Water. *Langmuir* **2013**, *29*, 581–593.
- [12] Larmier, K.; Nicolle, A.; Chizallet, C.; Cadran, N.; Maury, S.; Lamic-Humblot, A.-F.; Marceau, E.; Lauron-Pernot, H. Influence of Coadsorbed Water and Alcohol Molecules on Isopropyl Alcohol Dehydration on γ -Alumina: Multiscale Modeling of Experimental Kinetic Profiles. *ACS Catal.* **2016**, *6*, 1905–1920, Publisher: American Chemical Society.

Appendix E. Reactivity of shape-controlled crystals and metadynamics simulations:
Appendix

- [13] Larmier, K.; Chizallet, C.; Cadran, N.; Maury, S.; Abboud, J.; Lamic-Humblot, A.-F.; Marceau, E.; Lauron-Pernot, H. Mechanistic Investigation of Isopropanol Conversion on Alumina Catalysts: Location of Active Sites for Alkene/Ether Production. *ACS Catal.* **2015**, *5*, 4423–4437, Publisher: American Chemical Society.